PACIFIC EARTHQUAKE ENGINEERING
RESEARCH CENTER

Demand Fragility Surfaces for Bridges in Liquefied and Laterally Spreading Ground

Scott J. Brandenberg
Department of Civil and Environmental Engineering
University of California, Los Angeles

Jian Zhang
Department of Civil and Environmental Engineering
University of California, Los Angeles

Pirooz Kashighandi
Department of Civil and Environmental Engineering
University of California, Los Angeles

Yili Huo
Department of Civil and Environmental Engineering
University of California, Los Angeles

Minxing Zhao
Department of Civil and Environmental Engineering
University of California, Los Angeles

PEER 2011/01
MARCH 2011

Demand Fragility Surfaces for Bridges in Liquefied and Laterally Spreading Ground

Scott J. Brandenberg
Department of Civil and Environmental Engineering
University of California, Los Angeles

Jian Zhang
Department of Civil and Environmental Engineering
University of California, Los Angeles

Pirooz Kashighandi
Department of Civil and Environmental Engineering
University of California, Los Angeles

Yili Huo
Department of Civil and Environmental Engineering
University of California, Los Angeles

Minxing Zhao
Department of Civil and Environmental Engineering
University of California, Los Angeles

PEER Report 2011/01
Pacific Earthquake Engineering Research Center
College of Engineering
University of California, Berkeley

March 2011

ABSTRACT

This report presents demand fragility surfaces for bridges in liquefied and laterally spreading ground that represent probability P(EDP>edp|IM=im), where a vector of engineering demand parameters is presented and the intensity measure is taken as free-field lateral spreading ground displacement. Equivalent global nonlinear finite element analyses were used to generate the responses of bridges due to liquefaction-induced lateral spreading, while nonlinear dynamic time-history analyses were implemented to determine the response due to seismic shaking. A classification system was developed for the bridges based on the type of superstructure, how the superstructure connects to abutments and piers, and the age of the bridges. Model input parameters were represented using random variables to capture the variability in structural and geotechnical conditions at Caltrans bridge sites. Nonlinear equivalent static analyses were conducted with inputs sampled randomly using the Monte-Carlo simulation method. Covering a wide range of different structural and geotechnical configurations, demand fragility surfaces were provided, which are a significant improvement over existing relations. Previous relations were not derived systematically and are known to be overly-conservative. The study also compares the seismic vulnerability of different classes of typical Caltrans bridges subject to seismic shaking and liquefaction-induced lateral spreading. It finds that although the fragility functions subjected to either shaking or lateral spreading show significant correlation with the structural characterizations, differences emerge for ground shaking and lateral spreading conditions. The fragility surfaces presented herein are ideally suited for implementation within the Pacific Earthquake Engineering Research Center's methodology in a transportation network analysis, or as a screening tool for identifying a manageable subset of bridges for more systematic individual retrofit evaluation.

ACKNOWLEDGMENTS

This work was sponsored by the Pacific Earthquake Engineering Research Center's (PEER's) Program of Applied Earthquake Engineering Research of Lifelines Systems supported by the California Department of Transportation and the Pacific Gas and Electric Company. Any opinions, findings, and conclusions or recommendations expressed in this material are those of the authors and do not necessarily reflect those of the sponsors.

The authors would like to acknowledge the assistance of Tom Shantz, Fadel Alameddine, Mark Mahan, and Mark Yashinsky from Caltrans for aiding with as-built bridge drawings and Prakashan Korambath from UCLA for helping to set up OpenSees on the Hoffman 2 parallel computing cluster.

CONTENTS

ABSTRACT ..... **iii**
ACKNOWLEDGMENTS ..... **v**
TABLE OF CONTENTS ..... **vii**
LIST OF FIGURES ..... **xi**
LIST OF TABLES ..... **xvii**

1 INTRODUCTION **1**
1.1 Liquefaction and Lateral Spreading 1
1.2 Case Histories of Damage to Pile Foundations in Lateral Spreads 1
1.3 Implications for Caltrans Bridges 6
1.4 Available Fragility Functions 9
1.5 Analysis Method 13
1.6 Organization of the Report 14

2 GLOBAL EQUIVALENT STATIC ANALYSIS METHOD **17**
2.1 Structural Modeling 20
2.1.1 Pier Columns and Piles 20
2.1.2 Abutments, Superstructure, and Pile Caps 21
2.1.3 Bearings at Abutments 22
2.1.4 Bearings at Simply Supported Spans 24
2.2 Soil-Structure Interaction Modeling 25
2.2.1 Influence of Liquefaction on Passive Pressure Amplitude 26
2.2.1.1 Boundary Conditions Resulting in Rankine Passive Force 26
2.2.1.2 Influence of Underlying Weak Soil 30
2.2.1.3 Analytical Model 32
2.2.1.4 Discussion 34
2.2.1.5 Influence of Liquefaction on Passive Pressure Stiffness 37
2.2.1.6 Soil-Structure Interaction Elements on Piles 39
2.2.1.7 Selection of Inertia Loads 43
2.3 Example Analyses 45
2.3.1 Configuration of the Example Simply Supported Bridge with Seat-type Abutments 45

2.3.2 Effect of Different Displacement Patterns on the Response of the Bridge.....50
2.3.3 Effect of the Direction of the Inertia Demands on the Bridge Response.....53
2.3.4 Effect of Bridge Type on the Response of Bridges.....54
2.3.5 Comparison of Global Analyses and Local Analyses.....57
2.3.6 Effect of Pile Strength on the Response of the Bridges.....60
2.3.7 Pile Pinning Effect of Reducing Displacement Demands on Abutments.....62

3 INPUT PARAMETERS SELECTION.....67
3.1 Generic Bridge Configuration.....68
3.2 Structural Classification.....69
3.2.1 Vintage.....71
3.2.2 Structural Connection Type.....71
3.2.3 Number of Pier Columns per Bent.....72
3.2.4 Pile Type.....72
3.3 Selection of Bridge Input Parameter Distributions.....73
3.3.1 Span Lengths.....73
3.3.2 Pier Heights.....75
3.3.3 Superstructure Weight.....75
3.3.4 Pier Column Moment and Shear Capacity.....75
3.3.5 Bearings Parameters.....81
3.3.6 Pile Strengths.....83
3.4 Selection of Geotechnical Input Parameter Distributions.....85
3.4.1 Thickness of Natural Crust, Liquefied Sand, and Approach Embankments.....85
3.4.2 Undrained Shear Strength of Cohesive Nonliquefied Crust Material.....85
3.4.3 Lateral Loads from Embankment Soils.....87
3.4.4 Subgrade Reaction in Liquefied Sand.....87
3.4.5 Stiffness of Load Transfer in the Crust and Embankment.....92
3.4.6 Characterization of Axial Capacity.....92
3.4.7 Horizontal Variation of Lateral Spreading Surface Displacements.....92
3.4.8 Vertical Ground Deformation Profile.....94
3.5 Characterization of Inertia Demands on the Bridge.....94

4 FRAGILITY OF BRIDGES TO LATERAL SPREADING.....97
4.1 Performance-based Earthquake Engineering and Fragility Functions.....97
4.2 Generation of Demand Fragility Surfaces.....98
4.3 Fitting Fragility Surfaces to the Data.....104

4.4 Fragility Surface Results 108
4.4.1 Effect of Vintage on the Fragility of the Bridge 121
4.4.2 Effect of Structure Type on the Fragility of the Bridge 121
4.4.3 Effect of Pile Types on the Fragility of the Bridge 122
4.5 Correlation Tables 122
4.6 Example of Application of Fragility Surfaces 124
4.6.1 Site and Seismic Hazard Analysis 125
4.6.2 Liquefaction Triggering Evaluation 126
4.6.3 Ground Displacement Evaluation 127
4.6.4 Bridge Engineering Demand Parameter Evaluation 130

5 INFLUENCE OF DYNAMIC SHAKING COMPARED WITH LATERAL SPREADING 133
5.1 Introduction 133
5.2 Fragility Methods for Dynamic Shaking 135
5.2.1 Probabilistic Seismic Demand Analysis 135
5.2.2 Incremental Dynamic Analysis 136
5.3 Ground Motion and Bridge Modeling 137
5.3.1 Earthquake Ground Motion Selection and Intensity Measure 137
5.3.2 Damage Index and Limit States 137
5.3.3 Bridge Types 140
5.3.4 Numerical Models of Bridges 140
5.4 Fragility Anaysis for Dynamic Shaking 143
5.4.1 Analysis Example for Model E1 143
5.4.2 Fragility Functions of Different Bridge Types 145
5.5 Comparison of Fragility Results for Dynamic Shaking and Laterial Spreading 146
5.5.1 Simplified Procedure to Derive Fragility Functions for Lateral Spreading 146
5.5.2 Fragility Functions of Different Bridge Types under Liquefaction Induced Lateral Spreading 150
5.6 Summary 155

6 CONCLUSIONS AND FUTURE WORK 157
6.1 Research Findings and Conclusions 157
6.1 Future Work 158

REFERENCES 159

LIST OF FIGURES

Figure 1.1 Damage to steel piles of Showa Bridge. 2

Figure 1.2 Top of the wharf of Port of Oakland following the 1989 Loma Prieta earthquake. The cranes separated and could not operate as a result of the extension of the wharf 3

Figure 1.3 Soil profile and pile configuration of the wharf at the Port of Oakland....3

Figure 1.4 Damage to the battered piles supporting the wharf at the Port of Oakland during the 1989 Loma Prieta earthquake. 4

Figure 1.5 Unseating of the Nishinomiya Bridge as a result of lateral spreading during the 1995 Kobe earthquake.....5

Figure 1.6 Side view of the Landing Road Bridge in Whakatane, New Zealand, which suffered moderate damage due to 2 m (6.56 ft) of lateral spreading of the left bank during the 1987 Edgecumbe earthquake. 6

Figure 1.7 Distribution of California bridges by year of construction based on NBI database. 7

Figure 1.8 Schematic of a set of fragility curves for bridges with different vintages. 11

Figure 1.9 HAZUS fragility curves for damage to bridges as a result of lateral spreading 11

Figure 1.10 Estimated damage to bridges during the 1989 Loma Prieta earthquake. 12

Figure 1.11 Permanent offset in elastomeric bearing at Nagomi Bridge caused by ground deformation during the Niigata Chuetsu-Oki earthquake. 13

Figure 2.1 Fiber section of a 0.61 m (24 in.) CIDH pile model and the corresponding moment curvature relation. 21

Figure 2.2 Schematic of a seat-type abutment of the bridge. 22

Figure 2.3 Schematic of a simply supported bridge superstructure and the corresponding interface springs at the top of a pier. 25

Figure 2.4 Boundary conditions resulting in Rankine passive force for a 4 m- (13.12 ft-) thick cohesionless deposit: (a) frictionless wall, frictionless base; (b) rough wall, frictionless base; and (c) frictionless wall, rough base.....28

Figure 2.5 Passive pressure distributions for boundary conditions in Figure 2.4 at various distances behind the wall.....28

Figure 2.6 Deformed mesh and horizontal stresses for a 4 m- (157.5 in.-) thick cohesionless deposit with ϕ=35° and γ=20kN/m^3 over a 0.5 m- (19.7 in.-) thick weak layer with s_u=1 kPa. 31

Figure 2.7 Horizontal component of passive force versus s_u for various ϕ for (a) H=2 m (6.56 ft) and (b) H=4 m (13.12 ft). 31

Figure 2.8 Analytical model for estimating passive force for a cohesionless deposit resting on a weak layer. 33

Figure 2.9 Load cases wherein (a) positive δ is mobilized as passive bulge forms, and (b) negative δ is mobilized as crust settles. 35

Figure 2.10 Centrifuge model after liquefaction-induced deformation. The direction of slip between crust and pile group is ambiguous. 36

Figure 2.11 Mechanisms of spreading in nonliquefiable crust: (a) flowing mechanism and (b) equivalent block mechanism. 37

Figure 2.12 Load transfer in nonliquefiable crust: (a) recorded load-deflection data from centrifuge models and (b) normalized backbone load transfer relations 38

Figure 2.13 *p-y* behavior in liquefied sand for loose sand (left column) and medium dense sand (right column). 40

Figure 2.14 Stress-strain response and effective stress path for Sacramento River sand during undrained cyclic triaxial loading 41

Figure 2.15 Effect of peak free-field excess pore pressure ratio on the ultimate capacity of *p-y* materials in liquefied sand. 42

Figure 2.16 Schematic of the three-span simply supported bridge with seat-type abutments 46

Figure 2.17 CALTRANS acceleration response spectra for 5% damping for magnitude 7.25 ± 0.25 in site class D. 46

Figure 2.18 Global analysis load case 1 showing load pattern and deformed mesh (top) and deformed mesh and moment distribution in nonlinear beam column elements (bottom). Deformations amplified by a factor of 4.0. 51

Figure 2.19 Global analysis load case 2 showing load pattern and deformed m (top) and deformed mesh and moment distribution in nonlinear beam column elements (bottom). Deformations amplified by a factor of 2.0. 52

Figure. 2.20 Global analysis load case 3 showing load pattern and deformed mesh (top) and deformed mesh and moment distribution in nonlinear beam column elements (bottom). Deformations amplified by a factor of 4.0. 54

Figure 2.21 Schematic of the three-span continuous bridge with monolithic abutments. 55

Figure 2.22 Global analysis load case 4 (continuous bridge with monolithic abutments) showing load pattern and deformed mesh (top), and deformed mesh and moment distribution in nonlinear beam column elements (bottom). Deformations amplified by a factor of 4.0. 56

Figure 2.23 Local analysis 1 showing deformed mesh and moment distribution. Deformation × 1 58

Figure 2.24 Local analysis 2 showing deformed mesh and moment distribution. Deformation × 4 58

Figure 2.25 Local analysis 3 showing deformed mesh and moment distribution. Deformations × 4. 59

Figure 2.26 Global analysis load case 5 with CISS piles showing load pattern and deformed mesh (top) and deformed mesh and moment distribution in nonlinear beam column elements (bottom). Deformations amplified by a factor of 4.0. 61

Figure 2.27 Soil profile and its properties used in the pinning analysis of abutments. 63

Figure 2.28 Slope stability analyses performed using slide 5.0 and the associated failure surface for yield acceleration of $a_y = 0.0615g$.....64

Figure 2.29 Distribution of forces behind the abutment wall at the end of the global load case 1 analysis. 64

Figure 2.30 Results of the pinning analyses for different load cases 1, 2, and 3 at different peak ground motion levels for Kobe motion recorded at Port Island. 65

Figure 2.31 Ratio of pinning compatible displacement to free-field ground displacements for three load cases at different values of free-field ground displacement. 66

Figure 3.1 Template of the bridges for modeling and analyses: (a) bridges with continuous superstructure and monolithic abutments; (b) bridges with simply supported superstructure and seat-type abutments; and (c) bridges with continuous superstructure and seat-type abutments.....69

Figure 3.2 Classification of bridges based on vintage, structure type, number of piers, and type of piles. 70

Figure 3.3 Histograms of maximum span length of bridges from NBI database: (a) pre-1971 and (b) post-1971. 74

Figure 3.4 Examples of piles specification from as-built drawings: (a) 0.38 m (15 in.) precast concrete piles typically used in pre-1971 bridges; (b) post-1971 0.38 m (15 in.) precast piles; (c) post-1971 0.61 m (24 in.) CIDH piles; and (d) post-1971 0.61 m (24 in.) CISS piles. 84

Figure 3.5 Distribution of crust and liquefiable layer thickness based on USGS CPT logs for Northern California.....86

Figure 3.6 Soil and lateral spreading profile used in the example analyses. 90

Figure 3.7 Effective stress relations used in the example analyses calculated at the center of the liquefied sand layer. 90

Figure 3.8 *p-y* curves used in the example analyses at the center of the liquefied sand layer. 91

Figure 3.9 Soil and pile displacement and subgrade reaction and moment distribution for (a) $P_{ult} = 2xP_{ult\_API}$; (b) $P_{ult} = 1xP_{ult\_API}$; (c) $P_{ult} = 0.5 \times P_{ult\_API}$; and (d) m_p = 0.05.93 93

Figure 4.1 Generation of fragility function for pier curvature ductility of seven for post-1971 simply supported bridges with seat-type abutments and single-column piers; (a) probability mass function and (b) cumulative density function.....103

Figure 4.2 Fragility curves of two EDPs of simply supported bridges with seat-type abutments and single-column piers belonging to the post-1971 era: (a) pile cap displacement and (b) pier curvature ductility. 104

Figure 4.3 Linear regression of the values of fragility curve parameters: (a) logarithm of medians, (b) dispersion (standard deviation of logarithms of data), and (c) maximum probability for simply supported bridges with seat-type abutments and single column piers built post-1971. 106

Figure 4.4 Demand fragility surfaces plotted along with the discreet date for (a) pile cap displacement and (b) pier curvature ductility for simply supported bridges with seat-type abutments and single-column piers built post-1971. 108

Figure 4.5 Fragility functions for pier column curvature ductility for bridges with multi-column bents. Curvature ductility from top to bottom are 1 through 10 in increments of 1. 111

Figure 4.6 Fragility functions for pier column curvature ductility for bridges with single-column bents. Curvature ductility from top to bottom are 1 through 10 in increments of 1. 112

Figure 4.7 Fragility functions for pile cap displacement for bridges with multi-column bents. Pile cap displacements from top to bottom are 0.025 m (0.98 in.) to 0.25 m (9.84 in.) in increments of 0.25 m (9.84 in.). 113

Figure 4.8 Fragility functions for pile cap displacement for bridges with single-column bents. Pile cap displacement from top to bottom is 0.025 m (0.98 in.) to 0.25 m (9.84 in.) in increments of 0.025 m (0.98 in.). 114

Figure 4.9 Fragility functions for abutment displacement for bridges with multi-column bents. Abutment displacement from top to bottom is 0.025 m (0.98 in.) to 0.25 m (9.84 in.) in increments of 0.025 m (0.98 in.). 115

Figure 4.10 Fragility functions for abutment displacement for bridges with single-column bents. Abutment displacement from top to bottom is 0.025 m (0.98 in.) to 0.25 m (9.84 in.) in increments of 0.025 m (0.98 in.). 116

Figure 4.11 Fragility functions for abutment rotation for bridges with multi-column bents. Abutment rotation from top to bottom is 0.5% to 5% in increments of 0.5%. 117

Figure 4.12 Fragility functions for abutment rotation for bridges with single-column bents. Abutment rotation from top to bottom is 0.5% to 5% in increments of 0.5%. 118

Figure 4.13 Fragility functions for pile cap rotation for bridges with multi-column bents. Pile cap rotation from top to bottom is 0.5% to 5% in increments of 0.5%. 119

Figure 4.14 Fragility functions for pile cap rotation for bridges with single-column bents. Pile cap rotation from top to bottom is 0.5% to 5% in increments of 0.5%. 120

Figure 4.15 Hazard curves from probabilistic seismic hazard analysis of the Santa Monica site. 125

Figure 4.16 Distributions of magnitude contributions to seismic hazard. 126

Figure 4.17 Liquefaction triggering hazard curve for the Santa Monica site. 127

Figure 4.18 Free-field lateral spreading displacement hazard curve. 130

Figure 4.19 Fragility functions for post-1971 bridges with seat-type abutments, simply supported spans, multi-column bents, and 0.6 m- (1.97 ft-) diameter CIDH piles. Engineering demand parameters include: (a) pier column curvature ductility, (b) pile cap displacement, and (c) abutment displacement. 131
Figure 4.20 Hazard curves for (a) pier column curvature ductility, (b) pile cap displacement, and (c) abutment displacement. 131

Figure 5.1 Characteristics of selected earthquake ground motion records (horizontal component). 138
Figure 5.2 Sketches of the six bridge models. 141
Figure 5.3 Force-displacement relationships of column, isolation bearing, and gap element. 142
Figure 5.4 PSDA fragility analysis of Model E1. 144
Figure 5.5 Fragility functions of Model E1 using PSDA and IDA methods. 144
Figure 5.6 Fragility curves of six bridge models under seismic shaking. 147
Figure 5.7 Numerical modeling of lateral spreading to bridges. 148
Figure 5.8 Sketch of simulation for bridge and soil profile with liquefiable sand layer. 149
Figure 5.9 Bridge deformations under two lateral spreading load cases. 151
Figure 5.10 Fragility curves generated with Monte Carlo method and FOSM method. 151
Figure 5.11 Fragility curves of six bridge models under lateral spreading. 152
Figure 5.12 Mean IM values for six bridge models to reach various damage states when subject to seismic shaking and lateral spreading. 154

LIST OF TABLES

Table 2.1 *p*-multipliers, m_p, to account for liquefaction. 42

Table 2.2 Factors C_{liq} and C_{cc} for modification of the nonliquefied inertia loads.. 45

Table 2.3 Properties of three-span simply supported bridge with seat-type abutment. 47

Table 2.4 Thickness and properties of the soil layers in the layers used in the example problems. 47

Table 2.5 Summary of pier responses under different global and local loading conditions. ...51

Table 2.6 Comparison of the response between a simply supported bridge with seat-type abutments and a continuous bridge with monolithic abutments under the same loading conditions. 56

Table 2.7 Properties of the .61 m (24 in.) CISS piles....60

Table 2.8 Comparison of the response of the bridge with strong CISS piles under global and local analyses. 60

Table 3.1 Dead weight per unit area for the available pre-1971 Caltrans drawings. 76

Table 3.2 The median and dispersion of the normalized yield moment and the relationships between yield curvature and yield moment for circular and rectangular sections for both pre-1971 and post-1971 eras....77

Table 3.3 The fitting parameters for the natural log of medians of pier yield moments and the dispersion of the yield moments for circular and rectangular sections for both pre-1971 and post-1971 eras. 78

Table 3.4 The mean and standard deviation of the normalized shear capacity of the pier for both pre-1971 and post-1971 eras. 79

Table 3.5 The fitting parameters for the natural log of medians of pier shear capacity and the dispersion of the shear capacity for circular and rectangular sections for both pre-1971 and post-1971 eras. 80

Table 3.6 The fitting parameters for the natural log of medians of pier shear capacity and the dispersion of the shear capacity for circular and rectangular sections for both pre-1971 and post-1971 eras. 80

Table 3.7 The breakdown of elastomeric bearing heights for pre-1971 and post-1971 bridges. 81

Table 3.8 Mean and standard deviation of vertical stress on the elastomeric bearings for pre-1971 and post-1971 bridges. 81

Table 3.9 Yield moment and yield curvature for piles used in the analyses. 83

Table 3.10 Properties of the soil layers used in the example analyses,....89

Table 4.1 Engineering demand parameters and their recorded values for continuous bridges with monolithic abutments. 99
Table 4.2 Engineering demand parameters and their recorded values for simply supported bridges with seat-type abutments. 100
Table 4.3 Engineering demand parameters and their recorded values for continuous bridges with seat-type abutments. 101
Table 4.4 Generation of fragility function for curvature ductility of seven post-1971 simply supported bridges with seat-type abutments and single column piers. 102
Table 4.5 Fragility surface parameters for bridges with continuous superstructure, seat-type abutments, and single-column bents. 109
Table 4.6 Fragility surface parameters for bridges with continuous superstructure, seat-type abutments, and multi-column bents. 109
Table 4.7 Fragility surface parameters for bridges with continuous superstructure, monolithic abutments, and single-column bents. 109
Table 4.8 Fragility surface parameters for bridges with continuous superstructure, monolithic abutments, and multi-column bents. 110
Table 4.9 Fragility surface parameters for bridges with simply supported spans, seat-type abutments, and single-column bents. 110
Table 4.10 Fragility surface parameters for bridges with simply supported spans, seat-type abutments, and multi-column bents. 110
Table 4.11 Correlation coefficients among the natural logarithms of EDPs for bridges with continuous superstructure and seat-type abutments. 123
Table 4.12 Correlation coefficients among the natural logarithms of EDP's for bridges with continuous superstructures and monolithic abutments. 123
Table 4.13 Correlation coefficients among the natural logarithms of EDPs for bridges with simply supported spans. 124

Table 5.1 Definition of component level damage index of columns and bearings. 140
Table 5.2 Bridge component properties and modeling parameters. 143
Table 5.3 Probability properties of parameters of soil profile and foundation modeling. 148

1 Introduction

1.1 LIQUEFACTION AND LATERAL SPREADING

Liquefaction is defined as the strength loss of loose saturated cohesionless soils during undrained loading. The tendency for loose soils to contract during drained loading is expressed as generation of excess pore pressures during undrained loading, resulting in a reduction of effective stresses and loss of strength. Liquefaction often occurs during earthquakes, causing flow slides, lateral spreading, and settlements. This report focuses on lateral spreading as a result of earthquake-induced liquefaction and subsequent damage to bridges.

Lateral spreading is the permanent lateral deformation of gently-sloping ground due to liquefaction, typically on the order of centimeters up to a few meters. Lateral spreading occurs when driving shear stresses temporarily exceed the undrained shear strength of the liquefied soil, thereby causing an accumulation of displacement in the direction of static shear stress. Often, lateral spreading is associated with a cyclic mobility behavior in which inertia forces cause accumulation of displacement. Lateral spreading may also occur after strong shaking has ceased due to void redistribution. Static shear stresses are present in slopes or in level ground located near a free-face (usually adjacent to rivers, lakes, etc).

Lateral movement of the soil may result in a wide range of structural damage, ranging from none—when the structure is adequately strong to resist ground displacements—to collapse—when demands imposed by lateral spreading significantly exceed structural capacity.

1.2 CASE HISTORIES OF DAMAGE TO PILE FOUNDATIONS IN LATERAL SPREADS

Damage to structures as a result of liquefaction and lateral spreading in response to strong ground shaking is common. Figure 1.1 shows the collapse of Showa Bridge following the 1964

Niigata earthquake. Excessive lateral deformation of the liquefiable soils that supported the bridge caused damage to the pile foundations, resulting in large deformations of the piers that caused the decks of bridge to unseat and fall into the river.

Another example of lateral spreading was the damage incurred by wharf at the Port of Oakland during the 1989 Loma Prieta earthquake (Figures 1.2 to 1.4). Spreading of the rock fill material on top of liquefied loose hydraulic fill imposed significant loads on the piles that supported the wharf. The connection between the battered piles supporting the wharf and the soil contained a small unsupported length. During the earthquake the laterally stiff piles sustained large loads that exceeded their capacity, incurring damage at the point where they were connected to the wharf (Figure 1.4). The formation of a gap at the wharf-to-soil connection caused the crane rails to separate, rendering them useless for moving cargo onto and off freighter ships, which caused significant economic losses.

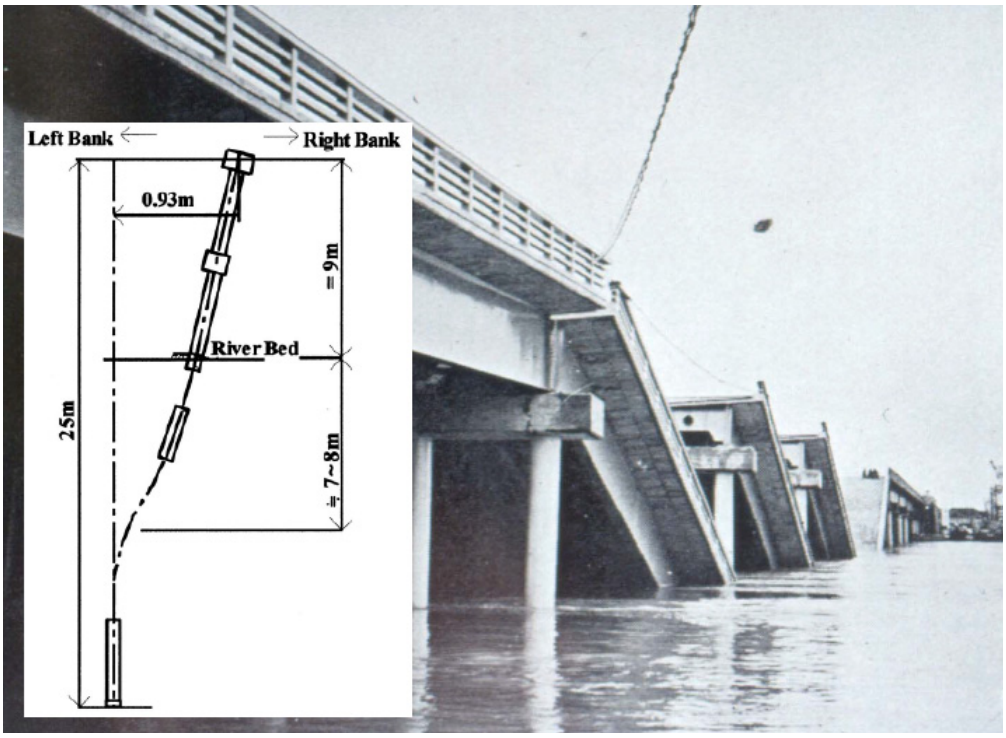

Figure 1.1 Damage to steel piles of Showa Bridge (Hamada 1992).

Figure 1.2 **Top of the wharf of Port of Oakland following the 1989 Loma Prieta earthquake. The cranes separated and could not operate as a result of the extension of the wharf (photo by John Egan, AMEC).**

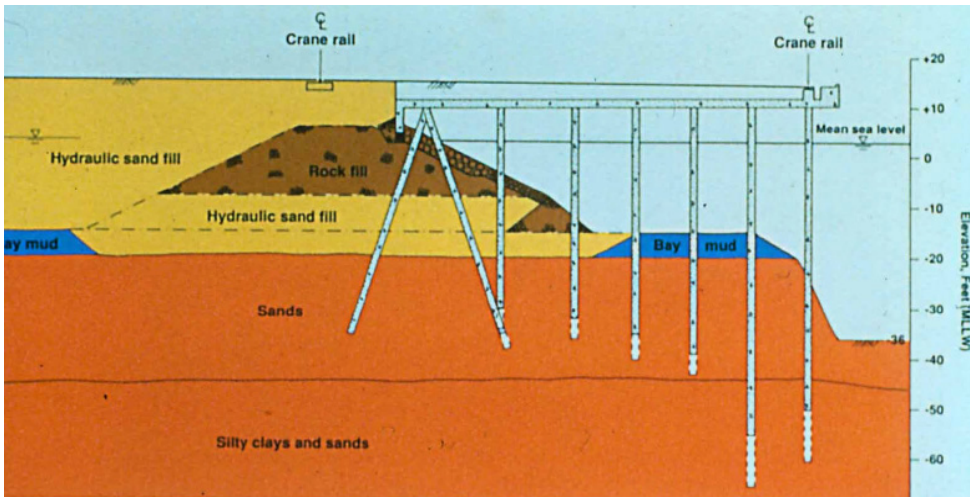

Figure 1.3 **Soil profile and pile configuration of the wharf at the Port of Oakland (photo by John Egan, AMEC).**

Figure 1.4 Damage to the battered piles supporting the wharf at the Port of Oakland during the 1989 Loma Prieta earthquake (photo by John Egan, AMEC).

Liquefaction has also damaged new structures that were designed to withstand its effects. The Nishinomiya Bridge in Kobe, Japan, is an example of a modern bridge where out-of-phase movement of the bridge abutments—due at least in part to the liquefaction and lateral spreading apparent in Figure 1.5—caused one of the span decks to fall off its seat during the 1995 Kobe earthquake. The bents of this bridge are supported on caissons rather than driven pile foundations, but the fundamental mechanisms of load transfer bear some similarities to load transfer against pile foundations.

Fortunately, not all case histories of damage to bridges and other structures that undergo lateral spreading are as dramatic as the abovementioned examples. In many cases the bridge or structure was subjected to large lateral spreading ground displacements and yet survived with minor to intermediate levels of repairable damage. Even though cases with little or no damage are often not well-documented or investigated, they are equally important from the engineering standpoint because they may provide valuable information about the factors responsible for acceptable performances of bridges under such severe demand. Therefore, analyzing such case histories is critical for additional insights into understanding the fundamental mechanisms of damage to structures under lateral spreading.

Despite lateral spreading of soils on one bank of the river, the Landing Road Bridge in Whakatane, New Zealand, suffered only moderate damage (see Figure 1.6) during the 1987 Edgecumbe earthquake. The ground liquefied and spread laterally up to 2 m (6.56 ft) against five spans in the left bank of the bridge. Some piers cracked, suffering about 1% permanent rotation; cracks were also visible near the head of some of the piles. Settlements of 0.3 to 0.5 m (11.81 to 19.69 in.) at one of the abutments made the bridge impassible after the earthquake. Buckled footpaths indicated compressive forces were mobilized in the superstructure (Berrill et al. 2001). The bridge was repaired by epoxy injections into the concrete cracks and the approach fill was repaired, providing access onto the bridge at the left abutment.

Figure 1.5 Unseating of the Nishinomiya Bridge as a result of lateral spreading during the 1995 Kobe earthquake.

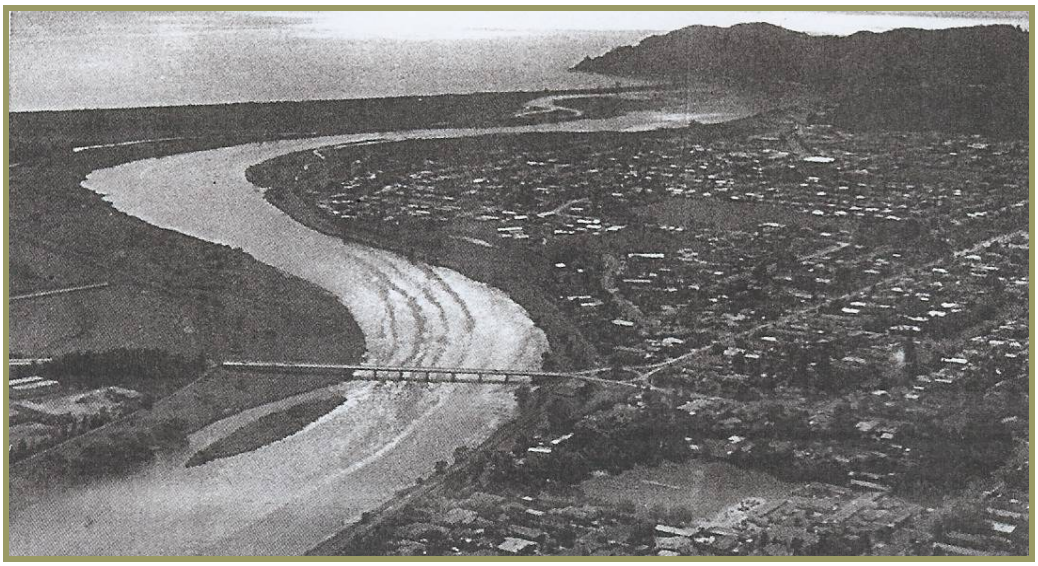

Figure 1.6 Side view of the Landing Road Bridge in Whakatane, New Zealand, which suffered moderate damage due to 2 m (6.56 ft) of lateral spreading of the left bank during the 1987 Edgecumbe earthquake.

During the 2007 Niigata Ken Chuetsu Oki earthquake in Kashiwazaki, Japan, a number of bridges with continuous superstructures and seat-type abutments were only moderately damaged despite as much as a meter of lateral spreading. Damage included permanent offsets in elastomeric bearings, cracked abutments, and permanent offsets at approaches, but nearly all of the bridges were in service within days after the earthquake.

1.3 IMPLICATIONS FOR CALTRANS BRIDGES

The California Department of Transportation (Caltrans) owns roughly 13,000 bridges that were constructed since 1900. From data extracted from National Bridge Inventory (NBI) database, Figure 1.7 shows the distribution of California bridges based on the year of construction.

Note that over half of the bridges in California were built before 1971, the year of the destructive San Fernando, California, earthquake. The damage caused by that earthquake resulted in major improvements to the building codes, including the addition of many seismic provisions to the codes. Because most of the California bridges were constructed prior to 1971 with limited considerations for seismic loading, a significant number of these bridges may be susceptible to damage under earthquake shaking. Many of the older-vintage bridges have been retrofitted to improve their performance during earthquake-induced ground shaking, but it is

unclear to what extent these retrofits will improve performance in laterally spreading ground. Although seismic codes were introduced for design of newer bridges, the knowledge of liquefaction and liquefaction-induced damage (e.g., lateral spreading) was very limited at that time, and more robust methods for analyzing bridges in liquefied ground have only recently emerged following the 1995 Kobe earthquake, which prompted a concerted research effort using centrifuge models, 1*g* shake table tests, blast-induced field liquefaction tests, and case history analysis.

Therefore, many older bridges as well as some of the newer bridges may be susceptible to damage or complete loss in an event of an earthquake if the underlying soils liquefy. Naturally, if the extent of anticipated damage from earthquake-induced liquefaction and lateral spreading is not currently known, those particular bridge configurations and locations that are susceptible to such damage have not yet been identified, but analyzing the entire suite of 13,000 bridges is not feasible. A screening procedure is therefore required to identify the bridges that (1) are in regions where liquefaction and lateral spreading might be expected to accompany earthquake shaking (the focus of a companion research study) and (2) are structurally most susceptible to the loads imposed by liquefaction and lateral spreading (the focus of this research).

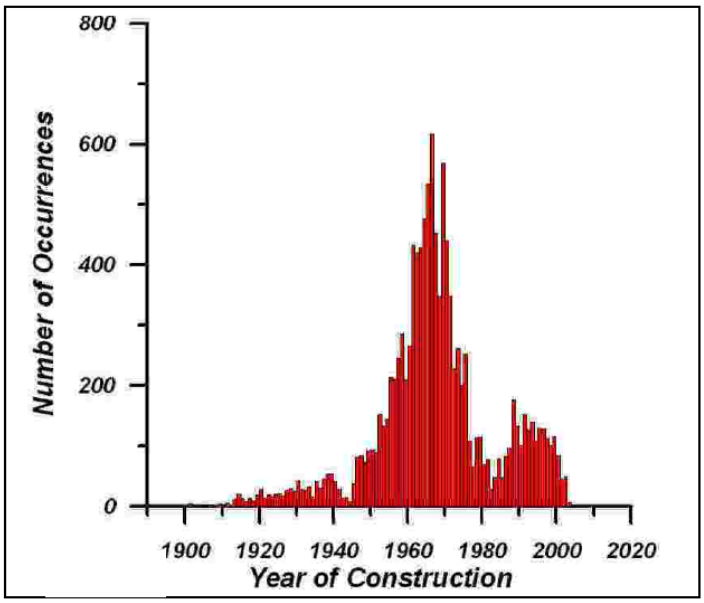

Figure 1.7 Distribution of California bridges by year of construction based on NBI database.

Caltrans has undertaken an extensive seismic retrofit program where bridges were screened based on structural response to ground shaking, but vulnerability to liquefaction and lateral spreading was not considered. The potential damage to a bridge during lateral spreading depends on physical properties of the bridge (structural and geometric configurations), the mechanical characteristics and deformation potential of the soils underlying the bridge, and ground motion. The primary mechanism of damage to bridges founded on liquefiable soils is large displacements of the bridge components in response to large ground displacements. Described below are three damage mechanisms typical of bridges subjected to lateral spreading:

- Large Relative Displacements between the Superstructure and the Substructure: This mode of damage applies to bridges with simply supported superstructure where the superstructure rests on bearings atop the piers and abutments. During lateral spreading different foundation components can move different amounts in different directions, thereby causing large relative displacement between the superstructure and substructure components. Large relative displacements may result in unseating of the decks of the bridge and collapse of some spans; this is what caused damage to the Showa and Nishinomiya Bridges.
- Excessive Curvature Ductility in Bridge Piers: Relative displacements between the pile caps and the superstructure may cause excessive flexural and/or shear demands in the piers. Effects of these demands can range from spalling of cover concrete to loss of axial capacity and possible collapse if axial loads cannot be redistributed. Modern ductile bridges can typically tolerate larger amounts of drift than older more brittle bridges. As an example of this damage mechanism, some cracks were observed in the shear walls at Landing Road Bridge due to the mobilization of larger curvature ductility.
- Excessive Curvature Ductility in Piles: Lateral spreading may induce large demands in piles due to kinematic interaction. Damage to the piles may result in large pile cap translation and rotation, and settlement due to loss of axial capacity in the piles. The extent of damage to the above-ground bridge components depends on the bridge configuration; in some cases pile damage may not manifest above ground. For example, piles beneath the Niigata family courthouse building were severely damaged in the 1964 Niigata earthquake, but the damage was only discovered about twenty years later when the foundation was excavated. Cracks in the piles of the Landing Road Bridge are another example of a similar damage mechanism.

Based on the vulnerability of the Caltrans bridges to these types of loading and damaged mechanisms described above, a screening tool is needed that evaluates the damage susceptibility of different types of bridges. Such a tool should answer two specific questions: (1) Is the bridge located in potentially liquefiable soils?; and (2) How susceptible is the bridge to damage if located in liquefiable soils? Knudsen et al. (2009) answered the first question: ground deformation potential for all ≈13,000 Caltrans bridge sites was estimated. This report herein addresses the second question by investigating various bridges with different structural properties and different soil properties under different load combinations to determine their susceptibility to lateral spreading. Bridges were categorized into several different structural classes, and a large number of bridge realizations within every class were analyzed using numerical models. Results are presented as demand fragility surfaces that relate mobilized engineering demand parameters (EDPs) to free-field lateral spreading ground displacement. The results of this study—combined with results from Knudsen et al. (2009)—provide a rational means for screening Caltrans bridges for damage potential due to liquefaction and lateral spreading.

1.4 AVAILABLE FRAGILITY FUNCTIONS

A fragility function has traditionally been defined as a probability of exceeding a damage measure (DM) conditioned on an EDP. Fragility functions have also been used to represent the probability of exceeding an EDP given and intensity measure (IM), or as the probability of exceeding a DM given an IM. Figure 1.8 shows a schematic of a set of fragility curves for bridges with different vintages that relates DM to IM.

In HAZUS (1999), which is a software program for loss estimation developed by FEMA, damage states for bridges are divided into five states and are defined as follows:

- **None** (ds_1) is defined by no damage to the bridge.
- **Slight/Minor Damage** (ds_2) is defined as minor cracking and spalling to the abutment, cracks in shear keys at abutments, minor spalling and cracks at hinges, minor spalling at the column (damage required no more than cosmetic repair), or minor cracking to the deck.
- **Moderate Damage** (ds_3) is defined as any column experiencing moderate (shear cracks) cracking and spalling (although the column is still structurally sound), moderate movement of the abutment [< 2 cm (0.79 in.)], extensive cracking and spalling of shear

keys, any connection having cracked shear keys or bent bolts, keeper bar failure without unseating, rocker bearing failure, or moderate settlement of the approach.

- **Extensive Damage** (ds_4) is defined as column degrading without collapse (shear failure where the column becomes structurally unsafe), significant residual movement at connections, or major settlement approach, vertical offset of the abutment, differential settlement at connections, and shear key failure at abutments.
- **Complete Damage** (ds_5) is defined as any column collapsing and connection losing all bearing support, which may lead to imminent deck collapse or tilting of the substructure due to foundation failure.

Even though the descriptions of the damage states in HAZUS are complex, existing fragility functions for damage to bridges as a result of liquefaction-induced lateral spreading based on free-field ground displacements are currently too elementary. The existing fragility functions in HAZUS were adopted from Basoz and Mander (1999). Based on HAZUS, regardless of type of bridge and its foundation components and characteristic of the soils underlying the bridge, 10 cm (3.9 in.) of ground displacement is sufficient to put the bridge in damage state 4 (extensive damage), and 35 cm (13.8 in.) of displacement is enough to cause complete damage (ds_5 or collapse) in the bridge. The graphical representation of the available fragility functions is shown in Figure 1.9.

These fragility functions were originally intended to characterize structural damage in single-span bridges due to abutment displacements, not originally intended to be used in analyses of liquefied ground. Extending this methodology to laterally spreading ground assumed that foundation displacements were equal to free-field ground displacements. However, free-field ground displacements would typically cause much lower foundation displacements in the structure because of pinning effects and compression, extension of the soils under lateral loading, or the flowing mechanism of soils around foundation components. Furthermore, different bridge characteristics would result in different bridge responses and different types of bridges would have different fragility functions (as they do for ground shaking in HAZUS).

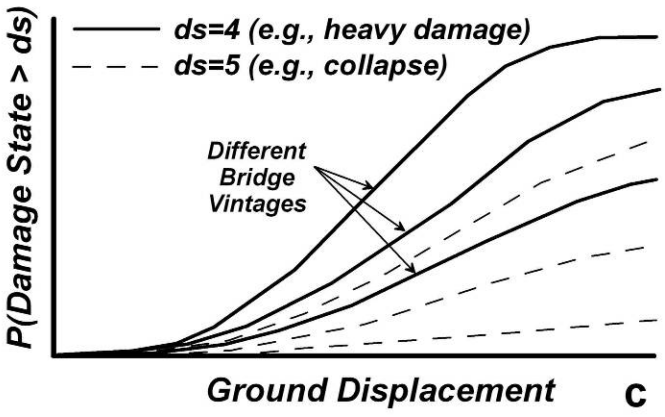

Figure 1.8 Schematic of a set of fragility curves for bridges with different vintages.

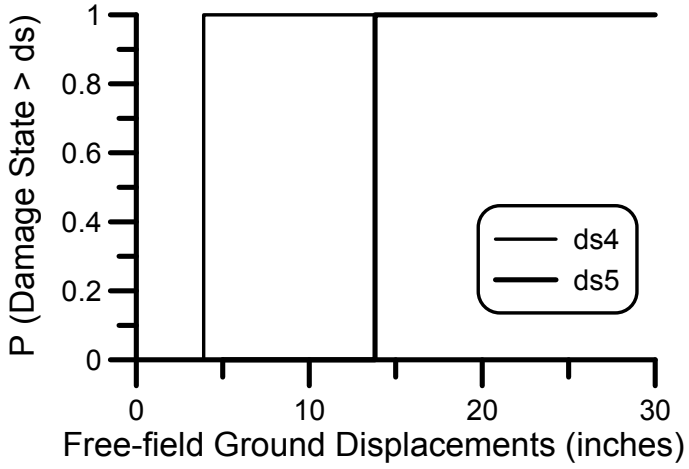

Figure 1.9 HAZUS fragility curves for damage to bridges as a result of lateral spreading.

The inappropriate use of HAZUS fragility functions is clearly evident in the relatively good performance of Landing Road Bridge despite as much as 2 m (6.56 ft) of lateral ground displacement near the bridge; HAZUS would have predicted a ds_5 while the damage to the bridge was classified as ds_3. The HAZUS fragility functions were also found to be inaccurate in a transportation network analysis by Kiremidjian et al. (2006), which predicted widespread bridge collapse caused by the 1989 Loma Prieta earthquake (Figure 1.10) due to liquefaction and lateral spreading. Such levels of collapse did not occur, and the collapses that did occur during the earthquake (i.e., the Cypress Structure and one span of the Bay Bridge) were not caused by liquefaction.

Additionally, the recent Niigata Chuetsu-Oki earthquake of July 16, 2007, in Japan caused lateral ground displacements near bridges on the order of tens of centimeters, which would be sufficient to categorize bridges in ds_4 or ds_5 based on HAZUS criteria. In fact, most of the bridges remained in service, experiencing only moderate damage consisting primarily of permanent offsets in the elastomeric bearings at the abutments and cracks in the abutments (Figure 1.11). Development of more reliable and meaningful fragility curves for different classes of bridges of different vintages or other simple properties is the focus of this project, as will be discussed in greater detail in the following chapters.

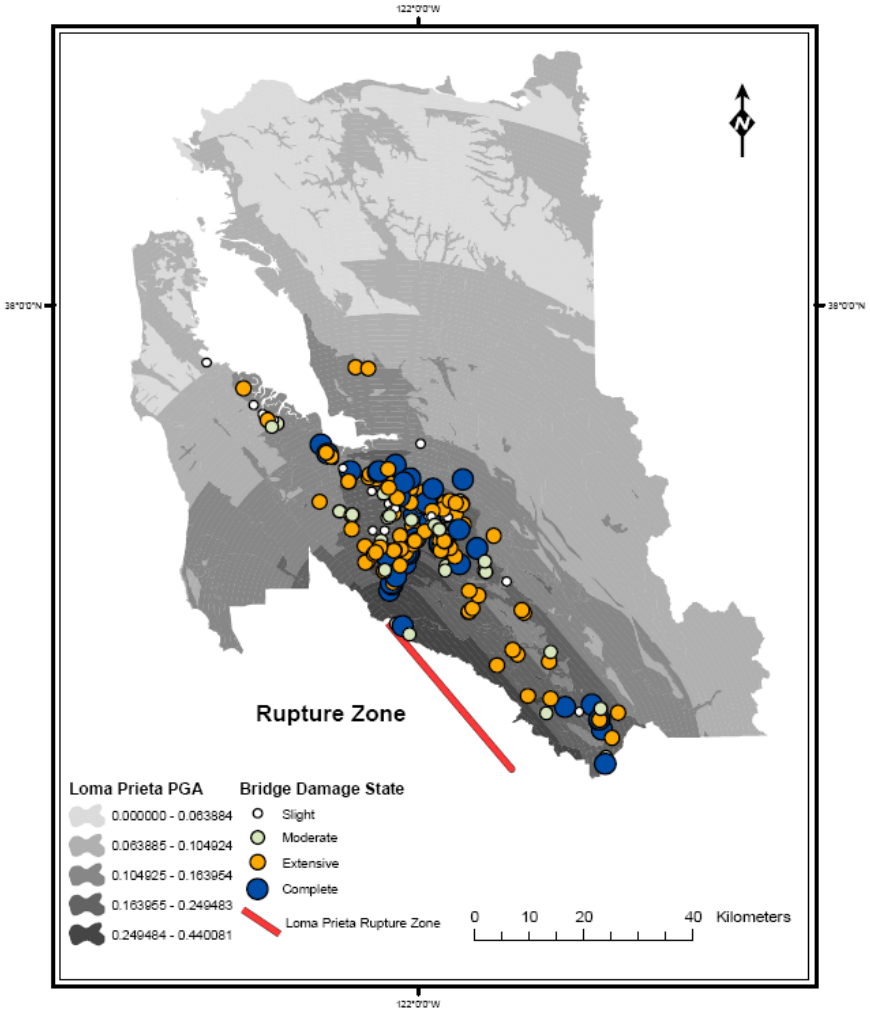

Figure 1.10 Estimated damage to bridges during the 1989 Loma Prieta earthquake (Kiremidjian et al. 2006).

Figure 1.11 Permanent offset in elastomeric bearing at Nagomi Bridge caused by ground deformation during the Niigata Chuetsu-Oki earthquake (Kayen et al. 2007).

1.5 ANALYSIS METHOD

A numerical method was adopted to evaluate bridges under liquefaction and lateral spreading demands. Discussed here are several methods available for analyzing bridges.

The ideal numerical model would include a three-dimensional representation of the soil using constitutive models that capture liquefaction, a global structural model of the entire bridge, and would impose ground shaking on the base of the soil. Because of the computational costs associated with such a complex model, only one such study has been conducted to date (Elgamal et al. 2008). Two-dimensional dynamic models of the bridge with continuum soil elements attached to the structural elements using soil-structure interaction zero length elements to predict the performance of a bridge during liquefaction and lateral spreading have also been developed (Kramer et al. 2008; Zhang et al. 2008). Unfortunately, these methods are also computationally expensive, often requiring several months to model and perform a limited number of dynamic analyses.

Evaluating the fragility of different classes of bridges requires performing many analyses of bridges with different structural configurations, structural properties, and geometries with different soil profiles. Although a considerable body of recent research has clarified many of the fundamental loading mechanisms between pile foundations in liquefied and laterally spreading ground (e.g., Boulanger and Tokimatsu 2006), many of these findings appear contradictory. Effort is now needed to synthesize the body of research into robust analysis methods that will provide accurate predictions of bridge performances in liquefied ground. Given the time constraints of this project, a simpler analysis method was developed to accurately predict bridge performance when subjected to liquefied ground with lateral spreading.

The Caltrans' Seismic Design Criteria (SDC) (2006) specifies several global methods for analyzing bridges exposed to ground shaking, including equivalent static analysis (ESA), elastic dynamic analysis (EDA) [otherwise known as response spectrum analysis (RSA)], nonlinear static pushover analysis, and nonlinear global dynamic analysis, also known as time-history analysis. Unfortunately, none of these analysis methods as outlined in the SDC is suitable for evaluating the bridge performance undergoing liquefaction and lateral spreading. The method proposed herein synthesizes the body of research of the loading mechanisms present during liquefaction and lateral spreading in order to evaluate the nonlinear performance of bridges under both displacements and inertial demands applied to the bridge during liquefaction and lateral spreading. This method is referred to as the nonlinear equivalent static analyses in this report, and the details about modeling and the boundary conditions used in this method is discussed in great depth in Chapter 2 of this report.

1.6 ORGANIZATION OF THE REPORT

This report evaluates the fragility of different classes of bridges by creating realistic finite element models of bridges using the OpenSees finite element platform, and generating demand fragility surfaces of different components of the bridge using the nonlinear equivalent static analyses method. This report consists of six chapters, organized as follows:

Chapter 2 presents the methodology of the global equivalent static analysis method used to perform the numerical analyses of the bridge models in OpenSees. The details of the modeling approach and the fundamental behaviors in liquefaction and lateral spreading found in recent

research are described, and several examples of the global equivalent static analyses are presented.

Chapter 3 outlines the basis for selecting the parameters used in the numerical models as well as specifying the classes of bridges that were analyzed. The distributions of the bridge parameters, geotechnical parameters, and inertia demands are presented. The output was sampled using the Monte Carlo method from the specified distributions used in the numerical models.

Chapter 4 discusses how the analyses were performed, how the EDPs were controlled, and how the fragility surfaces were fit to the raw recorded data. Next, the fragility surfaces for several classes of bridges are presented and trends noted. Correlations among the EDPs are discussed, as well as disaggregation of the input parameters.

Chapter 5 evaluates the fragility functions of different classes of typical bridges found in California when subject to seismic shaking and compares them to bridges subject to liquefaction-induced lateral spreading. Numerical models capable of simulating complex soil-structure interaction (SSI) effects are presented and nonlinear behavior of columns and connections are developed for each bridge class. The dynamic responses are obtained using nonlinear time-history analyses for a suite of 250 earthquake motions with increasing intensity. Fragility functions for each bridge class are derived and compared for both seismic shaking and lateral spreading. Significant correlation between the fragility functions and the structural characterizations are identified.

Chapter 6 presents a summary of the conclusions and provides some context for interpreting the value of the findings of the report. Limitations of the study and the need for future work are also discussed.

2 Global Equivalent Static Analysis Method

As mentioned in the previous chapter, those methods commonly used to evaluate the global performance of a bridge due to ground shaking are summarized in the Caltrans SDC (2006), and include ESA, EDA, nonlinear static pushover analysis, and nonlinear global dynamic analysis.

Equivalent static analysis applies equivalent static forces or spectral displacements at individual frames, with the seismic demand determined from a design response spectrum, therefore, ESA can reasonably estimate displacement demands for bridges whose response can be characterized by a predominantly translational mode of vibration, but may be inappropriate for curved or skew bridges, and bridges with many spans and/or expansion joints. Elastic dynamic analysis, which is also known as RSA, is a linear elastic multi-modal spectral analysis and should include sufficient number of modes to capture at least 90% mass participation in the longitudinal and transverse directions of the bridge. Because this method is a linear elastic method it can only indirectly account for sources of nonlinearity in the system, including the effects of surrounding soil, yielding of the structural components, opening and closing of expansion joints, and abutment behavior. According to Caltrans (SDC 2006), both ESA and EDA are only appropriate for Ordinary Standard bridges, implying that these methods are not suitable for bridge sites with the potential of liquefaction and lateral spreading.

Nonlinear static pushover analysis imposes an increasing displacement pattern to identify potential failure mechanisms and establish tolerable displacement limits of the bridge. In this method, displacements are applied incrementally to push the frame of the bridge in the nonlinear range until the potential collapse mechanism is reached. This is a recommended method for analyzing the inelastic response of bridges because it accounts for interaction of the bridge components and redistribution of the loads within different components. However, the applicability of this method for bridges under liquefaction and lateral spreading demands is not evaluated, and it is not immediately clear how the displacements demands to the superstructure

frames should be concurrently applied with the displacement demands due to lateral spreading at the foundation level or at the abutments.

Nonlinear global dynamic analysis, also known as time-history analysis, is the most accurate and robust method for evaluating bridge performance. Here, the response of the bridge is evaluated directly by applying a suite of ground motions at the boundaries of the model. In cases with only ground shaking, the structural engineers typically model the foundation using simple SSI elements at the boundaries of the bridge frame. However, this method of applying the boundary conditions cannot capture the complex response of the bridge during liquefaction and lateral spreading that may involve significant displacements and rotation of the foundations. Therefore, the proper modeling of the bridge under liquefaction and lateral spreading using nonlinear global dynamic analysis requires explicitly modeling the structure (including the foundation) and soil elements with advanced soil constitutive models that can capture complex behavior of soils during liquefaction and lateral spreading, including generation and dissipation of pore pressures and reduction of shear strength of the soil during liquefaction.

The most robust method for performing nonlinear global analysis of a bridge in liquefied ground is to use a three-dimensional soil continuum with constitutive models that captures liquefaction behavior (e.g., Elgamal et al. 2008). Such models explicitly capture SSI in liquefied ground by directly modeling the soil continuum and nonlinear pile elements, and do not require SSI elements. Unfortunately, this approach is extremely computationally expensive and not a viable option except for key bridges.

A less computationally expensive dynamic approach involves modeling the bridge in two dimensions, with two-dimensional soil continuum elements (e.g., Zhang et al. 2008; Kramer et al. 2008). However, because SSI is inherently a three-dimensional problem, SSI elements (i.e., *p-y*, *t-z*, and *q-z*) are required at the interface of the soil elements and the structural elements to capture the three-dimensional loading mechanisms. The two-dimensional soil mesh provides a free-field displacement that is imposed on the free-ends of the SSI elements, which can be adjusted to account for the effects of liquefaction [e.g., the PyLiq1 material in OpenSees (Boulanger et al. 2003)]. While the cost of performing this type of two-dimensional analyses is significantly lower than the three-dimensional analyses, they are still computationally very demanding and thus inappropriate for routine evaluations of ordinary bridges.

Caltrans' SDC (2006) also mentions stand-alone local analyses of a single component (e.g., a single pier) of the bridge in longitudinal and transverse directions. Local analysis is the

most common approach for analyzing piles in liquefied ground because software platforms such as LPile are amenable to this type of analysis (e.g., Brandenberg et al. 2007; Ashford and Juirnarongrit 2006). Local analysis may be appropriate in cases where boundary conditions imposed on the foundation from the superstructure are clearly understood. However, these boundary conditions are often not known *a priori* because loads may be transmitted between adjacent piers through axial forces in the superstructure. For example, the displacement and rotation demands at the top of a single pier depend on how the lateral spreading demands on the foundation of that pier are transmitted to other piers or abutments through axial loads in the superstructure. Furthermore, lateral spreading at one pier may place demands on other piers and abutments in nonliquefied ground, and these demands are very difficult to assess using local analysis methods. Although global analyses of a bridge can capture these important features, local analyses cannot. Examples of global analyses of a bridge are presented later in this chapter, and a bridge's response is compared with examples of an individual component of the bridge using local equivalent static analysis. This comparison has been done to provide guidance on cases where local analysis is sufficient and where global analysis is needed.

The method proposed here is the nonlinear equivalent static global analysis, wherein a global structural model of the bridge (including foundation elements) is constructed from nonlinear beam-column elements, SSI elements are attached to embedded components, and free-field ground displacements are imposed on the free-ends of the SSI elements simultaneously with inertia demands consistent with the effects of liquefaction. To reduce the computational complexity, a soil continuum is not modeled. This approach incorporates the recent body of research and advances in understanding the load transfer mechanisms during liquefaction and lateral spreading, but uses a computationally less demanding approach. The details of the modeling and boundary conditions are discussed in the following sections of this chapter.

Global analysis of bridges in liquefied ground requires more collaboration between the geotechnical and structural engineers than local analyses and demands a more sophisticated level of modeling, where all the structural and foundation elements of the bridge are modeled and soil-structure elements are appropriately specified to account for complex soil behaviors observed during liquefaction and lateral spreading. Numerical modeling programs, such as OpenSees and SAP2000, are capable of performing this level of modeling. In this study, all numerical analyses were performed using the OpenSees finite element platform (McKenna and Fenves 2006) developed by Pacific Earthquake Engineering Research Center (PEER).

2.1 STRUCTURAL MODELING

The numerical modeling of the bridges selected was performed in two dimensions, and the lateral spreading displacements and inertial demands were applied in the longitudinal direction of the bridge; these models do not take into account those bridges with a curved geometry or skew. Also, bridges with significant lateral spreading demands in the transverse direction are not considered here.

Two-dimensional beam column elements with three-degrees of freedom per node were required to model the longitudinal response of the bridge. The models used in this study utilized three-dimensional beam column elements with six-degrees of freedom per node, with the out-of-plane DOF's constrained to restrict response to the two-dimensional plane of interest. This approach was adopted so that the bridge models could be adapted to three-dimensional loading conditions for future research studies. Multi-column bents and pile groups with multiple members in the out-of-plane direction were represented using single elements in the plane, with structural properties adjusted to represent the number of out-of-plane members.

2.1.1 Pier Columns and Piles

The pier columns and piles were modeled using nonlinear beam-column elements. A bilinear moment curvature relationship was aggregated with linear elastic shear deformation response and elastic axial response. Each nonlinear beam-column elements consisted three integration points, with two of the points at the nodes where maximum bending moments were anticipated (i.e., Lobatto integration).

Moment-curvature relationships of pier columns were evaluated using fiber-section analyses of columns, with proper size and longitudinal and transverse reinforcement ratios as well as proper axial load ratios. Subsequently the moment-curvature relationship was approximated as a bilinear curve using the Hardening material model in OpenSees by specifying the initial stiffness of moment-curvature curve (EI_{eff}), the yield moment of the column (M_y) and the post-yield stiffness of the curve, which is conveniently chosen to be 5% of the initial stiffness of the column. The axial and shear force-deformation relationships were modeled elastically with stiffness equal to EA, and GA, respectively. The moment-curvature response of the piles was obtained using the fiber-section analysis program Xtract by Imbsen. The moment-curvature

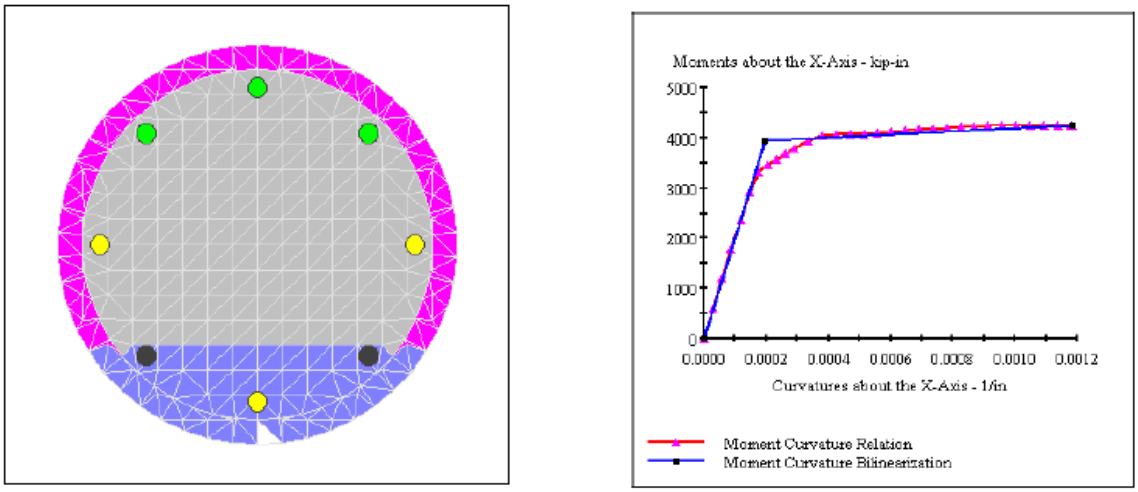

Figure 2.1 Fiber section of a 0.61 m (24 in.) CIDH pile model and the corresponding moment curvature relation.

relationship was then approximated using a bilinear relationship similar to the pier column elements. Figure 2.1 shows an example of a moment curvature analysis performed in Xtract for a 0.61 cm (24 in.) cast-in-drilled-hole (CIDH) pile.

2.1.2 Abutments, Superstructure, and Pile Caps

The abutments, superstructure, and pile caps were assumed to remain linearly elastic under the applied boundary conditions. Hence, linear elastic beam-column elements were used for modeling. For these elements only the elastic properties of the materials, i.e., modulus of elasticity (E) and moment of inertia (I), as well as the cross-sectional area (A) of the elements, were needed. Pile caps and abutments do not behave as beams because they violate the plane-sections assumption in beam theory; therefore, the EI and EA values for these elements were selected to be so large that they behaved essentially as rigid bodies. The EI and EA for the superstructure elements were based on the cross-sectional properties of the reinforced concrete box girder section. For those bridges with simply supported superstructure or seat-type abutments, the interface between the superstructure deck and the bent caps or the abutments were modeled with zero-length springs with appropriate types and capacities.

2.1.3 Bearings at Abutments

Figure 2.2 shows the schematic of a typical seat-type abutment, as well as the different types of springs needed to capture the response at the abutments. As seen in this figure, three types of springs were needed for the seat-type abutments.

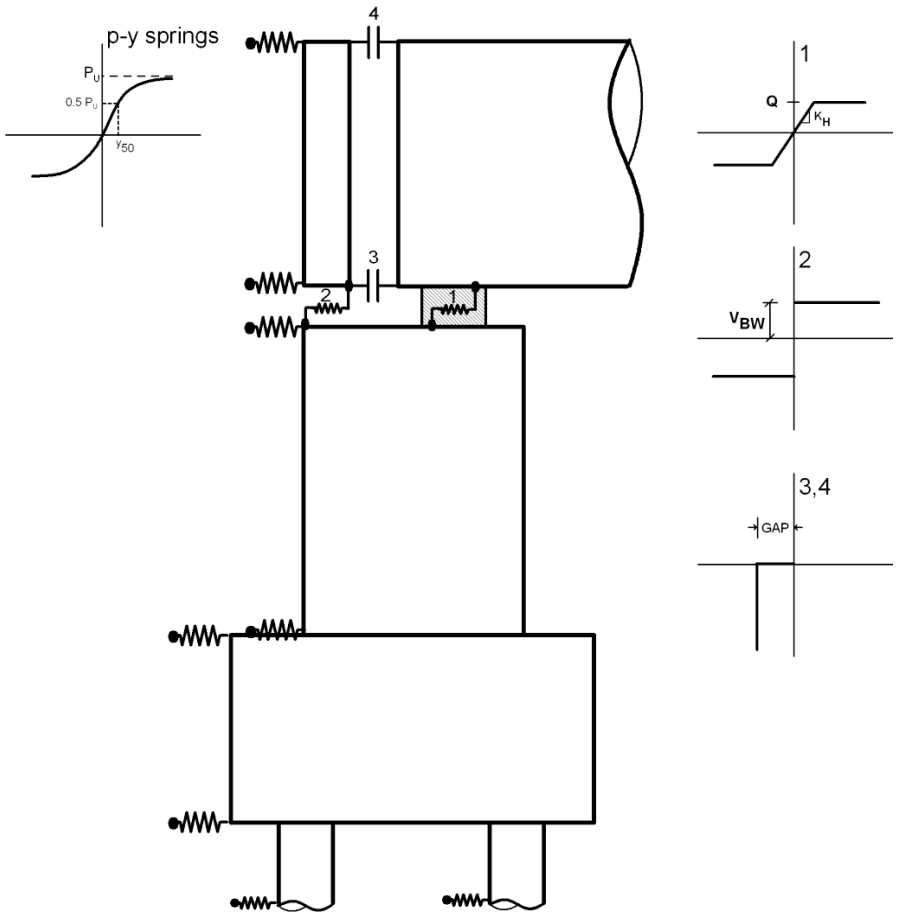

Figure 2.2 Schematic of a seat-type abutment of the bridge.

Spring 1 connects the superstructure deck node to the node at the top of the stem wall and models the horizontal load transfer mechanism at the abutment bearing. The bearing load deformation usually can be captured by an elastoplastic material spring in which the capacity of the bearing (i.e., plastic ordinate) is Q and the horizontal stiffness of the bearing is K_H. For elastomeric bearings, the capacity, Q, is calculated using Coulomb friction as follows:

$$Q = \mu.N \tag{2.1}$$

where N is the normal tributary force acting on the bearing, and μ is the coefficient of friction of the elastomeric bearing. The coefficient of the friction for the elastomeric bearing is between 0.35 and 0.4 according to SDC (2006). The horizontal stiffness of the bearing K_H is calculated using the following formula:

$$K_H = \frac{G.A}{t_r} \tag{2.2}$$

where A is surface area of the bearing pads, t_r is total thickness of the bearing pads, and G is effective shear modulus of rubber $\approx$ 1 MN/m^2 (150 psi). Consequently, the yield displacement of the bearing is calculated as:

$$U_y = \frac{Q}{K_H} \tag{2.3}$$

In modern bridges, typically the total surface area of the elastomeric bearings is selected so that the vertical stress on the bearings, σ_v, does not exceed 100 psi (~ 690 kPa).

Rocking and rollout displacements of the bearings are important design considerations for dynamic shaking of the bridges. Multi-layer bearings with steel sheets in between the rubber pads are typically used to increase the vertical stiffness of the bearing by modifying its shape factor, reducing any damage due to rocking or rollout of the bearings. However, bearings with the same total rubber pad thickness essentially have the same horizontal stiffness. Because the loading demands in the nonlinear equivalent static analyses are applied statically and incrementally, dynamic responses of the bearings (i.e., rocking and rollout) are not captured. Thus, the vertical degrees of the freedom of the two nodes connecting to spring 1 are equal, which causes the spring to be rigid in vertical direction since the two nodes move together.

Spring 2 is a horizontally oriented spring connecting the top node of the stem wall to the bottom node of the back wall of the abutment. This spring follows a rigid plastic load deformation relationship with a capacity, V_{BW}, equal to the shear capacity of the connection between the back wall and the stem wall. Note that to mobilize the passive soil resistance of the approach embankment, modern abutment backwalls are designed to break away from the stem wall. This spring causes the two nodes to move together until the shear capacity of the backwall

is exceeded, at which point the backwall is no longer connected to the stem wall and can translate into or away from the abutment backfill depending on the direction of the loading.

Springs 3 and 4 model the expansion joint gap between the superstructure deck end nodes and the nodes at the top and bottom of the backwall. These springs do not carry any load in tension or compression unless they are compressed the distance of the expansion gap—typically 2.54 cm (1 in.) —at which point they behave rigidly, allowing the loads to be carried by soil *p-y* springs as well as the bridge structural elements. The end element of the deck is extended vertically using a rigid elastic beam-column element, so that the top node of the deck could be connected to the top node of the backwall. This way of modeling the deck enforces compliance between backwall rotation and superstructure rotation at the abutment when the gap is closed both at the top and bottom of the backwall (Springs 3 and 4).

Diaphragm abutments are also sometimes used in Caltrans bridges, and these moment-resisting connections were modeled by having the stiff abutment beam column element share a node with the superstructure element. Hence, a 90° angle was maintained between the superstructure and abutment, though the connection could rotate.

2.1.4 Bearings at Simply Supported Spans

Figure 2.3 shows the schematic of a typical connection of simply supported spans and the required spring to model this connection properly. Two types of springs exist at this connection. Springs 1 and 2 are horizontally oriented elasto-plastic springs connecting the top node of the pier column to the end nodes of the two spans sitting above it. These springs are symmetrical and model the stiffness and shear capacity of the interface between the deck spans and pier columns in a similar manner as the bearing spring in the abutment (i.e., Spring 1 in Figure 2.2). Generally speaking, the capacity of these springs is equal to the shear capacity of the interface, while the stiffness of the springs is governed by the amount of relative displacements between the deck and the pier column at the connection before the shear capacity of the connection is reached. Consequently, in the case where the interface is an elastomeric bearing, the stiffness and capacity of the springs follows the relationships mentioned earlier for the abutment bearings. In the case

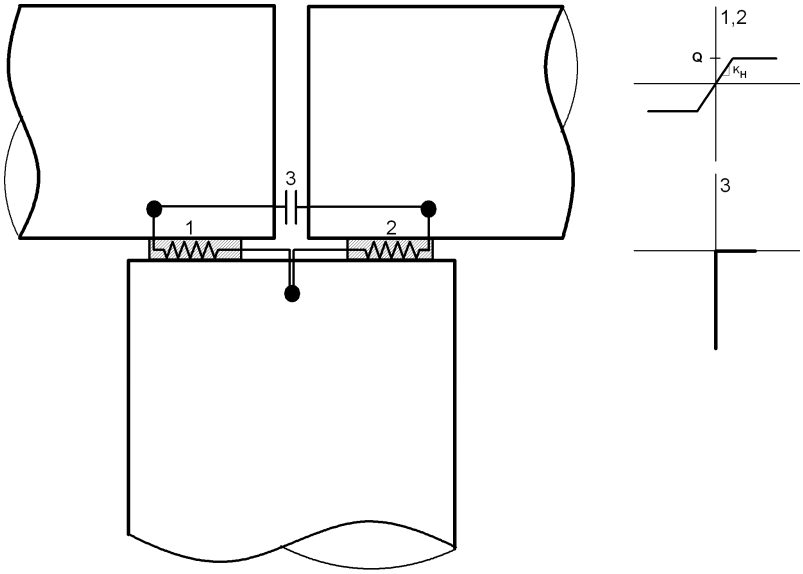

Figure 2.3 Schematic of a simply supported bridge superstructure and the corresponding interface springs at the top of a pier.

where the interface is grouted and the superstructure is connected to the pier column using dowels, the capacity of Springs 1 and 2 would equal the shear capacity of the dowels and the grout, while the stiffness of the springs would essentially be rigid. Adjusting the capacities and the stiffnesses of these springs allows for appropriate modeling of other kind of interfaces typically used in construction of these connections.

Spring 3 is a horizontally oriented no-tension rigid spring connecting the end nodes of the two spans of the deck, allowing the spans of the deck to move away from each other without interacting with the other span. However, once the spans are compressed to each other, the spring becomes rigid resulting in the two spans moving together without penetration of one span into the other.

2.2 SOIL-STRUCTURE INTERACTION MODELING

To model the SSI-interaction effects at the bridge abutment components (i.e., abutment walls and piles) and the foundation components supporting the pier columns (i.e., piles and pile cap), a beam on a nonlinear Winkler foundation approach is used. The soil-structure elements include *p-y* springs for lateral interaction, *t-z* springs for axial interaction, and *q-z* springs for pile tip bearing. The SSI interaction effects on piles are fundamentally different from the non-pile

components of the bridge. Thus, the discussion on the SSI-interaction modeling is divided between SSI interaction springs on pile caps and abutment walls, and SSI interaction springs on piles.

2.2.1 Influence of Liquefaction on Passive Pressure Amplitude

Passive earth pressure theories in relatively uniform soil profiles are well-established and calibrated with load test data (e.g., Romstad et al. 1995; Mokwa and Duncan 2001; Rollins and Sparks 2002; Lemnitzer et al. 2009). However, practical problems often require estimating passive pressures for non-uniform soil conditions in which a relatively strong layer overlies a weak layer. Examples include embankments constructed on soft clay and liquefaction-induced lateral spreading of a nonliquefied crust layer against embedded foundation elements. Relatively little research has been devoted to characterizing the influence of underlying weak soil on the mobilization of passive pressures. This section uses finite element simulations to demonstrate that underlying weak soil can significantly affect mobilization of passive pressures and presents simple analytical models for estimating passive force in such cases.

2.2.1.1 Boundary Conditions Resulting in Rankine Passive Force

Rankine (1856) earth pressure theory is widely recognized as appropriate for cases where a frictionless soil/wall contact exists, whereas log-spiral theory (e.g., Caquot and Kerisel 1948) is appropriate for estimating passive pressures with some wall friction. Terzaghi (1936) noted that uniform Rankine earth pressure can be realized only for soil deposits with frictionless contacts along the vertical boundaries (i.e., a wall) and also along the base of the deposit. A frictionless contact along a vertical boundary may be a realistic assumption for smooth walls, but the contact at the base of a deposit is typically rough because the interface strength is equal to the strength of the weaker soil layer. Hence, Terzaghi concluded that Rankine stress states can exist "only in our imaginations" and discouraged the use of Rankine earth pressure theory. However, the boundary conditions required for Rankine earth pressure may be nearly realized when a weak layer underlies the deposit. It is currently unclear how reduction in friction along the base of a deposit affects mobilization of passive earth pressure.

To illustrate the boundary conditions required to obtain Rankine passive force, a set of finite element simulations was performed for a 4 m- (13.12 ft-) thick cohesionless backfill ($\gamma =$

20 kN/m^3, ϕ=35°) with various boundary conditions at the soil/wall interface and along the base of the soil deposit. Figure 2.4 illustrates the three cases in which (a) the soil/wall interface and base are both frictionless, (b) the soil/wall interface is rough but the base is frictionless, and (c) the soil/wall interface is frictionless but the base is rough (i.e., uniform soil exists below the deposit). The analyses were performed using Phase^2 7.0, which is part of the Rocscience software package. A Mohr-Coulomb material model was used with elastic constants E = 52 MPa and ν = 0.3, which corresponds to a reasonable strain-compatible shear wave velocity of 100 m/sec. The wall was translated horizontally 0.2 m (7.87 in.) into the backfill (sufficient to mobilize passive pressure), and the resulting contours of horizontal stress, σ_{xx}, are plotted superposed on the deformed meshes in Figure 2.4. Additionally, Figure 2.5 shows σ_{xx} versus depth at distances of 0, 1, 2, and 4 m (3.28, 6.56, and 13.12 ft) behind the wall.

Regarding Figures 2.4a and 2.5a (frictionless wall and base), σ_{xx} exhibits a triangular earth pressure distribution that is the same at every position behind the wall along the x-axis. This load case results in a uniform state of Rankine passive failure everywhere in the deposit, wherein $\sigma_{xx} = K_p \cdot \sigma_{yy}$ is the major principal stress, σ_{yy} is the minor principal stress, and K_p = [1+sin(ϕ)]/[1-sin(ϕ)] = 3.69. Also presented in Figure 2.5 is the horizontal component of the passive force, P_{pH}, which was computed by numerical integration of the σ_{xx} distribution. The computed values of P_{pH} are in reasonable agreement with the value computed using Rankine earth pressure theory of $P_{pH} = K_p \cdot \gamma \cdot H^2/2$ = 590 kN/m, with the small difference (about 1%) attributed to the numerical convergence tolerance and approximations in numerical integration of the σ_{xx} distribution.

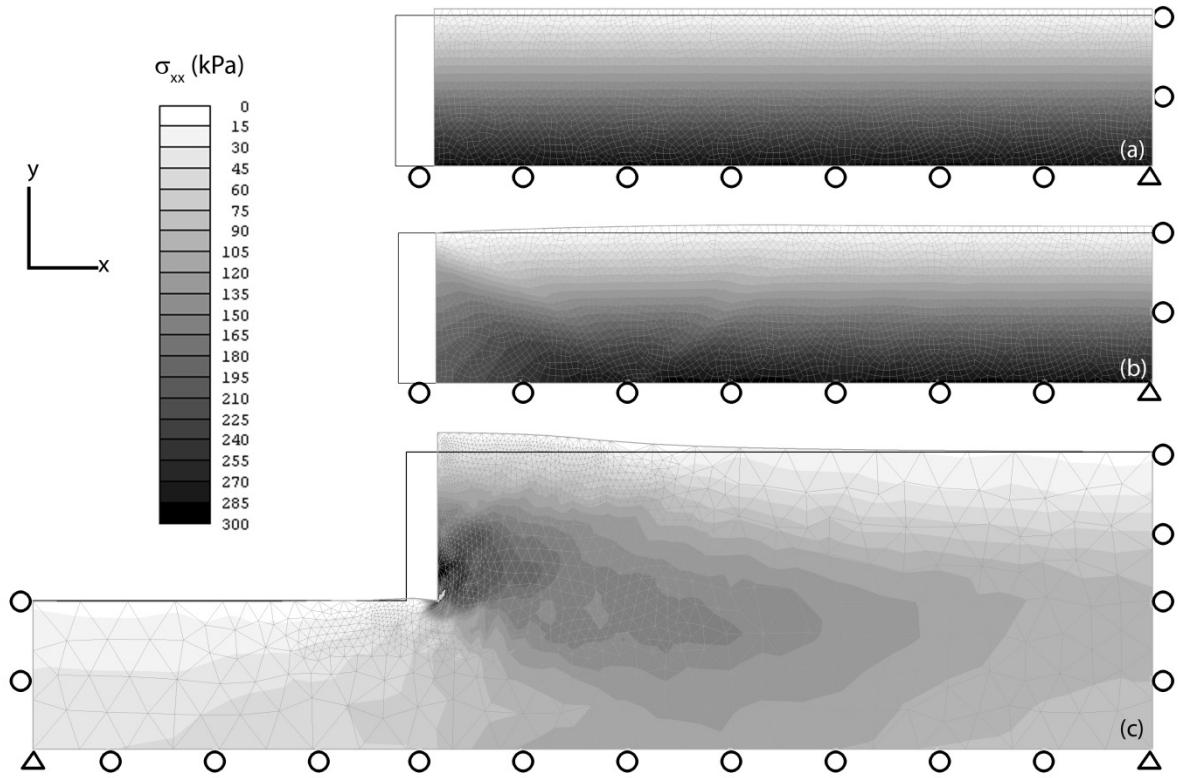

Figure 2.4 Boundary conditions resulting in Rankine passive force for a 4 m- (13.12 ft-) thick cohesionless deposit: (a) frictionless wall, frictionless base; (b) rough wall, frictionless base; and (c) frictionless wall, rough base.

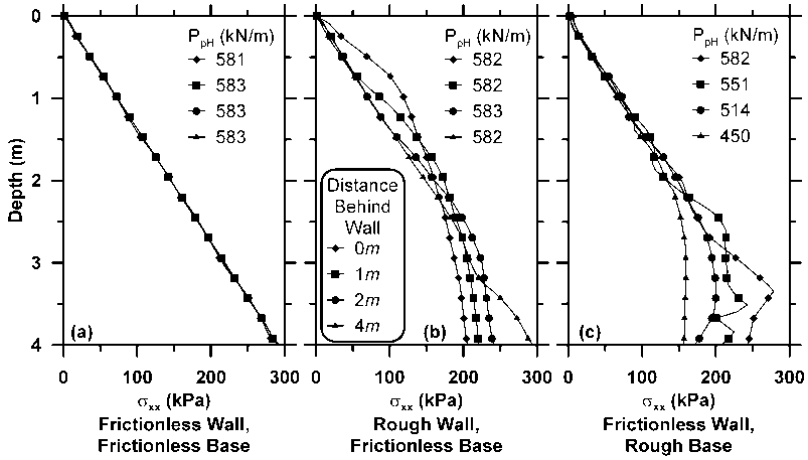

Figure 2.5 Passive pressure distributions for boundary conditions in Figure 2.4 at various distances behind the wall.

Regarding Figures 2.4b and 2.5b (frictionless base, rough wall), friction between the wall and backfill causes the distribution of σ_{xx} to vary spatially with distance behind the wall. For example, at $x = 0$ the earth pressure distribution is curved such that σ_{xx} is larger than the Rankine passive pressure near the top of the wall and lower than the Rankine passive pressure near the bottom of the wall. The earth pressure distribution becomes less curved as distance-to-wall x increases and is nearly triangular at $x = 4$ m (13.12 ft). At $x > 3H$ a uniform Rankine earth pressure distribution is observed. Hence, irregularities in the earth pressure distribution decrease as x increases, eventually transitioning to a uniform Rankine distribution. This observation is consistent with the friction-induced arching effect on active pressure mobilization studied by Paik and Salgado (2003), wherein principal stress rotation is largest at the wall interface (i.e., where τ_{xy} is maximum) and decreases with distance away from the wall, eventually reaching a condition wherein principal stress directions are vertical and horizontal.

Passive forces computed in Figure 2.5b as the integral of σ_{xx} with depth are all nearly identical to those in Figure 2.5a and consistent with Rankine passive force. This observation, contrary to the common expectation that wall friction causes passive force to deviate from the Rankine passive force, can be explained by observing a free-body diagram of the soil deposit between the wall on the left side of the deposit and a vertical slice at any point where $x > 3H$. A uniform Rankine stress state is observed on the right side of the free body such that the resultant force acting from right to left is equal to the Rankine passive force. Since shear stresses imposed on the top and bottom of the deposit are zero, the horizontal resultant force acting on the left side of the deposit must also be the Rankine passive force by horizontal force equilibrium. Hence, we can conclude that Rankine passive force (i.e., P_{pH}) is correct for long deposits with a frictionless base, regardless of whether the wall is rough or smooth. However, horizontal stresses (i.e., σ_{xx}) exhibit deviations from Rankine pressures immediately behind the wall, and the position of the resultant is higher than $1/3H$ due to the curved distribution acting on the wall.

Regarding Figures 2.4c and 2.5c (frictionless wall, rough base), a traditional passive bulge is observed in the soil behind the wall. Although the pressure distribution is approximately triangular in the upper portion of the wall, irregularities exist near the bottom of the wall. Nevertheless, at $x = 0$ the resultant force is $P_{pH} = 582$ kN/m, which is reasonably consistent with Rankine earth pressure theory. However, unlike the previous two cases, the P_{pH} values attenuate with distance as failure is confined to a region immediately behind the wall.

The conclusion that can clearly be drawn from Figures 2.4 and 2.5 is that Rankine earth pressure theory correctly represents the passive resultant force P_{pH} for cases where either the soil/wall interface is frictionless and/or the base of the soil deposit is frictionless. Friction along either interface will cause σ_{xx} to locally deviate from the Rankine condition, but the resultant is the same. Even for cases with a rough wall, Rankine earth pressure theory provides the correct passive force if the base is frictionless.

2.2.1.2 Influence of Underlying Weak Soil

Having established that Rankine earth pressure theory produces accurate P_{pH} values for cases with a frictionless base, we now turn our attention to the case wherein the soil below the deposit is weak, but not entirely frictionless. This boundary condition is pertinent for embankments compacted on soft clay and for liquefaction-induced lateral spreads where the nonliquefied spreading crust typically exerts a dominant loading component on embedded structures as it is carried atop weak liquefied soil. A suite of finite element studies was carried out wherein a cohesionless sand deposit rested atop a 0.5 m- (19.69 in-) thick weak soil layer modeled as a Mohr-Coulomb material with constant undrained shear strength, s_u (i.e., $c = s_u$, and $\phi = 0$).

The analysis was performed in two steps: (1) first, a gravity analysis was performed in which the base of the deposit was constrained against displacement and the vertical boundaries were constrained against horizontal displacement and free vertically; and (2) plastic loading in which 0.2 m (7.87 in.) horizontal displacement was imposed on the sand backfill and reaction forces recorded during gravity analysis were imposed on the left side of the underlying weak soil. The wall was assumed to be rough (i.e., vertical displacements were constrained to zero on the left side of the sand deposit, thereby implying $\delta = \phi$), and the right side of the deposit was constrained only against horizontal displacement and was free to displace vertically. The horizontal component of the passive force was computed by integrating the horizontal stress on the left vertical face of the deposit. Analyses were performed for undrained shear strengths of the weak layer of s_u = 1, 2, 5, 10, 20, and 40 kPa, and friction angles in the cohesionless sand deposit of $\phi = 30°$, 35°, and 40°. Figure 2.6 shows a deformed mesh and contours of σ_{xx} for s_u = 1 kPa and $\phi = 35°$.

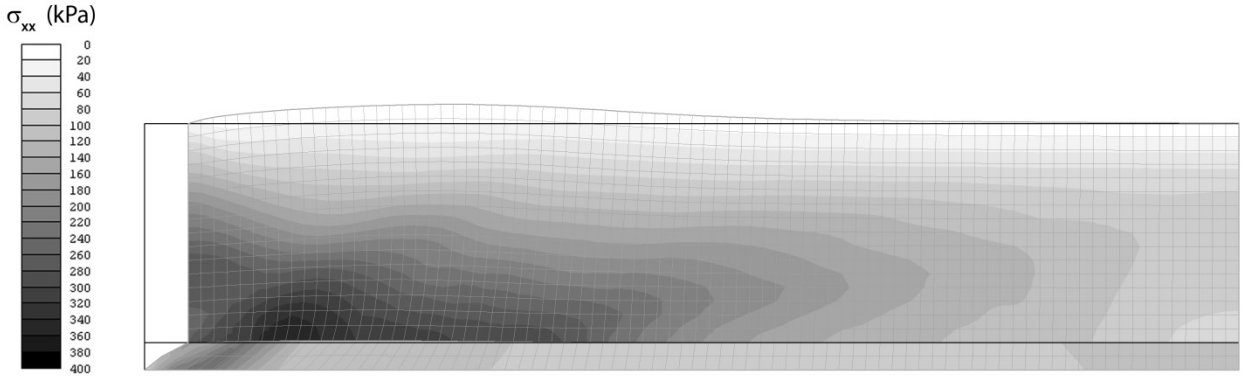

Figure 2.6 Deformed mesh and horizontal stresses for a 4 m- (157.5 in.-) thick cohesionless deposit with ϕ=35° and γ=20kN/m^3 over a 0.5 m- (19.7 in.-) thick weak layer with s_u=1 kPa.

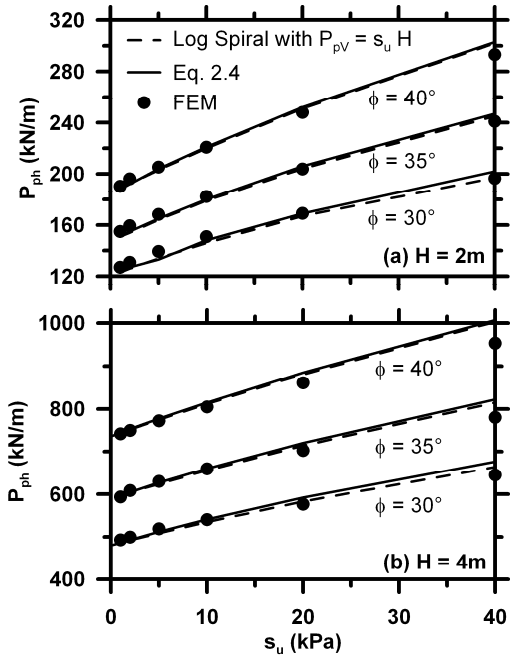

Figure 2.7 Horizontal component of passive force versus s_u for various ϕ for (a) H=2 m (6.56 ft) and (b) H=4 m (13.12 ft).

Results of the computed passive force values are plotted in Figure 2.7. At small values of s_u the passive force is only slightly larger than the Rankine passive force; as s_u increases, the passive force also increases. This observation is analogous to traditional log-spiral passive earth pressure theories in which increasing the soil/wall interface friction angle, δ, increases the passive force.

2.2.1.3 Analytical Model

The finite element method is useful for computing passive force for any combination of backfill properties, wall properties, and underlying soil properties, but a simpler solution would be useful since the time and expense required to perform a finite element analysis may not be justified for many projects. Consider the free-body diagram in Figure 2.8 that incorporates the strength of the underlying weak layer using a failure surface consisting of two linear segments; one horizontal segment through the underlying weak layer and another through the cohesionless backfill at an angle of 45°-ϕ/2 from the horizontal direction. This solution is similar to the Coulomb earth pressure theory since a planar failure surface is assumed. An expression for $P_{pH\theta}$ can be obtained by dividing the free-body diagram into two regions and enforcing force equilibrium (Equation 2.4). To find the solution for passive pressure, P_{pH}, the value θ_{cr} that minimizes $P_{pH\theta}$ must be solved. A closed-form solution for θ_{cr} is too unwieldy, but P_{pH} can be solved numerically using Newton-Raphson iteration, or simply by varying θ over a suitable range with a suitably small increment and computing the minimum $P_{pH\theta}$. Note that the solution for P_{pH} does not depend on P_{pV}, and P_{pV} is included in the free-body diagram in Figure 2.8 for completeness even though it has no effect on the solution. The lack of effect due to P_{pV} on the solution is consistent with Figure 2.4b, which shows that the earth pressure resultant is independent of wall friction when the base is frictionless.

$$P_{pH\theta} = \frac{\gamma H^2}{2} \frac{\left[\tan\left(45° - \frac{\phi}{2}\right) + \tan(\theta)\right] \tan\left(45° + \frac{\phi}{2}\right) \sin(\theta + \phi)}{\tan\left(45° - \frac{\phi}{2}\right) \tan(\theta) \left[\cos(\theta + \phi) \tan\left(45° + \frac{\phi}{2}\right) + \sin(\theta + \phi)\right]} + \frac{s_u H}{\tan(\theta)} \tag{2.4}$$

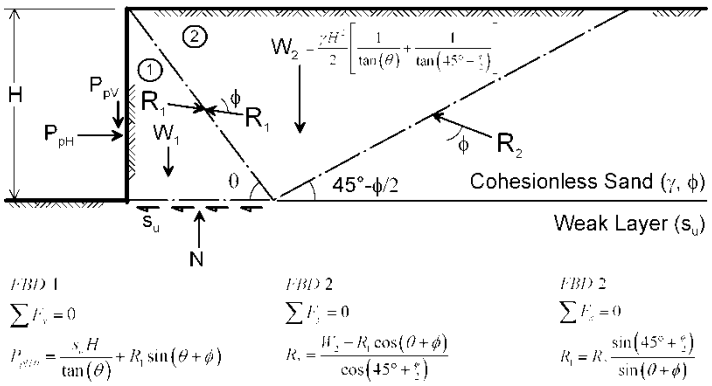

Figure 2.8 Analytical model for estimating passive force for a cohesionless deposit resting on a weak layer.

Note that the solution for Equation 2.4 is very similar to traditional Coulomb earth pressure theory if the soil/wall interface friction angle is adjusted such that $P_{pV} = s_u H$ (i.e., such that the average frictional stress acting on the wall is equal to s_u). Furthermore, Coulomb earth pressure theory is known to over-predict passive pressures when the interface friction angle between the wall and the backfill is large since the resulting log-spiral failure surface is not well-approximated by a plane. Based on these observations, another approach was also evaluated for estimating passive pressure in which a log-spiral method was utilized with an equivalent interface friction angle, δ_{eq}, selected such that $P_{pV} = s_u H$. The solution for δ_{eq} was obtained iteratively by (1) selecting a trial value of δ_{eq}, (2) computing $P_p = (\gamma H^2/2) \cdot K_p(\phi, \delta_{eq})$, (3) computing $P_{pV} = P_p \cdot \sin(\delta_{eq})$, and (4) repeating (1) through (3) until $P_{pV} = s_u H$. After computing δ_{eq}, the horizontal component of the passive force was computed as $P_{pH} = P_p \cdot \cos(\delta_{eq})$. The relation by Zhu and Qian (2000) was used to compute $K_p(\phi, \delta_{eq})$ combinations.

Solutions for P_{pH} corresponding to the combinations of H, ϕ, and s_u included in the finite element study were computed using both analytical solution methods; the results are superposed on the finite element solutions in Figure 2.7. The analytical solutions are in reasonable agreement with the finite element solutions, with differences less than 5%. For larger s_u values, the planar failure surface in Figure 2.8 predicts slightly larger P_{pH} than the log-spiral method with $P_{pV} = s_u H$. Friction along the base of the deposit causes curvature of the failure surface, hence the log-spiral mechanism more accurately represents the true failure mechanism. Neither method constitutes a mechanically rigorous solution, but both are very similar and agree well with the

finite element simulations, indicating that they are accurate within the range of input parameters studied in the finite element solutions. Both analytical methods are presented to give users an option for ease of implementation.

2.2.1.4 Discussion

The solutions presented herein are most appropriate when the underlying layer is weak relative to the passive pressures mobilized in the cohesionless deposit; they may be inappropriate for cases where the underlying layer is strong. In particular, a high s_u or low P_p value may result in a condition where $\delta_{eq}>\phi$, and the proposed analytical methodology is not validated for this condition. Numerical solutions or other appropriate methods should be used in such cases. This study applies only to two-dimensional loading conditions, but three-dimensional effects are known to increase passive force due to horizontal spreading of stresses. Three-dimensional effects would be anticipated to increase passive force for finite-width structures in the layered profiles studied herein, but it is unclear whether three-dimensional correction factors formulated for uniform soil conditions (e.g., Ovesen 1964; Duncan and Mokwa 2001) can be accurately applied.

In traditional passive earth pressure theory (and for the equations derived in this report), the soil is assumed to exert an upward friction stress on the wall since the soil typically bulges up as the wall is pushed horizontally into the soil (Figure 2.9a). However, when soil liquefies and spreads laterally, settlement is often caused by extensional strain in the crust and by sand boil formation in underlying liquefiable layers; therefore, it is conceivable that the direction of interface friction force may be reversed if the crust settles as it spreads laterally (Figure 2.9b). Hence, the direction in which P_{pV} acts is uncertain for liquefaction problems. If a down-drag force is mobilized, the passive force will be less than the Rankine passive force.

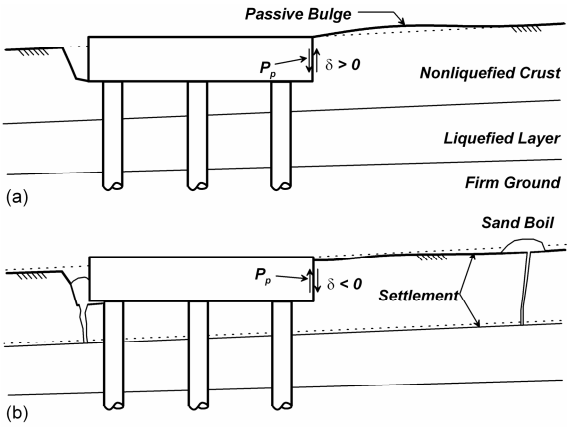

Figure 2.9 Load cases wherein (a) positive δ is mobilized as passive bulge forms, and (b) negative δ is mobilized as crust settles.

Uncertainty in the direction of P_{pV} is further illustrated in Figure 2.10, which shows the position of soil layers before and after applying a sequence of earthquake motions for centrifuge model SJB03 (Brandenberg et al. 2005). The nonliquefiable crust layer consisted of over-consolidated bay mud with a layer of coarse sand on top to protect the clay from desiccation due to wind currents during spinning. The crust was underlain by a liquefiable loose layer of Nevada sand (D_R = 35%) over dense Nevada sand (D_R = 75%). The model was subjected to a sequence of motions that liquefied the loose sand and caused the crust to spread laterally toward the water channel with displacements on the order of tens of centimeters in model scale at the toe of the slope. A passive bulge is clearly apparent on the crust surface upslope from the pile cap, hence it is reasonable to conclude that the upper portion of the spreading crust exerted an upward interface friction stress on the pile cap; this is consistent with the direction commonly assumed for passive earth pressure theory. However, settlement of the bottom of the clay layer is apparent behind the pile cap where the thickness of the clay layer increased with some clay moving upward and some moving downward. It is therefore unclear whether the resultant of the friction on the pile cap acted upward or downward. Brandenberg et al. (2005) found that Rankine earth pressure theory produced reasonable predictions of measured crust loads, but clear conclusions could not be obtained from the measured data because it was difficult to separate the passive force from the other components of horizontal force (i.e., friction between the sides and base of the cap and the spreading crust, loads on the pile segments beneath the cap).

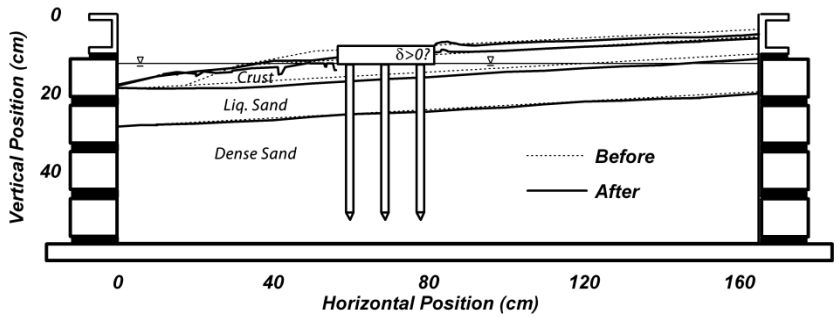

Figure 2.10 Centrifuge model after liquefaction-induced deformation. The direction of slip between crust and pile group is ambiguous.

Passive pressure in the presence of liquefaction and lateral spreading is more uncertain than for traditional problems in the absence of liquefaction. Additionally, passive pressure constitutes a driving force for lateral spreading problems, but a resisting force to an externally applied load for traditional problems. One should consider whether an upper-bound or lower-bound estimate of passive pressure is conservative for a particular problem. For traditional earth pressure problems, under-estimating passive pressure is conservative and the possibility that settlement could reduce passive force should be considered. For lateral spreading problems over-estimating passive pressure is conservative, and therefore assuming down drag at the soil/wall interface would be unconservative.

This section presented cases wherein the weak layer lies immediately beneath the deposit, but often a weak layer lies some distance below the deposit. For example, an abutment backwall often occupies the upper few meters of a much thicker embankment, and liquefaction of the soil underlying the embankment deep below the abutment wall may occur. It is currently unclear how a deep weak layer affects passive pressure mobilization, though the influence would be anticipated to reduce as depth to the weak layer increases.

The total crust load from the nonliquefied crust spreading against the embedded part of a structure (i.e., pile group or abutment wall), is the smaller of the load calculated by the two mechanisms (Figure 2.11). In the individual mechanism the soil spreads around the piles or around the sides of a pile cap or an abutment wall, and components of lateral crust load are passive pressure against the pile cap, friction between the cap and crust, and lateral loads on the pile segments beneath the cap. In the block mechanism the soil is trapped between the piles and the whole group acts as an equivalent block, and components of lateral loading are passive

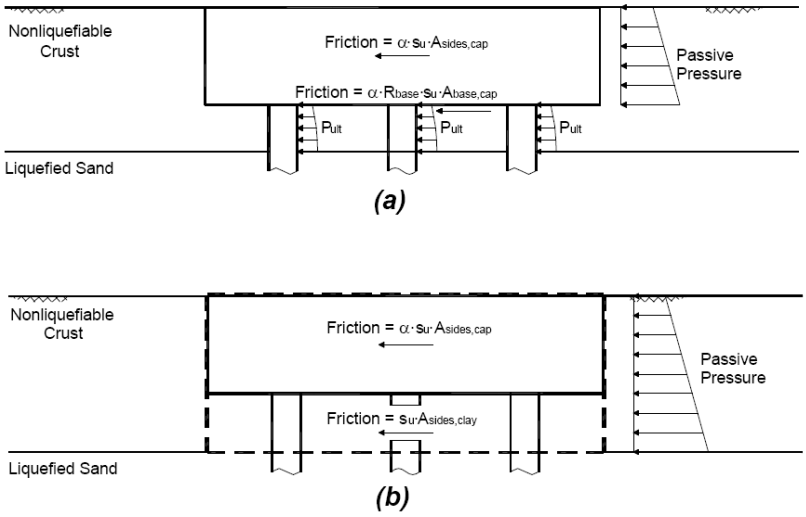

Figure 2.11 Mechanisms of spreading in nonliquefiable crust: (a) flowing mechanism and (b) equivalent block mechanism.

pressure on the equivalent block (i.e., through the entire crust thickness), and friction between the equivalent block and crust. Figure 2.11 represents the two mechanisms of spreading. The mechanism with the lower overall crust load controls. For cases where the block mechanism controls, the sum of *p*-*y* element capacities in the crust should be reduced by a *p*-multiplier so that the total crust load is equal to that computed for the block mechanism.

2.2.1.5 Influence of Liquefaction on Passive Pressure Stiffness

In a classical retaining wall problem at a site where the soils do not liquefy, the passive earth pressures develop in the backfill soils if the retaining wall is pushed into the soil. This might be the case when the diaphragm wall (abutment wall) of a bridge is pushed into the abutment by earthquake shaking. Static load tests in nonliquefied ground have shown that the ultimate passive pressures are mobilized at a wall displacement of 1% to 7% of the wall height. For example, Rollins and Sparks (2002) performed static load tests on pile groups in granular soil and observed that the peak load was mobilized at displacements of about 2.5% to 6% of the wall height, while Duncan and Mokwa (2001) and Mokwa and Duncan (2001) reported peak load occurring at displacements of about 1% to 4% of the pile cap height. Abutment wall tests performed by Lemnitzer et al. (2009) also showed that the peak passive load was attained at about 3% of the wall height.

However, the stiffness of the load transfer is fundamentally different for the cases where the nonliquefiable crust is spreading against a pile cap or abutment wall or another embedded component of the bridge. Brandenberg et al. (2007) showed that underlying soft soil (including liquefied sand) softens the load transfer between a crust and embedded bridge component. The primary cause of this soft response is the reduction of friction along the base of the spreading crust due to liquefaction of the underlying soils. Additional contributions may also come from gaps and cracks in the crust, and cyclic degradation in clayey crusts. The liquefaction of the ground under the crust influences distribution of stresses in the crust by creating an almost frictionless boundary that permits horizontal stresses to spread to large distances upslope from the embedded component, thereby increasing the zone of influence. Relative displacement is the integral of horizontal displacement in the zone of influence, hence a large zone of influence equates to a soft load transfer behavior. Centrifuge tests performed by Brandenberg et al. (2007) shows that the load transfer response in the nonliquefied crust is about an order of magnitude softer that the traditional *p-y* response in nonliquefiable soil profiles, meaning that an order of magnitude larger relative displacement is required to mobilize passive pressures (Figure 2.12). Therefore, in order to capture the load transfer observed in nonliquefied crust, the stiffness of the traditional *p-y* curves should be modified to account for this soft response. This can be done by adjusting the y_{50} value (deflection at one-half the ultimate soil resistance) in clays and by adjusting the modulus of subgrade reaction, k, for sands so that the shape of the *p-y* curve resembles the soft load transfer response of the nonliquefied crust.

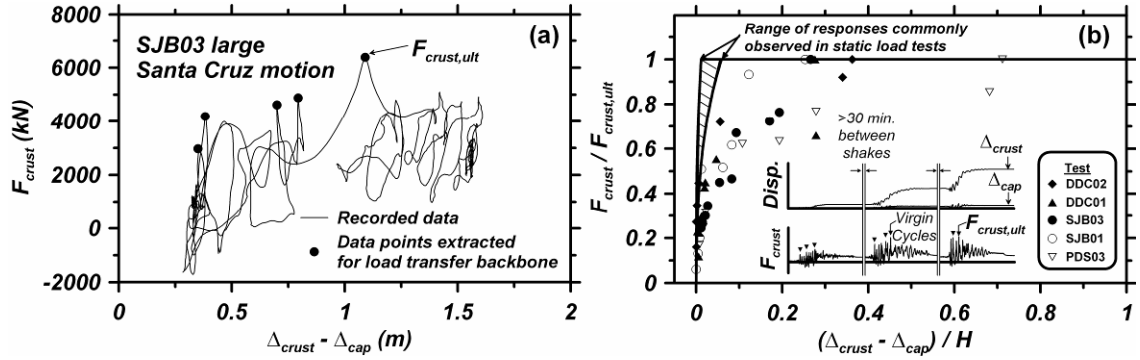

Figure 2.12 Load transfer in nonliquefiable crust: (a) recorded load-deflection data from centrifuge models and (b) normalized backbone load transfer relations (Brandenberg et al. 2007).

Brandenberg et al. (2007) proposed a mathematical model for determining the proper load transfer behavior for lateral spreading of the nonliquefied against a stationary pile cap. This procedure was used in determining the appropriate stiffness of the *p-y* springs at the piles caps and also abutment walls.

2.2.1.6 Soil-Structure Interaction Elements on Piles

Three different types of SSI springs are necessary for modeling the interaction of the piles and the surrounding soils: *p-y* elements are used to model lateral interaction, *t-z* elements are used to model friction between the soil and piles, and *Q-z* elements are used to model pile end bearing. The SSI elements on the piles were based on existing relationships for piles in nonliquefied ground and subsequently modified for the effects of liquefaction.

The *p-y* elements in clay followed relations developed by Matlock (1970) and *p-y* elements in sand followed API (1993). Matlock's equations are in the following form:

$$\frac{p}{p_{ult}} = 0.5\left(\frac{y}{y_{50}}\right)^{1/3} \tag{2.5}$$

where, p is soil resistance, y is deflection, p_{ult} is ultimate soil resistance, and y_{50} is deflection at one-half the ultimate soil resistance. The capacity of the *p-y* spring, p_{ult}, depends only on pile diameter and undrained shear strength of clay at deeper depths; at shallow depth, it also depends on the depth and unit weight of the clay. The parameter y_{50} is the measure of stiffness of the spring.

The API (1993) *p-y* curves for sands follow the form:

$$p = Ap_{ult}\tanh\left(\frac{kx}{Ap_{ult}}y\right) \tag{2.6}$$

where, k is the modulus of subgrade reaction of sand, x is depth of interest, and A is a factor to account for cyclic or static loading. The capacity of the spring, p_{ult}, in sands depends on the friction angle of the sand and its unit weight.

The *p-y* elements were modeled using the PySimple1 material available in OpenSees assigned to zero-length elements oriented normal to the length of the piles and attached at pile

nodes. The PySimple1 material fits a hyperbolic load-displacement function to the forms suggested by Matlock (1970) (PySimple1 Type 1) and API (1993) (PySimple1 Type 2). The PySimple1Gen command was used to automate the PySimple1 materials and zeroLength elements (which would be an otherwise tedious task to perform by hand since different materials are required at different depths along the piles).

Although these relationships provide good approximations and are appropriate for characterizing lateral interaction of the piles in clayey and sandy soils in sites where no liquefaction is present, the *p-y* behavior in sites where liquefaction occurs is much more complex. The dynamic load deflection behavior in liquefied sands was first observed by Wilson et al. (1998; 2000) by back-calculation of the results of dynamic centrifuge model tests of pile-supported structures (Figure 2.13).

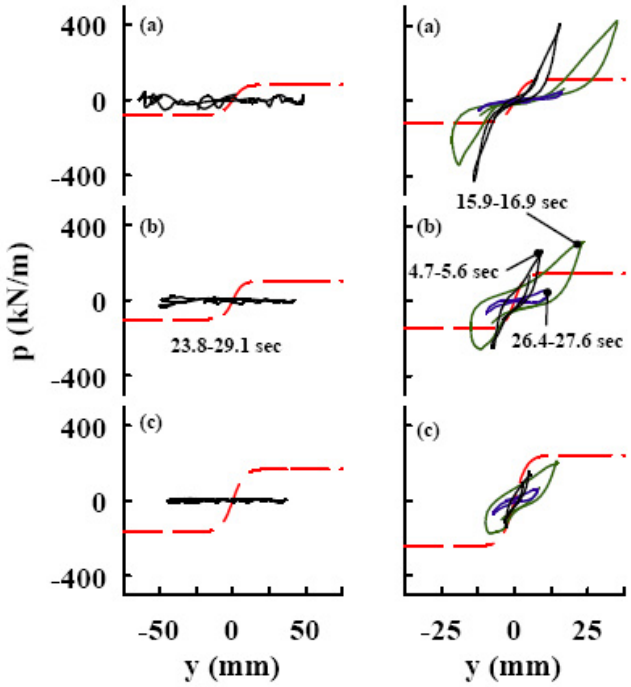

Figure 2.13 ***p-y*** **behavior in liquefied sand for loose sand (left column) and medium dense sand (right column).**

As can be seen in Figure 2.13, for loose sand (D_r = 35 %) the *p-y* response is very soft and weak relative to the traditional API (1993) curves. However the medium dense sand (D_r = 55 %) exhibits an inverted s-shaped displacement-hardening behavior, similar to the stress-strain

behavior in undrained loading of dilative saturated sands. Several studies [e.g., Tokimatsu et al. (2001); Ashford and Rollins (2002); Rollins et al. (2005)] have since observed similar responses as the response observed by Wilson et al. (1998; 2000).

The inverted *s*-shape of the load transfer is attributed to dilatancy of the medium dense sand during undrained loading. Sands that are dense of the critical state have the tendency to dilate, and since there is no plastic volumetric strain in undrained loading, the dilatant tendency manifests as a drop in pore pressure and associated increase in effective stress. The increase in effective stresses causes the soil to strain-stiffen, thereby causing the inverted *s*-shaped stress-strain behavior (Figure 2.14).

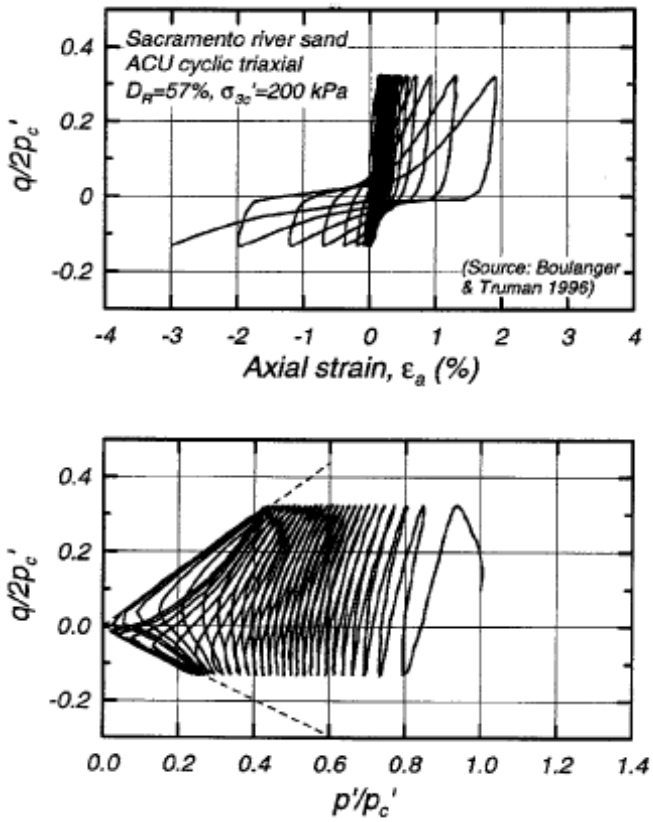

Figure 2.14 Stress-strain response and effective stress path for Sacramento River sand during undrained cyclic triaxial loading (Boulanger and Idriss 2006).

These features of dynamic *p-y* behavior in liquefied soil cannot be reasonably captured in static analysis. The most common approach for softening *p-y* elements to account for liquefaction is to apply reduction factors in the form of *p*-multipliers to the traditional API (1993) sand *p-y* curves. Brandenberg (2005) proposed *p*-multipliers for liquefied sands based on

penetration resistance of the sand, using $(N_1)_{60\text{-CS}}$, which is a directly related to the relative density of the sand, as summarized in Table 2.1. The *p*-multipliers in Table 2.1 are appropriate for conditions where excess pore pressure ratios reach unity. However, excess pore pressure ratios often reach an intermediate value between 0 and 1. Dobry et al. (1995) suggests that the *p*-multiplier can be linearly interpolated, as shown in Figure 2.15.

Table 2.1 *p*-multipliers, m_p, to account for liquefaction (Brandenberg 2005).

$(N_1)_{60\text{-CS}}$	m_p
<8	0.0 to 0.1
8-16	0.05 to 0.2
16-24	0.1 to 0.3
>24	0.2 to 0.5

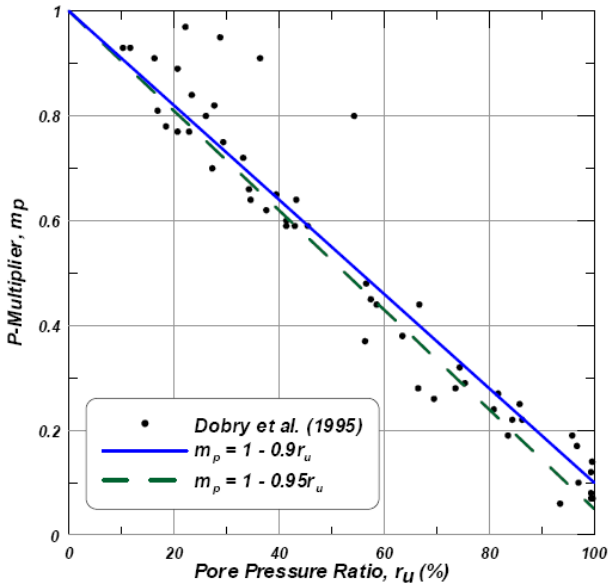

Figure 2.15 Effect of peak free-field excess pore pressure ratio on the ultimate capacity of *p-y* materials in liquefied sand (Dobry et al. 1995).

For piles in group configurations located in nonliquefied soil, often there is a group effect, causing a reduction in loads on the nonleading rows of piles. These group effects are usually accounted for by applying group effect multipliers. The group effects were accounted for the portions of the piles that were embedded in dense nonliquefiable soils. These group effects

should not be applied in the portions of the piles that were embedded in liquefiable sands since the liquefied sand is weak (Rollins et al. 2005), thus group multipliers were not included for liquefied sands. For *p-y* springs on portions of the piles embedded in the nonliquefiable crust, the stiffness of the *p-y* springs (y_{50}) should be modified in a similar manner as the *p-y* springs behind an abutment wall or a pile cap, as described in the previous section.

Axial interaction of the piles with the surrounding soil is modeled using *t-z* springs. *T-z* springs in the analyses were modeled by assigning TzSimple1 material to the zero-length elements oriented along the length of the piles. The free node of the zero-length *t-z* elements were fixed in all directions. The TzSimple1 material was symmetrical similar to the PySimple1 material. Little is known about the effects of liquefaction on the behavior of *t-z* elements. In the absence of data, *p*-multipliers may be assumed to characterize the effects of liquefaction on *t-z* behavior as well. Therefore, similar *p*-multipliers as the *p*-multipliers for liquefaction effects on the *p-y* springs were also applied to the *t-z* springs.

Tip bearing capacity of the piles was modeled by attaching *q-z* springs at the tip of the piles along the length of the pile. The free node of the *q-z* springs should also be fixed in all directions. In the OpenSees analyses, the QzSimple1 material was used for the *q-z* zero-length elements. Unlike the PySimple1 and TzSimple1 material in Opensees, the QzSimple1 material is not symmetrical since the capacity of the springs is much less in tension than it is in compression. As a result, care should be taken in orienting the zero-length element in the correct direction.

2.2.1.7 Selection of Inertia Loads

Inertia forces can occur simultaneously with lateral spreading displacement demands, and the two loads should be accounted for simultaneously in global equivalent static analysis procedures. However, the inertia demands must be altered to account for the effects of liquefaction. Changes in inertia demands compared with those for the nonliquefied case are caused by (1) the influence of liquefaction on site response, and (2) inertia forces acting out-of-phase with ground displacements. Brandenberg et al. (2005) showed that inertia demands may occur during lateral spreading, and can be an important contributor to the lateral loads on the foundation. A number of case histories and model studies have shown that lateral spreading may also occur after ground shaking has ceased due to void redistribution. For example, the Landing Road Bridge and

Showa Bridge were both affected by lateral spreading that occurred after shaking had stopped. For design, assuming the inertia demands and lateral spreading demands occur simultaneously is prudent. The probability of having zero inertia force can also be included in a probabilistic framework in performance-based earthquake engineering (PBEE).

Boulanger et al. (2007) presented two modification factors for adjusting the inertia demands to account for the effects of liquefaction. Table 2.2 shows the suggested modification factors to use in the equation:

$$Sa_{liq} = C_{cc}.C_{liq}.Sa_{\max\_nonliq} \tag{2.7}$$

where Sa_{liq} is the spectral acceleration when liquefaction is present, and $Sa_{\max\_nonliq}$ is the spectral acceleration for the nonliquefaction case. C_{liq} quantifies the influence of liquefaction on surface motion and is equal to the ratio of the peak horizontal surface acceleration with liquefaction to the peak horizontal surface acceleration without liquefaction. C_{cc} quantifies the phasing between the inertia demand and the total peak demand, expressed as the inertia value at the time that the critical loading cycle occurred (i.e., when the peak bending moment was measured in the piles) divided by the peak inertia value for the entire record. The values of C_{liq} and C_{cc} were based on dynamic finite element models calibrated with centrifuge test data. C_{liq} and C_{cc} varied with the frequency content of the ground motion that was imposed on the base of the finite element models, with low-frequency motions exciting the liquefied soil more than high-frequency motions. The frequency content of the motion was quantified as $Sa_{T=1s}$ / $Sa_{T=0s}$. The input motions appropriate for the analyses performed by Boulanger et al. (2007) would be rock motions, assuming that the site response analysis is performed on the soil layers lying above rock. Based on the spectral shapes for the Caltrans SDC, the middle row in Table 2.2 corresponding to $Sa_{T=1s} / Sa_{T=0s}$ = 0.5 to 1.6 contains the controlling factors. These factors should be applied to the ground surface motion expected without liquefaction.

Inertia demands are typically applied as displacements in spectral design of bridges. However, applying spectral displacements is complicated by the simultaneous application of lateral spreading displacements because only global boundary conditions can be controlled in a numerical model, whereas the displacement demand is a relative displacement measure. Applying the inertia demands as forces rather than displacements is more convenient and is permitted in the Caltrans SDC. However, this approach may not be numerically stable if a collapse mechanism forms.

Table 2.2 Factors C_{liq} and C_{cc} for modification of the nonliquefied inertia loads (Boulanger et al. 2007).

Response spectra for nonliquefied condition, $Sa_{T=1s} / Sa_{T=0s}$	Pile cap		Superstructure	
	C_{liq}	C_{cc}	C_{liq}	C_{cc}
1.7 – 2.4	1.4	0.85	0.75	0.65
0.5 – 1.6	0.75	0.85	0.55	0.65
≤ 0.4	0.35	0.85	0.45	0.65

2.3 EXAMPLE ANALYSES

In this section, a few examples of the nonlinear global equivalent static analyses are presented and explained in detail. The examples are intended to demonstrate the global ESA method that was used to derive the fragility functions in Chapter 4, and to show features of interaction among bridge components captured using global analysis that cannot be modeled using a local analysis. First a perfectly symmetrical three-span simply supported bridge with equal-length spans and single-column bents of the same height and dimensions, with seat-type abutments under several lateral spreading displacement patterns, is considered. Then the global response is compared with local analyses of a single component of the bridge (i.e., a single pile group and pier column) under similar loading conditions, and the differences between the local and global analyses are investigated. Finally, the response of this bridge under a certain loading conditions is compared with the response of a similar bridge with continuous super-structure and monolithic abutments under similar loading conditions.

2.3.1 Configuration of the Example Simply Supported Bridge with Seat-type Abutments

This example bridge is a simply supported three-span straight bridge with equal spans with circular identical single-column bents (Figure 2.16 and Table 2.3). Each bent is supported on a 3×4 group of 0.61m (24 in.) CIDH reinforced concrete piles connected by a 1 m- (3.28-ft) thick 4 m × 5 m (13.12 ft × 16.40 ft) pile cap, with the longer dimension in the transverse direction of the bridge. The superstructure is a 12.2 m (40 ft) wide concrete box-girder structure supported on

pile-supported seat-type abutments with a total height of 3.3 m (10.83 ft) for the backwall and stem wall. The abutments are supported on a 0.7 m (2.30 ft) pile cap that itself rests on two rows of six 0.61 m (24 in.) CIDH piles. The superstructure rests on elastomeric bearings with total pad thickness 0.051 m (2 in.) at the abutments, while they are connected at the top of pier columns using dowels (i.e., pinned connection).

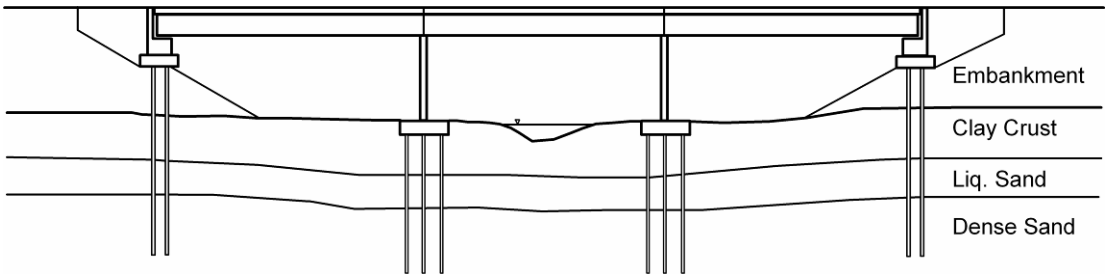

Figure 2.16 Schematic of the three-span simply supported bridge with seat-type abutments.

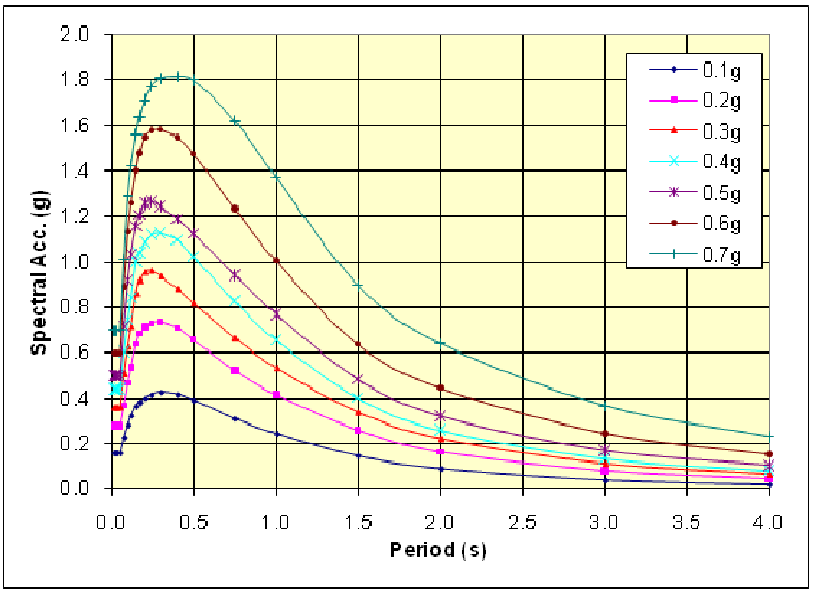

Figure 2.17 CALTRANS acceleration response spectra for 5% damping for magnitude 7.25 ± 0.25 in site class D.

Table 2.3 Properties of three-span simply supported bridge with seat-type abutment.

Parameter	Value
Spans Length	25 m
Pier Height	6.5 m
Pier Diameter	1.46 m
Pier Yield Moment	7011 kN.m
Pier Initial Stiffness, EI	2.107×10^6 kN.m^2
Pier Shear Capacity	3049 kN
Pile Diameter	0.61 m
Pile Yield Moment	400 kN.m
Pile Initial Stiffness	5.797×10^4 kN.m^2
Bearing Height	0.051 m
Bearing Capacity	490 kN
Bearing Yield Displacement	0.035 m

Table 2.4 Thickness and properties of the soil layers in the layers used in the example problems.

Soil Layer	Thickness of the layer (m)	Unit Weight, γ (kN/m3)	Friction Angle, φ (degrees)	Cohesion, (kPa)	Subgrade Reaction, k (kN/m^3)	m_p
Embankment	6	20	38	20	80-1357 *	1
Natural Crust	3	19	0	70	-	1
Liquefied Sand	2	19	32	-	25,541	0.05
Dense Sand	-	20	38	-	55,450	0.65 **

* The subgrade reaction stiffness at the embankment crust is adjusted to match the y_{50} value calculated using Brandenberg et al. (20070 relations for the stiffness of the nonliquefiable crust.
** The multiplier in the dense sand layer is selected based on Dobry et al.(1995) assuming an excess pore pressure of about 40%.

The soil profile used in this example is a typical liquefiable site soil profile. In this example, the natural crust overlying the liquefied sand layer is a clayey crust. The ground water

level is assumed to be at surface of the crust. The properties of the soils in this soil profile are summarized in Table 2.4.

The *p*-multiplier in the liquefied sand is selected to be 0.05 based on recommendations by Brandenberg (2005) and Dobry et al. (1995). The *p*-multiplier for the dense sand underlying the liquefied sand was selected using the relation recommended by Dobry et al. (1995) ($m_p = 1 - 0.95 r_u$), assuming an excess pore water pressure of about 40%.

The stiffness of the *p-y* springs in the nonliquefied crust was estimated using the relations presented by Brandenberg et al. (2007) for both the crust at the abutment (embankment fill and nonliquefied crust) and the clayey crust at the intermediate piers; the y_{50} values for the crust at the abutment and pile caps were estimated to be 0.2 m (7.87 in.) and 0.05 m (1.97 in.), respectively. The subgrade reaction in the embankment fill sands was adjusted so that the load transfer at the embankment is consistent with the soft response typical of nonliquefied crusts spreading over liquefied sand layers.

The displacement profile in liquefied ground often exhibits a discontinuity at the interface of the liquefied sand and the nonliquefied crust. The discontinuity is caused by the relative sliding of nonliquefied crust over liquefiable sands due to void redistribution (Malvick et al. 2008). In these examples the displacement at the interface of the crust and the liquefied sand is half of the displacement in the liquefied crust. The displacements in the denser sand layer are zero. The displacements in the liquefied sand layer increase linearly (i.e., constant strain), while the displacements in the crust are constant throughout the thickness of the layer (i.e., zero strain). The inertia loads on the bridge were calculated by estimating the spectral acceleration S_a of the bridge in a nonliquefied site (i.e., $S_{a\,\max\_nonliq}$) and modifying the demand using the modifications for the demand in liquefiable sites, as discussed earlier. The S_a of the bridge in a nonliquefied site was obtained from Caltrans' Acceleration Response Spectra (ARS) shown in Figure 2.17 at the desired level of shaking and using the appropriate soil class site, based on the first-mode natural period of the bridge. The period of the bridge in the longitudinal direction was approximated according to the formula:

$$T = 2\pi \sqrt{\frac{m_{trib.}}{k_{cl}}} \tag{2.8}$$

where, $m_{trib.}$ is the tributary mass acting on each of the columns, and k_{cl} is the stiffness of the column. The lateral stiffness of the column for a simply supported bridge can be calculated to be:

$$k_{cl} = \frac{3EI_{eff}}{h^3} \tag{2.9}$$

where, EI_{eff} is the effective bending stiffness of the column, and h is the height of the column.

The lateral stiffness of this continuous bridge is: $k_{cl} = 3 \times (2.107 \times 10^6 \text{ kN.m}^2) / (6.5 \text{ m})^3 = 23{,}107 \text{ kN/m}$ and the tributary of mass acting on each pier is $m_{trib.} = 308.8Mg$. Subsequently, the fundamental period of the bridge in the longitudinal direction can be approximated to be $T = 2\pi\sqrt{308.8Mg / 23{,}107 \text{ kN/m}} = 0.73 \text{ sec.}$ Lengthening of the natural period of the bridge due to liquefaction is accommodated using the C_{cc} and C_{liq} factors suggested by Boulanger et al. (2007).

The shear wave velocity of this site associated with the first 30 m (98.43 ft) ($V_{s_{30}}$) of this profile was estimated to be about 270 m/sec (885.83 ft/sec), which, puts this site in site class D (i.e., 180 $< V_{s_{30}} <$ 360) according to Caltrans SDC (2006). The nonliquefiable S_a for a bridge located in site class D, undergoing rock shaking of $a_{\max} = 0.4g$ during an earthquake of magnitude 7.25 ± 0.25 using the ARS curves available in Caltrans SDC is 0.85*g* at the period of this bridge. The liquefied S_a for this bridge is then, 0.3g ($C_{cc} = 0.65, C_{liq.} = 0.55$).

Lateral spreading displacements may occur in many different combinations at different bridge components. For example, spreading might occur only on one side of a channel, or on both sides. Spreading may be larger at a pier near a channel than at the abutment further upslope. Furthermore, the maximum demand on the bridge components may occur when the direction of the application of the inertia is in the direction of lateral spreading, or when the direction of the inertial force is against the direction of spreading. Therefore, it is important to consider different possible scenarios (i.e., load cases) when performing nonlinear global equivalent static analyses. The examples that follow explore several possible load cases and bridge configurations.

2.3.2 Effect of Different Displacement Patterns on the Response of the Bridge

Table 2.5 summarizes the response of the piers of the example bridge described above under different global and local loading conditions. Load case 1 (Figure 2.18) considers the bridge under lateral spreading displacements happening in the left spreading feature (i.e., left abutment and left pier) of the bridge with 0.50 m (1.64 ft) of free-field ground displacement at the left abutment with 2 m (6.56 ft) of lateral spreading at the left pier. It is also assumed that in this loading condition the inertia is still present while the lateral spreading is occurring. In this load case, the inertia load is considered to be happening in the direction of spreading. As a result, inertia loads were applied as a force equal to the product of the mass and spectral acceleration S_a of the bridge, while the displacement demands on the bridge were linearly increasing.

Under this loading condition the entire bridge is moving from left-to–right under the combined effects of lateral spreading and inertia demands. Large demands are mobilized in the piles supporting the left abutment and the left pier, which are the locations where lateral spreading displacements were imposed. The pile cap displacement at the left pier is 0.34 m (1.12 ft), while the superstructure displacement is 0.30 m (11.81 in.), which places only 0.04 m (1.58 in.) of displacement demand on the pier. In contrast, the pile cap displacement at the right pier is less than 0.02 m (0.79 in.), while the displacement of the top of the pier is 0.30 m (11.81 in.), placing a much more significant displacement demand that yields the pier and mobilizing a curvature ductility of 9.5 (M_{max} = -9980 kN·m). This global analysis demonstrates how lateral spreading demands on some bridge components can transfer demands to other components founded in firm ground. This type of interaction can only be properly modeled using a global analysis.

Table 2.5 Summary of pier responses under different global and local loading conditions.

Analysis ID	$M_{\max}$ (kN·m)		Δ_{cap} (m)		μ_ϕ		$\Delta_{Top\ Pier}$ (m)		θ_{Cap} (%)	
	Left Pier	Right Pier	Left Pier	Right Pier	Left Pier	Right Pier	Left Pier	Right Pier	Left Pier	Right Pier
Global 1	5771	-9980	0.34	0.018	< 1	9.5	0.3	0.3	-0.04	-0.76
Global 2	-6436	-6238	0.015	0.014	< 1	< 1	0.078	0.074	-0.31	0.28
Global 3	6759	-9007	0.26	0.01	< 1	6.7	0.19	0.19	0	0.47
Local 1	-5710	N/A	1.965	N/A	< 1	N/A	3.94	N/A	-29.8	N/A
Local 2	9228	N/A	0.168	N/A	7.3	N/A	0	N/A	-0.1	N/A
Local 3	5710	N/A	0.319	N/A	< 1	N/A	0.282	N/A	-0.03	N/A

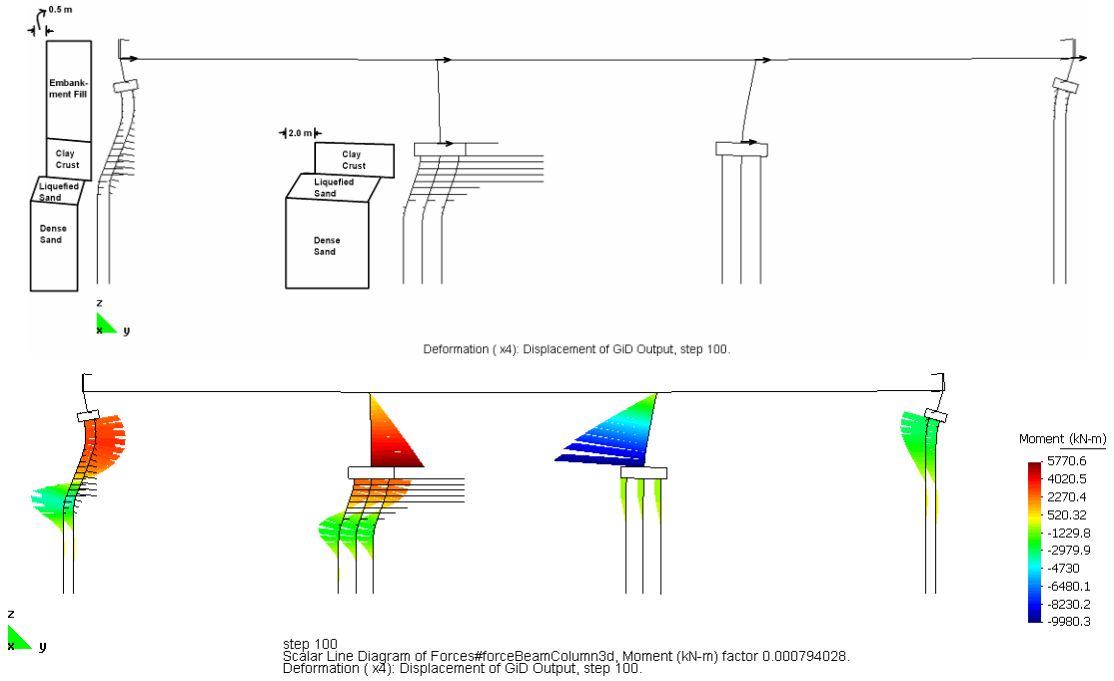

Figure 2.18 Global analysis load case 1 showing load pattern and deformed mesh (top) and deformed mesh and moment distribution in nonlinear beam column elements (bottom). Deformations amplified by a factor of 4.0.

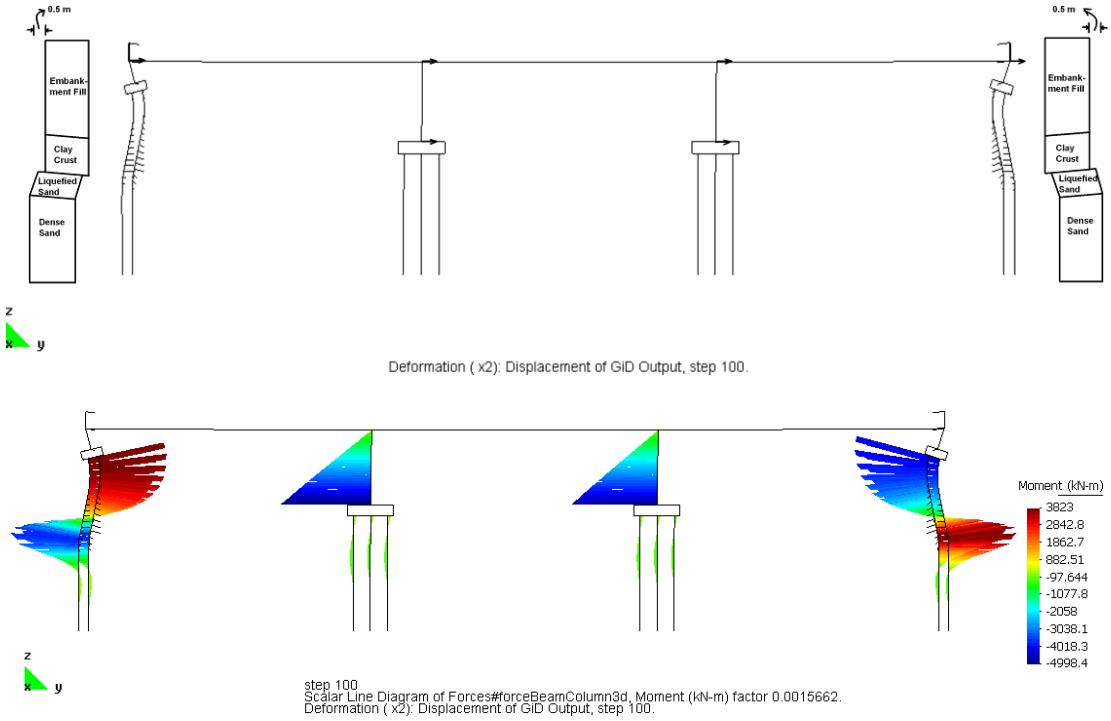

Figure 2.19 Global analysis load case 2 showing load pattern and deformed m (top) and deformed mesh and moment distribution in nonlinear beam column elements (bottom). Deformations amplified by a factor of 2.0.

Load case 2 considers the bridge under symmetrical displacement demand from both abutments of the bridge, such that the lateral spreading displacements are equal in magnitude [maximum ground displacement is 0.5 m (19.69 in.)] but opposite in direction toward the center of the bridge. The inertia demand is also present and is applied from left to right. This loading condition is shown in Figure 2.19, with the corresponding deformed mesh and the bending moment distributions on the piles and the piers of the bridge. Since the spreading is perfectly symmetrical, the only demand on the piers comes from the inertia load that is being concurrently applied with lateral spreading displacements which moves the superstructure about 0.08 m (3.15 in.) to the right. However, the inertia demand is not large enough to cause the pier columns to yield. The piles supporting the abutments suffer extensive deformations to the extent that failure is expected; thereby reducing their axial load carrying capacity.

While the analysis clearly predicts extensive damage to these piles, the amount of damage predicted may be unreasonable for several reasons. The large demands are, in part, an artifact of the Winkler assumption that the *p-y* element behaviors are independent of the adjacent elements and the fact that free-field ground displacements are being imposed on the piles. In

essence these assumptions result in an unrealistic soil deformation pattern wherein the actual soil deformation would be small behind the abutment backwall and large deeper down at the piles. A two- or three-dimensional pinning analysis would more reasonably capture the manner in which the forces imposed on the embankment by the abutment backwall would reduce deformations in the underlying soils; such an analysis is beyond the scope of this work. Nevertheless, the predicted abutment displacement is consistent with the bridge deformation mechanism observed at several bridges in past earthquakes (e.g., in Kashiwazaki during the 2007 Niigata Chuetsu-Oki earthquake; Kayen et al. 2007).

2.3.3 Effect of the Direction of the Inertia Demands on the Bridge Response

Inertia demand on bridges and other structures during an earthquake is transient and alternating in all directions. As a result, when liquefaction and lateral spreading occurs at the site of the bridge during an earthquake, at an instant in time the inertia load acting on the bridge can range from being perfectly in-phase with the lateral spreading displacement demands to being perfectly out-of-phase. Thus, it is important to consider the inertia loads in-phase and out-of-phase with lateral spreading since the overall demand may be more severe in one case or the other.

Load case 3 (Figure 2.20) has the same lateral spreading demand as load case 1 (Figure 2.18), however the inertia demand in load case 3 is out-of-phase with lateral spreading demands. Here, the displacement demand due to inertia in the opposite direction of spreading displacement demand increases the bending moment in the left pier from 5771 $\mathrm{kN \cdot m}$ to 6759 $\mathrm{kN \cdot m}$. While this demand is still lower than the yield moment of the pier (7011 $\mathrm{kN \cdot m}$), it is obvious that load cases with out-of-phase inertia may result in higher demands on the piers, causing them to yield or reach higher curvature ductilities. On the other hand, the inertia acting in the opposite direction of spreading results in lowering the superstructure displacement from 0.3 m to 0.19 m (11.81 in to 7.48 in). This results in reduction of displacement demands on the right pier causing a reduction in curvature ductility from 9.5 to 6.7 (M_{max} = -9980 $\mathrm{kN \cdot m}$ to M_{max} = -9007 $\mathrm{kN \cdot m}$). Pile cap displacement at the left pier is also reduced from 0.34 m to 0.26 m (1.12 ft to 0.85 ft). Generally speaking, the demand on the bridge can be significantly affected by the direction of inertia, and the above example points to the importance of considering both load cases when evaluating the performance of the bridge under liquefaction-induced demands.

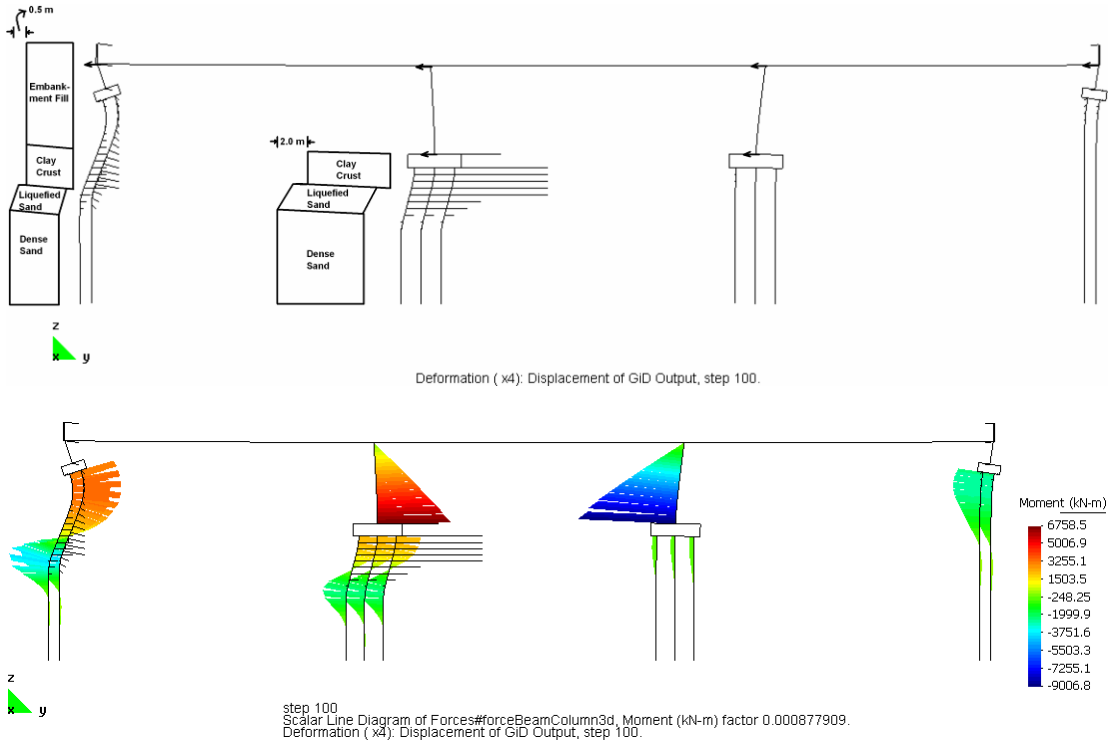

Figure. 2.20 Global analysis load case 3 showing load pattern and deformed mesh (top) and deformed mesh and moment distribution in nonlinear beam column elements (bottom). Deformations amplified by a factor of 4.0.

2.3.4 Effect of Bridge Type on the Response of Bridges

In order to investigate the effect of bridge type on the response of the bridge under lateral spreading demands, consider a bridge similar to the bridges in load cases 1 to 3 compared to a bridge with exactly the same geometry but with a continuous superstructure and with monolithic abutments. The superstructure is connected to a 3-m (9.84 ft-) tall diaphragm wall supported on a single row of six 0.61 m (24 in) CIDH piles (Figure 2.21) (consistent with common foundations for diaphragm abutments). The boundary conditions of this bridge are different (i.e., fixed-fixed), therefore, the period of the bridge should be calculated based on a lateral stiffness of a column fixed at both top and bottom, as follows:

$$k_{cl} = \frac{12EI_{eff}}{h^3} \tag{2.10}$$

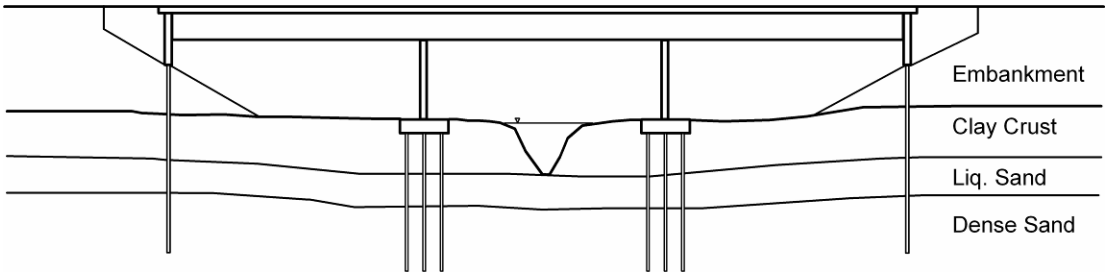

Figure 2.21 Schematic of the three-span continuous bridge with monolithic abutments.

Therefore, $k_{cl} = 12 \times (2.107 \times 10^6 \text{ kN.m}^2) / (6.5 \text{ m})^3 = 92,428 \text{ kN/m}$ and subsequently the period of the bridge is $T = 2\pi\sqrt{308.8Mg/92,428 \text{ kN/m}} = 0.37 \text{ sec}$. The nonliquefiable S_a for a bridge located in site class D, undergoing rock shaking of $a_{\max} = 0.4g$ during an earthquake of magnitude 7.25 ± 0.25 using the ARS curves, is $1.10g$ at the period of this bridge. The liquefied S_a for this bridge is then, $0.4g$ ($C_{cc} = 0.65, C_{liq.} = 0.55$).

Load case 4 (Figure 2.22) considers this continuous bridge under the same lateral spreading displacement pattern as in load case 1 [i.e., 2 m (6.56 ft) of spreading at the left pier and 0.5 m (19.69 in.) of spreading at the left abutment], and with inertia acting in-phase with the lateral spreading demands but with inertia demands associated with a S_a equal to $0.4g$ based on the period of this bridge. Table 2.6 shows the comparison of the results of the two bridges considered in load cases 1 and 4.

As can be seen in Figure 2.22, the moment distribution mobilized at the end of load case 4 shows a double curvature as would be expected in bridges with columns with double fixity. Compared with the bridge with seat type abutments, the diaphragm abutments increase the stiffness of the bridge and reduce the superstructure displacement from 0.3 m to 0.13 m (11.81 in. to 5.12 in.). Also the pile cap displacements at the left pier reduced from 0.34 m to about 0.15 m (13.39 in. to 5.91 in). Furthermore, the stiffer right pier in this case, imposes more displacement and rotation demand at the right pile cap because of the displacement of the superstructure.

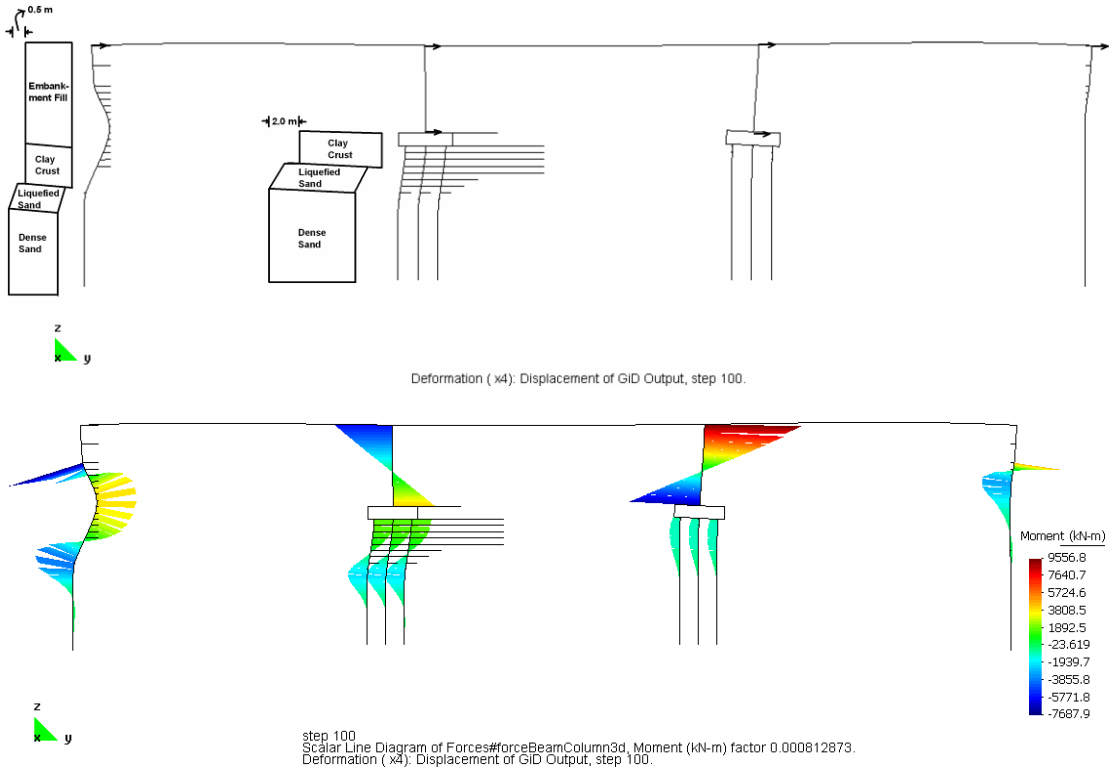

Figure 2.22 Global analysis load case 4 (continuous bridge with monolithic abutments) showing load pattern and deformed mesh (top), and deformed mesh and moment distribution in nonlinear beam column elements (bottom). Deformations amplified by a factor of 4.0.

Table 2.6 Comparison of the response between a simply supported bridge with seat-type abutments and a continuous bridge with monolithic abutments under the same loading conditions.

Analysis ID	$M_{\max}$ (kN·m)		Δ_{cap} (m)		μ_ϕ		$\Delta_{Top\ Pier}$ (m)		θ_{Cap} (%)	
	Left Pier	Right Pier	Left Pier	Right Pier	Left Pier	Right Pier	Left Pier	Right Pier	Left Pier	Right Pier
Global 1	5771	-9980	0.34	0.018	<1	9.5	0.3	0.3	-0.04	-0.76
Global 4	-5734	9557	0.146	0.035	<1	8.3	0.136	0.132	0	-1.3

2.3.5 Comparison of Global Analyses and Local Analyses

Although global equivalent static analyses can capture the interaction between different bridge components, the computational demand required to model the entire bridge is often not justified and local analysis of a single sub-system is performed instead. Unfortunately, local analysis does not directly capture the interaction of multiple sub-systems, therefore, the boundary conditions imposed in the local analysis should envelope the possible global boundary conditions. In this section, local analyses of a single pier are performed and compared with the global analyses. The left pier and pile group are modeled in the local analysis, and several different boundary conditions are imposed at the top of the pier. The rotational restraint at the top of the pier is free for a simply supported bridge and fixed for a monolithic bridge. The displacement degrees of freedom are modeled separately in order to capture possible global loading mechanisms. First, the inertia force is imposed in-phase with lateral spreading displacements to represent a condition where the superstructure displacement is driven largely by inertia loading (Figure 2.23). Second, the top of the pier is held fixed at zero displacement to model the possible case where the superstructure is held in place by other sub-systems in nonliquefiable stable ground (Figure 2.24), which in turn fixes the top of the pier against displacement. Finally, the inertia force is imposed in the opposite direction from lateral spreading displacements as this condition may cause large displacement demands on the pier (Figure 2.25). The free-field ground deformation profile applied to the left pier in global load cases 1 and 3 is applied to the pile group in the local analysis.

Global load case 1 and local load case 1 have identical displacement and inertia demands, yet the response of the local analyses did not capture the response observed in the global load case 1. The local analysis predicts significant displacement at the pile cap [1.97 m (6.46 ft)] due to yielding of the piles and a pile cap rotation of about 30%. The superstructure displacement is 3.94 m (12.93 ft). The difference between the local and global analysis here is that the local analysis does not permit the pier to help resist lateral loads from the spreading soil by transferring forces to the abutments and the other pier.

Local load case 2 attempts to better capture the distribution of forces through the pier to other components by fixing the top of the pier against horizontal translation. Compared with global analysis 1, local load case 2 predicts smaller pile cap displacement [(0.17 m (6.70 in.)]

compared with 0.34 m (1.12 ft) and larger flexural demand on the pier (M_{max} = 9228 kN·m compared with 5771 kN·m), causing the pier to reach a curvature ductility of 7.3.

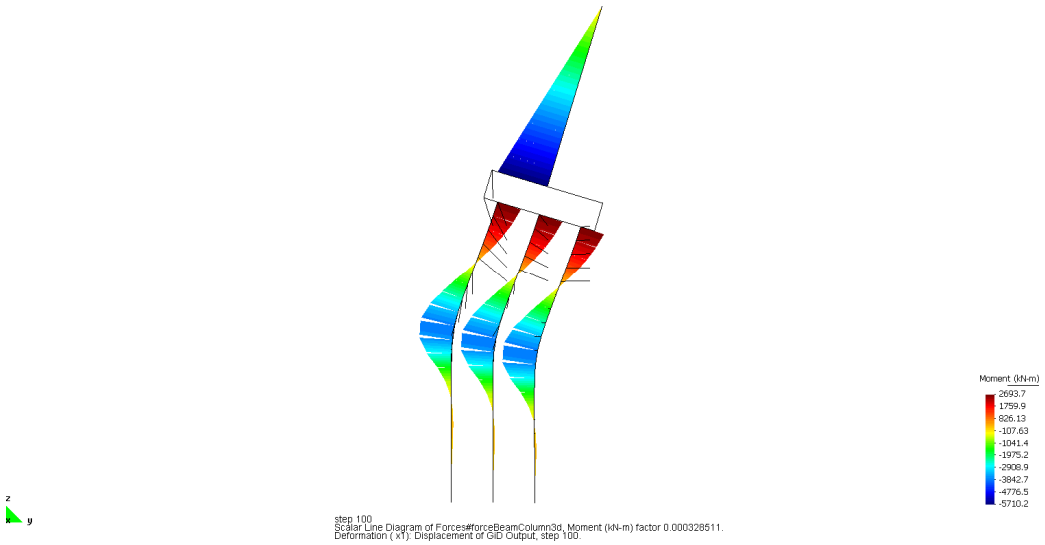

Figure 2.23 Local analysis 1 showing deformed mesh and moment distribution. Deformation × 1.

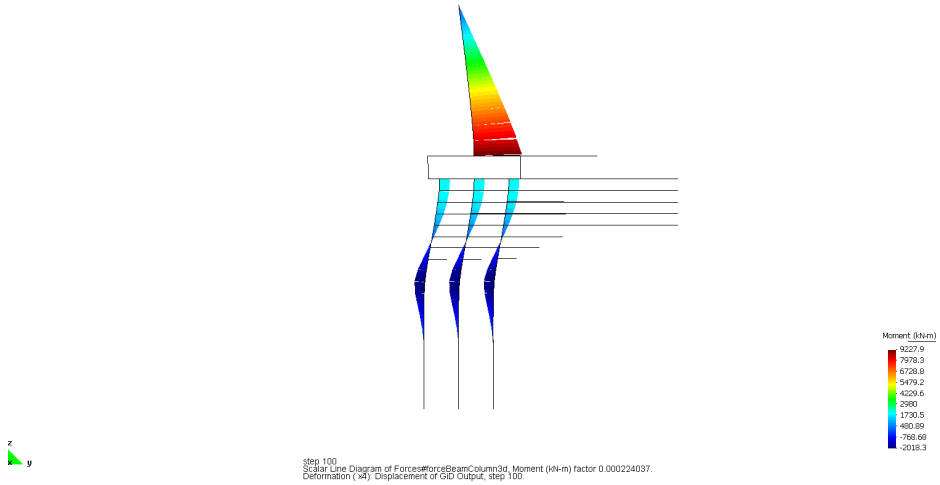

Figure 2.24 Local analysis 2 showing deformed mesh and moment distribution. Deformation × 4.

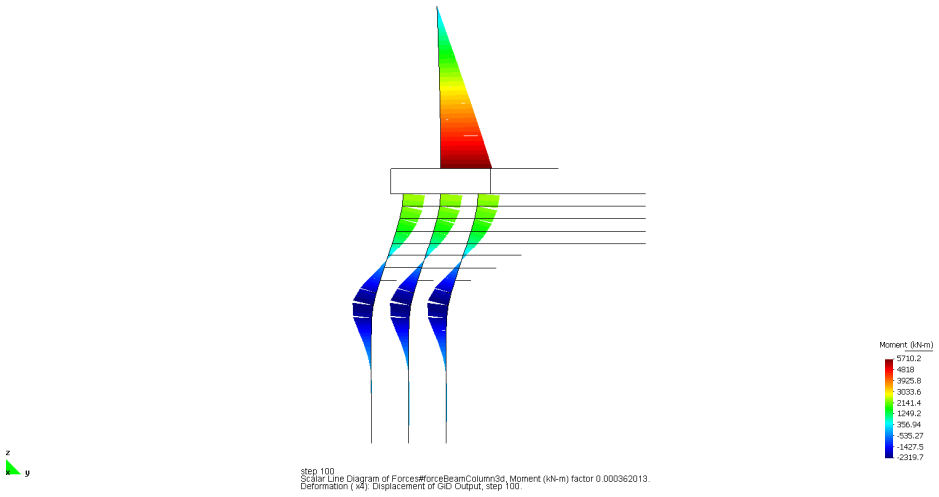

Figure 2.25 Local analysis 3 showing deformed mesh and moment distribution. Deformations × 4.

Global load case 3 and local load case 3 (Figure 2.25) have the same free-field ground deformation profile and inertia demand, with inertia load acting out-of-phase relative to the lateral spreading displacements. However, differences arise in the predicted response. Local load case 3 predicts large pier top displacement [0.28 m (11.02 in.) compared with 0.19 m (7.48 in.)], larger pile cap displacement [0.319 m (12.56 in.) compared with 0.26 m (10.24 in.)] and smaller bending moment demand (5710 kN·m compared with 6759 kN·m). These trends are consistent with the distribution of demands from the pier to other components through the superstructure in the global analysis.

Clearly, the local analysis approach differs significantly from the global analysis method, but in general the three different loading conditions imposed in the local analyses enveloped the responses from the global analyses. Here, significant pile cap displacements and demands on the piers would be predicted using either global or local analysis methods, with a similar conclusion that the foundation performance is inadequate. Therefore, local analysis may be a feasible design tool, with the acknowledgment that global analysis is believed to more accurately model the behavior of the entire bridge. The purpose of this report is not to formulate a design method but rather to evaluate the behavior of bridges (many of them are old and fragile) to liquefaction and lateral spreading. The global method is better suited to this goal.

Table 2.7 Properties of the .61 m (24 in.) CISS piles.

Parameter	Value
Pile Diameter	0.61 m
Pile Yield Moment	1977 kN.m
Pile Initial Stiffness	2.865×10^5 kN.m^2

Table 2.8 Comparison of the response of the bridge with strong CISS piles under global and local analyses.

Analysis ID	$M_{\max}$ (kN·m)		Δ_{cap} (m)		μ_ϕ		$\Delta_{Top\ Pier}$ (m)		θ_{Cap} (%)	
	Left Pier	Right Pier	Left Pier	Right Pier	Left Pier	Right Pier	Left Pier	Right Pier	Left Pier	Right Pier
Global 5	2518	-5404	0.04	0.003	<1	<1	0.048	0.048	0	0
Local 4	-5710	N/A	0.147	N/A	<1	N/A	0.36	N/A	-2.6	N/A
Local 5	4967	N/A	0.027	N/A	<1	N/A	0	N/A	-0.11	N/A
Local 6	5710	N/A	0.025	N/A	<1	N/A	-0.007	N/A	-0.11	N/A

2.3.6 Effect of Pile Strength on the Response of the Bridges

Having determined that the foundation in the previous examples would be considered inadequate from a design perspective, the analysis was repeated with larger diameter piles, which we will refer to as global case 5. Global load case 1 (i.e., inertia load in-phase with lateral spreading displacements) was repeated with the 0.61 m (24 in.) CIDH piles are substituted with 0.61 m (24 in.) cast-in-steel-shell (CISS) piles, with properties summarized in Table 2.7. Local load cases 1, 2, and 3 were also repeated with the 0.61 m (24 in.) CISS piles, and called local load case 4, 5, and 6, so that a comparison between the local load cases can be made with the global analysis. Table 2.8 summarizes the results of the analyses performed using 0.61 m (24 in.) CISS piles.

Figure 2.26 shows the deformed mesh and moment distribution for the global load case 5 with CISS piles, which are clearly much more effective than the CIDH piles in resisting lateral spreading demands on the bridge. The pile cap supporting the left pier displaced only 0.04 m (1.58 in.) [compared with 0.34 m (1.12 ft) for the CIDH piles] despite 2 m (6.56 ft) of lateral

spreading displacements being applied at this pier. Also the superstructure displaced less than 0.05 m (1.64 ft). Neither pier column yielded with the CISS piles because the pile cap did not displace significantly.

The local load cases better envelope the global response for the CISS piles, indicating that local analyses are more than adequate when the foundation performance is good. This is consistent with the observation that (1) the primary difference between the local and global analysis is the ability of the latter to distribute demands to other components through the superstructure, and (2) less demand is distributed through the pier to the superstructure when the foundations are stiff and strong. This confirms the previous observation that local analysis can be a useful design tool, but global analysis is better for predicting the distribution of demands throughout the bridge.

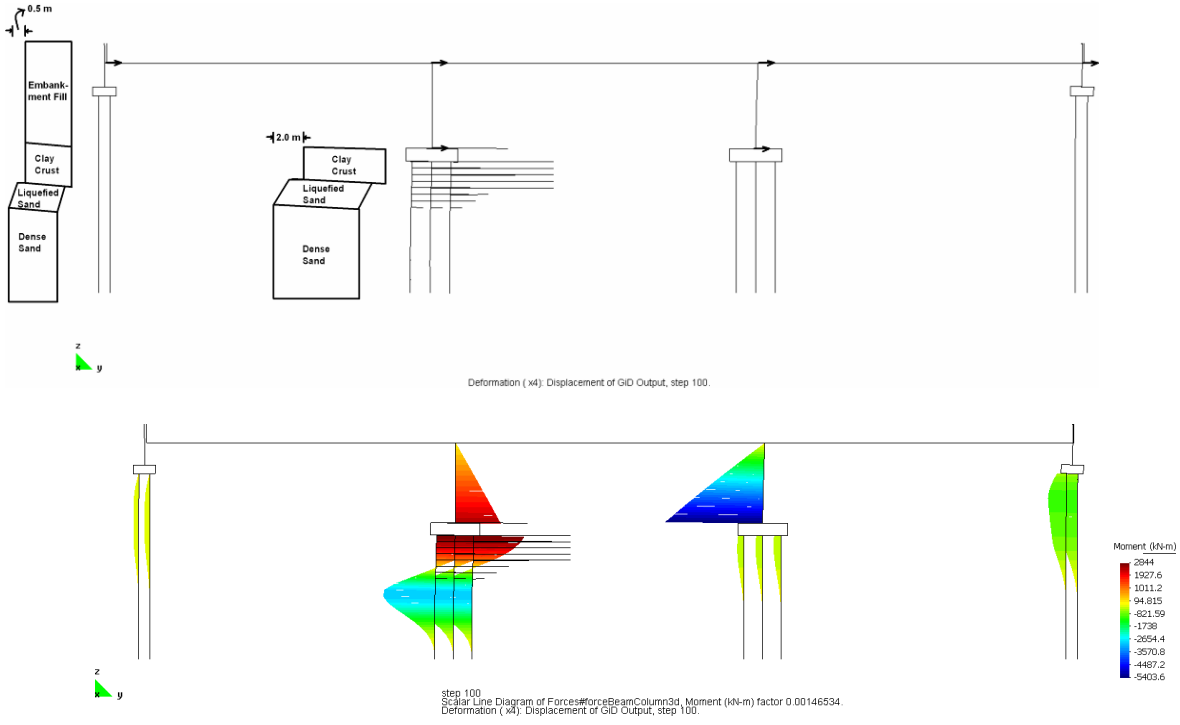

Figure 2.26 Global analysis load case 5 with CISS piles showing load pattern and deformed mesh (top) and deformed mesh and moment distribution in nonlinear beam column elements (bottom). Deformations amplified by a factor of 4.0.

2.3.7 Pile Pinning Effect of Reducing Displacement Demands on Abutments

Abutment walls and piles at the abutments reduce the displacement demands imposed on the bridge by restraining the finite-width slope. This reduction in demand has been called "pile pinning," although bridge components other than the piles also contribute to pinning. The procedure is referred to as a "pinning" analysis herein. Free-field lateral spreading ground deformation is not the appropriate demand to place on bridge components in a finite-sized lateral spread (e.g., when the out-of-plane thickness is small for an embankment, or when the upslope extent of the spread is small). Rather, a displacement demand that is compatible with the pinning forces should be used. A pinning-compatible displacement is determined by performing a two-step procedure first proposed by the Transportation Research Board (TRB 2002) and subsequently updated by Boulanger et al. (2007). These methods, originally developed for local analysis, have been extended to global analysis in this study.

The first step of the procedure involves performing an equivalent static analysis where the embankment soils are displaced against the bridge to develop a relation between the mobilized forces and free-field ground surface displacement. The distribution of horizontal force mobilized against the embedded structural components is recorded to model the restraining forces imposed on the spreading soil in the second step. As noted by Boulanger et al. (2007), the restraining force mobilized at a given amount of free-field ground displacement is not equal to the restraining force that exists during the entire earthquake. Rather, the restraining force begins at zero and eventually reaches its final value at the end of lateral spreading. Hence, Boulanger et al. (2007) suggested taking the running average of the relation between restraining force and free-field ground displacement to use in combination with the Newmark sliding block analysis in the second step.

The second step involves a sequence of slope stability analyses to find the yield acceleration of the embankment associated with various levels of restraining force, and a Newmark sliding block analysis to identify the ground displacement associated with that yield acceleration. The restraining forces can be represented by directly imposing the distribution of forces in the *p*-*y* springs on the slope or by representing the distribution as a resultant force acting at the centroid of the distribution. The limit equilibrium analysis is conducted for a unit thickness (i.e., out of the plane of the problem); therefore, the restraining force must be multiplied by an appropriate thickness of the embankment to obtain units of force. Boulanger et

al. (2007) found that using a width equal to only the width of the pile group is inadequate because stresses attenuate geometrically in the embankment; they recommend using the full crest width plus half of the side slope mass to determine an appropriate equivalent width. After performing both steps, the mobilized force versus ground displacement is plotted on the same figure as the restraining force versus Newmark displacement, and the intersection of this plot is the displacement-compatible solution.

An example of the pinning procedure is performed for the three different global load cases 1, 2, and 3 for the bridge in the example problem. Step 1 of the pinning procedure was therefore already completed in previous sections, and step 2 was completed using slope stability analyses in the Rocscience program Slide 5.0 combined with a Newmark sliding block analysis for a ground motion recorded at Port Island, Kobe, scaled to peak ground accelerations (PGA) of 0.2*g*, 0.3*g*, and 0.4*g*. Obviously, the amplitude of Newmark displacements also depend on the frequency content and duration of the ground motion, but those effects were ignored for this analysis.

The soil properties used for the slope stability analyses are summarized in Figure 2.27. The embankment was 6 m (19.69 ft) tall. The clay crust and the liquefied sand layers were 3 and 2 m (9.84 and 6.56 ft) tall, respectively. The equivalent width of the embankment was calculated to be 18.2 m (59.71 ft) using recommendations by Boulanger et al. (2007), and the length of backfill embankment for the slope stability analyses was limited to 30 m (93.43 ft) (five times the height of the embankment). The yield acceleration (i.e., a_y) of the embankment with no pinning force present was calculated to be 0.0615*g* using Spencer's (1967) method (Figure 2.28).

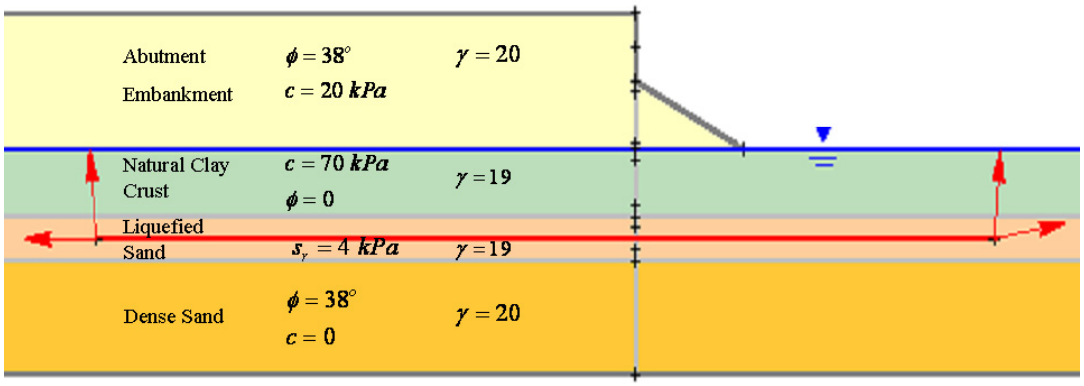

Figure 2.27 Soil profile and its properties used in the pinning analysis of abutments.

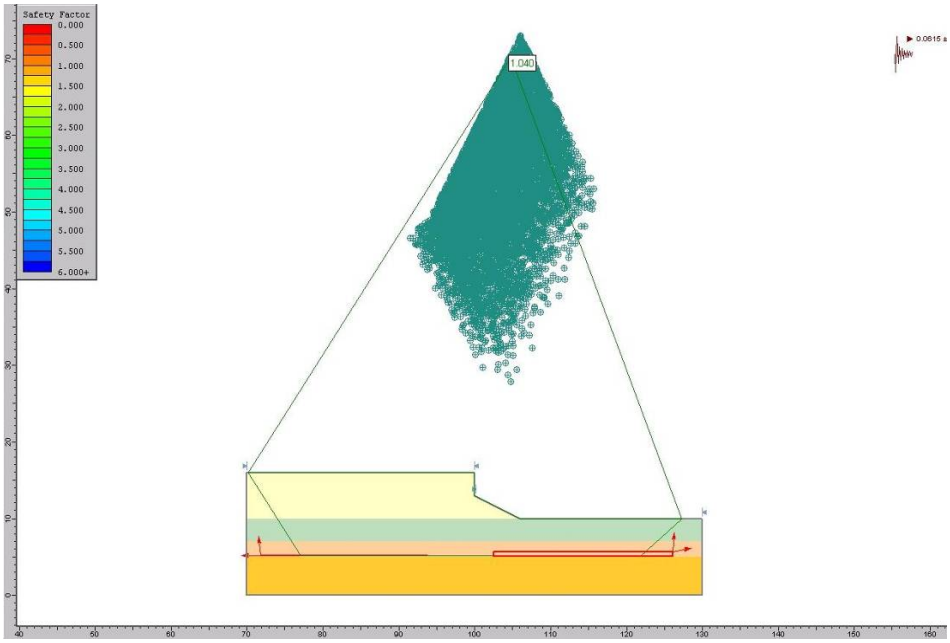

Figure 2.28 Slope stability analyses performed using slide 5.0 and the associated failure surface for yield acceleration of $a_y = 0.0615g$.

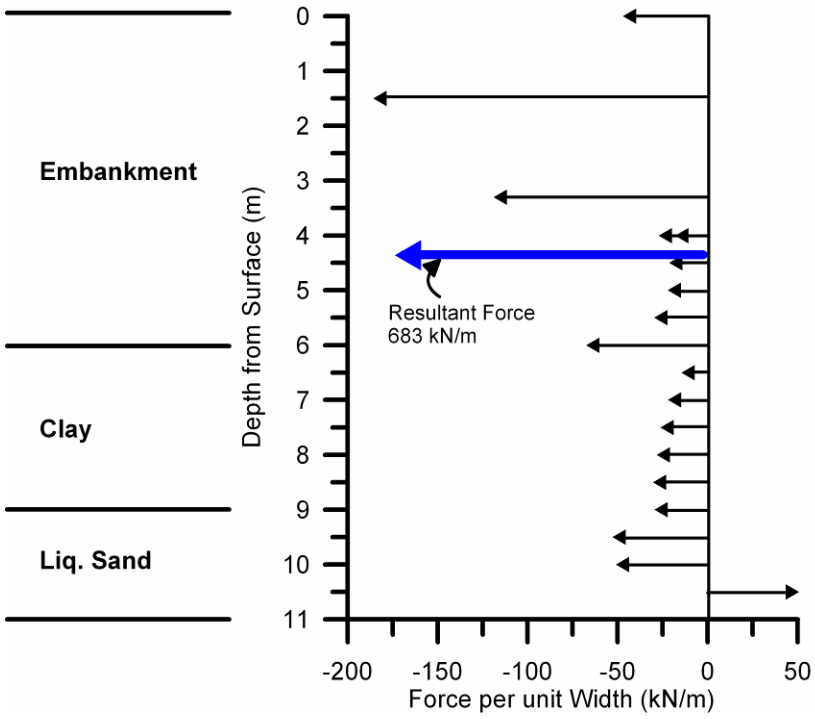

Figure 2.29 Distribution of forces behind the abutment wall at the end of the global load case 1 analysis.

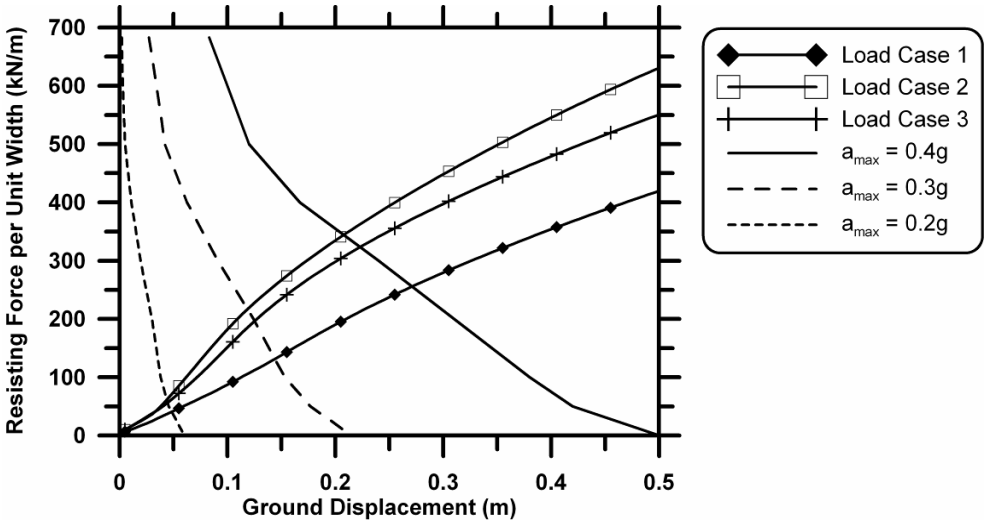

Figure 2.30 Results of the pinning analyses for different load cases 1, 2, and 3 at different peak ground motion levels for Kobe motion recorded at Port Island.

Figure 2.29 shows the distribution of the forces on the abutment piles at the end of the global load case 1. The distribution was represented as the resultant acting at a depth of 4.35 m (14.27 ft). The location of the equivalent force is assumed to be constant for different values of the resisting force, even though the location somewhat varies by the magnitude and the distribution of the forces behind the wall for every load case.

Figure 2.30 shows the results of the pinning analyses for load cases 1, 2, and 3. As can be seen in Figure 2.30, the amount of restraining force mobilized at the abutment depends on the pattern of lateral spreading displacements imposed on the bridge. The softest response is global load case 1, where the entire left side of the bridge is being pushed by lateral spreading soil. This load case is the least effective at pinning the spreading embankment. The stiffest response is global load case 2, where symmetrical lateral spreading demands are imposed in opposite directions, while inertia load is applied from left to right. This load case is the most effective at pinning the spreading embankment because the superstructure acts as a strut. Global load case 3, which has inertia demand out-of-phase from the lateral spreading demands, is more effective than global load case 1 in pinning the embankment displacements, but less effective than global load case 2.

Furthermore, the pinning is more effective for stronger motions. Figure 2.31 shows the reduction in the ratio of the pinning-compatible displacements to free-field displacements, which is the intersection of the two steps of the pinning analysis for different values of ground

displacements. For all load cases the reduction in lateral spreading displacement demands becomes more significant as the free-field displacement (or PGA) increases.

On average, the pinning compatible displacement is about three fourths of the free-field ground displacement for these load cases. From a design perspective, the pinning procedure outlined in this section can easily be repeated for other bridges and load cases with only a modest increase in effort. However, the procedure is too onerous for the large number of analyses performed by Kashighandi (2009) because it would require repeating both the slope stability analysis and the global equivalent static analysis for each of the thousands of simulations; therefore, as discussed in Chapter 4, the displacements at the abutments were decreased by 25% from their estimated free-field values to approximately incorporate the influence of pinning. This reduction is important because demands on the bridge are ultimately related to free-field lateral spreading ground displacement, which is a convenient metric that can be estimated using a number of different approaches. A reduction was not required for the pile group supporting the piers because the extent of lateral spreading soil was assumed to be very large for these components such that the free-field demand was appropriate.

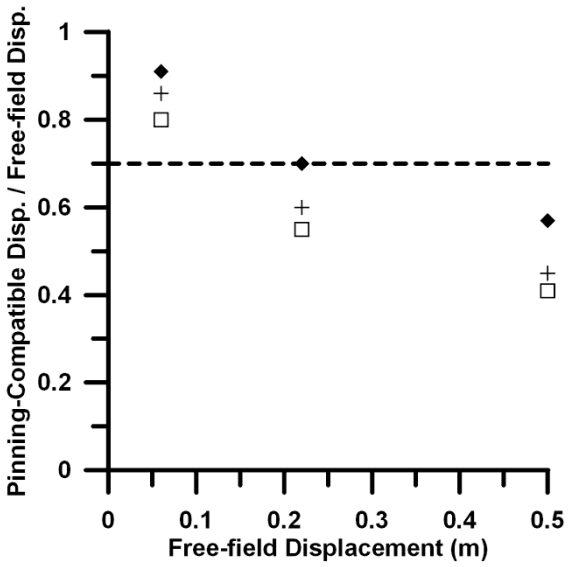

Figure 2.31 Ratio of pinning compatible displacement to free-field ground displacements for three load cases at different values of free-field ground displacement.

3 Input Parameters Selection

Several approaches exist to characterize the potential for liquefaction-induced damage to the more than 12,000 Caltrans-owned bridges. The most robust approach would involve a systematic individual evaluation of every single bridge using the current state-of-the-art analysis procedures. Not only would this approach be essentially impossible because it would require too much time and money, it would also be wasteful because many bridges may be located at sites that are not susceptible to liquefaction. Another approach would analyze a smaller, statistically representative sample of the total bridge population and extrapolate findings to the remaining bridges that were left unanalyzed. Although this approach appears more reasonable, a statistically representative sample would be needed to capture the various combinations of structural configurations and soil conditions that exist for the entire bridge population, which would still involve an unreasonably large effort. Furthermore, obtaining as-built bridge drawings from the Caltrans database would be time-consuming.

The approach adopted in this study was to use a small set of as-built drawings combined with information available from the NBI to develop a simple classification system based on structural properties such as vintage, type of connection between piers and abutments, number of pier columns per bent, and type of foundation. Structural properties such as span length and pier height were varied within each class to represent the variations identified in the NBI. A generic three-span bridge configuration was used throughout the analyses. Soil conditions for the liquefiable soil profiles were based on the USGS database of cone penetrometer soundings in the San Francisco Bay Area. The structural and geotechnical input parameters were represented as probability density functions. In some cases a large amount of data was available to define these input distributions (e.g., the NBI had maximum span length for all Caltrans bridges), while in other cases very little data was available. Consulting with Caltrans bridge designers and

engineering judgment was used when the available data was insufficient to accurately define distributions and correlations among the inputs.

After defining distributions and correlation coefficients for all of the input parameters, individual realizations were obtained by randomly picking discrete input parameter values from their underlying distributions to construct a numerical model of the bridge. The task of automatically constructing a numerical model based on random inputs was facilitated by the scripting capabilities of the TCL language used to control OpenSees. Thousands of realizations were obtained by the Monte Carlo method. The remainder of this chapter presents the manner in which the distributions and correlations for the input parameters were defined.

3.1 GENERIC BRIDGE CONFIGURATION

Figure 3.1 shows the generic three-span template that was used throughout this study. This template was selected because it is the simplest configuration that permits study of the different types of loading conditions studied. For example, lateral spreading could occur at the left embankment and pier, but not at the right embankment and pier, or it could occur on both sides of the bridge toward the center. Fewer spans might limit the possible load combinations, while additional spans would probably not add significant information to the study. All of the spans had the same length and the two piers had equal heights. The abutments and piers were supported on pile groups. The pile groups with 0.38 m- (15 in.-) diameter Precast piles had 20 piles in a group (i.e., a 4x5 configuration), while the pile groups with larger 0.61 m- (24 in.-) diameter CIDH and CISS piles had 12 piles per group (i.e., a 3x4 configuration). The deck width was assigned a fixed value of 12.2 m (i.e., 40 ft), which is typical of two-lane highway super-structure deck width. Dead loads were estimated using deck section weight calculations based on sixteen pre-1971 as-built bridge drawings, and the dead load values were subsequently used to size the piers.

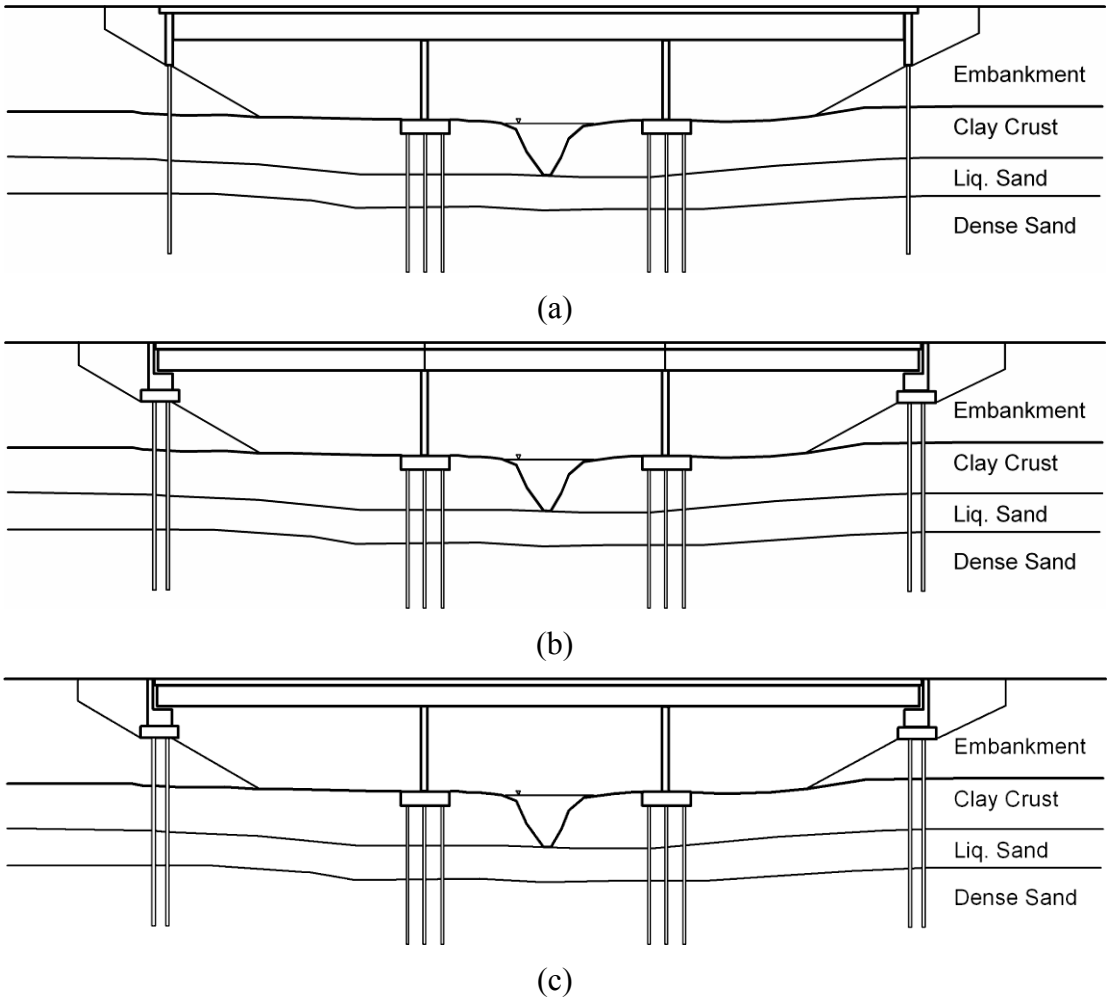

Figure 3.1 Template of the bridges for modeling and analyses: (a) bridges with continuous superstructure and monolithic abutments; (b) bridges with simply supported superstructure and seat-type abutments; and (c) bridges with continuous superstructure and seat-type abutments.

3.2 STRUCTURAL CLASSIFICATION

Figure 3.2 is a flowchart depicting the structural classification system adopted in this study. The bridges are classified based on vintage, structure type, number of columns per bent, and pile types, as discussed in detail in the sections that follow.

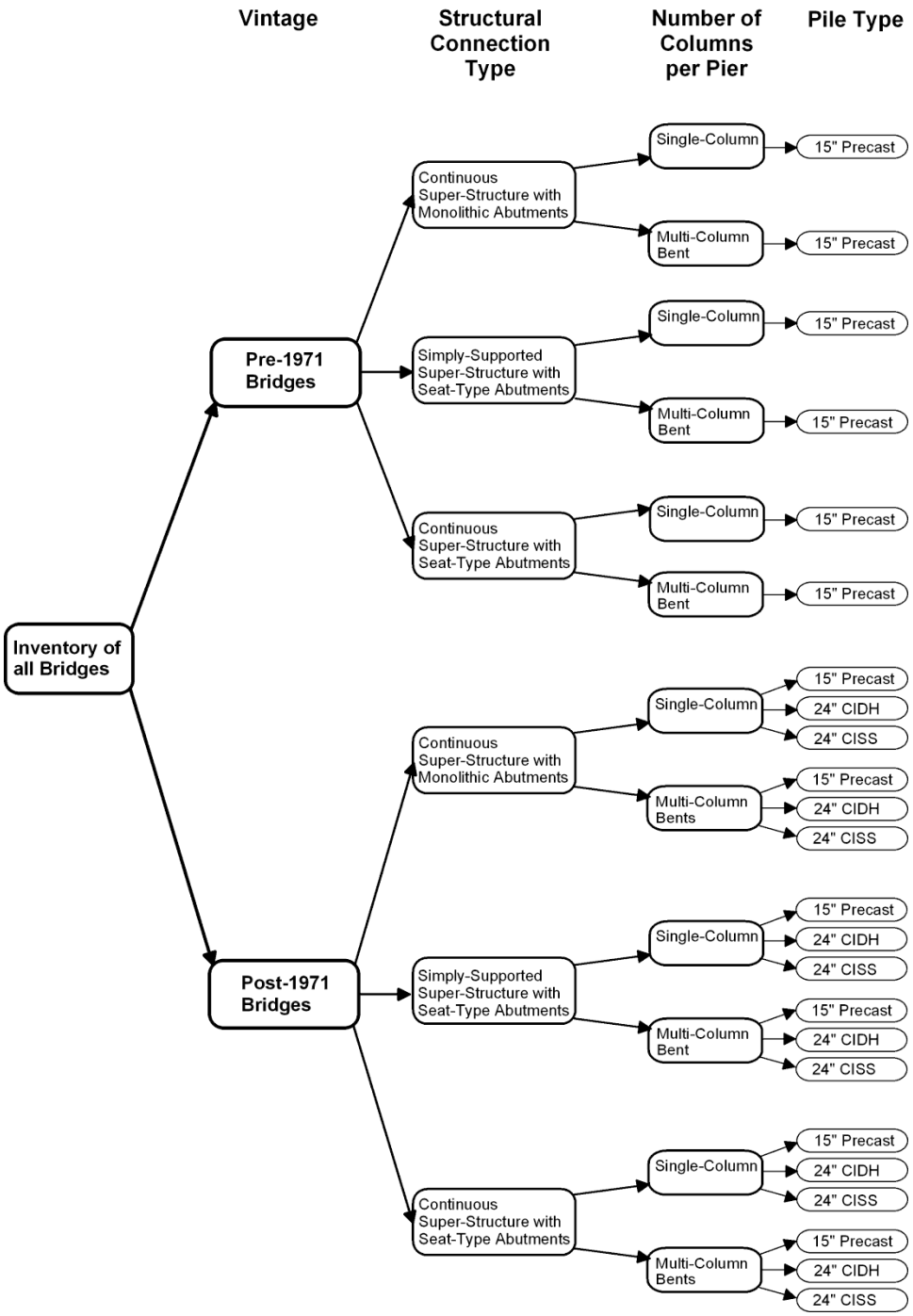

Figure 3.2 Classification of bridges based on vintage, structure type, number of piers, and type of piles.

3.2.1 Vintage

As design codes have evolved and improved over the years, the structural properties of a bridge are strongly related to the year in which the bridge was designed. Based on personal communication with Caltrans bridge designers, certain landmark dates are associated with major changes in bridge structural design codes. The most significant changes were introduced after the 1971 San Fernando and 1994 Northridge earthquakes. Piers for bridges designed prior to 1971 generally had low shear (transverse) reinforcement, and therefore did not exhibit much ductility. After 1971 more shear reinforcement was required in bridge piers to improve ductility. Code revisions following the Northridge earthquake involved primarily structural detailing and connections. Modeling connection details was beyond the scope of this project (all moment resisting connections were implemented by having the beam column elements share nodes, hence 90° connections); therefore, the 1994 code revision was not reflected in the classification system. Because design strategies focused on supporting the vertical load demands, older vintage bridges tend to be supported on small-diameter pile foundations that have very little lateral capacity. Newer vintage bridges, however, are often supported on bigger diameter piles, such as CIDH, CISS, and steel pipe piles, which exhibit significantly improved lateral load stiffness and capacity. This is reflected in the classification system, where various different pile types are assigned to newer vintage bridges. Although various types of piles were also evident in the as-built drawings for the older vintage bridges, these piles also exhibited equally poor lateral load carrying capacity, therefore, varying the properties of the piles was deemed unnecessary.

3.2.2 Structural Connection Type

The connection between the superstructure and the abutments and piers effects the distribution of shear and bending moment demands to the various bridge components. The types of abutments considered in this study are seat-type—where the superstructure rests on top of a bearing attached to the abutment—and monolithic—where the abutment provides a moment-resisting connection to the superstructure. Seat-type abutments typically have a gap is between the superstructure and abutment backwall. Superstructures were considered either continuous—where the entire superstructure is a monolithic member—or as simply supported where the superstructure is composed of multiple segments. Connections between the superstructure and the tops of the piers were modeled as either pinned or resting on an elastomeric bearing for the

simply supported bridges. In this study, the bridges were categorized into three major classes: continuous bridges with monolithic abutments, simply supported bridges with seat-type abutments, and continuous bridges with seat-type abutments.

3.2.3 Number of Pier Columns per Bent

This study adopted as a criterion the number of pier columns per bent because multi-column bents tend to have higher moment and shear capacities compared with their single-column counterparts. Bridges with continuous superstructures and multi-column bents are designed with a pin connection to the pile cap, and with single column bents are designed with a fixed moment-resisting connection. This translates to major differences in the fragility of different components of these two types of piers.

For simply supported bridges the pier columns are fixed into the pile cap since there is no moment-resisting connection at the top of the pier column. Hence, the multi-column bents exhibit higher flexural capacity but no difference in structural configuration. The difference between a single-column and multi-column bent is more important for transverse loading than for longitudinal loading since a multi-column bent forms a frame that can be much stiffer than a single-column. However, all analyses in this report are along the longitudinal axis of the bridge.

3.2.4 Pile Type

The type of piles used in the bridge foundation has a significant effect on its performance under liquefaction and lateral spreading demands. Older bridges (i.e., pre-1971) mostly had small diameter [0.36 m- (14 in.-) to 0.41 m- (16 in.-) diameter] piles that were primarily designed for axial load bearing, without much consideration for lateral loading. They would generally be considered unsuitable for bridges located in liquefiable soils based on today's design standards, but are nevertheless important to model for characterizing performance of the older vintage bridges.

A broader range of pile types appears in the post-1971 bridges. Three individual pile types were considered for the newer vintage bridges, including 0.38 cm- (15 in.-) diameter precast concrete piles, 0.61 cm- (24 in.-) diameter CIDH reinforced concrete piles and 0.61 m- (24 in.-) diameter CISS piles. These larger diameter CIDH and CISS piles are being more widely used in newer bridges, especially when the potential of liquefaction and lateral spreading

is present at the site of the bridge. Although larger-diameter drilled shafts are often used in new bridge designs, these large shafts were not considered in this study.

3.3 SELECTION OF BRIDGE INPUT PARAMETER DISTRIBUTIONS

Selection of statistical distributions for, and correlations among, input parameters for this study was based on (1) a set of sixteen as-built drawings of bridges built before 1971 and four as-built drawings of bridges constructed after 1971 provided by Tom Shantz (Caltrans), (2) the NBI, (3) personal communication with Caltrans bridge designers, (4) geotechnical information from the USGS database of cone penetration test records in the San Francisco Bay Area, and (5) engineering judgment when adequate information was unavailable.

3.3.1 Span Lengths

The maximum span length of bridges is listed in the NBI database. Figure 3.3 shows the histograms of the maximum span lengths for both the pre-1971 and post-1971 California bridges according to the NBI database. The newer bridges tend to have longer span lengths and also longer maximum span lengths. The distribution of maximum span length includes a number of short span lengths, which are probably associated with short single-span crossings, rendering them inappropriate for use in the three-span template. The remaining part of the distribution can be reasonably approximated by a normal distribution. The pre-1971 bridges were generated with spans sampled from a truncated normal distribution with mean of 21.6 m (70.87 ft), standard deviation of 13.3 m (43.64 ft), and truncation limits of 10 m (32.81 ft) and 60 m (196.85 ft), while post-1971 bridges had span lengths sampled from a truncated normal distribution with mean of 35.8 m (117.45 ft) and standard deviation of 17.7 m (58.07 ft) and the same truncation limits. The distribution was truncated to prevent analysis of very short or very long spans.

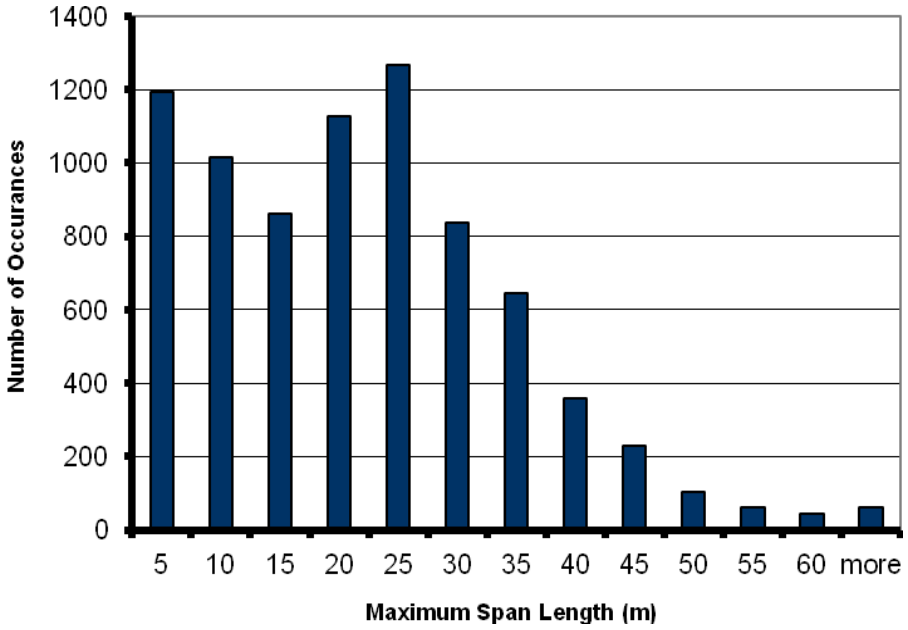

(a)

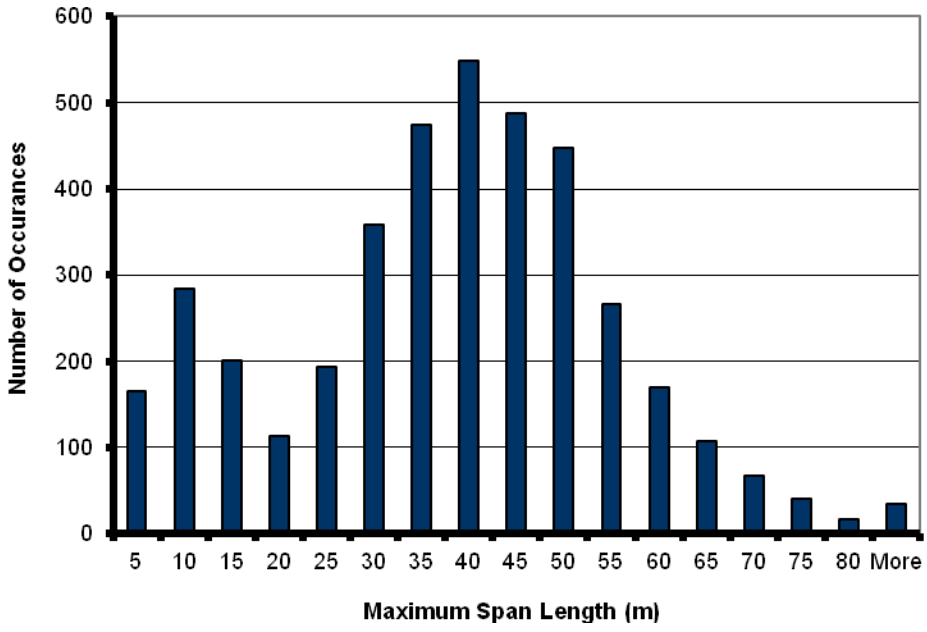

(b)

Figure 3.3 Histograms of maximum span length of bridges from NBI database: (a) pre-1971 and (b) post-1971.

3.3.2 Pier Heights

The NBI lists Minimum Vertical Under-clearance for bridges that cross other roads or railways, and Minimum Navigational Vertical Clearance is listed for bridges that cross rivers, but neither relates directly to pier height. As a result, the distribution of the pier heights was based on the limited number of drawings provided by Caltrans and engineering judgment. A truncated normal distribution was assumed for pier height, with a mean of 6.5 m (21.33 ft), a standard deviation of 1.65 m (5.41 ft), and truncation limits of 2 m (6.56 ft). The truncation limit was used to prevent analysis of unrealistically short piers.

3.3.3 Superstructure Weight

The distribution of the superstructure weight is important for the gravity analysis, as well as for establishing the inertia demand on the bridge. The dead load weight per tributary length per width of the deck was computed for sixteen pre-1971 as-built drawings provided by Caltrans, as summarized in Table 3.1. Based on Table 3.1, the distribution of the deck dead weight per area was assumed to be normally distributed with a mean of 9.1 kN/m^2 and a standard deviation of 1.5 kN/m^2.The weight of the superstructure was correlated with the size of the piers, as described next.

3.3.4 Pier Column Moment and Shear Capacity

The size of the piers is well correlated with the dead load acting on the pier and the axial load ratio (i.e., the ratio of the axial load to axial capacity of pier). Axial load ratio of the piers can vary from less than 1% (e.g., some pier walls) to more than 10% (e.g., some single-column piers). The as-built drawings were used to estimate distributions of axial load ratio. In general, axial load ratios were larger for the single-column bents and smaller for the multi-column bents. The mean axial load ratios were estimated to be 0.06 for the single-column piers and 0.04 and 0.03 for two-column and three-column piers, with standard deviations of 0.007, 0.006, and 0.005 for single column, two-column and three-column piers, respectively. These axial load ratios were used to size the piers based on the weight per area of the columns, which embedded the

Table 3.1 Dead weight per unit area for the available pre-1971 Caltrans drawings.

Bridge Number	Deck width B (m)	Equal-weight concrete area A (m^2)	Weight per Trib. Length W (kN/m)	Ratio W/B (kN/m^2)
1	16.5	6.65	166.3	10.1
2	8.5	3.57	89.3	10.5
3	11.9	5.55	138.8	11.7
4	12.28	5.33	133.4	10.9
5	48.8	29.40	735.0	15.1
6	51.2	11.64	291.0	5.7
7	10.0	3.02	75.4	7.5
8	9.4	4.05	101.3	10.8
9	10.4	3.38	84.5	8.1
10	24.4	10.31	257.5	10.6
11	9.1	2.98	74.4	8.2
12	11.2	2.74	68.5	6.1
13	9.75	3.32	82.9	8.5
14	12.2	3.88	97.1	7.95
15	10.4	2.71	67.7	6.5
16	11.6	3.54	88.4	7.62

correlation between the span length and pier column capacity. The gross areas of the piers were calculated by dividing the total axial capacity per column (back calculated from the axial load ratio) divided by the compressive strength of concrete ($f_c^{'}$).

After sizing the pier diameter, the flexural capacity was computed. Rather than individually computing flexural capacity for each pier diameter, a suite of Monte Carlo moment-curvature analyses of the sections were conducted in OpenSees with representative distributions of steel strength (f_y), compressive strength of concrete ($f_c^{'}$), section effective depth (d), longitudinal reinforcement ratio (ρ), confined to unconfined concrete strength ratio ($f_{c_{confined}}^{'} \Big/ f_{c_{unconfined}}^{'}$) for both the pre-1971 and post-1971 eras. Based on the analysis results, flexural and shear capacities were defined using statistical dimensionless parameters. Yield moment of a column is defined using Equation 3.1:

$$M_y^{'} = \frac{M_y}{f_c^{'} A_g d\,[1+(n-1)\rho]} \tag{3.1}$$

where, M_y is the yield moment of the column, A_g is the gross area of the column, d is the effective depth of the section, n is E_s/E_c (i.e., the ratio of the modulus of elasticity of steel to concrete, or so called modular ratio), ρ is the longitudinal reinforcement ratio, which equals A_s/A_g, and $M_y^{'}$ is the normalized yield moment of the column.

The dimensionless yield moment, $M_y^{'}$, was found to be log-normally distributed, with mean and standard deviation as listed in Table 3.2. The yield curvature values were also recorded from the moment-curvature analyses and the resulting relations are also listed in Table 3.2. Yield curvature is an important parameter since the curvature ductility of the piers is an important demand measure on the piers of the columns.

Table 3.2 The median and dispersion of the normalized yield moment and the relationships between yield curvature and yield moment for circular and rectangular sections for both pre-1971 and post-1971 eras.

Section Shape	Vintage	Log-Normal Distribution of $M_y^{'}$		Relationship of yield curvature, ϕ_y and yield moment, M_y
		λ	ξ	
Circular Sections	Pre-1971	-2.65	0.24	$\phi_y = 0.00866e^{\left(-\frac{M_y}{679.0}\right)} + 0.00257$
	Post-1971	-2.42	0.23	$\phi_y = 0.00532e^{\left(-\frac{M_y}{795.2}\right)} + 0.00211$
Rectangular Sections	Pre-1971	-2.73	0.22	$\phi_y = 0.0123e^{\left(-\frac{M_y}{956.6}\right)} + 0.00332$
	Post-1971	-2.48	0.22	$\phi_y = 0.00711e^{\left(-\frac{M_y}{1145.8}\right)} + 0.00268$

Table 3.3 The fitting parameters for the natural log of medians of pier yield moments and the dispersion of the yield moments for circular and rectangular sections for both pre-1971 and post-1971 eras.

Vintage	Column Shape	Number of Columns per Pier	Fitting Parameters for $\ln(M_y)$		Standard deviation, ξ
			A_1	A_2	
Pre-1971	Circular	1	7.5559	2.3272	0.355
		2	8.1377	2.3713	0.358
		3	8.5011	2.3672	0.357
	Rectangular	1	7.8237	2.2632	0.356
		2	8.4064	2.3160	0.360
		3	8.7643	2.3166	0.359
Post-1971	Circular	1	7.9747	2.3700	0.344
		2	8.5589	2.4089	0.347
		3	8.9220	2.4153	0.348
	Rectangular	1	8.2881	2.3261	0.356
		2	8.8742	2.3693	0.359
		3	9.2358	2.3729	0.359

Using the normalized relationship of Equation 3.1 and the distributions in Table 3.2, yield moment was specified directly in terms of pier column diameter, D, using Equation 3.2, where $\ln(M_y)$ is the natural log of the median of yield moment for a column with a diameter of D, $\ln(D)$ is the natural log of the column diameter (or smaller dimension for rectangular columns), and A_1 and A_2 are regression constants.

$$\ln\left(M_y\right) = A_1 + A_2 \times \left(D\right) \tag{3.2}$$

The yield moment of the piers are log-normally distributed with median computed from Equation 3.1 and with fitting parameters and standard deviation listed in Table 3.3. In a similar fashion, a normalized relationship for shear capacity of the piers was also computed as shown in Equation 3.3, where V_d is the shear capacity of the piers, A_e is the effective area of the pier (approximated as 0.8 times the gross area of the pier), $f_c^{'}$ is the compressive strength of concrete (must be in units of kPa), f_{yh} is the strength of transverse steel, ρ_t is the transverse reinforcement ratio, and $V_d^{'}$ is the normalized shear capacity of piers. The normalized shear capacity of the pier

columns, $V_d^{'}$, was found to be normally distributed, with mean and standard deviations listed in Table 3.4.

$$V'_d = \frac{V_d}{A_e\sqrt{f'_c}\left(5.65 + \frac{f_{yh}\rho_t}{2\sqrt{f'_c}}\right)} \tag{3.3}$$

Similar to the case with yield moment of columns, using the normalized relationship of Equation 3.3, the shear capacity was directly related to pier column diameter using the form in Equation 3.4, where ln(V_d) is the natural log of the median of the shear capacity, and B_1 and B_2 are fitting parameters. Table 3.5 summarizes the fitting parameters for the natural log of the medians for a pier with diameter (or smaller dimension) of D and the dispersion associated with the log-normal distributions.

$$\ln\left(V_d\right) = B_1 + B_2 \times \ln\left(D\right) \tag{3.4}$$

Using the abovementioned relationships, correlation between span length and pier size/capacity was maintained in a reasonable way. Table 3.6 summarizes the median and dispersions of the moment and shear capacities for single-column and multi-column bridges belonging to both pre-1971 and post-1971 eras. The capacities for the multi-column bents represent the sum of capacities of the columns in the bent.

Table 3.4 The mean and standard deviation of the normalized shear capacity of the pier for both pre-1971 and post-1971 eras.

Section Shape	Vintage	Normal Distribution of $V_d^{'}$	
		μ	σ
Circular Sections	Pre-1971	1.087	0.018
	Post-1971	1.189	0.034
Rectangular Sections	Pre-1971	1.028	0.009
	Post-1971	1.054	0.013

Table 3.5 The fitting parameters for the natural log of medians of pier shear capacity and the dispersion of the shear capacity for circular and rectangular sections for both pre-1971 and post-1971 eras.

Vintage	Column Shape	Number of Columns per Pier	Fitting Parameters for $\ln(V_d)$		Standard deviation, ξ
			B_1	B_2	
Pre-1971	Circular	1	6.8585	1.7329	0.150
		2	7.5078	1.7480	0.151
		3	7.8990	1.7437	0.150
	Rectangular	1	7.3097	1.6414	0.188
		2	7.9494	1.6613	0.189
		3	8.3344	1.6545	0.188
Post-1971	Circular	1	7.3371	1.8367	0.232
		2	8.0016	1.8512	0.232
		3	8.3997	1.8457	0.232
	Rectangular	1	7.7733	1.7220	0.246
		2	8.4257	1.7375	0.246
		3	8.8152	1.7313	0.246

Table 3.6 The fitting parameters for the natural log of medians of pier shear capacity and the dispersion of the shear capacity for circular and rectangular sections for both pre-1971 and post-1971 eras.

Vintage	Column Type	Moment Median and Standard Deviation		Shear Median and Standard Deviation	
		λ $(kN.m)$	ξ	λ (kN)	ξ
Pre-1971	Single-Column	4040	0.77	1763	0.52
	Multi-Column	5982	0.79	3115	0.54
Post-1971	Single-Column	8478	0.78	3774	0.57
	Multi-Column	11970	0.81	6475	0.61

3.3.5 Bearings Parameters

Bridges with seat-type abutments were assumed to be supported on elastomeric bearings (see details in Chapter 2). Connections between the pier top and the superstructure were assumed to be either on elastomeric bearings, pin connections (i.e., grouted dowels), or a concrete-to-concrete seat. Each type of bearing was evenly distributed (i.e., one-third of bearings were elastomeric, one-third were pin connections, and one-third were concrete-to-concrete seat). Data were unavailable to select these values and assignment of equal percentages is admittedly subjective. Given that, these three types of connection essentially cover a wide range of possibilities as far as the connection of the spans at the top of the piers.

Properties of the elastomeric bearings were based primarily on the as-built drawings. Strain mobilized in an elastomeric bearing is a function of the bearing displacement and the height of the bearing. Table 3.7 summarizes the breakdown of the bearing heights that were used for the elastomeric bearings in bridges belonging to both the pre-1971 and post-1971 eras. The values selected were based on the available as-built drawings.

Table 3.7 The breakdown of elastomeric bearing heights for pre-1971 and post-1971 bridges.

Bearing Thickness (in.)	Pre-1971	Post-1971
1	25%	N/A
1.5	25%	N/A
2	50%	50%
3	N/A	50%

Table 3.8 Mean and standard deviation of vertical stress on the elastomeric bearings for pre-1971 and post-1971 bridges.

Bearing Vertical Stress	Pre-1971	Post-1971
Mean	690 kPa (100 psi)	1035 kPa (150 psi)
Standard Deviation	103 kPa (15 psi)	173 kPa (25 psi)

To compute the load-deformation characteristics of the elastomeric bearings, their stiffness and ultimate capacity had to be estimated. Per recommendations by Caltrans (SDC 2006), the capacity of the elastomeric bearings was set to 35% of the weight acting on the bearing, The yield displacement of the bearing was computed using Equation 3.5 and is dependent on the shear modulus of the bearing material, bearing thickness, and vertical stress acting on the bearing. In modern bearing design, the total surface area of the bearing pads are selected so that the vertical stress on the bearings does not significantly exceed 100 psi (i.e., 690 kPa). Vertical stresses on the bearings were calculated for the available as-built drawings. According to the available drawings, the distribution of the vertical stresses on the bearings was assumed to be normally distributed, with means and standard deviations summarized in Table 3.8.

The yield displacement was calculated using the following mathematical manipulations, where U_y equals yield displacement of the bearing, t_r equals the total thickness of the bearing pad, σ_v equals the vertical stress on the bearing, and G equals the shear modulus of rubber (~1 MPa).

$$U_y = \frac{Q}{K_H} = \frac{Q}{\left(\frac{G.A}{t_r}\right)} = \frac{\cancel{Q}}{\frac{G}{t_r}.\frac{\cancel{Q}}{\sigma_v}} = \frac{t_r.\sigma_v}{G} \tag{3.5}$$

The load-deformation of the bearing was determined using the three parameters of bearing ultimate capacity (Q), total bearing pad height (t_r), and the vertical stress acting on the bearing (σ_v). The load-deformation behavior was assumed to be elastic perfectly-plastic.

An elastic perfectly-plastic material was also assumed for the analyses with the concrete-to-concrete interface, and the stiffness of the linear portion of the load-deformation was set to a large value making the load-deformation essentially rigid-plastic. For ease of implementation in OpenSees, using the same elastic perfectly-plastic material for all types of bearings was convenient, even though some bearing types were essentially rigid-plastic. For the analyses where the dowels were used to connect the superstructure to the pier, the capacity of the load-deformation (i.e., plastic capacity value) was set to the shear capacity of the dowels, with stiffness set very high making the response rigid-plastic. Shear capacity of the dowels was based on observations from the as-built drawings combined with judgment.

3.3.6 Pile Strengths

Figure 3.4 shows a few examples of the piles that were commonly used in California bridges. Lateral loading of piles was rarely considered in designing the typical pre-1971 bridge, and the type of piles encountered in the as-built drawings of those bridges were generally 0.38 cm- (15 in.-) diameter piles of varying strengths not designed to resist lateral loading, yielding fairly quickly under demands of lateral spreading. Therefore, for all of the classes of the pre-1971 bridges, only one type of precast piles was considered in the analyses. The strength and the yield curvature of the pre-1971 piles are listed in Table 3.9.

For post-1971 bridges, three different types of piles were considered. A variety of the 0.36 m to 0.41 m (14 in. to 16 in.) precast concrete piles with different configurations were modeled using Xtract. Based on those Xtract section analyses, the yield moment of these small-diameter newer precast concrete piles were assigned a log-normal distribution, while a normal distribution with very small variation was assigned to their yield curvatures; 0.61 m (24 in.) CIDH and 0.61 m (24 in.) CISS piles were also considered in the analyses of the post-1971 bridges. These piles are typically much stronger that the small-diameter piles and are more commonly used in the design of modern bridges. The yield moment and yield curvature of these piles were also performed in Xtract, however, the values were not varied in the analyses.

Table 3.9 Yield moment and yield curvature for piles used in the analyses.

Vintage	Pile Type	Mean or Median Moment (*kN/m*)	Dispersion	Mean Yield Curvature (*1/m*)	Standard Deviation
Pre-1971	0.38 m (15 in.) precast	84	N/A	0.011	N/A
Post-1971	0.38 m (15 in.) precast	180 (Median)	0.25	0.0123	0.0005
	0.61 m (24 in.) CIDH	400	N/A	0.0069	N/A
	0.61 m (24 in.) CISS	1977	N/A	0.0069	N/A

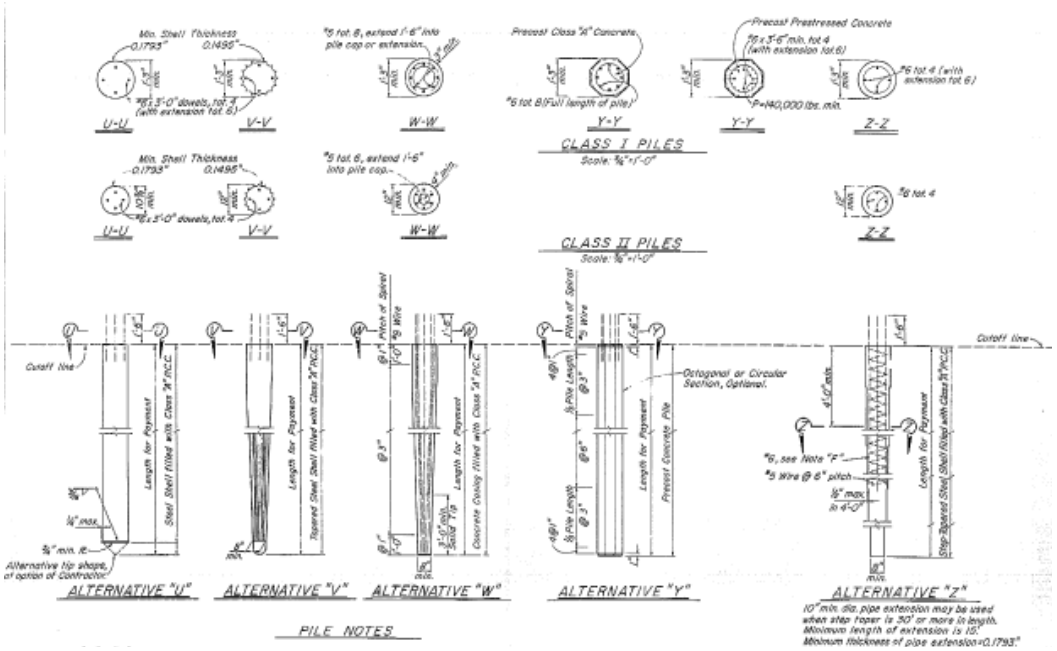

(a)

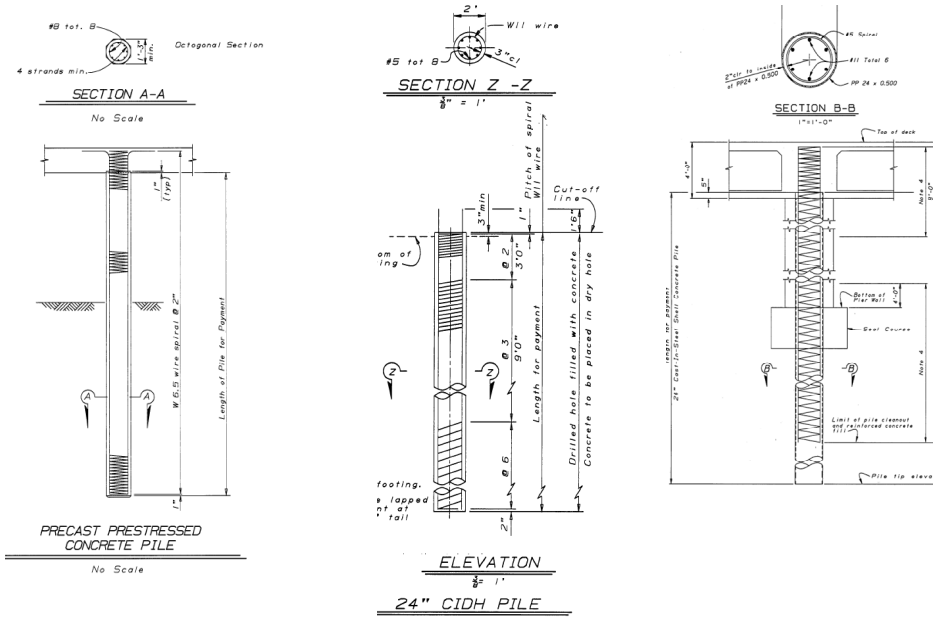

(b) (c)

Figure 3.4 Examples of piles specification from as-built drawings: (a) 0.38 m (15 in.) precast concrete piles typically used in pre-1971 bridges; (b) post-1971 0.38 m (15 in.) precast piles; (c) post-1971 0.61 m (24 in.) CIDH piles; and (d) post-1971 0.61 m (24 in.) CISS piles.

3.4 SELECTION OF GEOTECHNICAL INPUT PARAMETER DISTRIBUTIONS

The geotechnical parameters defined in the analyses herein include the strength and thicknesses of the soil layers, the load-transfer between soil and embedded bridge components, and the lateral spreading deformation profile. Each of these inputs is discussed below.

3.4.1 Thickness of Natural Crust, Liquefied Sand, and Approach Embankments

The thickness and variation of the natural crust and thickness of the liquefiable sand were selected primarily based on the distribution of CPT logs for Northern California, available on the USGS website (http://earthquake.usgs.gov/regional/nca/cpt/). Figure 3.5 depicts distributions of thickness and average CPT tip resistance in nonliquefied crust layers. Nonliquefied crust material was separated into fine-grained and coarse-grained soils. The thickness of the crust materials can go even beyond 10 m (32.81 ft) in some cases, but lateral spreading and other surface manifestations of liquefaction are typically limited to shallower layers (e.g., Ishihara 1985). Hence, the thickness of the crust was assumed to be uniformly distributed between zero and 6 m (19.69 ft).

The histogram of the liquefied sands thickness can be roughly approximated by log-normal distributions. Based on this histogram, the thickness of the liquefied sand layer was assumed to be log-normally distributed with a median of 3 m (9.84 ft) and dispersion of 0.7 [i.e., ln(2)]. The distribution of thickness of the embankment was rather subjective. It was assumed that the thickness of the embankment would vary uniformly between 3 m and 9 m (9.84 ft and 29.53 ft) to capture the reasonable range of typical approach embankments.

3.4.2 Undrained Shear Strength of Cohesive Nonliquefied Crust Material

The undrained shear strength of clayey crust soils was estimated from the average CPT cone tip resistance values summarized in Figure 3.5. The median value of cone tip resistance (q_t) is about 3.0 MPa, which corresponds to an undrained shear strength of 200 kPa according to Equation 3.6, where q_t equals the tip resistance of the cone, σ_v equals total vertical stress, and N_{kt} equals empirical value between 10 and 20, with 15 as an average.

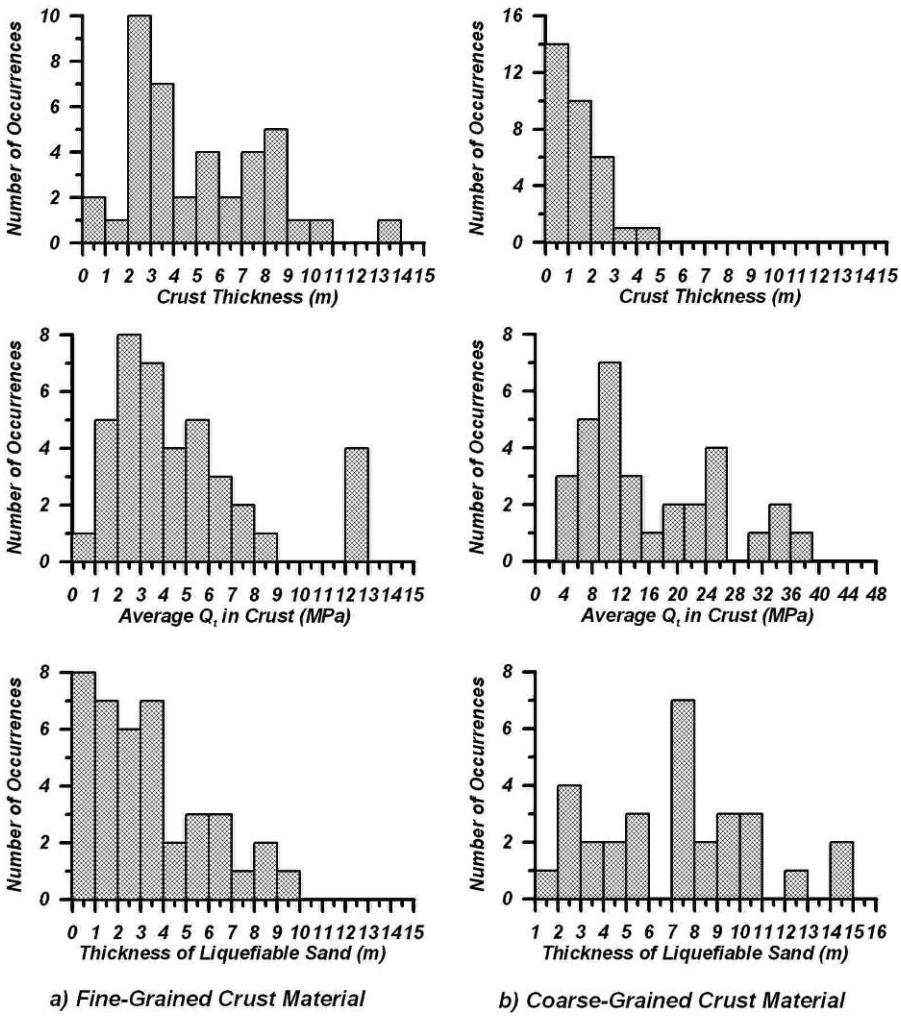

Figure 3.5 Distribution of crust and liquefiable layer thickness based on USGS CPT logs for Northern California.

$$S_u = \frac{q_t - \sigma_v}{N_{kt}} \tag{3.6}$$

However, this undrained shear strength is larger than would be anticipated for near-shore sediments overlying liquefiable sands. Engineering judgment was used to reduce the median value of undrained shear strength to 70 kPa, which is consistent with strengths that would be anticipated for a desiccated crust above the ground water table. The distribution of the strength was assumed to be log-normally distributed with $\sigma_{ln} = 0.75$.

3.4.3 Lateral Loads from Embankment Soils

The embankment load consists of two components: the passive pressures behind the abutment wall and the load mobilized by the piles supporting the abutment walls. Passive pressure, computed using Rankine earth pressure theory, was assumed to be log-normally distributed with σ_{ln} = 0.75. The large standard deviation is caused by uncertainty in the interface friction (as discussed in Chapter 2). The embankment backfill was assumed to have a baseline friction angle of $\phi = 38^o$ and baseline apparent cohesion of $c = 20$ kPa .

The ultimate values of lateral loads on the piles (p_{ult}) were computed using the API (1993) sand *p-y* curves from the baseline set of soil properties, and the distribution was assumed log-normal with σ_{ln} = 0.75. For convenience, these distributions were implemented by computing the median value of passive pressure (or p_{ult}) using the baseline set of input parameters, and subsequently multiplying by a *p*-multiplier with median value of 1.0 and $\sigma_{\ln} = 0.75$. Note that this is different than assuming that the fundamental soil properties are random variables and subsequently computing p_{ult}. Directly assigning a median and standard deviation to crust load rather than the fundamental soil properties is based on the analysis in Chapter 2 that quantified the influence of interface friction angle uncertainty on passive pressure.

3.4.4 Subgrade Reaction in Liquefied Sand

Soil-structure interaction in the liquefied sand was modeled by applying a *p*-multiplier to the drained *p-y* curve to reduce its capacity. The distribution of the *p*-multipliers in the sand was chosen based on the recommendations of Brandenberg (2005) (see Table 2.1). For loose sandy material $\left[(N_1)_{60-CS} < 8\right]$ Brandenberg recommends using a *p*-multiplier between 0.0 and 0.1. Therefore, here, the *p*-multiplier of liquefied sand was assigned a truncated normal distribution, with a mean of 0.05 and a standard deviation of 0.025, truncated at values below 0.01.

The *p-y* behavior of liquefied sand back-calculated from full-scale field test and small-scale centrifuge tests exhibit a concaved upward response attributed to the dilatancy of the sand, (Wilson et al. 2000; Rollins et al. 2005). Despite widespread acknowledgment that *p-y* behavior in liquefied ground can exhibit this type of behavior due to dilatancy, static analysis approaches traditionally have utilized a *p*-multiplier approach where the *p-y* behavior is modeled as being artificially soft and weak. The reluctance to model concave up behavior in static lateral spreading

analysis procedures is due to a mismatch in the assumed ground displacement profile and the strength of the *p-y* behavior. The basic idea is thus: a sand that is weak enough to exhibit large shear strains which manifest as lateral spreading should also be weak as it flows around a pile. By assuming the sand is weak enough to exhibit large shear strains (say 50%) but powerful enough to exert a large downslope force on a pile due to lateral spreading seems inconsistent. A more likely scenario is that the sand may transiently exhibit pore pressure reduction during shaking due to dilatancy (either from free-field strains due to site response or from local strains imposed by the pile); the increment of shear strain mobilized during this cycle would be very small since the soil would be transiently stiff. As pore pressures rise back to 1 and the soil re-liquefies, it would then strain again and flow past the pile.

Studies that have shown large subgrade reaction forces mobilized by liquefied sand have also shown that these subgrade reaction forces act to resist downslope displacement of the pile. Rollins et al. (2005) demonstrated that large forces could be mobilized in static load tests in blast-induced liquefied soil, and that the sand could provide significant stiffness to react against the actuator. Wilson et al. (2000) showed that liquefied sand could provide significant resistance to inertia-driven downslope pile displacement. Brandenberg et al. (2005) showed that liquefied sand could provide a large upslope resisting force against the combined effects of inertia and lateral spreading of an overlying clay layer. Never has a study shown that liquefied sand can mobilize a large downslope driving force against a pile during periods of dilatancy-induced pore pressure decreases, presumably because the dilatant sand does not exhibit large strain increments during the instants when pore pressures transiently drop. Therefore, in static analysis procedures, imposing large shear strains in a liquefied sand layer combined with a concave up dilatant *p-y* material is inappropriate, resulting in overestimation of the demands on the pile.

To clarify this matter, an example problem is presented here that shows the expected response of a single 0.61 m (24 in.) CIDH pile under lateral spreading demands of liquefied sand (without a crust) against the pile, using a few cases of a hardening *p-y* behavior as well as the recommended approach, which applies a *p*-multiplier to the traditional strain-softening response as presented by API (1993*) p-y* curves. The pile is modeled to behave elastically with stiffness equal to the initial (pre-yield) stiffness of the pile obtained using section analysis of the pile in Xtract, with properties as shown in Table 2.7. The hardening shape of the *p-y* behavior as observed in Wilson et al. (2000) was modeled using PyLiq2 Material in OpenSees by applying effective stresses in the form of a second-order polynomial, as follows:

$$\sigma_v^{'} = \left(y / y_{\max}\right)^2 \sigma_{vf}^{'} \tag{3.7}$$

in which

$$\sigma_{vf}^{'} = F \cdot \sigma_{vi}^{'} \tag{3.8}$$

where F is the ratio of the ultimate effective stress to the initial effective stress prior to liquefaction, y equals lateral displacement, and $y_{\max}$ is maximum value of lateral displacement. Centrifuge tests performed by Wilson et al. (2000) showed that the ultimate load may be smaller or larger than the ultimate load as predicted by API (1993) curves. For the purpose of this example, the analyses were performed with F values equal to 2, 1, and 0.5.

In this example, lateral spreading occurs over 5 m (16.40 ft) of liquefied sand (with no nonliquefied crust) overlying denser sands (Figure 3.6). The extent of lateral spreading displacement at the surface is 0.5 m (1.64 ft), and the strain is constant in the liquefied sand. Soil properties of the layers are summarized in Table 3.10.

Figure 3.7 shows the effective stress as a function of displacement ratio for cases with final effective stresses double, same, and half the initial effective stress, as well as the nonliquefied effective stress at the middle of the liquefied sand layer [depth = 2.5 m (8.21 ft)], with an effective stress of 20 kN/m^2. Figure 3.8 shows the p-y behavior in the middle of the liquefied sand layer [2.5 m (8.21 ft)] for the three hardening cases, as well as for the traditional API and the recommended approach (p-multiplier approach).

Table 3.10 Properties of the soil layers used in the example analyses,

Layer	Depth to top of the layer (m)	γ (kN/m^3)	ϕ'	η_h (kN/m^3)
Loose sand	0	18	32	9,500
Dense sand	5	18	38	32,600

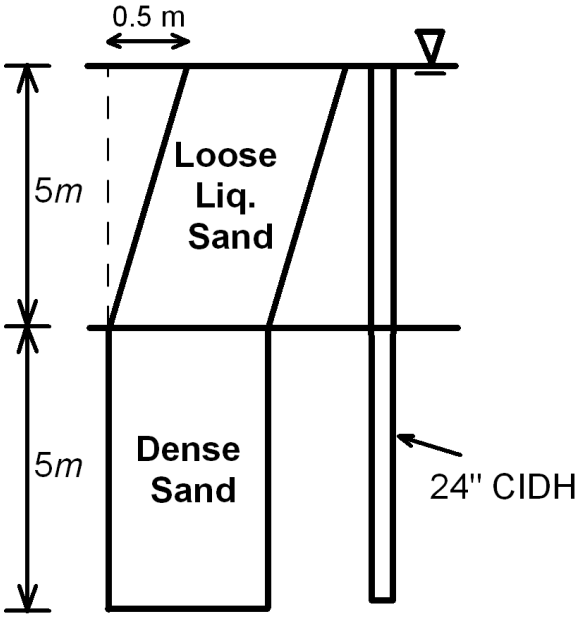

Figure 3.6 Soil and lateral spreading profile used in the example analyses.

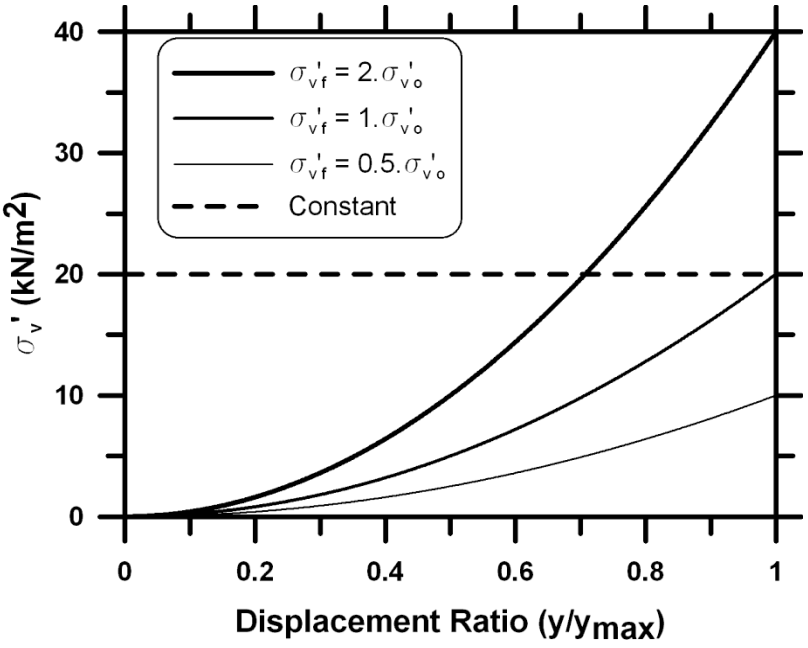

Figure 3.7 Effective stress relations used in the example analyses calculated at the center of the liquefied sand layer.

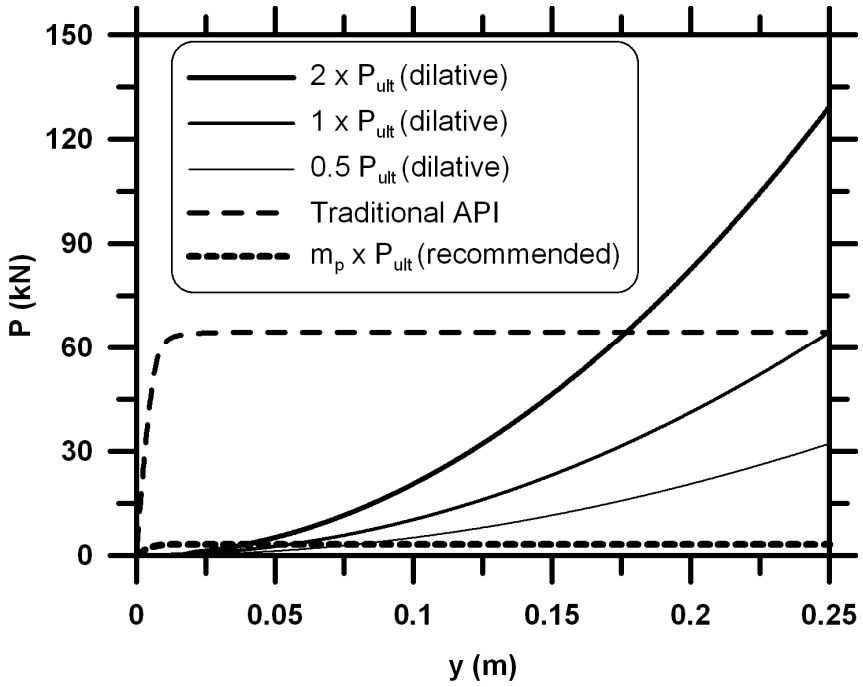

Figure 3.8 ***p-y*** **curves used in the example analyses at the center of the liquefied sand layer.**

Analyses were performed for four different *p-y* behaviors (see Figure 3.8) with the first three using the polynomial hardening curves with ultimate loads equal to 2, 1, and 0.5 times the API ultimate load, respectively. The last analysis was performed using a softened *p-y* curve with a *p*-multipler of 0.05 applied to the traditional API *p-y* curve. Figure 3.9 shows the predicted soil and pile displacements as well as the subgrade reaction and moment distribution along the pile for different cases of this example analysis. As can be seen in Figure 3.9, the hardening shape of the *p-y* curves predicts significant displacements of the 0.61 m (24 in.) CIDH piles under a modest lateral spreading displacement of 0.5 m (1.64 ft), in which the top of the pile displaces 0.35 m (1.15 ft), 0.25 m (9.84 in.), and 0.15 m (5.91 in.) for load cases 1, 2, and 3, respectively. Also, the mobilized moment in the pile for the hardening load cases far exceeds the moment capacity of the pile (M_y ~ 400 kN/m), which would have resulted in significant curvature ductility in the pile had it been modeled nonlinearly. Such high displacement level of a large diameter 0.61 m (24 in.) CIDH pile under only 0.5 m (1.64 ft) of lateral spreading and in the absence of a nonliquefiable crust does not agree with the expected response of these piles based on case history evaluation and model test studies. The *p*-multipler approach (i.e., load case 4) predicts a pile displacement of 0.02 m (0.79 in.), which is deemed more reasonable.

3.4.5 Stiffness of Load Transfer in the Crust and Embankment

The stiffness of the load transfer in the nonliquefied crust in a liquefied site is significantly (an order of magnitude) softer that the stiffness of soils in nonliquefied ground. Following the model presented by Brandenberg et al. (2007), the load transfer response was calculated for load transfer between the abutment and the approach embankment, and between the pile cap and spreading crust layer. The baseline value of y_{50} were 0.20 m (7.87 in.) for the abutments and 0.05 m (1.97 m) for the pile caps. The y_{50} value was assigned a truncated normal distribution with a COV of 0.5, truncated at 0.005 m (0.20 in.) at piers and at 0.020 m (.79 in.) for the abutments.

3.4.6 Characterization of Axial Capacity

Axial capacity of the foundation comes from the *t-z* springs along the length of the piles and the *q-z* springs at the tip of the piles. While the *t-z* relations are known for the nonliquefied ground, little is known about *t-z* relations in liquefied sites. Given the lack of information, the *p*-multipliers were also applied to the *t-z* relations. The baseline axial capacity of the bridge in any foundation component is simply the sum of the *t-z* springs and the *q-z* springs in the piles. In order to account for the variability of axial capacity, axial capacity multipliers were applied to the baseline values of the *t-z* and *q-z* springs. Similar to the *p*-multipliers in the liquefied sand, a truncated normal distribution with a mean of 1.0, a standard deviation of 0.5 (i.e., COV = 0.5) and a truncation value of 0.01 was applied to the multiplier of *t-z* and *q-z* springs.

3.4.7 Horizontal Variation of Lateral Spreading Surface Displacements

Lateral spreading ground surface displacements are known to exhibit significant horizontal variability throughout a spread feature (e.g., Faris 2004). The size of a lateral spread can be large or small relative to a bridge, and it is conceivable that ground displacements at some components are large and zero at others, or be nearly the same at multiple components. In order to capture the horizontal variability in the patterns of lateral spreading ground surface

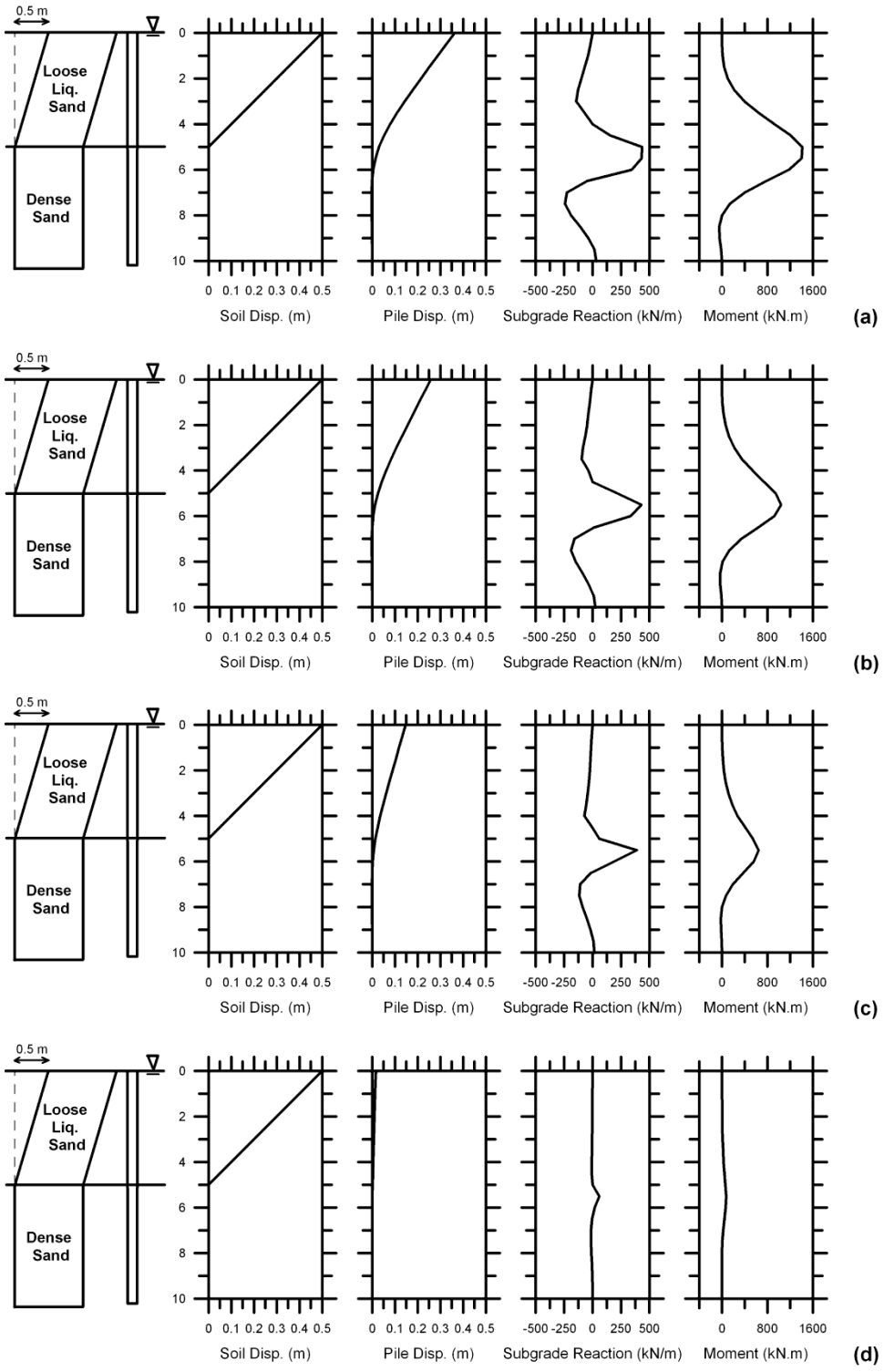

Figure 3.9 Soil and pile displacement and subgrade reaction and moment distribution for (a) $P_{ult} = 2x P_{ult\_API}$; (b) $P_{ult} = 1x P_{ult\_API}$; (c) $P_{ult} = 0.5$ x P_{ult_API} ; and (d) $m_p = 0.05$.

displacement, the left side (i.e., the left abutment and the left pier) and the right side (i.e., the right abutment and the right pier) of the bridge were treated as separate spread features. The spreading is randomized but correlated so that the ratio of the displacements of the two components in the spread feature (e.g., ratio of displacement of the left pier to the displacement of the left abutment) follows a lognormal distribution with a median of 1.0 and a dispersion of ln(3). Furthermore, one third of the load cases involved lateral spreading only on the left side of the bridge (left abutment and the left intermediate pier), one third with spreading only on the right side (right abutment and the right intermediate pier), and one third with spreading on both sides. Ground displacements were randomly selected at each component in accordance with these statistics and subsequently scaled so that the maximum ground displacement applied in all of the analyses was set to 2.0 m (6.56 ft). Ground displacements at the abutments were subsequently reduced by 25% to account for the pinning effect, based on the results of the pinning analyses as explained in Chapter 2.

3.4.8 Vertical Ground Deformation Profile

The vertical profile of ground deformation is also highly uncertain. Studies with a permeable nonliquefied crust layer were associated with a continuous displacement profile (e.g., Abdoun et al. 2003), whereas studies with a low-permeability crust have exhibited a displacement discontinuity at the interface (e.g., Malvick 2008; Brandenberg et al. 2005). The ground surface displacement can therefore be attributed to a combination of shear strains in the various soil layers (mostly in the liquefied layer) and interface slip as the crust spreads on top of the liquefied layers. For simplicity in this study, shear strains in the nonliquefied layers were assumed to be zero, with the ground surface displacement entirely attributed to a combination of shear strain in the liquefied sand and interface slip. The amount of slip at the interface was represented by the ratio of displacement at the top of the liquefied layer to the displacement of the nonliquefied crust layer. This ratio was assumed uniformly distributed between 0 and 1. The shear strain in the loose sand layer was set to provide the remaining fraction of ground surface displacement.

3.5 CHARACTERIZATION OF INERTIA DEMANDS ON THE BRIDGE

Lateral spreading ground displacement during liquefaction may occur during ground shaking, and it is also possible that the lateral spreading may occur after the ground shaking has finished.

Therefore, inertia demands were applied concurrently with lateral spreading displacement only in 50% of the analyses within each class, while for the other 50% of the analyses no inertia was present during the analysis. When inertia was present in the analyses the inertia demand on the bridge was applied as a force equal to the product of the mass and S_a for liquefaction, as noted in Chapter 2. The natural period of the bridge was computed based on the mass of the superstructure and the fixed-base stiffness of the piers. Spectral accelerations were selected from the Caltrans SDC acceleration response spectra for site class D and a moment magnitude of 7.25 ± 0.25. Peak ground acceleration was assumed to be either $0.2g$, $0.3g$, or $0.4g$ since response spectra are available for these PGA's. The response spectra for peak rock acceleration of $0.1g$ was believed to be small enough not to cause liquefaction and/or liquefaction-induced lateral spreading, and therefore was not used in the analyses. Once the S_a for nonliquefaction was selected, the S_a for liquefaction was calculated using liquefaction modifiers recommended by Boulanger et al. (2007) as stated in Chapter 2. The inertia force was linearly increased simultaneously with ground displacements and reached its peak value when the ground displacement reached 0.5 m (1.64 ft). Inertia force was kept constant as ground deformation was increased beyond 0.5 m (1.64 ft). This approach was consistent with the expected maximum transient ground deformation during a single inertia cycle based on centrifuge test observations.

4 Fragility of Bridges to Lateral Spreading

4.1 PERFORMANCE-BASED EARTHQUAKE ENGINEERING AND FRAGILITY FUNCTIONS

The Pacific Earthquake Engineering Research Center developed a PBEE methodology defined by the triple integral in Equation 4.1,

$$P(DV > dv) = \int_{dm}\int_{edp}\int_{im} G_{DV|DM}(dv \mid dm).\left|dG_{DM|EDP}(dm \mid edp)\right| \cdot \left|dG_{EDP|IM}(edp \mid im)\right| \cdot \left|dG_{IM}(im)\right| \tag{4.1}$$

where *DV* is the decision variable, *DM* is the damage measure, *EDP* is the engineering demand parameter, *dv* is the value of decision variable, *dm* is the value of the damage measure, *edp* is the value of the engineering demand parameter, and *im* is the value of the intensity measure.

To solve the triple integral, probabilistic relations are needed to define EDP given IM, DM given EDP, and DV given DM. Fragility functions typically quantify the probability of exceeding a DM given an EDP (e.g., Porter et al. 2007), though the term has also been applied to functions that represent probability of exceeding an EDP given an IM (Mackie and Stojadinovic, 2005) or probability of exceeding a DM given an IM (HAZUS 1999). Fragility functions are therefore a critical component of PBEE. Fragility functions can also be represented as surfaces when expressed over some range of IM and EDP values; these functions have been called "demand fragility surfaces" by Mackie and Stojadinovic (2005).

This chapter focuses on producing demand fragility surfaces characterizing probability of exceeding common EDPs for bridges (i.e., pier column curvature ductility, abutment displacement, pile cap displacement) as functions of free-field permanent ground surface displacement, the most important and useful IM to characterize liquefaction-induced lateral

spreading. The fragility demand surfaces are produced numerically using thousands of realizations of a finite element model in which the inputs were randomly selected as detailed in Chapter 3 (i.e., Monte Carlo simulation). Correlation among EDP values is important for estimating DM using the demand fragility surfaces, so correlation coefficients among EDPs are also presented. Finally, disaggregation of the results is used to identify the input parameters that most significantly contribute to the demand fragility surfaces of bridges due to liquefaction-induced lateral spreading.

4.2 GENERATION OF DEMAND FRAGILITY SURFACES

Demand fragility surfaces were generated using Monte Carlo simulations involving thousands of realizations of a nonlinear equivalent static global analysis. Input parameters were randomly selected from their assigned distributions using the uniform random number generator in TCL combined with a Box-Muller transform (Box and Muller 1958) for any variables that were not uniformly distributed (i.e., for variables with normal and log-normal distributions). During the analyses the free-field lateral ground displacement was increased incrementally and the values of the IM (i.e., the maximum free-field ground surface displacement among the various bridge components) were recorded when specified levels of several EDPs were mobilized. Tables 4.1, 4.2, and 4.3 present the EDPs that were monitored during the analyses for continuous bridges with monolithic abutments, simply supported bridges with seat-type abutments, and continuous bridges with seat-type abutments, respectively, and ground displacements were recorded when the EDP first reached the "initial value" and subsequently at each "incremental value" thereafter. The analysis proceeded until the maximum free-field ground displacement reached 2 m (6.56 ft) or until a limiting demand on a bridge pier was reached, defined as either exceeding a curvature ductility of 11 in one of the pier columns, exceeding the shear capacity of a pier column, or having a span displacement exceed the seat length for a simply supported span. These limits were established (1) based on the assumption that this level of mobilized EDP in the pier column would constitute serious damage and continuing the analysis would have little physical meaning, and (2) numerical convergence became difficult at such large levels of structural nonlinearity.

Table 4.1 Engineering demand parameters and their recorded values for continuous bridges with monolithic abutments.

EDP	Performance Group	Initial Value	Incremental Value	Unit
Curvature Ductility in Piers	Pier 2	1	1	NA
	Pier 3	1	1	NA
Pile Cap Displacement	Pier 2	0.025	0.025	(m)
	Pier 2	0.025	0.025	(m)
Pile Cap Rotation	Pier 2	0.5	0.5	%
	Pier 3	0.5	0.5	%
Abutment Displacement	Abutment 1	0.025	0.025	(m)
	Abutment 4	0.025	0.025	(m)
Abutment Rotation	Abutment 1	0.5	0.5	%
	Abutment 4	0.5	0.5	%
Pier Pile Curvature Ductility	Pier 2	1	2	NA
	Pier 3	1	2	NA
Abutment Pile Curvature Ductility	Abutment 1	1	2	NA
	Abutment 4	1	2	NA

Table 4.2 Engineering demand parameters and their recorded values for simply supported bridges with seat-type abutments.

EDP	Performance Group	Initial Value	Incremental Value	Unit
Curvature Ductility in Piers	Pier 2	1	1	NA
	Pier 3	1	1	NA
Pile Cap Displacement	Pier 2	0.025	0.025	(m)
	Pier 3	0.025	0.025	(m)
Pile Cap Rotation	Pier 2	0.5	0.5	%
	Pier 3	0.5	0.5	%
Abutment Displacement	Abutment 1	0.025	0.025	(m)
	Abutment 4	0.025	0.025	(m)
Abutment Rotation	Abutment 1	0.5	0.5	%
	Abutment 4	0.5	0.5	%
Pier Pile Curvature Ductility	Pier 2	1	2	NA
	Pier 3	1	2	NA
Abutment Pile Curvature Ductility	Abutment 1	1	2	NA
	Abutment 4	1	2	NA
Strains in Bearings	Abutment 1	50	50	%
	Pier 2	50	50	%
	Pier 3	50	50	%
	Abutment 4	50	50	%
Unseating	Any Pier or Abutment	0.38	NA	(m)

Table 4.3 Engineering demand parameters and their recorded values for continuous bridges with seat-type abutments.

EDP	Performance Group	Initial Value	Incremental Value	Unit
Curvature Ductility in Piers	Pier 2	1	1	NA
	Pier 3	1	1	NA
Pile Cap Displacement	Pier 2	0.025	0.025	(m)
	Pier 2	0.025	0.025	(m)
Pile Cap Rotation	Pier 2	0.5	0.5	%
	Pier 3	0.5	0.5	%
Abutment Displacement	Abutment 1	0.025	0.025	(m)
	Abutment 4	0.025	0.025	(m)
Abutment Rotation	Abutment 1	0.5	0.5	%
	Abutment 4	0.5	0.5	%
Pier Pile Curvature Ductility	Pier 2	1	2	NA
	Pier 3	1	2	NA
Abutment Pile Curvature Ductility	Abutment 1	1	2	NA
	Abutment 4	1	2	NA
Strains in Bearings	Abutment 1	50	50	%
	Abutment 4	50	50	%
Unseating	Unseating in any Abutment	0.38	NA	(m)

Table 4.4 Generation of fragility function for curvature ductility of seven post-1971 simply supported bridges with seat-type abutments and single column piers.

Sorted D_{FF}	Probability Mass	Cumulative Prob. Dens.
0.044	0.001105	0
0.049	0.001105	1.11E-03
0.053	0.001105	2.21E-03
0.054	0.001105	3.32E-03
0.055	0.001105	4.42E-03
0.057	0.001105	5.53E-03
0.058	0.001105	6.63E-03
:	:	:
:	:	:
:	:	:
1.838	0.001105	0.393
1.905	0.001105	0.394

Once the analyses were completed, the free-field ground displacements required to mobilize a given EDP value were sorted in increasing order and plotted as a histogram reflecting the cumulative probability mass function. The probability mass assigned to each discrete analysis was equal to $1/N$, where N was the number of analyses in a given data set (typically 1000). Separate cumulative probability mass functions were developed for each EDP type (e.g., pier curvature ductility), each EDP value within that type (e.g., curvature ductility of 1, 2, 3, …), and for each class of bridge. The process is best demonstrated through an example. Table 4.4 shows the exercise of generating the fragility function for maximum curvature ductility of seven in any of the piers of the set of analyses of post-1971 simply supported bridges with seat-type abutments and single-column piers.

The first column is the array of free-field ground displacements required to mobilize a maximum curvature ductility of seven in the piers. The probability mass of all of the analyses are the same as listed in the second column. For this particular set of analyses, 95 runs failed to converge. These runs were excluded from the set of analyses, hence each analysis has a probability mass of 1/905 = 0.001105.

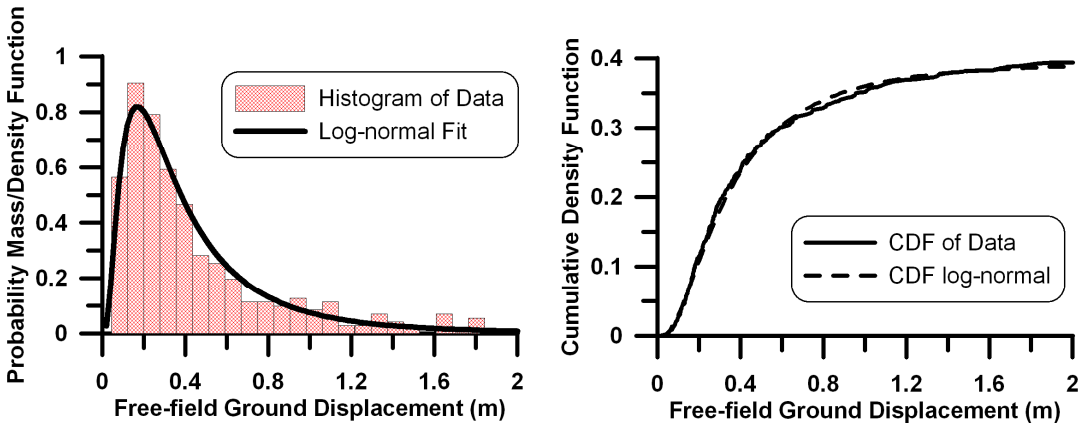

(a) (b)

Figure 4.1 Generation of fragility function for pier curvature ductility of seven for post-1971 simply supported bridges with seat-type abutments and single-column piers; (a) probability mass function and (b) cumulative density function.

Figure 4.1a shows the histogram of the probability mass distributions of free-field displacements to reach a curvature ductility of seven presented in Table 4.4. The cumulative distribution of the actual data is shown on Figure 4.1b, with the corresponding log-normal distribution superimposed on the distribution of the data. As can be seen in the figure, the log-normal distribution fits the data very well.

Cumulative probability density functions for typical random variables range from 0 to 1. The fragility function shown in Figure 4.1 does not reach an ultimate value of 1 but rather reaches a value of only 0.394 as ground displacement reaches 2 m (6.56 ft). Furthermore, the slope of the fragility function becomes very flat at 2 m (6.56 ft) of free-field ground displacement, and the fragility function will not reach a cumulative probability density of 1.0 regardless of how large the free-field ground displacement becomes. The physical explanation for this behavior is that some bridges are strong enough to induce passive failure in the spreading soil (i.e., to mobilize the full capacities of the *p-y* elements) without reaching a curvature ductility of seven in any of the pier columns. For such cases, the lateral spreading displacement can continue to infinity without inducing further damage to the bridge. Hence, the fragility functions in this report are mixed random variables with some probability mass lumped at infinite ground displacement.

4.3 FITTING FRAGILITY SURFACES TO THE DATA

The fragility function in the previous section was generated numerically by summing the probability mass of each discrete case, but a more convenient representation of the fragility function can be obtained by fitting a functional form to the discrete data (as the fragility functions in this study were well-approximated as log-normal distributions). One option would be to specify a median and standard deviation for each value of EDP for each analysis case, but this would result in a very large number of constants. The approach adopted here was to utilize six constants to fully define the demand fragility surface. Each of the six constants is presented by an example in the following paragraphs.

For a simply supported bridge with seat-type abutments and single-column piers belonging to the post-1971 era, ten different EDPs are recorded, as listed in Table 4.2. The fragility results of two of the EDPs, pile cap displacement, and pier curvature ductility are shown in Figure 4.2.

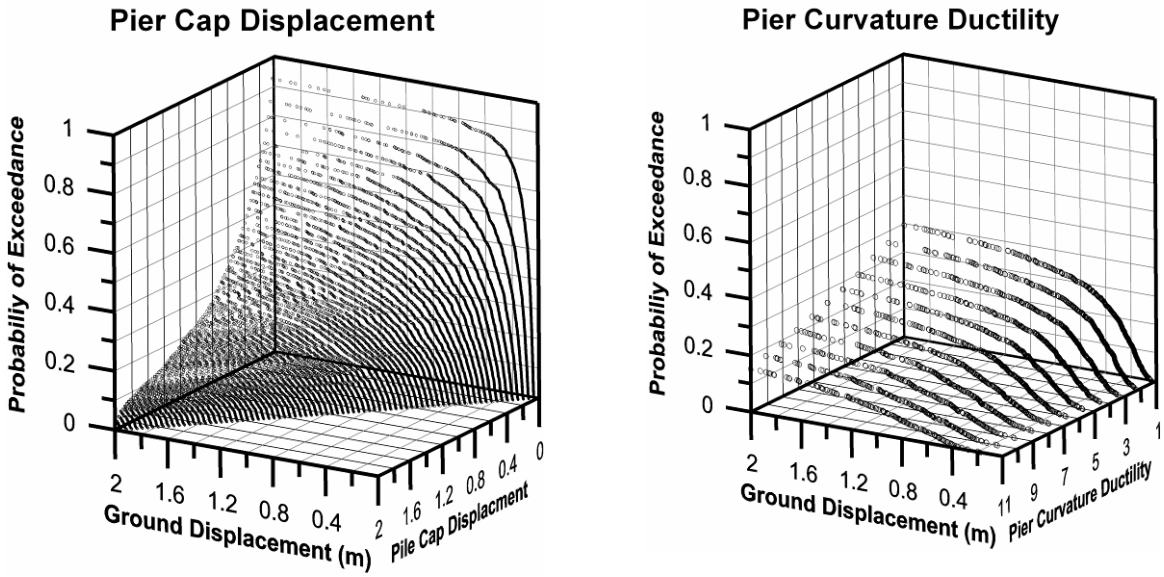

(a) (b)

Figure 4.2 Fragility curves of two EDPs of simply supported bridges with seat-type abutments and single-column piers belonging to the post-1971 era: (a) pile cap displacement and (b) pier curvature ductility.

The fragility functions at every EDP value can be defined by a median λ, a standard deviation of natural logarithms of the data ξ, and an additional scalar value representing the limiting value of cumulative probability (i.e., the amount of probability mass included in the finite range of free-field ground displacement, also equal to 1 minus the probability mass lumped at a ground displacement of infinity). This involves specifying 80 different constants for cap displacement and 11 different constants for pier curvature ductility. Repeating this process for the other EDPs in Tables 4.1, 4.2, and 4.3 and for all of the classes of bridges results in an unmanageable representation of the fragility functions. The alternative approach adopted in this study is to use linear regression to define the medians, standard deviations, and peak probabilities as functions of the EDP. Linear regression requires specification of a slope and an intercept value, hence two constants each are required for median, standard deviation, and maximum probability, and the entire demand fragility surface can therefore be defined by six constants. Figure 4.3 shows the linear regressions of the natural logarithms of median, standard deviation, and peak probability for pile cap displacement of the abovementioned class of bridges. As shown in the figure, all three parameters can be represented fairly well using a linear regression versus logarithms of the EDP values, though there is some misfit particularly at lower values of EDP. Some misfit must be accepted as a tradeoff for the convenience of expressing the demand fragility surfaces using a manageable set of constants. The formulas for the three lines can be summarized as follows:

$$\lambda = \beta_0 + \beta_1 \cdot \ln(edp) \tag{4.6}$$

$$\xi = \beta_2 + \beta_3 \cdot \ln(edp) \tag{4.7}$$

$$\mathrm{p}_{max} = \beta_4 + \beta_5 \cdot \ln(edp) \le 1.0 \tag{4.8}$$

where λ is the logarithm of median of the log-normal distribution, ξ is the standard deviation of natural logs of data, and p_{max} is the maximum probability at 2 m (6.56 ft) of ground displacement at each EDP value.

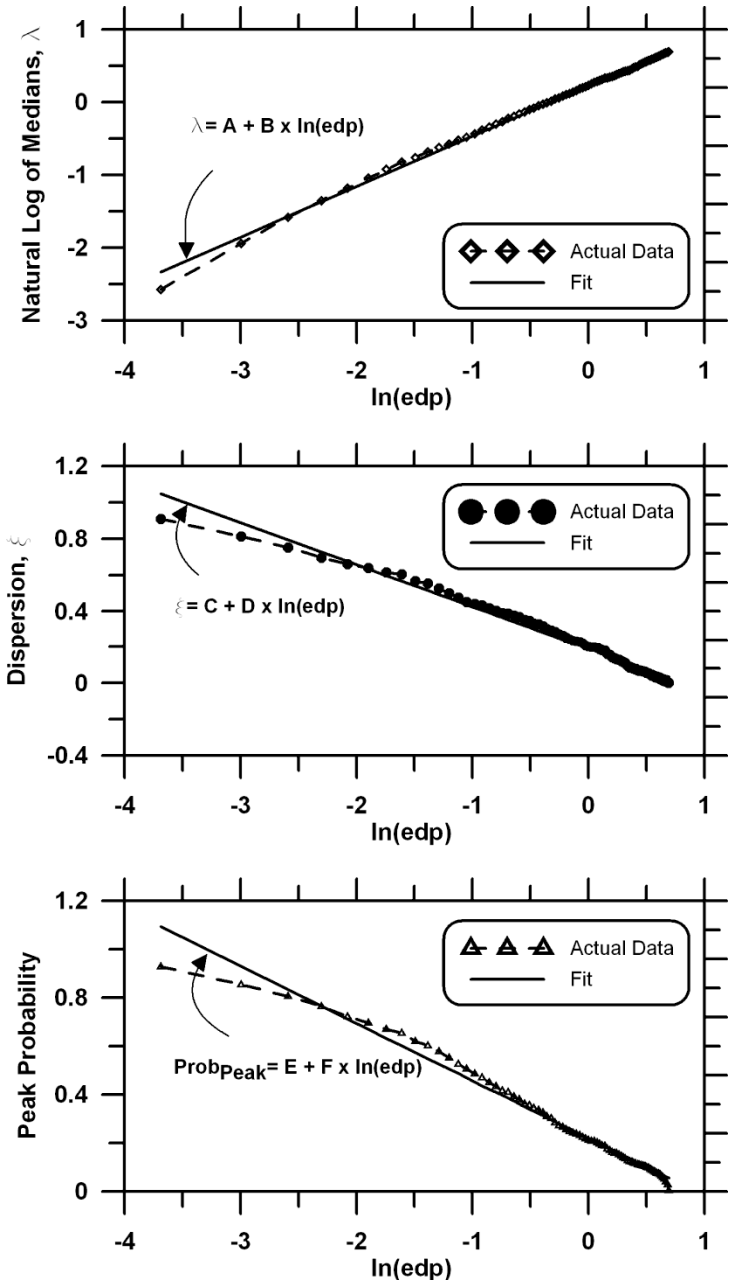

Figure 4.3 Linear regression of the values of fragility curve parameters: (a) logarithm of medians, (b) dispersion (standard deviation of logarithms of data), and (c) maximum probability for simply supported bridges with seat-type abutments and single column piers built post-1971.

The form of Equation 4.8 permits $p_{max} > 1$, which is a violation of probability theory. This can be seen in the misfit in Figure 4.3 at low *edp* values where the data lie below the linear trend. The data are all below a cumulative probability of 1.0, but the linear trend extends above 1.0. Hence, p_{max} was truncated to have a maximum value of 1.0. For some EDPs a log-

transformation of the *edp* values did not produce a linear fit, and a better linear fit was obtained based on the values of the variables themselves. Hence, p_{max} for some EDPs was defined as follows:

$$p_{max} = \beta_4 + \beta_5 \cdot edp \leq 1.0 \tag{4.9}$$

By utilizing the equations of the lines presented in Equations 4.6 through 4.9 for every value of IM (i.e., ground displacement) and every value of EDP (*edp*), the probability of exceedance can be calculated using Equation 4.10 for all EDPs other than curvature ductility in the piers, for which Equation 4.11 should be used.

$$P(EDP < edp \mid IM = im) = 0 \leq \underbrace{\Phi\left(\frac{\ln(im) - (\beta_0 + \beta_1 \cdot \ln(edp))}{(\beta_2 + \beta_3 \cdot \ln(edp))}\right)}_{\text{Standard Normal Cumulative Distribution}} \cdot \underbrace{\left(\beta_4 + \beta_5 \cdot \ln(edp)\right)}_{\text{Peak Probability at edp value}} \leq 1 \tag{4.10}$$

$$P(EDP < edp \mid IM = im) = 0 \leq \underbrace{\Phi\left(\frac{\ln(im) - (\beta_0 + \beta_1 \cdot \ln(edp))}{(\beta_2 + \beta_3 \cdot \ln(edp))}\right)}_{\text{Standard Normal Cumulative Distribution}} \cdot \underbrace{\left(\beta_4 + \beta_5 \cdot edp\right)}_{\text{Peak Probability at edp value}} \leq 1 \tag{4.11}$$

In Equations 4.10 and 4.11, Φ is the standard normal cumulative distribution function, *im* is the free-field ground displacement in meters, and *edp* is an engineering demand parameter in the same units as defined in this report (meters for displacement, radians for rotation).

Equations 4.10 and 4.11 provide a convenient means of specifying the entire demand fragility surface using only six variables. In a few instances there is a misfit of the surface generated values for probability of exceeding certain EDPs above 1 or below 0. Since these values were statistically meaningless, the values of probabilities of exceedance were truncated between 0 and 1. Figure 4.4 shows demand fragility surfaces plotted along with the discreet data for pile cap displacement and pier curvature ductility in the above-mentioned class of bridges. The degree of misfit between the data and the surface in Figure 4.4 is characteristic of the misfit for other EDPs. As can be seen in the figure, the probability of exceedance of pile cap displacement at low *edp* value of 0.025 m (0.98 in.) exceeds 1 due to the misfit of the fragility surface; thus the fragility surface was truncated at 1.

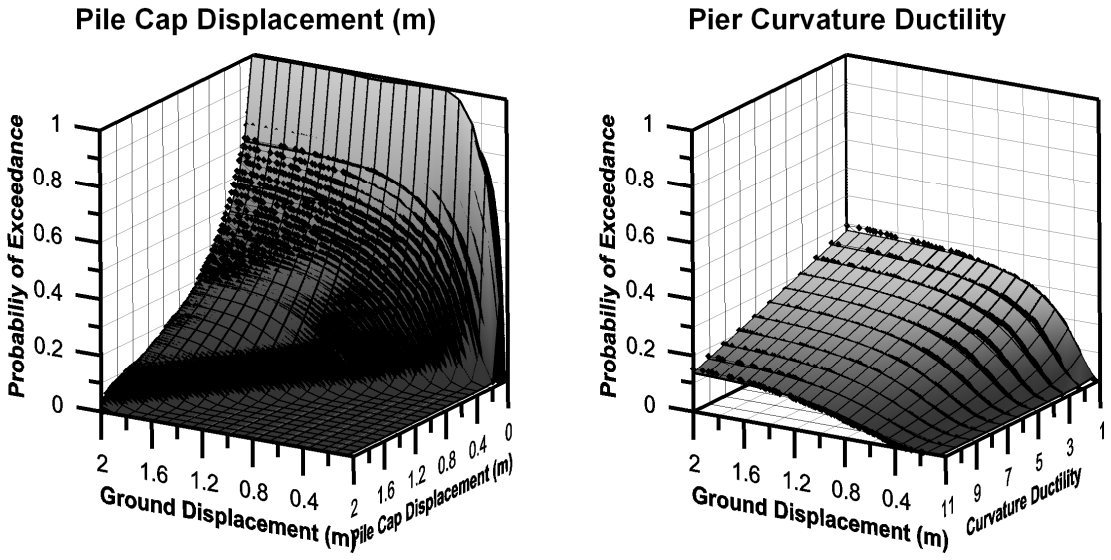

(a) (b)

Figure 4.4 Demand fragility surfaces plotted along with the discreet date for (a) pile cap displacement and (b) pier curvature ductility for simply supported bridges with seat-type abutments and single-column piers built post-1971.

4.4 FRAGILITY SURFACE RESULTS

Using the fitting method explained above, fragility surfaces were created for all recorded EDPs for all classes of bridges that were analyzed in this study. Tables 4.5 through 4.10 summarize the parameters for fitting the fragility surfaces for all 24 different classes of bridges analyzed as well as the appropriate equation to be used for each EDP for fitting the fragility surface. Coefficients of variation (R^2) of the fits were mostly above 0.9 with the lowest values near 0.8, indicating that the fitted surfaces agree reasonably well with the discrete data. Plots of the fitted fragility surfaces for different EDPs for all the classes of bridges analyzed are summarized in Figures 4.5 through 4.15.

Table 4.5 Fragility surface parameters for bridges with continuous superstructure, seat-type abutments, and single-column bents.

	Post-1971																		Pre-1971						Eq.
	0.6m diameter CISS piles						0.6m diameter CIDH piles						0.38m diameter precast concrete piles						0.38m diameter precast concrete piles						
Engineering Demand Parameter	β_1	β_2	β_3	β_4	β_5	β_6	β_1	β_2	β_3	β_4	β_5	β_6	β_1	β_2	β_3	β_4	β_5	β_6	β_1	β_2	β_3	β_4	β_5	β_6	No.
Pier Column Curvature Ductility	-1.764	0.465	0.842	-0.091	0.850	-0.048	-1.806	0.475	0.867	-0.082	0.903	-0.038	-1.847	0.489	0.814	-0.065	0.969	-0.038	-2.510	0.546	0.754	-0.031	1.040	-0.033	4.11
Pile Cap Displacement (m)	0.502	0.686	0.344	-0.132	0.025	-0.242	0.608	0.793	0.299	-0.157	0.185	-0.260	0.585	0.843	0.307	-0.141	0.294	-0.235	0.525	0.920	0.324	-0.116	0.225	-0.260	4.10
Abutment Displacement (m)	0.446	0.752	0.164	-0.196	0.434	-0.179	0.530	0.761	0.169	-0.189	0.369	-0.205	0.591	0.816	0.195	-0.157	0.369	-0.208	0.691	0.759	0.175	-0.163	0.260	-0.201	4.10
Abutment Rotation (%)	1.190	0.597	0.378	-0.065	-0.139	-0.252	0.538	0.503	0.407	-0.048	0.625	-0.083	0.436	0.524	0.420	-0.029	0.770	-0.046	1.831	1.031	0.424	-0.011	0.726	-0.060	4.10
Pile Cap Rotation (%)	1.433	0.573	0.285	-0.088	-0.447	-0.257	1.914	0.726	0.048	-0.148	-0.315	-0.252	1.941	0.782	0.231	-0.097	-0.274	-0.272	2.044	0.861	0.547	-0.025	-0.221	-0.236	4.10
Strain in Abutment Bearings	-0.880	0.395	0.665	-0.154	0.637	-0.042	-0.713	0.330	0.756	-0.196	0.502	-0.021	-0.884	0.453	0.694	-0.166	0.471	-0.016	-1.806	0.942	0.830	-0.151	0.546	-0.063	4.10

Table 4.6 Fragility surface parameters for bridges with continuous superstructure, seat-type abutments, and multi-column bents.

	Post-1971																		Pre-1971						Eq.
	0.6m diameter CISS piles						0.6m diameter CIDH piles						0.38m diameter precast concrete piles						0.38m diameter precast concrete piles						
Engineering Demand Parameter	β_1	β_2	β_3	β_4	β_5	β_6	β_1	β_2	β_3	β_4	β_5	β_6	β_1	β_2	β_3	β_4	β_5	β_6	β_1	β_2	β_3	β_4	β_5	β_6	No.
Pier Column Curvature Ductility	-1.546	0.458	0.790	-0.094	0.805	-0.046	-1.583	0.462	0.837	-0.100	0.831	-0.031	-1.766	0.503	0.789	-0.083	0.847	-0.025	-2.181	0.564	0.739	-0.036	0.965	-0.021	4.11
Pile Cap Displacement (m)	0.398	0.727	0.329	-0.158	0.070	-0.245	0.510	0.822	0.339	-0.141	0.402	-0.185	0.420	0.831	0.357	-0.140	0.475	-0.179	0.277	0.825	0.348	-0.131	0.525	-0.175	4.10
Abutment Displacement (m)	0.486	0.753	0.164	-0.196	0.400	-0.204	0.574	0.778	0.165	-0.189	0.390	-0.215	0.598	0.804	0.186	-0.167	0.388	-0.208	0.710	0.745	0.156	-0.170	0.329	-0.210	4.10
Abutment Rotation (%)	1.328	0.624	0.271	-0.091	-0.098	-0.241	0.558	0.501	0.369	-0.054	0.636	-0.082	0.406	0.512	0.378	-0.040	0.817	-0.038	1.888	1.028	0.370	-0.032	0.869	-0.030	4.10
Pile Cap Rotation (%)	1.357	0.602	0.216	-0.118	-0.447	-0.268	1.089	0.480	0.167	-0.147	0.025	-0.109	1.004	0.462	0.484	-0.085	0.079	-0.114	0.386	0.378	0.536	-0.116	0.297	-0.045	4.10
Strain in Abutment Bearings	-0.744	0.357	0.638	-0.130	0.677	-0.075	-0.635	0.331	0.723	-0.184	0.519	-0.036	-0.698	0.346	0.744	-0.191	0.459	-0.026	-1.607	0.859	0.830	-0.188	0.561	-0.070	4.10

Table 4.7 Fragility surface parameters for bridges with continuous superstructure, monolithic abutments, and single-column bents.

	Post-1971																		Pre-1971						Eq.
	0.6m diameter CISS piles						0.6m diameter CIDH piles						0.38m diameter precast concrete piles						0.38m diameter precast concrete piles						
Engineering Demand Parameter	β_1	β_2	β_3	β_4	β_5	β_6	β_1	β_2	β_3	β_4	β_5	β_6	β_1	β_2	β_3	β_4	β_5	β_6	β_1	β_2	β_3	β_4	β_5	β_6	No.
Pier Column Curvature Ductility	-1.544	0.429	0.994	-0.102	0.957	-0.059	-1.627	0.440	0.970	-0.097	0.982	-0.057	-1.762	0.457	1.007	-0.115	1.010	-0.050	-2.387	0.529	1.039	-0.090	1.099	-0.050	4.11
Pile Cap Displacement (m)	0.569	0.632	0.266	-0.218	-0.079	-0.253	0.506	0.661	0.239	-0.221	-0.034	-0.266	0.780	0.829	0.294	-0.187	0.009	-0.313	0.725	0.901	0.254	-0.206	-0.006	-0.312	4.10
Abutment Displacement (m)	0.806	0.564	0.175	-0.138	-0.089	-0.276	0.671	0.524	0.288	-0.104	-0.057	-0.265	0.864	0.616	0.244	-0.118	-0.010	-0.258	0.731	0.548	0.229	-0.125	0.061	-0.200	4.10
Abutment Rotation (%)	1.859	0.727	-0.123	-0.189	-0.506	-0.316	1.936	0.744	-0.073	-0.178	-0.550	-0.323	1.939	0.723	0.064	-0.148	-0.521	-0.301	2.168	0.741	-0.262	-0.230	-0.391	-0.239	4.10
Pile Cap Rotation (%)	1.562	0.535	0.056	-0.147	-0.538	-0.262	1.005	0.465	0.054	-0.171	-0.499	-0.267	1.719	0.706	0.236	-0.132	-0.618	-0.340	1.672	0.744	0.149	-0.168	-0.491	-0.287	4.10

Table 4.8 Fragility surface parameters for bridges with continuous superstructure, monolithic abutments, and multi-column bents.

	Post-1971																		Pre-1971						Eq.
	0.6m diameter CISS piles						0.6m diameter CIDH piles						0.38m diameter precast concrete piles						0.38m diameter precast concrete piles						
Engineering Demand Parameter	β_1	β_2	β_3	β_4	β_5	β_6	β_1	β_2	β_3	β_4	β_5	β_6	β_1	β_2	β_3	β_4	β_5	β_6	β_1	β_2	β_3	β_4	β_5	β_6	No.
Pier Column Curvature Ductility	-1.176	0.398	0.859	-0.101	0.859	-0.055	-1.346	0.390	0.927	-0.114	0.919	-0.049	-1.482	0.426	0.964	-0.130	0.880	-0.043	-2.110	0.502	1.033	-0.106	1.051	-0.043	4.11
Pile Cap Displacement (m)	0.504	0.547	0.315	-0.184	-0.166	-0.280	0.652	0.707	0.252	-0.201	-0.032	-0.313	0.536	0.776	0.355	-0.185	0.172	-0.264	0.801	0.890	0.277	-0.205	-0.007	-0.335	4.10
Abutment Displacement (m)	0.966	0.618	0.050	-0.183	-0.161	-0.301	0.866	0.604	0.166	-0.136	-0.066	-0.290	0.905	0.610	0.176	-0.137	-0.013	-0.275	0.869	0.589	0.240	-0.103	0.015	-0.227	4.10
Abutment Rotation (%)	1.841	0.710	-0.114	-0.192	-0.556	-0.332	2.101	0.777	-0.073	-0.176	-0.700	-0.361	2.245	0.784	-0.098	-0.179	-0.609	-0.326	1.974	0.701	0.000	-0.156	-0.518	-0.278	4.10
Pile Cap Rotation (%)	1.080	0.390	0.426	-0.048	-0.721	-0.309	1.343	0.546	0.011	-0.180	-0.695	-0.343	0.748	0.418	0.313	-0.107	-0.165	-0.163	1.936	0.797	0.100	-0.182	-0.694	-0.362	4.10

Table 4.9 Fragility surface parameters for bridges with simply supported spans, seat-type abutments, and single-column bents.

	Post-1971																		Pre-1971						Eq.
	0.6m diameter CISS piles						0.6m diameter CIDH piles						0.38m diameter precast concrete piles						0.38m diameter precast concrete piles						
Engineering Demand Parameter	β_1	β_2	β_3	β_4	β_5	β_6	β_1	β_2	β_3	β_4	β_5	β_6	β_1	β_2	β_3	β_4	β_5	β_6	β_1	β_2	β_3	β_4	β_5	β_6	No.
Pier Column Curvature Ductility	-1.312	0.394	0.838	-0.116	0.426	-0.027	-1.272	0.414	0.855	-0.137	0.464	-0.026	-1.260	0.395	0.847	-0.131	0.492	-0.025	-1.665	0.499	0.835	-0.096	0.749	-0.024	4.11
Pile Cap Displacement (m)	0.279	0.636	0.298	-0.187	0.147	-0.209	0.347	0.757	0.286	-0.177	0.494	-0.137	0.327	0.819	0.291	-0.172	0.722	-0.079	0.252	0.811	0.282	-0.169	0.780	-0.075	4.10
Abutment Displacement (m)	0.485	0.762	0.161	-0.206	0.489	-0.183	0.613	0.782	0.187	-0.191	0.373	-0.221	0.580	0.810	0.208	-0.171	0.418	-0.203	0.598	0.822	0.174	-0.167	0.471	-0.184	4.10
Abutment Rotation (%)	1.347	0.633	0.218	-0.110	-0.011	-0.220	0.693	0.527	0.356	-0.065	0.616	-0.082	0.491	0.519	0.395	-0.039	0.774	-0.047	0.220	0.469	0.241	-0.072	0.788	-0.043	4.10
Pile Cap Rotation (%)	1.319	0.515	0.142	-0.118	-0.385	-0.248	1.088	0.494	0.190	-0.130	-0.210	-0.179	1.090	0.551	0.083	-0.162	0.024	-0.164	1.092	0.567	0.174	-0.129	0.216	-0.102	4.10
Strain in Abutment Bearings	-0.660	0.339	0.653	-0.142	0.691	-0.057	-0.422	0.272	0.704	-0.164	0.447	-0.043	-0.724	0.369	0.672	-0.099	0.419	-0.020	-1.513	0.768	0.838	-0.230	0.542	-0.076	4.10
Strain in Pier Bearings	-0.922	0.384	0.716	-0.106	0.453	-0.068	-0.891	0.410	0.700	-0.146	0.497	-0.038	-0.849	0.375	0.690	-0.125	0.617	-0.038	-1.151	0.416	0.810	-0.144	0.569	0.019	4.10

Table 4.10 Fragility surface parameters for bridges with simply supported spans, seat-type abutments, and multi-column bents.

	Post-1971																		Pre-1971						Eq.
	0.6m diameter CISS piles						0.6m diameter CIDH piles						0.38m diameter precast concrete piles						0.38m diameter precast concrete piles						
Engineering Demand Parameter	β_1	β_2	β_3	β_4	β_5	β_6	β_1	β_2	β_3	β_4	β_5	β_6	β_1	β_2	β_3	β_4	β_5	β_6	β_1	β_2	β_3	β_4	β_5	β_6	No.
Pier Column Curvature Ductility	-1.073	0.362	0.775	-0.091	0.282	-0.020	-0.890	0.363	0.777	-0.132	0.322	-0.023	-1.260	0.395	0.847	-0.131	0.492	-0.025	-1.345	0.440	0.840	-0.144	0.590	-0.024	4.11
Pile Cap Displacement (m)	0.435	0.660	0.331	-0.170	0.139	-0.201	0.376	0.755	0.301	-0.176	0.495	-0.134	0.327	0.819	0.291	-0.172	0.722	-0.079	0.278	0.826	0.310	-0.155	0.849	-0.051	4.10
Abutment Displacement (m)	0.521	0.761	0.167	-0.203	0.476	-0.184	0.613	0.789	0.172	-0.195	0.377	-0.226	0.580	0.810	0.208	-0.171	0.418	-0.203	0.622	0.809	0.200	-0.160	0.432	-0.207	4.10
Abutment Rotation (%)	1.404	0.642	0.222	-0.108	-0.110	-0.243	0.718	0.540	0.378	-0.059	0.616	-0.084	0.491	0.519	0.395	-0.039	0.774	-0.047	0.330	0.487	0.352	-0.050	0.838	-0.034	4.10
Pile Cap Rotation (%)	1.499	0.560	0.064	-0.139	-0.317	-0.228	1.157	0.533	0.208	-0.125	-0.228	-0.191	1.090	0.551	0.083	-0.162	0.024	-0.164	1.200	0.610	0.272	-0.109	0.225	-0.107	4.10
Strain in Abutment Bearings	-0.600	0.326	0.661	-0.149	0.701	-0.064	-0.437	0.273	0.691	-0.154	0.468	-0.055	-0.724	0.369	0.672	-0.099	0.419	-0.020	-1.320	0.723	0.882	-0.255	0.494	-0.070	4.10
Strain in Pier Bearings	-0.856	0.403	0.680	-0.118	0.465	-0.089	-0.889	0.427	0.699	-0.152	0.492	-0.037	-0.849	0.375	0.690	-0.125	0.617	-0.038	-1.130	0.387	0.851	-0.169	0.630	-0.003	4.10

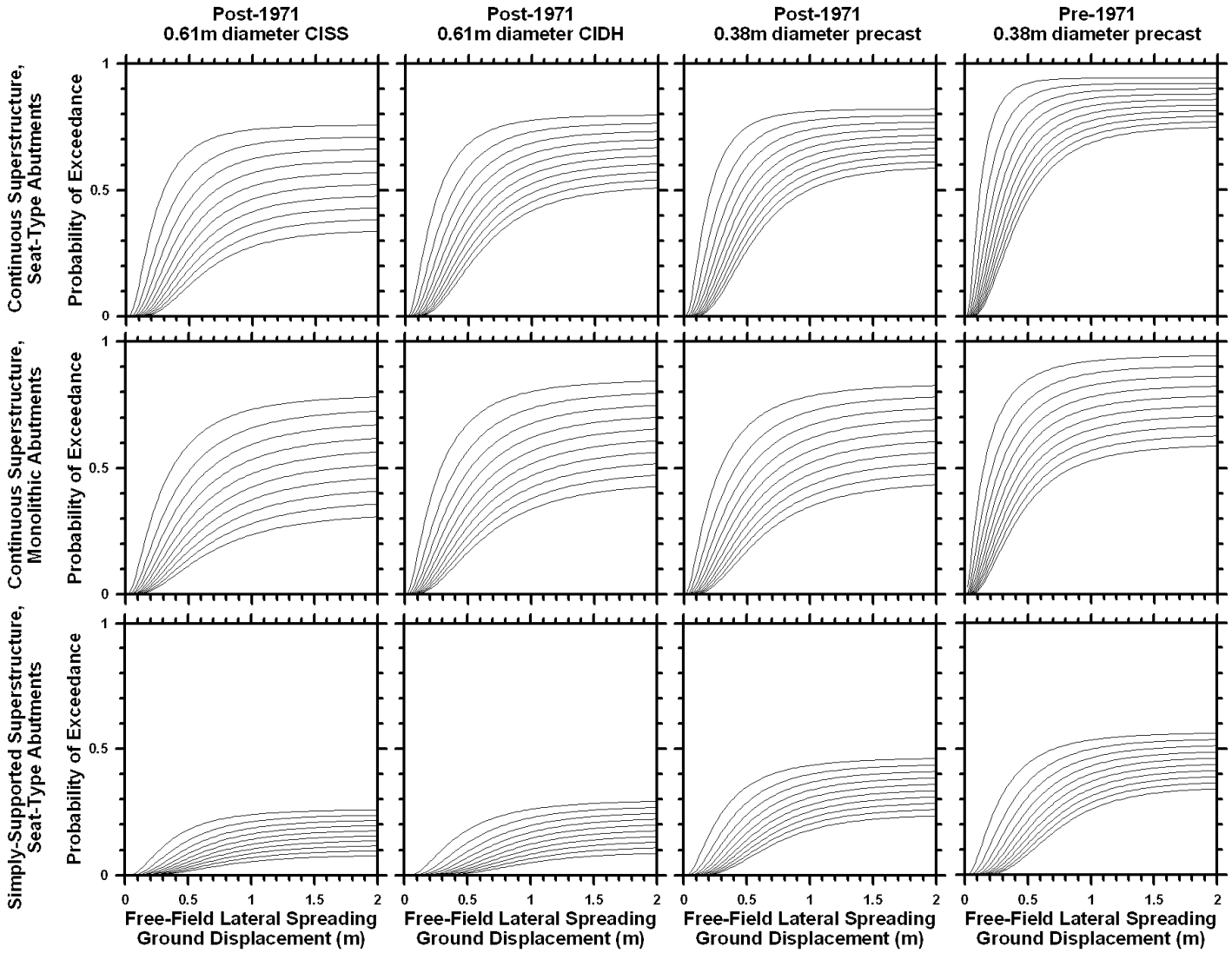

Figure 4.5 Fragility functions for pier column curvature ductility for bridges with multi-column bents. Curvature ductility from top to bottom are 1 through 10 in increments of 1.

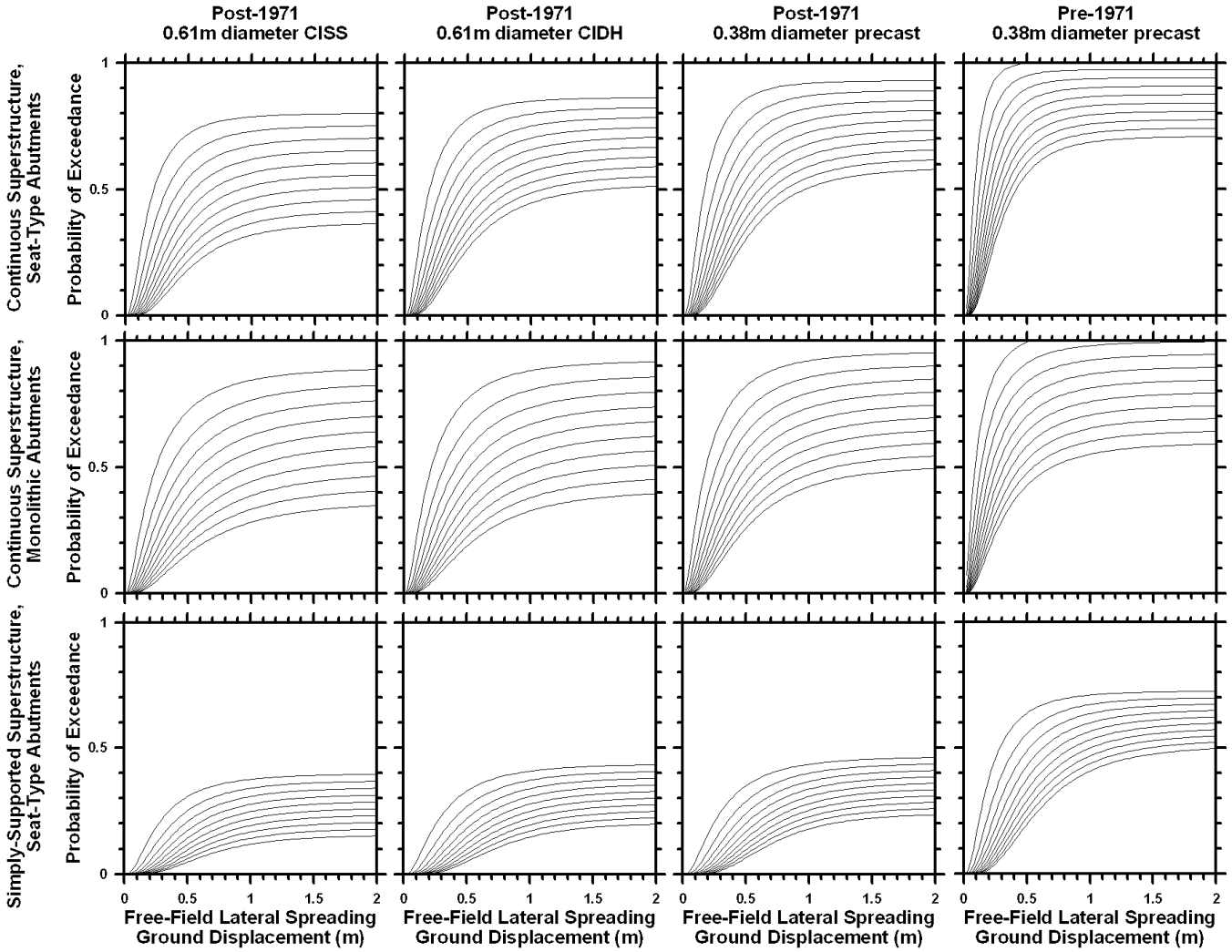

Figure 4.6 Fragility functions for pier column curvature ductility for bridges with single-column bents. Curvature ductility from top to bottom are 1 through 10 in increments of 1.

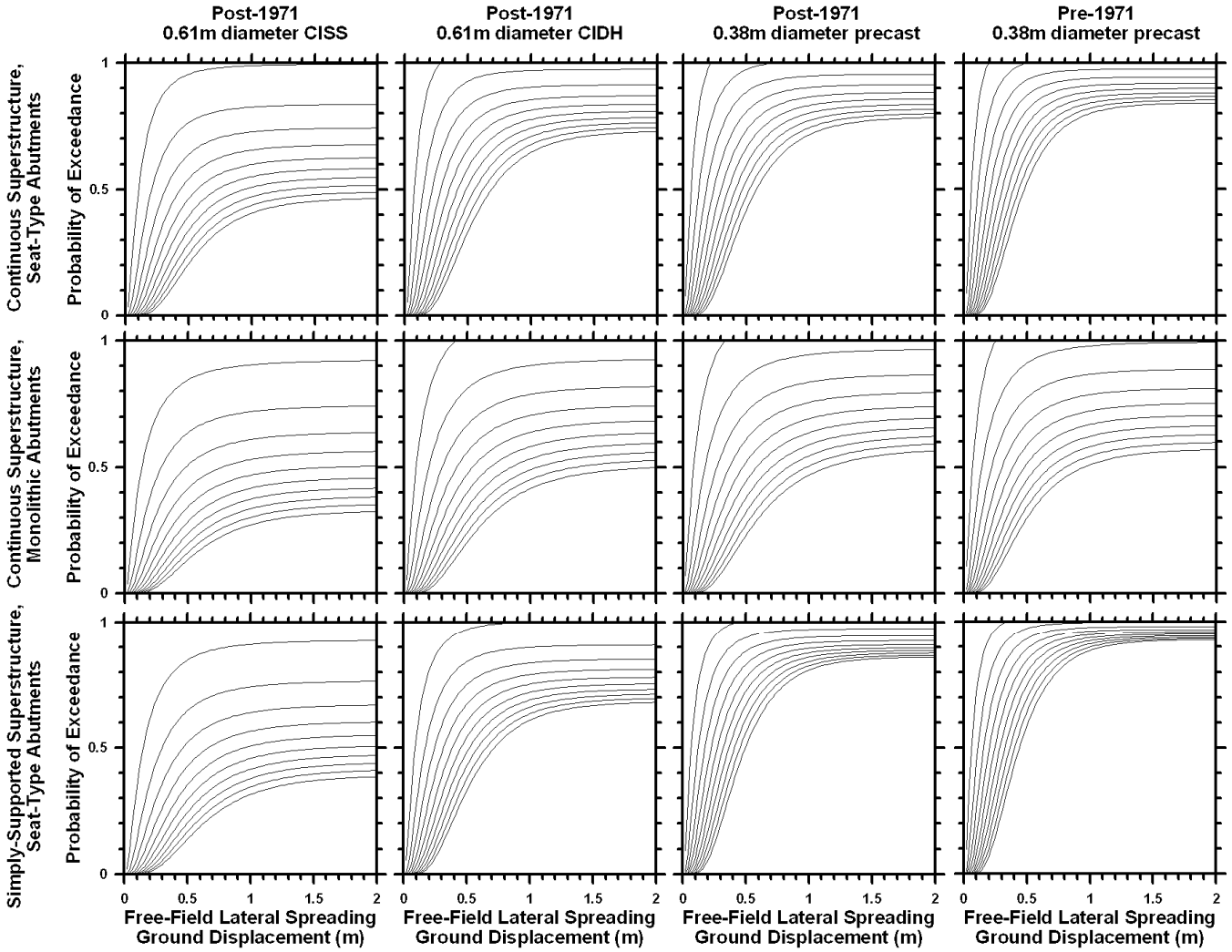

Figure 4.7 Fragility functions for pile cap displacement for bridges with multi-column bents. Pile cap displacements from top to bottom are 0.025 m (0.98 in.) to 0.25 m (9.84 in.) in increments of 0.25 m (9.84 in.).

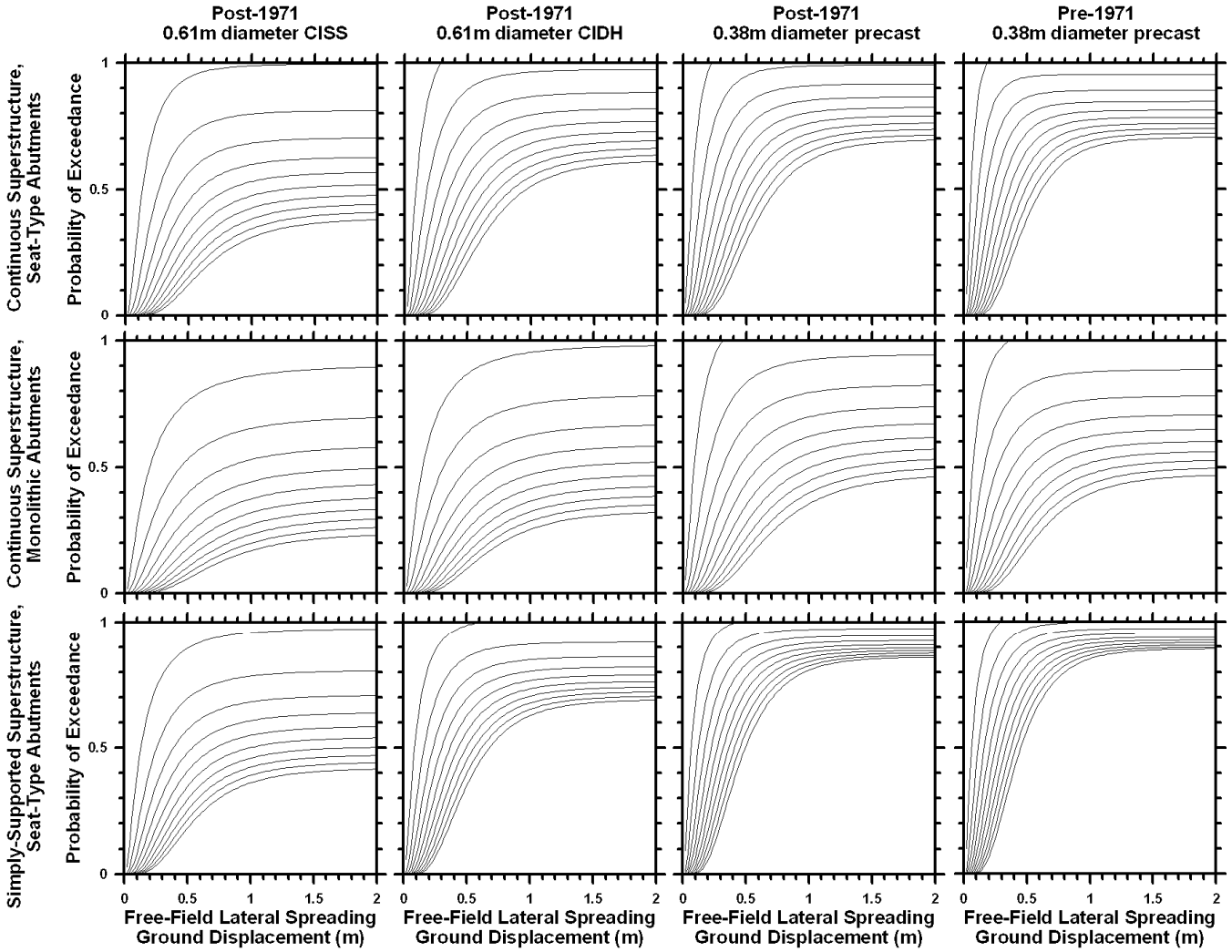

Figure 4.8 Fragility functions for pile cap displacement for bridges with single-column bents. Pile cap displacement from top to bottom is 0.025 m (0.98 in.) to 0.25 m (9.84 in.) in increments of 0.025 m (0.98 in.).

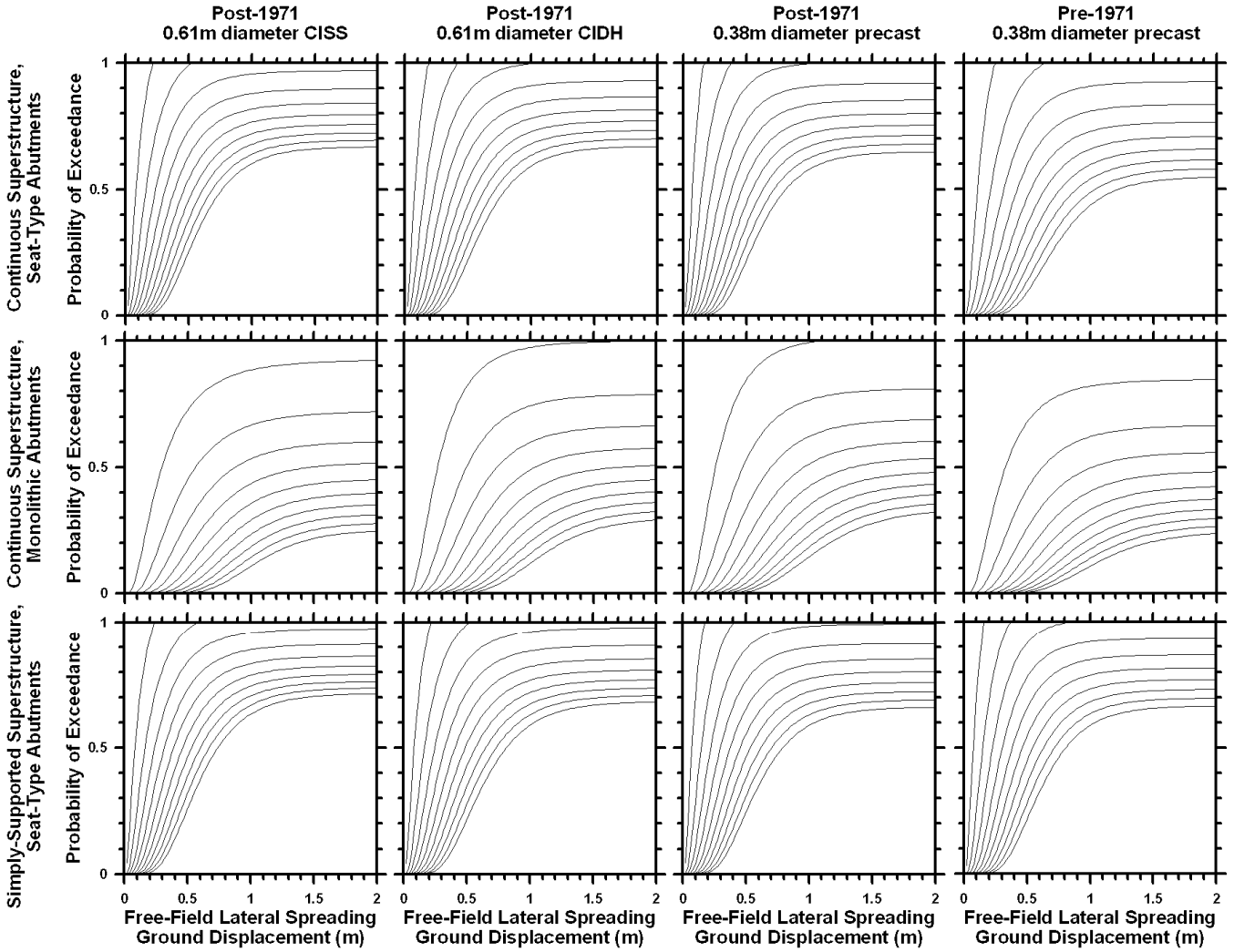

Figure 4.9 Fragility functions for abutment displacement for bridges with multi-column bents. Abutment displacement from top to bottom is 0.025 m (0.98 in.) to 0.25 m (9.84 in.) in increments of 0.025 m (0.98 in.).

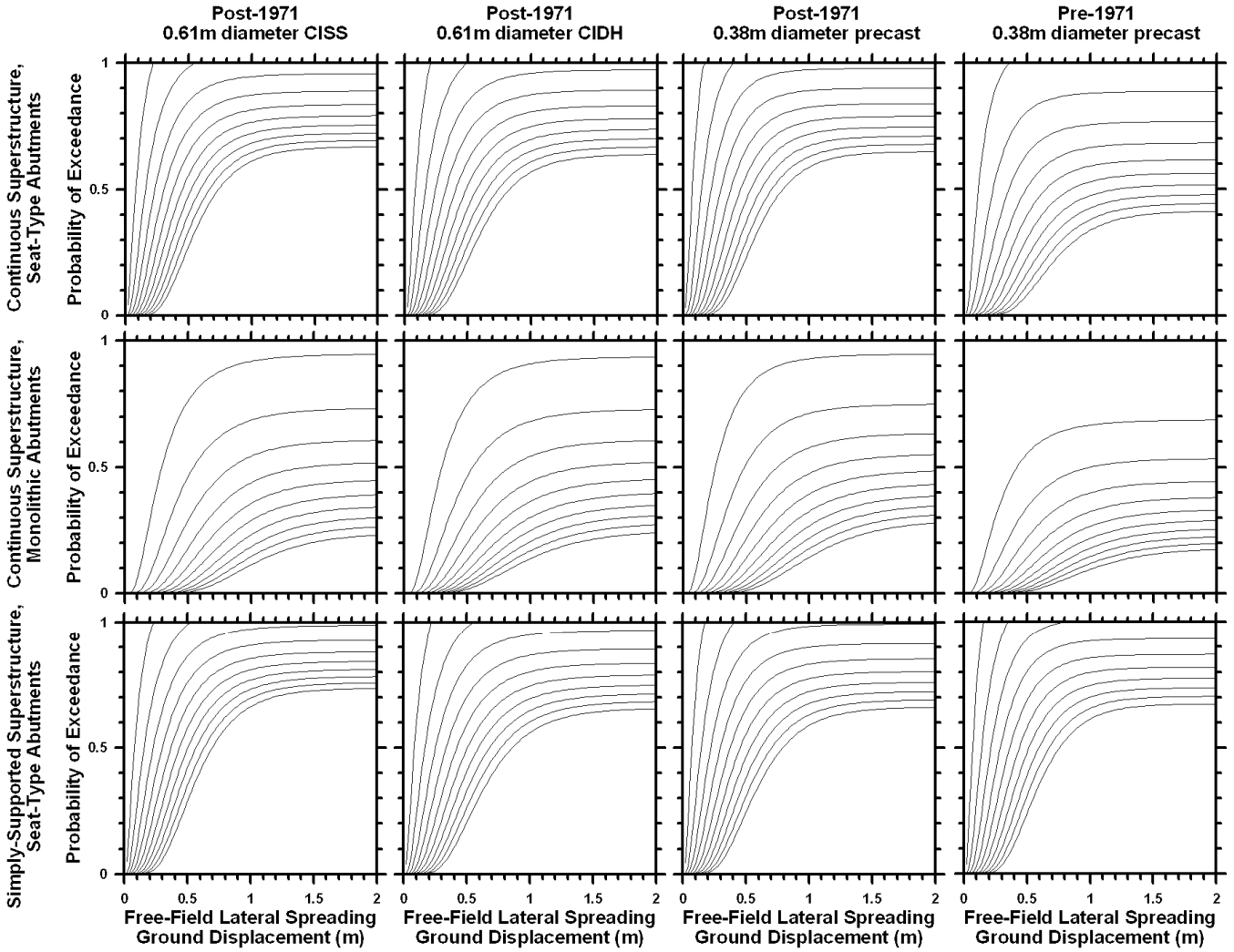

Figure 4.10 Fragility functions for abutment displacement for bridges with single-column bents. Abutment displacement from top to bottom is 0.025 m (0.98 in.) to 0.25 m (9.84 in.) in increments of 0.025 m (0.98 in.).

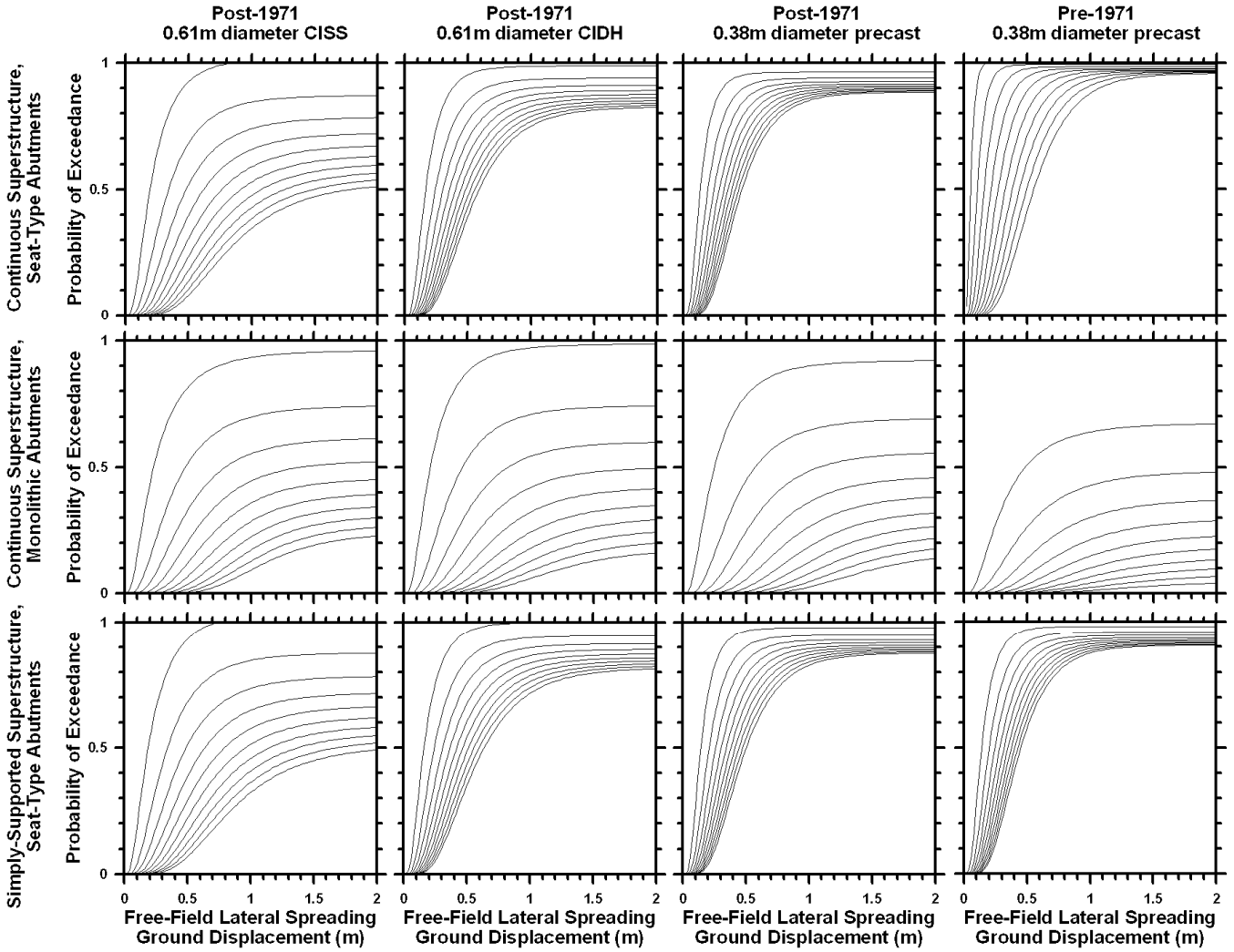

Figure 4.11 Fragility functions for abutment rotation for bridges with multi-column bents. Abutment rotation from top to bottom is 0.5% to 5% in increments of 0.5%.

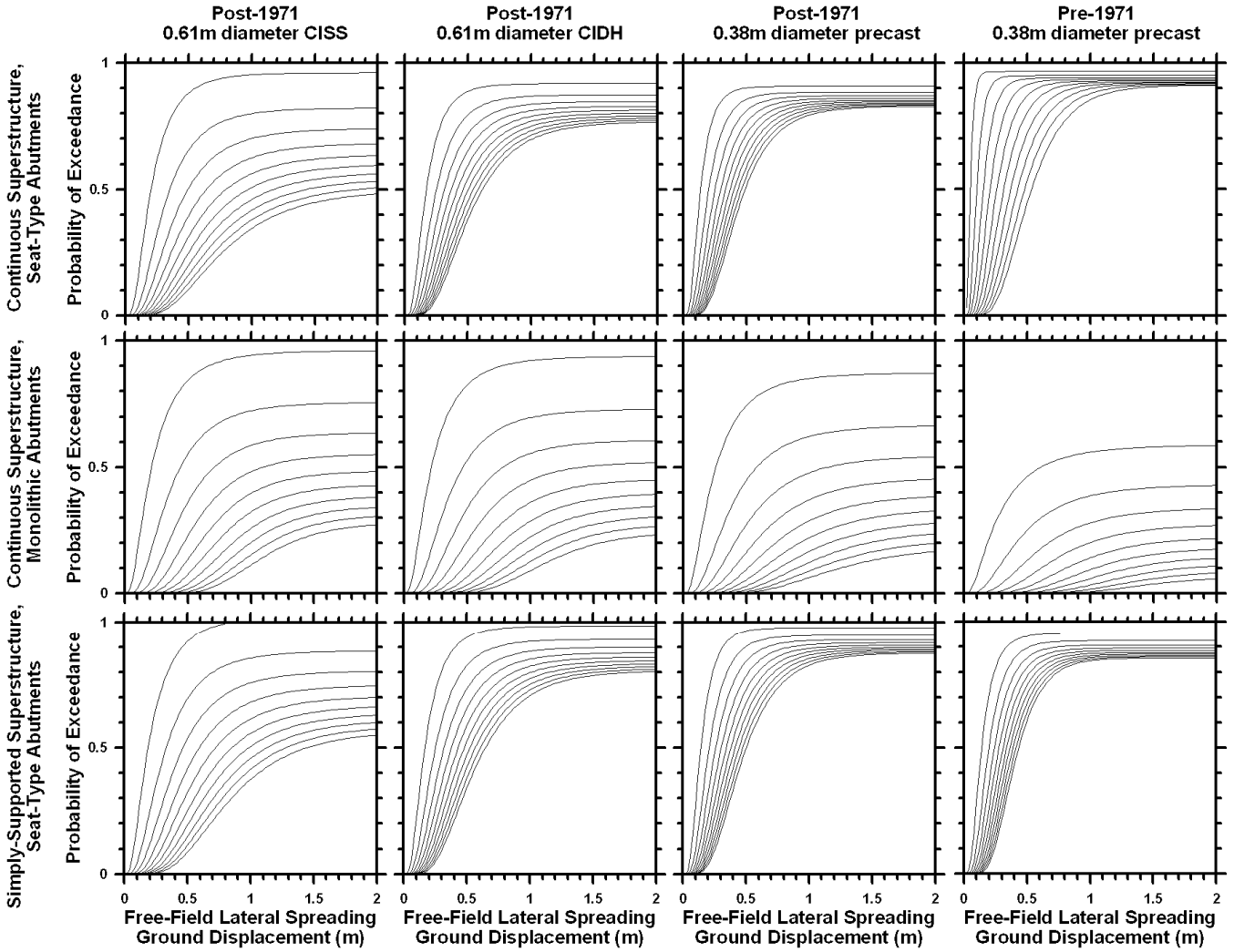

Figure 4.12 Fragility functions for abutment rotation for bridges with single-column bents. Abutment rotation from top to bottom is 0.5% to 5% in increments of 0.5%.

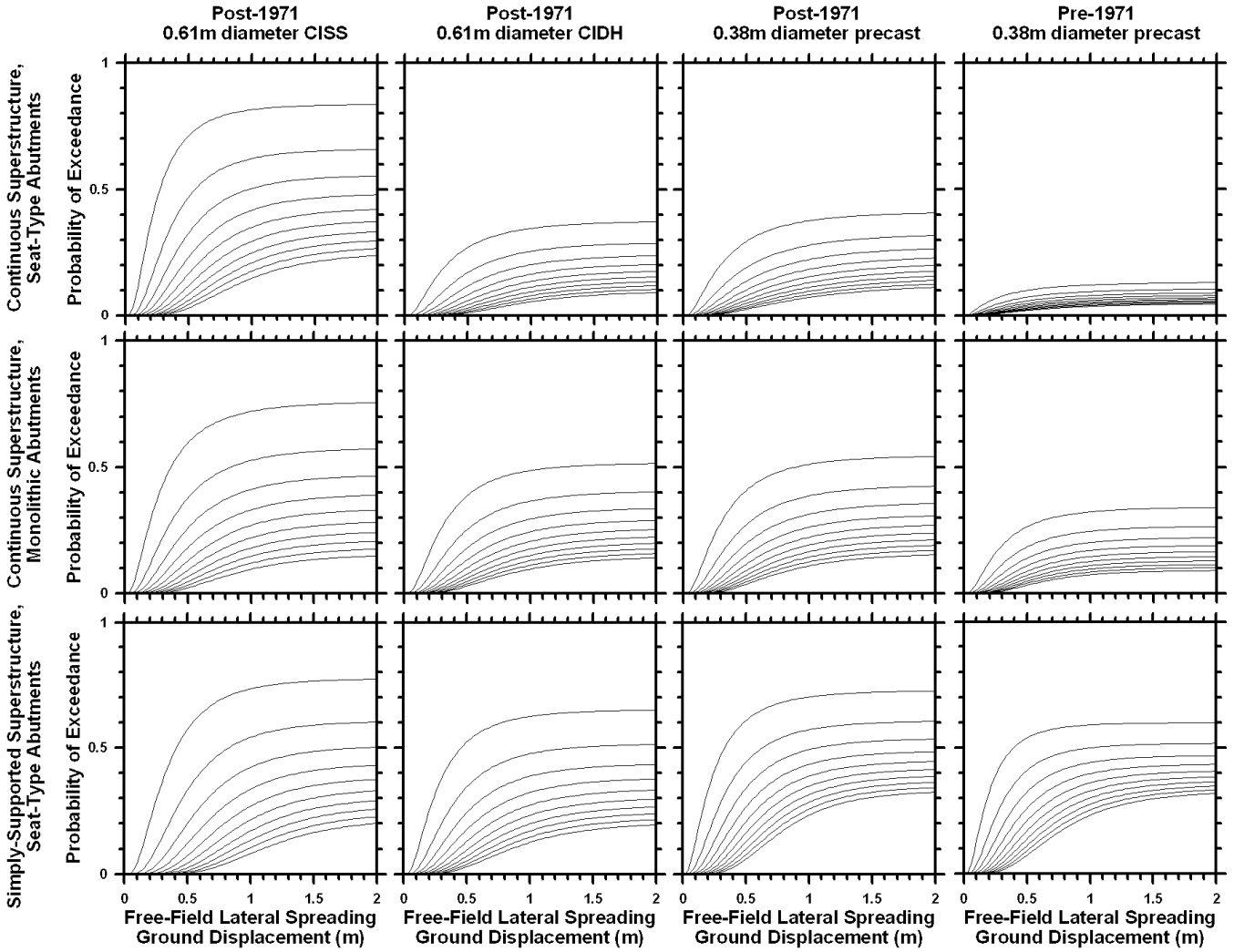

Figure 4.13 Fragility functions for pile cap rotation for bridges with multi-column bents. Pile cap rotation from top to bottom is 0.5% to 5% in increments of 0.5%.

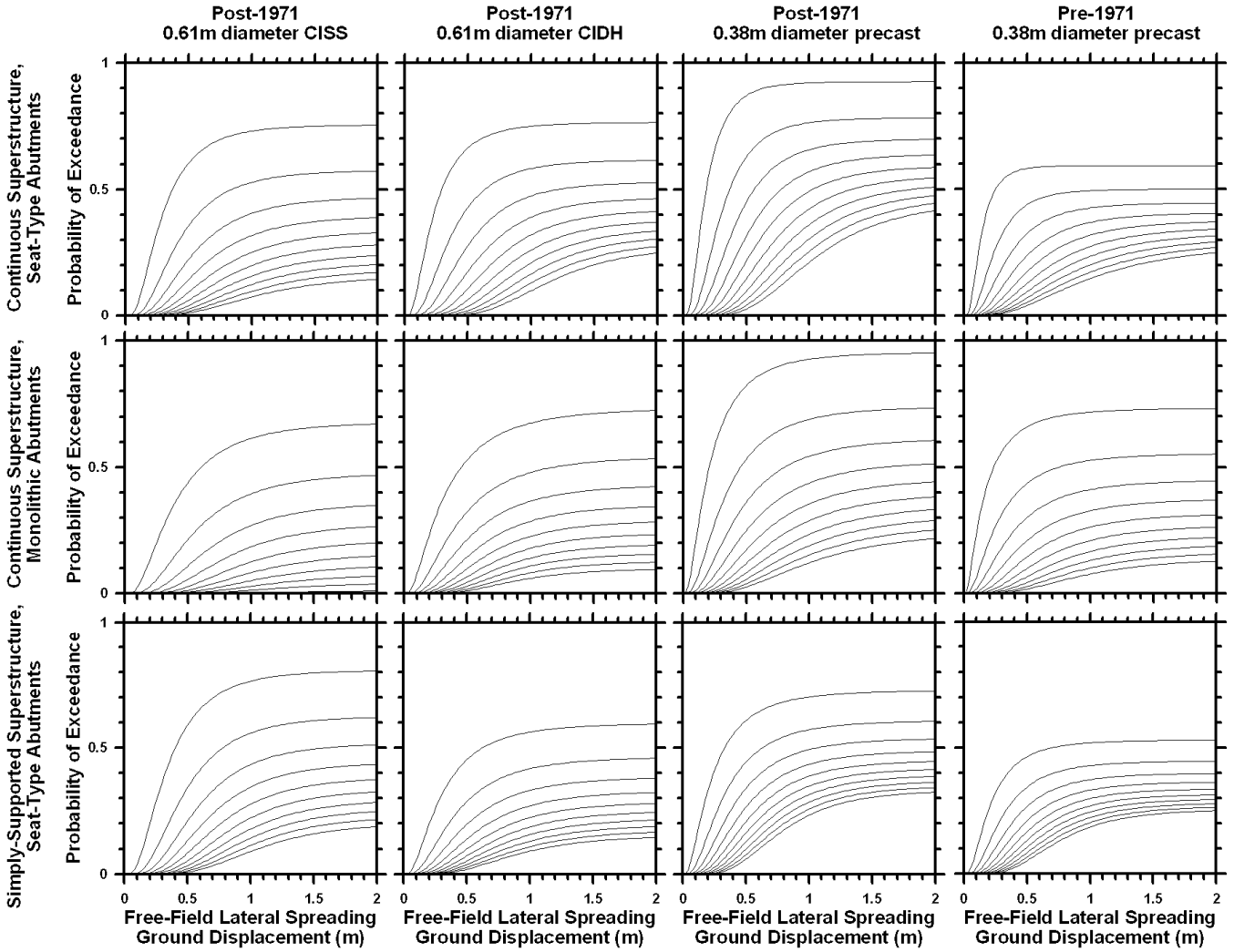

Figure 4.14 Fragility functions for pile cap rotation for bridges with single-column bents. Pile cap rotation from top to bottom is 0.5% to 5% in increments of 0.5%.

The following sections explain some of the trends observed in the fragility functions in Figures 4.5 to 4.14.

4.4.1 Effect of Vintage on the Fragility of the Bridge

Bridges built prior to 1971 have piers with low shear reinforcement and lower yield moment (and shear capacity) relative to the new vintage bridges. The relatively weak piers result in higher mobilized curvature ductility in the pier columns for a given free-field ground displacement compared with the newer-vintage bridges. The older vintage bridges were supported on pile foundations with lower flexural capacity compared to newer vintage bridges. However, the fragility functions for pile cap displacement are similar to the post-1971 bridges, with the same diameter (but slightly stronger) piles. This trend likely reflects that the smaller-diameter piles are poorly suited to resisting lateral spreading demands and a slight increase in capacity provides little benefit. However, the larger-diameter CIDH and CISS foundations exhibited lower cap displacements. Pile cap rotations were slightly lower for the pre-1971 vintage bridges with single-column bents. The cause of this behavior is based on the following observations: (1) pile cap rotation is caused by axial failure of the piles; (2) axial failure of the piles requires a certain amount of lateral load to be transferred from the laterally spreading soil; (3) the pre-1971 piles yield at relatively small ground displacements; and (4) yielding of the piles prevents axial failure of the pile tips thereby reducing pile cap rotation. Hence, the low pile cap rotation should not be considered a sign of good performance because these pile groups are likely to exhibit large translations.

4.4.2 Effect of Structure Type on the Fragility of the Bridge

Differences in the connection between the pier columns and superstructure (continuous or simply supported spans), and differences in abutment type (seat-type or monolithic) has a significant impact on the fragility functions. Pier columns for the simply supported bridges are free to rotate at the top; therefore, the pier columns are more flexible relative to a continuous bridge with double fixity at the top and bottom connections. This flexibility results in lower mobilized curvature ductility for a given amount of displacement, hence the fragility functions for pier column curvature ductility are lowest for bridges with simply supported spans. However, multiple case histories have shown that bridges with simply supported spans are vulnerable to

lateral spreading due to unseating rather than flexural failure of the pier columns. Hence, pile cap displacement may be a more relevant EDP for characterizing collapse potential of these bridges. The fragility functions indicate that pile cap displacements are largest for bridges with simply supported spans, which was expected.

Bridges with continuous superstructures and multi-column bents are typically designed with a pin connection between the pier columns and pile caps, whereas bridges with single-column bents are designed with fixed-fixed connections to avoid a collapse mechanism in the transverse direction. Furthermore, the capacity of the pier columns in a multi-column bent tends to be higher than the capacity of a single-column. As a result, bridges with multi-column bents exhibit lower curvature ductility for a given amount of lateral spreading ground displacement than their single-column counterparts.

4.4.3 Effect of Pile Types on the Fragility of the Bridge

The effect of the pile type is quite clear in the fragility functions. Larger-diameter, stronger piles result in lower mobilized pier column curvature ductility and pile cap displacement. These two EDPs are probably the most relevant for understanding damage potential: large diameter piles are beneficial. Larger-diameter piles may actually increase pile cap rotation compared with weaker piles simply because more load is transferred to the pile foundation, thereby increasing the chance that the pile tips will fail in compression or pull out thereby causing large cap rotations.

4.5 CORRELATION TABLES

Mobilized EDPs are correlated for a given ground displacement. This is intuitive as pile cap displacement is correlated with pile cap rotation since the deformation mechanism involves both translation and rotation. Correlation can also be more indirect, wherein demands in one component are transferred to another component by axial stresses in the superstructure. For example, abutment displacement is correlated with pile cap displacement for bridges with continuous superstructures, but not for bridges with simply supported spans. Quantifying the correlation among EDPs is important when a vector of EDPs is used to define a specific damage state. For example, one may choose to define a damage state as being a pile cap displacement larger than 0.3 m (11.81 in.) and a pier column curvature ductility larger than 4 and an abutment

displacement larger than 0.1 m (3.94 in.). To define the probability of exceedance of this vector of EDPs, correlation among the EDPs must be quantified and included.

Correlation coefficients were computed from the sample of the natural logarithms of the EDP values at various free-field ground displacements for each class of bridge. The coefficients were found to be basically independent of vintage and pile type, but dependent on structural configuration and weakly dependent on free-field ground displacement. A representative free-field ground displacement of 0.80 m (31.50 in.) was selected. Correlation coefficients tended to be lower for lower free-field ground displacements, reaching a plateau around 0.80 m (31.50 in.). Tables 4.11, 4.12, and 4.13 present correlation coefficients among EDPs for the different structural configurations.

Table 4.11 Correlation coefficients among the natural logarithms of EDPs for bridges with continuous superstructure and seat-type abutments.

	Single-Column Bents						Multi-Column Bents					
	Abutment Disp	Abutment Rotation	Cap Disp.	Cap Rotation	Pier Curvature Ductility	Abutment Bearing Strain	Abutment Disp	Abutment Rotation	Cap Disp.	Cap Rotation	Pier Curvature Ductility	Abutment Bearing Strain
Abutment Disp	1.00	0.20	0.56	0.53	0.30	0.68	1.00	0.24	0.47	0.35	0.33	0.61
Abutment Rotation	0.20	1.00	0.12	0.22	0.14	0.07	0.24	1.00	0.14	0.21	0.17	0.10
Cap Disp	0.56	0.12	1.00	0.68	0.35	0.03	0.47	0.14	1.00	0.48	0.42	0.03
Cap Rotation	0.53	0.22	0.68	1.00	0.51	0.01	0.35	0.21	0.48	1.00	0.13	0.03
Pier Curvature Ductility	0.30	0.14	0.35	0.51	1.00	0.06	0.33	0.17	0.42	0.13	1.00	0.02
Abutment Bearing Strain	0.68	0.07	0.03	0.01	0.06	1.00	0.61	0.10	0.03	0.03	0.02	1.00

Table 4.12 Correlation coefficients among the natural logarithms of EDP's for bridges with continuous superstructures and monolithic abutments.

	Single-Column Bents					Multi-Column Bents				
	Abutment Disp	Abutment Rotation	Cap Disp.	Cap Rotation	Pier Curvature Ductility	Abutment Disp	Abutment Rotation	Cap Disp.	Cap Rotation	Pier Curvature Ductility
Abutment Disp	1.00	0.43	0.63	0.58	0.39	1.00	0.47	0.59	0.50	0.36
Abutment Rotation	0.43	1.00	0.14	0.28	0.26	0.47	1.00	0.15	0.29	0.17
Cap Disp	0.63	0.14	1.00	0.67	0.38	0.59	0.15	1.00	0.60	0.50
Cap Rotation	0.58	0.28	0.67	1.00	0.52	0.50	0.29	0.60	1.00	0.47
Pier Curvature Ductility	0.39	0.26	0.38	0.52	1.00	0.36	0.17	0.50	0.47	1.00

Table 4.13 Correlation coefficients among the natural logarithms of EDPs for bridges with simply supported spans.

	Single-Column Bents							Multi-Column Bents						
	Abutment Disp	Abutment Rotation	Cap Disp.	Cap Rotation	Pier Curvature Ductility	Abutment Bearing Strain	Pier Bearing Strain	Abutment Disp	Abutment Rotation	Cap Disp.	Cap Rotation	Pier Curvature Ductility	Abutment Bearing Strain	Pier Bearing Strain
Abutment Disp	1.00	0.40	0.10	0.14	0.20	0.68	0.06	1.00	0.35	0.06	0.12	0.08	0.71	0.08
Abutment Rotation	0.40	1.00	-0.04	0.12	0.12	-0.12	-0.03	0.35	1.00	-0.06	0.14	0.00	-0.10	-0.02
Cap Disp	0.10	-0.04	1.00	0.58	0.37	-0.04	0.41	0.06	-0.06	1.00	0.58	0.42	-0.08	0.37
Cap Rotation	0.14	0.12	0.58	1.00	0.08	-0.11	0.06	0.12	0.14	0.58	1.00	0.03	-0.09	0.07
Pier Curvature Ductility	0.20	0.12	0.37	0.08	1.00	-0.02	-0.11	0.08	0.00	0.42	0.03	1.00	0.04	-0.03
Abutment Bearing Strain	0.68	-0.12	-0.04	-0.11	-0.02	1.00	-0.06	0.71	-0.10	-0.08	-0.09	0.04	1.00	-0.05
Pier Bearing Strain	0.06	-0.03	0.41	0.06	-0.11	-0.06	1.00	0.08	-0.02	0.37	0.07	-0.03	-0.05	1.00

The highest correlation coefficients were observed for bridges with continuous superstructures and monolithic abutments. These bridges have the largest degree of connectivity among components; hence, deformations at one component tend to be associated with deformations at other components due to transmission of demands through the superstructure. Similarly, the lowest correlation coefficients were observed for bridges with seat-type abutments and simply supported spans.

The correlation coefficient is a measure of the linear relation between random variables. Some of the EDPs exhibited a more complex nonlinear relationship. For simplicity's sake, however, the authors suggest assuming that the distribution of a vector of EDPs can be characterized as a standard multivariate normal distribution with the covariance matrix computed from the reported correlation coefficients and variances. Closed-form solutions for cumulative probability density functions of multivariate normal distributions do not exist, therefore, the distributions must be computed numerically. One useful approach involves a Monte Carlo simulation, where correlation can be preserved using Cholesky factorization of the correlation matrix. The authors have deliberately refrained from defining damage states from the EDPs, instead selecting to present the EDP values that permits users to either directly utilize the EDPs in loss estimation or to define their own damage states as an intermediate step.

4.6 EXAMPLE OF APPLICATION OF FRAGILITY SURFACES

This section demonstrates how the fragility functions may be utilized for a specific site where limited structural information is available (i.e., enough is available to place the bridge in one of the classification systems presented in this report, but not enough to run a bridge-specific structural analysis). The example problem consists of a probabilistic seismic hazard analysis

(hazard curve and disaggregation), probabilistic liquefaction evaluation, and probabilistic lateral spreading displacement estimation. The free-field lateral spreading ground displacement hazard curve was integrated with the fragility functions presented here to compute mean annual rate of exceedance of various bridge EDPs due to liquefaction and lateral spreading.

4.6.1 Site and Seismic Hazard Analysis

A site in Santa Monica, California (118.492°W, 34.015°N), was selected for this example problem. This is the same site analyzed by Kramer and Mayfield (2007), which provides a convenient means of validating the liquefaction hazard curve with their results. A probabilistic seismic hazard analysis was performed using OpenSHA (Field et al. 2003), with Vs_{30} = 300 m/sec. The seismic hazard curve and magnitude disaggregation are shown in Figures 4.15 and 4.16. The soil profile at the site consists of a 2.0 m- (6.56 ft-) thick nonliquefied crust with unit weight γ = 18 kN/m^3 lies over a clean liquefiable sand with $(N_1)_{60}$ = 10. The ground gently slopes at an angle of β = 2° and can be reasonably represented as an infinite slope.

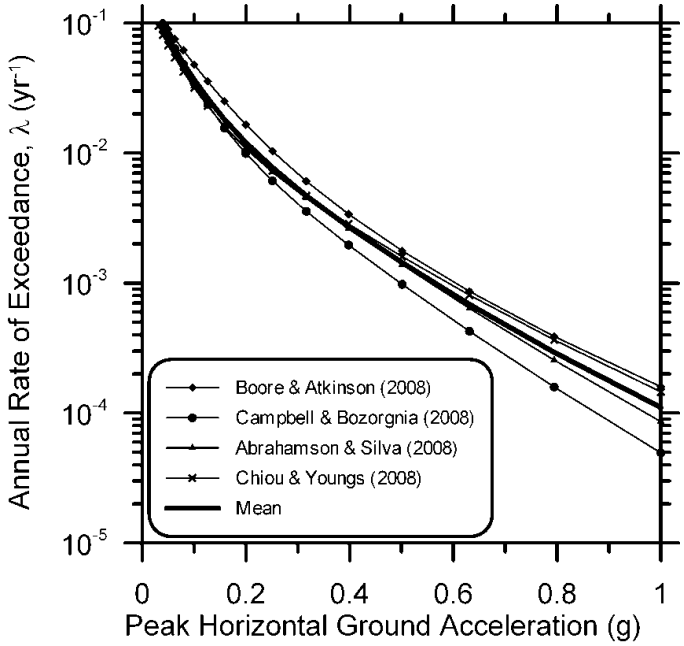

Figure 4.15 Hazard curves from probabilistic seismic hazard analysis of the Santa Monica site.

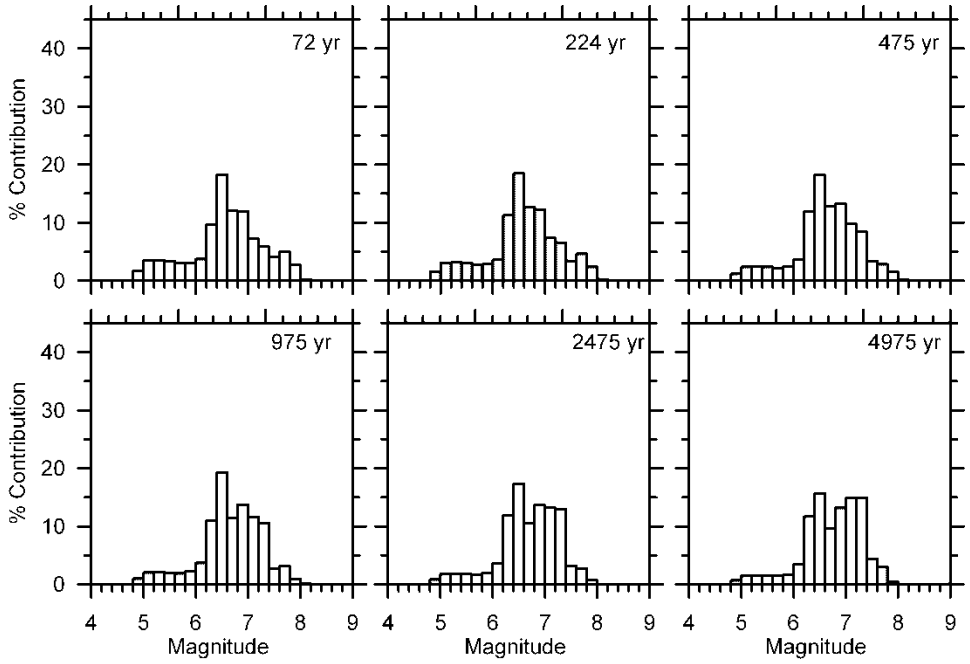

Figure 4.16 Distributions of magnitude contributions to seismic hazard.

4.6.2 Liquefaction Triggering Evaluation

The next step in the analysis is computing the annual rate of exceedance of triggering of liquefaction using the mean hazard curve from Figure 4.15. Kramer and Mayfield (2007) outlined a framework for computing annual rate of non-exceedance of liquefaction that is adopted in this study. The approach is based on the probabilistic liquefaction triggering framework developed by Cetin et al. (2004), using the regression constants that account for measurement/estimation errors. Equation 4.12 defines probability of factor of safety against liquefaction (FS_L) dropping below a value (FS_L^*) given $(N_1)_{60}$, fines content FC cyclic stress ratio CSR_{eq}, moment magnitude $M_{w,}$ and vertical effective stress $\sigma_{v0}^{'}$.

$$P\left[FS_L < FS_L^* \mid PGA, M_w\right] = \Phi\left[-\frac{(N_1)_{60}(1+0.004FC) - 13.79\ln CSR_{eq} - 29.06\ln M_w - 3.82\ln(\sigma_{vo}^{'}/p_a) + 0.06FC + 15.25}{4.21}\right] \quad (4.12)$$

The cyclic stress ratio is defined as $CSR_{eq} = 0.65\left(PGA/g\right)\left(\sigma_v/\sigma_{vo}'\right)r_d$ where the stress reduction factor r_d was treated deterministically (Golesorkhi 1989). Uncertainty in r_d is anticipated to have negligible effect on the hazard analysis because the site is so shallow and r_d is near unity. Peak horizontal ground acceleration is not sufficient to characterize liquefaction

triggering, and magnitude appears as well due to the influence of duration and frequency content. Hence, the hazard calculation must be integrated over PGA and M_w, which requires the disaggregation shown in Figure 4.16. Equation 4.13 defines the probability of non-exceedance of factor of safety against liquefaction, where the summations indicate discrete numerical integration over an adequate range of PGA and M_w values using the binning method, wherein the probability density functions are divided into small slices for numerical integration (after Kramer and Mayfield 2007).

$$\Lambda_{FS_L^*} = \sum_{j=1}^{N_{M_w}} \sum_{i=1}^{N_{PGA}} P\left[FS_L < FS_L^* \mid PGA_i, M_{w_j} \right] \Delta\lambda_{PGA,M_w} \tag{4.13}$$

Figure 4.17 shows the mean annual rate of non-exceedance of factor of safety against liquefaction, which is similar to the Santa Monica site presented by Kramer and Mayfield (2007) (see Figure 9 in their paper). The return period for FS_L<1 is about 100 years (i.e., Λ=0.01 yr^{-1}).

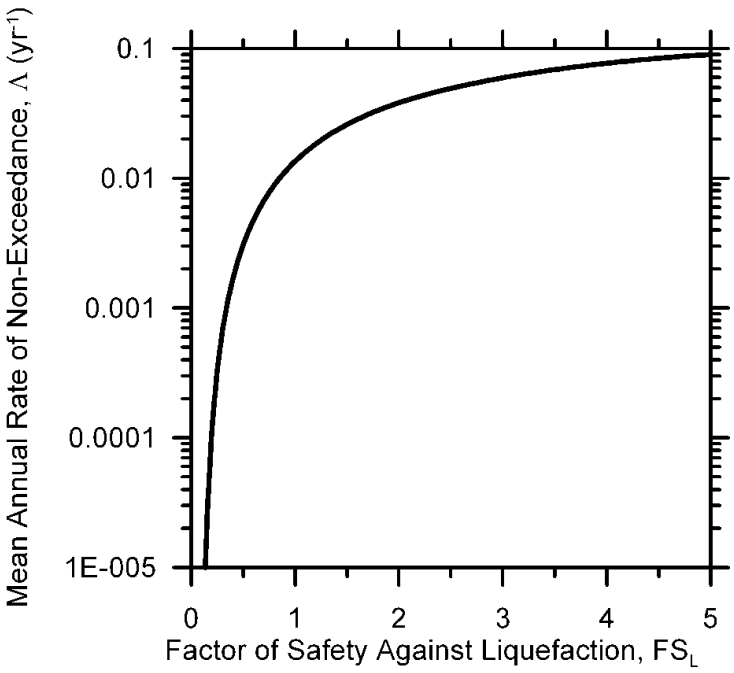

Figure 4.17 Liquefaction triggering hazard curve for the Santa Monica site.

4.6.3 Ground Displacement Evaluation

The next step in the procedure is computing the mean annual rate of exceedance of lateral spreading ground displacement for this site. A number of methods for estimating lateral

spreading displacements exist, and including multiple approaches is important for quantifying the effects of epistemic uncertainty. For simplicity's sake, only a single approach is utilized here although the methodology can easily be extended to other methods. The approach by Bray and Travasarou (2007) for computing permanent ground displacements is combined with the approach by Olson and Stark (2002) for estimating undrained residual strength of liquefied sand. For $(N_1)_{60}$ = 10, the mean value of $s_r / \sigma_v^{'} = 0.1$ based on the Olson and Stark suggestion, hence μ_{sr} = 0.1(2 m)(18 kN/m^3) = 3.6 kPa. Furthermore, the standard deviation is σ_{sr} = 0.025(2 m)(18 kN/m^3) = 0.9 kPa. The static driving shear stress is τ_{stat} = (2 m)(18 kN/m^3)sin(2°) = 1.3 kPa. If the static driving shear stress exceeds the undrained residual strength, then a flow slide occurs and ground displacement is large. Assuming that s_r is log-normally distributed, the probability of a flow slide can be computed using Equation 4.14, where Φ is the standard normal cumulative distribution function.

$$P\left[FlowSlide \mid Liq\right] = \Phi\left[\frac{\ln \tau_{stat} - \ln s_r}{\sqrt{1 - \frac{\sigma_{sr}^{\ 2}}{\mu_{sr}^{\ 2}}}}\right] \tag{4.14}$$

For cases when a flow slide does not occur, the lateral spreading ground displacement is computed using the methodology of Bray and Travasarou (2007) defined in Equation 4.15, where k_y is the yield acceleration. For an infinite slope, $k_y = (s_r - \tau_{stat})/\gamma H\cos\beta$.

$$\begin{aligned}
&P(D=0) = 1 - \Phi\left(-1.76 - 3.22\ln(k_y) + 3.52\ln(\text{PGA})\right)\\
&P(D>d \mid D>0) = 1 - \Phi\left(\frac{\ln(d) - \ln(\hat{d})}{0.66}\right)\\
&\ln(\hat{d}) = -0.22 - 2.83\ln(k_y) - 0.333(\ln(k_y))^2 + 0.566\ln(k_y)\ln(\text{PGA})\\
&\qquad + 3.04\ln(\text{PGA}) - 0.244(\ln(PGA))^2 + 0.278(M_w - 7)
\end{aligned} \tag{4.15}$$

The probability of lateral spreading ground displacement exceeding some value, *d*, conditioned on the occurrence of liquefaction is given in Equation 4.16, where the summation

indicates numerical integration by the binning method over the random variable k_y, which depends on random variable s_r.

$$P(D > d \mid Liq) = \sum_{i=1}^{N_{k_y}} [1 - P(D = 0)][P(D > d \mid D > 0)][1 - P(FlowSlide \mid Liq)]\Delta k_y + P(FlowSlide \mid Liq) \tag{4.16}$$

The mean annual rate of exceedance of free-field lateral spreading ground displacement is computed by inserting the conditional probability defined in Equation 4.16 in the hazard integral, as defined in Equation 4.17.

$$\lambda_D = \sum_{j=1}^{N_M} \sum_{i=1}^{N_{PGA}} P(D > d \mid Liq) P(Liq \mid PGA, M_w) \Delta\lambda_{PGA,M_w} \tag{4.17}$$

Figure 4.18 shows the lateral spreading ground displacement hazard curve for the example problem, which was computed using 30 bins for PGA and k_y, and 17 bins for magnitude, for a total of 15,300 computations. Also shown in Figure 4.18 are several values of ground displacement computed deterministically by taking the PGA associated with some hazard level combined with the modal magnitude (M_w = 6.5 in this case), mean k_y value, and mean lateral spreading displacement value computed using Equation 4.15. In this case, the deterministic approach underestimates the true ground displacement hazard primarily because (1) the modal magnitude was used and higher magnitudes contribute to larger displacements according to a nonlinear relation, and (2) the mean value of the liquefied undrained strength was used and lower undrained strengths produce larger displacements according to a nonlinear relation. Kramer and Mayfield (2007) also showed how inconsistencies between the probabilistic and deterministic approaches to liquefaction triggering evaluation arise due to nonlinearities in the equations, and the mismatch depends on the slope of the hazard curve. These observations indicate that the return period associated with a design level ground motion may not be the same as the return period for a deterministically-computed engineering response parameter, and utilizing the performance-based approach is the only way to provide consistency.

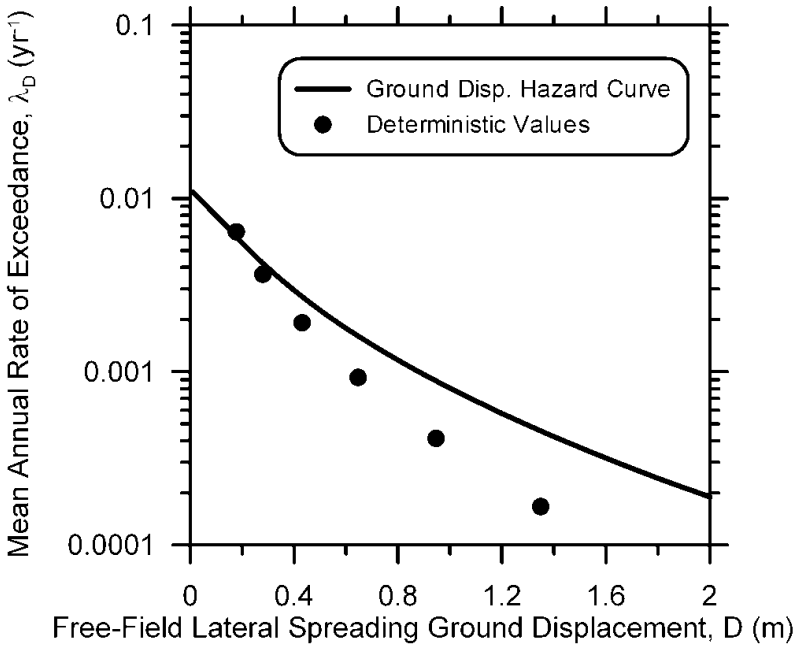

Figure 4.18 Free-field lateral spreading displacement hazard curve.

4.6.4 Bridge Engineering Demand Parameter Evaluation

Example demand fragility surfaces are shown in Figure 4.19 for bridges constructed after 1971 with simply supported spans, seat-type abutments, and 0.61 m (24 in.) CIDH deep foundations supporting the pile caps and abutments. The fragility function equations were inserted into the hazard integral to define the mean annual rate of exceedance of the three EDP values (Equation 4.18).

$$\lambda_{EDP} = \sum_{j=1}^{N_M} \sum_{i=1}^{N_{PGA}} P(EDP > edp \mid D) P(D > d \mid Liq) P(Liq \mid PGA, M_w) \Delta\lambda_{PGA,M_w} \tag{4.18}$$

The EDP hazard curves are plotted in Figure 4.20. The 10% in 50-year EDP values ($\lambda = 2.1\text{x}10^{-3}$ yr^{-1} and a return period = 475 years) are pile cap displacement = 0.1 m (3.94 in), the pier column remains elastic, and abutment displacement = 0.16 m (6.30 in.). These EDP hazard curves provide for better decision-making compared with the standard-of-practice approach of selecting a probabilistic ground motion and performing engineering calculations deterministically.

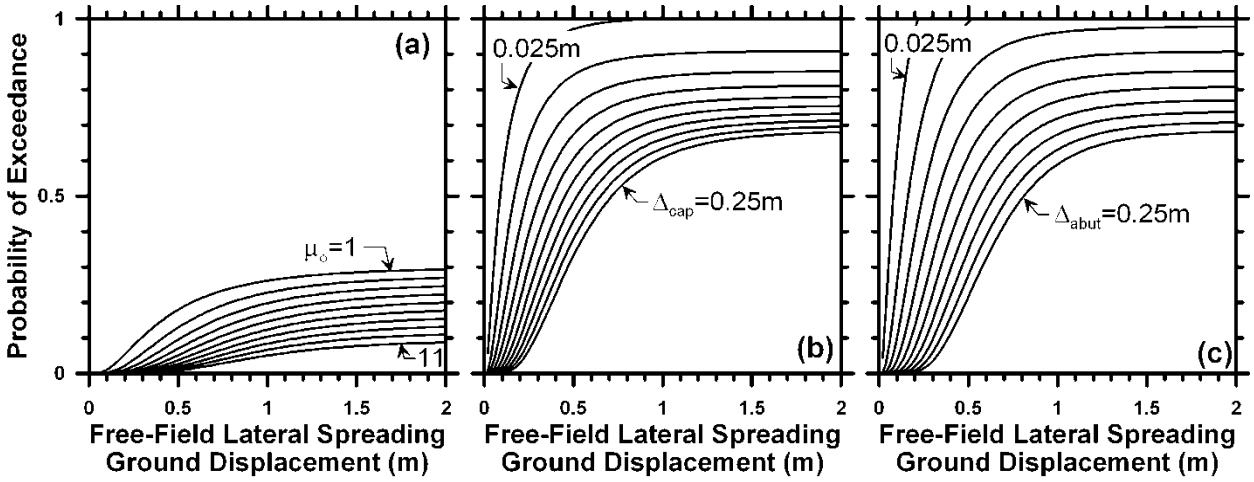

Figure 4.19 Fragility functions for post-1971 bridges with seat-type abutments, simply supported spans, multi-column bents, and 0.6 m- (1.97 ft-) diameter CIDH piles. Engineering demand parameters include: (a) pier column curvature ductility, (b) pile cap displacement, and (c) abutment displacement.

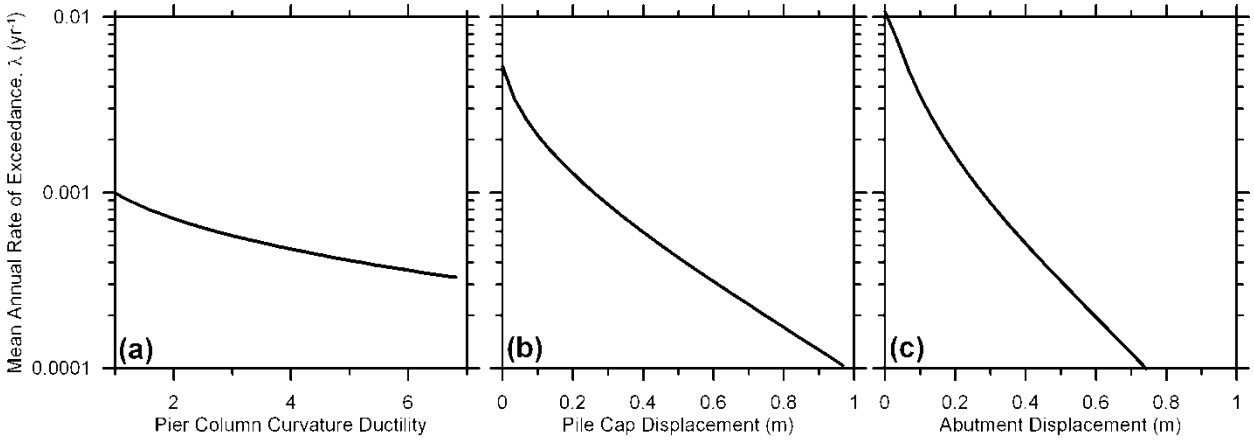

Figure 4.20 Hazard curves for (a) pier column curvature ductility, (b) pile cap displacement, and (c) abutment displacement.

5 Influence of Dynamic Shaking Compared with Lateral Spreading

Early in this project during the evaluation of structural configurations and development of the bridge classification system, a study was performed to investigate how different structural configurations are affected by strong ground motion in the absence of liquefaction compared with cases with liquefaction and lateral spreading. The comparison was made by computing fragility functions for various configurations of bridges subjected to dynamic shaking and also to liquefaction-induced lateral spreading, and then noting how fragility functions depended on structural configuration. The structural configurations, soil properties, and statistical methods used to generate the fragility functions are different from the methods presented in Chapter 3. However, this study is useful to include because it provides a comparison of fragility functions with and without liquefaction, and it shows how various structural configurations are affected differently by strong ground motion and by liquefaction and lateral spreading. These conclusions, potentially important for retrofit decisions, show that both hazard types must be considered simultaneously to arrive at suitable retrofit methodologies for bridges.

5.1 INTRODUCTION

Highway bridges are susceptible to damage due to two significant earthquake-induced mechanisms: seismic shaking and liquefaction-induced lateral spreading. Increased horizontal and vertical load due to dynamic effects under seismic shaking is considered the most dominant cause of bridge damages (Priestley et al. 1996; Basöz and Kiremidjian 1998). The column failure experienced by the Hanshin expressway during the 1995 Kobe earthquake (Kawashima and Unjoh 1997) and bridge collapse of the Cypress Street Viaduct during the 1989 Loma Prieta earthquake (Chen and Duan 2003) are examples of failures caused by excessive seismic loading.

For bridges built on liquefiable soil, earthquake-induced liquefaction and lateral spreading have significant impact on foundation weakening/failure and subsequent structural damage. The span unseating of the Nishinomiya Bridge during the 1995 Kobe earthquake (Wilson 2003) and collapse of the Showa Bridge during the 1964 Niigata earthquake (Yasuda and Berrill 2000) are examples of spectacular failures caused by liquefaction.

Nevertheless, there are many bridges that have performed reasonably well under either seismic shaking or lateral spreading. For example, the Landing Road Bridge suffered only moderate and reparable damage, despite as much as 2.0 m (6.56 ft) of lateral spreading of the surrounding soils during the 1987 Edgecumbe earthquake (Berrill et al. 2001). Study of detailed structural configurations (e.g., column detailing, superstructure type, material, connection, continuity at support and foundation type, etc.) and soil conditions (strength and thickness of any nonliquefiable crust layer, thickness of the liquefiable layer, etc.) render different damage-resistant capability for bridges. Furthermore, the failure mechanisms of bridges exhibited by seismic shaking or liquefaction-induced lateral spreading inevitably show different patterns due to distinct load transferring mechanisms, resulting in differences in damage potential under these two situations. Evaluating the damage potential of different classes of bridges under seismic shaking and liquefaction-induced lateral spreading is, therefore, critical for any design or retrofit strategies.

There are inherent variabilities and uncertainties associated with the seismic responses of bridges due to liquefaction-induced lateral spreading (e.g., structural properties, soil properties, liquefaction mechanism and ground movement, etc.) or seismic shaking (e.g., structural properties, earthquake motion characteristics, etc.). To address this issue, the fragility function method has been used to provide a comprehensive evaluation of bridge response and damage potential under seismic shaking. Fragility functions, which relate the damage probability of bridges to either the intensity measure of earthquake input motions (e.g., PGA) or liquefaction-induced ground displacement, are generated and compared for six types of typical highway bridges in California in order to evaluate the effects of structural characterizations on the damage probability of bridges. Nonlinear dynamic time-history analyses were used to derive the fragility functions of bridges under seismic shaking, while an equivalent static procedure (see Chapter 2) was used to derive the fragility functions of bridges under liquefaction-induced lateral spreading. Important structural and foundation parameters were also identified to provide a comprehensive evaluation of bridge response under earthquake loading.

5.2 FRAGILITY METHODS FOR DYNAMIC SHAKING

Unlike the Monte Carlo method used in previously discussed lateral spreading fragility analysis, the following dynamic shaking fragility analysis employs probabilistic seismic demand model (PSDM) to derive analytical fragility functions using nonlinear time history responses of bridges. The PSDM can be developed using a 'cloud' approach or 'scaling' (like 'stripe') approach (Baker and Cornell 2006) to relate the EDPs to the ground motion intensity measures (IMs). The 'cloud' approach uses unscaled earthquake ground motions. With the 'scaling' approach, all motions are scaled to selective intensity levels corresponding to a prescribed seismic hazard level and incremental dynamic analysis (IDA) is performed at different hazard levels. In this study, the 'cloud' approach is termed as PSDA (Probabilistic Seismic Demand Analysis), while the 'scaling' approach is termed as IDA.

5.2.1 Probabilistic Seismic Demand Analysis

The PSDA method utilizes regression analysis to obtain the mean and standard deviation for each limit state by assuming a logarithmic correlation between median EDP and an appropriately selected IM:

$$EDP = a\left(IM\right)^{b} \text{ or } \ln EDP = \ln a + b \ln IM \tag{5.1}$$

where the parameters a and b are regression coefficients obtained from the response data of nonlinear time-history analyses. The remaining variability in ln(EDP) at a given IM is assumed to have a constant variance for all IM range, and the standard variation is estimated as follows (Baker and Cornell 2006):

$$\xi_{EDP|IM} = \sqrt{\frac{\sum_{i=1}^{n}\left[\ln\left(EDP_i\right) - \left(\ln a + b \ln IM_i\right)\right]^2}{n-2}} \tag{5.2}$$

Subsequently, the EDPs are converted to the damage index (DI) that is compared with the limit states (LS) corresponding to various damage states (DS) dictated by a capacity model. If the DI is the same as the EDP, by further assuming a log-normal distribution of EDP at a given IM, the fragility functions (i.e., the conditional probability of reaching a certain damage state for a given IM) are written as:

$$P\left[DI \geq LS \middle| IM\right] = 1 - \int_0^{LS} \frac{1}{\sqrt{2\pi} \cdot \xi_{EDP|IM} \cdot edp} \cdot \exp\left\{ - \frac{\left[\ln(edp) - \ln\left(a \cdot IM^b\right)\right]^2}{2\left(\xi_{EDP|IM}\right)^2} \right\} d(edp) \qquad (5.3)$$

where $\xi_{EDP|IM}$ is the standard deviation of simulation data from the logarithmic correlation between median *EDP* and *IM* (obtained from Equation 5.2).

5.2.2 Incremental Dynamic Analysis

In contrast to the PSDA method, the IDA method requires more computational effort because of the scaling of earthquake motions to different IM levels, i.e., through increments. However, no *a priori* assumption needs to be made in terms of probabilistic distribution of seismic demand in order to derive the fragility curves. Nonlinear time-history analysis is conducted at every IM level. The occurrence ratio of a specified damage state is computed and directly used as the damage probability at the given IM level, i.e., the damage probability is calculated as the ratio of the number of damage cases n_i at and beyond the damage state i over the number of total simulation cases N at a given IM level (Karim and Yamazaki 2001):

$$P\left[DI \geq LS \middle| IM\right] = \frac{n_i}{N} \quad (i=1 \text{ to } 4) \qquad (5.4)$$

In most cases, IDA fragility curves can be fitted with either a normal cumulative distribution function:

$$P[DI \geq LS \mid IM] = \int_{-\infty}^{IM} \frac{1}{\sqrt{2\pi}\sigma_{IM}} \exp\left[- \frac{\left(im - \mu_{IM}\right)^2}{2\sigma_{IM}^2} \right] d(im) \qquad (5.5)$$

or a log-normal cumulative distribution function:

$$P[DI \geq LS \middle| IM] = \int_0^{IM} \frac{1}{im\sqrt{2\pi}\xi_{IM}} \exp\left\{ - \frac{\left[\ln(im) - \lambda_{IM}\right]^2}{2\xi_{IM}^2} \right\} d(im) \qquad (5.6)$$

where σ_{IM} and μ_{IM} are standard deviation and mean value, respectively, of IM to reach the specified damage state based on the normal distribution, while ξ_{IM} and λ_{IM} are standard deviation and mean value, respectively, of IM to reach the specified damage state based on the log-normal distribution.

5.3 GROUND MOTION AND BRIDGE MODELING

5.3.1 Earthquake Ground Motion Selection and Intensity Measure

Both the PSDA and IDA methods rely on a large number of nonlinear time-history analyses to derive the fragility functions, therefore, a significant number of earthquake records need to be selected so that a conceptually and statistically better prediction of bridge response can be obtained. In this study, 250 sets of earthquake ground motion records were selected from the PEER strong motion database (http://peer.berkeley.edu/smcat), and the records were applied in transverse, longitudinal and vertical directions simultaneously in the time-history analysis.

Figure 5.1 shows the distribution of PGA, peak ground velocity (PGV), spectral acceleration (S_a) at period T=0.5 sec, earthquake magnitude M, and distance to epicenter r (as well as the site conditions of the selected ground motion records). The site conditions are characterized based on the average shear wave velocity to a depth of 30 m (98.43 ft) according to the USGS site classification criteria.

The ground motions are characterized by the IM, and the choice of IM plays a crucial role both in running the fragility analysis and interpreting simulation results. Peak ground acceleration is adopted as the IM for earthquake input in this study, based on the linear consistency criterion suggested by Mackie and Stojadinović (2003) and with the consideration of its efficiency, practicality, and hazard computability as discussed by Padgett et al. (2008).

5.3.2 Damage Index and Limit States

The seismic responses of bridges are depicted and monitored by EDPs. Subsequently, the EDPs are related to the DI for various DSs using their corresponding LSs based on physical phenomenon or theoretical judgment. The fragility function method generally classifies the damage into four levels: slight, moderate, extensive and collapse damage, labeled here as DS 1, 2, 3, and 4, respectively. For conventional highway bridges, columns—the most critical component—are often forced into the nonlinear range under strong earthquake shaking. A number of studies have developed the criteria for DI and corresponding LS based on damage status or loss of load-carrying capacity. Commonly used DI measures for columns are curvature ductility, displacement ductility, and residual displacement, etc., and the four damage states defined by HAZUS (FEMA 2007) are usually adopted. In this study, the curvature ductility, μ_κ,

is adopted as DI for columns, and the corresponding LS values are those adopted by Choi et al. (2004).

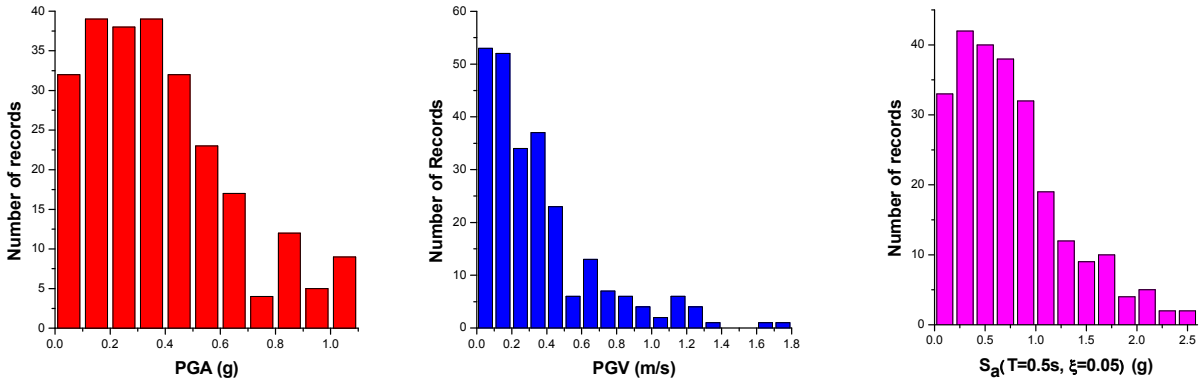

(a) *PGA* (b) *PGV* (c) S_a *(T=0.5s, ξ=0.05)*

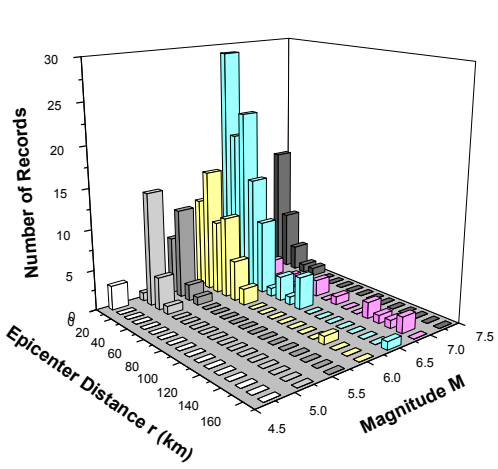

(d) Magnitude and epicenter distance (*M*, *r*)

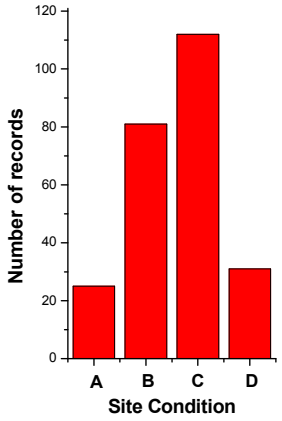

(e) Site condition

Figure 5.1 Characteristics of selected earthquake ground motion records (horizontal component).

For bridges with seat-type abutments or isolation devices, the bearings might experience large displacements, resulting in damage of isolation devices and neighboring structural members in addition to damaging the columns. The damage states of isolation devices are determined based on experimental observation, as well as considering resulting pounding and unseating. Typically, either bearing displacement or shear strain is used to describe the damage states. Here, generic isolation bearings with mechanical properties resembling lead rubber bearings were used at the seat-type abutments and pier tops (if applicable), and the shear strain was used to capture the damage states in bearings. Table 5.1 lists the EDP, DI, DS, and corresponding LS definitions for these two components. Although the modern isolation bearings can experience shear strain up to 400% before failure, such large shear strain will result in large displacement, possibly causing significant pounding or unseating. Therefore, a maximum 250% shear strain is adopted, corresponding to 0.25 m (9.84 in.) maximum displacement.

During earthquake shaking, piers and bearings may exhibit different component damage states that combine into a comprehensive damage state for the bridge system, which is hard to describe by only one component DI. Previous studies suggest that system fragility can be derived based on functionality or repair cost after earthquake (Mackie and Stojadinović 2007), or it can be generated based on component level fragility functions (Nielson and DesRoches 2007). In this study, a composite DS was designed (see Equation 5.7). The proportion ratio 0.75 for columns and 0.25 for bearings was determined synthetically by considering the relative component importance for load-carrying capacity during earthquakes and the repair cost after earthquakes.

$$DS_{System} = \begin{cases} \text{int}\left(0.75 \cdot DS_{Pier} + 0.25 \cdot DS_{Bearing}\right) & DS_{Pier}, DS_{Bearing} < 4 \\ 4 & DS_{Pier} \text{ or } DS_{Bearing} = 4 \end{cases} \tag{5.7}$$

Table 5.1 Definition of component level damage index of columns and bearings.

Component	EDP or DI definition	Slight (*DS*=1)	Moderate (*DS*=2)	Extensive (*DS*=3)	Collapse (*DS*=4)
Columns[+]	Section ductility μ_k	μ_k >1	μ_k >2	μ_k >4	μ_k >7
Bearings	Shear strain γ	γ>100%	γ>150%	γ>200%	γ>250%

[+]Choi et al. 2004

5.3.3 Bridge Types

Typical bridge designs were evaluated by reviewing the drawings of numerous bridges obtained from the Caltrans. Six bridge models (see Figure 5.2) were selected to represent the most common highway bridge types, with different variations of a multi-span straight bridge with single column construction. The bridge with pier bent (i.e., multiple columns), though not considered in this chapter, is another common type of construction in California and has been studied in Chapter 4 for lateral spreading scenarios. Model E1 represents a continuous bridge with monolithic abutments. In contrast to model E1, models E2-E6 all have seat-type abutments. Model E2 represents a continuous bridge with seat-type abutments. Model E3 is similar to Model E2 except that it has an expansion joint at the center of the mid-span. Model E4 is isolated at the pier tops with continuous deck, while model E5 has an expansion joint at the mid-span in addition to the isolation. In model E6, simply supported connections are adopted at the pier top, and the adjacent decks are pin connected to prevent collapse. The structural properties of bridge components are taken from two real Caltrans bridges that were built before 1971 and are therefore characteristic of older-vintage bridges designed before adoption of modern seismic codes. A previous study (Zhang et al. 2008) has shown that the location of expansion joints, if kept in a reasonable and practical range, has no obvious effect on the seismic response of bridges with straight alignment and symmetrical geometry, so here its location was not varied.

5.3.4 Numerical Models of Bridges

Numerical models were generated using software platform OpenSees. Elastic beam elements were used for the bridge deck, and nonlinear fiber section beam elements were used to model the

columns. The RC column was 1.83 m (72 in.) in diameter is reinforced with twenty-six No. 11 longitudinal bars and No. 4 transverse reinforcements at 0.30 cm (12 in.) intervals. Figure 5.3a plots the force-displacement relationship of a single column from the pushover analysis using fiber elements in OpenSees. The force-displacement relationship of the column can be roughly approximated with a bilinear regression curve. Hence the column has an elastic stiffness of $K_{1,C}$=1.10×10^{5}kN/m and characteristic strength of Q_C=1.36×10^{3}kN as indicated by the bilinear

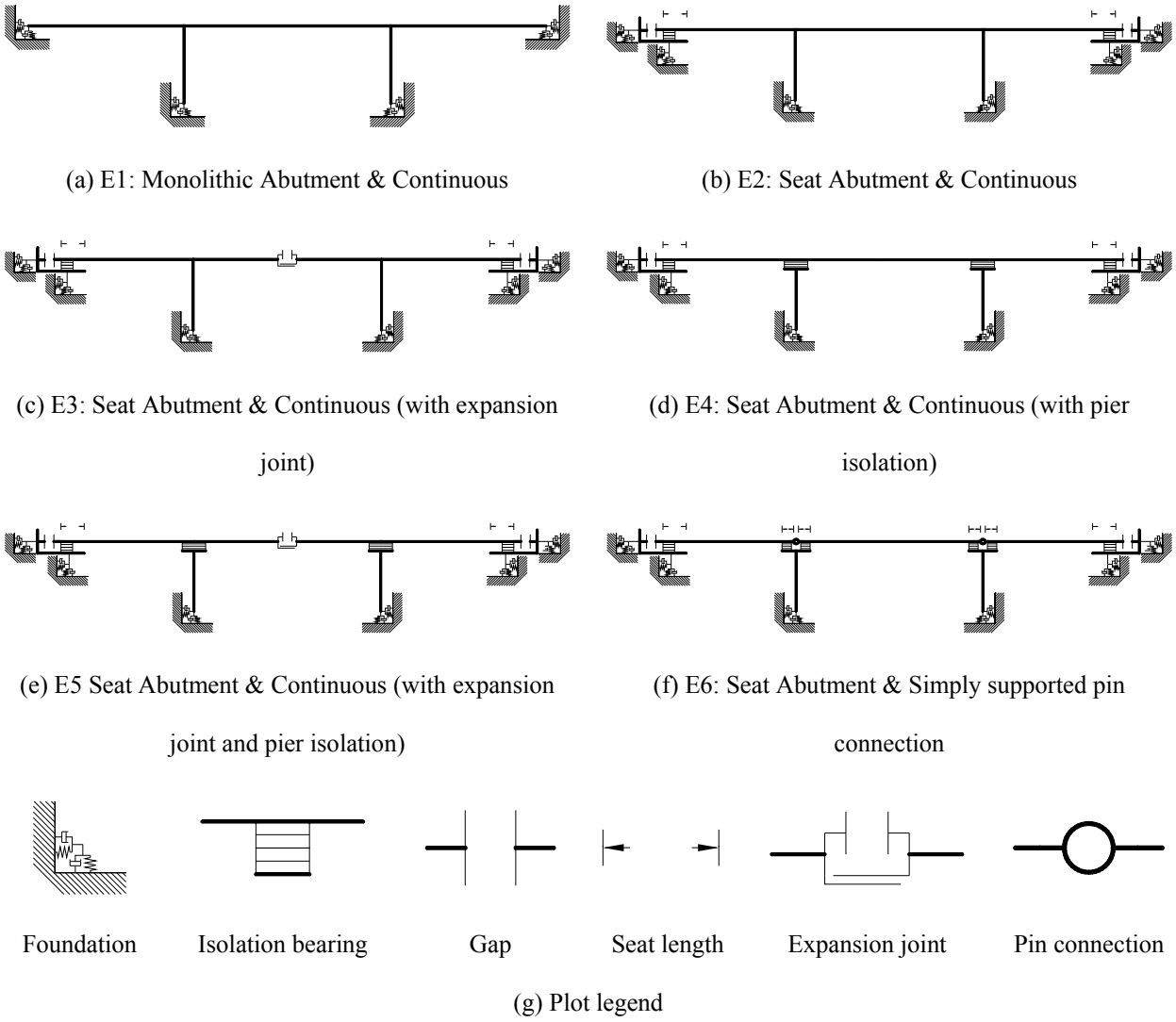

Figure 5.2 Sketches of the six bridge models.

curve; this represents a typical design for bridges built before 1971. The middle span is 30 m (98.43 ft) long while the other two spans are 20 m (65.62 ft) each. Seismic isolation bearings were modeled with bilinear springs for horizontal load-carrying properties and elastic springs for vertical properties (Kumar and Paul 2007). The bearing parameters were selected based on the optimum design parameters presented in Zhang and Huo (2009). Figure 5.3b plots the force-displacement relationships of the bearing and its modeling parameters, $K_{1,B}$, $K_{2,B}$, and Q_B. Gap elements were employed to simulate the gap closing and the effects of pounding between the deck and abutments. Figure 5.3c shows the force-displacement relationship of the gap element with a 0.0254 m (1 in.) opening. The seat length [maximum 0.25 m (9.84 in.)] during earthquake shaking and lateral spreading was monitored and the analysis terminated if the seat length reduces to zero, i.e., unseating is impending. The SSI was simulated with springs and dashpots representing the stiffness and damping of foundations supporting columns and embankment at end abutments, whose properties were determined by the methods developed by Zhang and Makris (2002a, b). Table 5.2 summarizes the properties and modeling parameters of key bridges components.

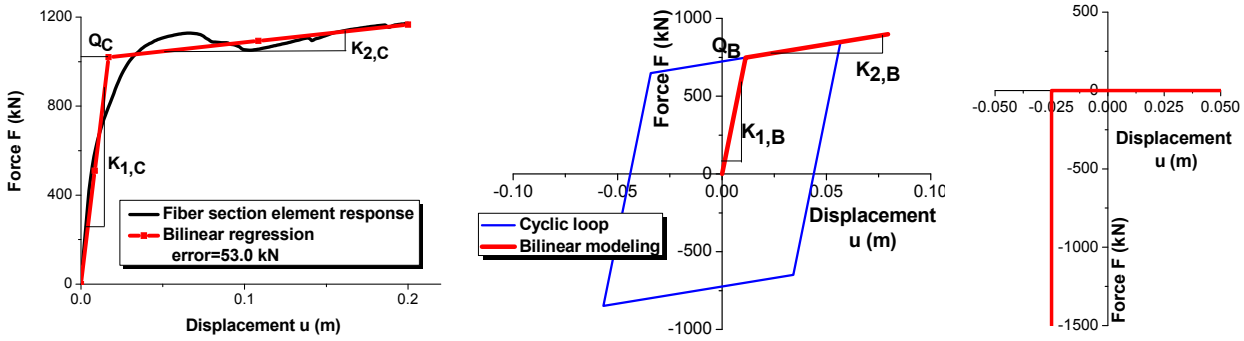

(a) Column (b) Isolation bearing (c) Gap

Figure 5.3 Force-displacement relationships of column, isolation bearing, and gap element.

Table 5.2 Bridge component properties and modeling parameters.

	Deck	Columns	Bearings	Gaps
Properties	Box girder with spans of 20m/30m/20m	Circular section (d=72in) with 26#11 (longitudinal) and #4@12in (transverse) reinforcement	Elastomeric rubber bearing for seat-type abutments and isolation at top of pier	Gap distance: 0.025m
Modeling and parameters	Elastic beam elements	Fiber section beam elements $K_{1,C}=1.10\times10^5 kN/m$ $Q_C=1.36\times10^3 kN$	Bilinear (horizontal) and linear (vertical) springs. $Q_B=0.55Q_C$ $K_{1,B}=0.60K_{1,C}$ $K_{2,B}=K_{1,B}/30$	Gap elements: Δ_y=-0.025m

5.4 FRAGILITY ANAYSIS FOR DYNAMIC SHAKING

5.4.1 Analysis Example for Model E1

Model E1 was studied first as an example to demonstrate the implementation of the PSDA and IDA methods. Using the PSDA method, Figure 5.4a shows the data points of the computed section curvature κ (rad/m) (*EDP*) versus the corresponding PGA (*IM*) of unscaled ground motions in logarithmic scale; a linear regression provides a reliable relationship between *IM* and *EDP* and an estimation of the standard deviation. Based on Equations 5.1 and 5.2, the parameters of the regression were obtained (a=0.00331 and b=1.866) while the standard deviation of the distribution was computed as $\xi_{EDP|IM}$=0.360. With Equation 5.3, the fragility data at each PGA level of the specified damage state could be calculated, and the fragility functions were then derived with these data, as shown in Figure 5.4b.

With the IDA method, the 250 sets of records were scaled to 25 PGA levels from 0.06*g* to 1.50*g* in 0.06*g* increments. The fragility functions were then derived following Equation 5.4, with the data from 6250 (250 × 25) nonlinear dynamic analyses. Figure 5.5a shows the 'raw' fragility curves and the regression curves generated using cumulative normal (Equation 5.5) or lognormal (Equation 5.6) distribution functions. Both normal and log-normal distributions yielded similar results compared to the raw data. Figure 5.5b compares the fragility curves generated by the PSDA and IDA methods, respectively. Note that the two methods yield comparable results at slight and moderate damage states, but different results for extensive and

collapse states. The IDA method is generally more reliable than the PSDA method because the fragility functions are based on many more simulation cases and no pre-assumed relationship between the EDP and IM is assumed [some possible bias from the record scaling process has been pointed out by previous studies (Luco and Bazzuro 2007)]. Some errors or bias are introduced into the PSDA method due to a single assumption relating EDP to IM despite the damage states. In particular, the lack of large intensity earthquake motion records (as shown in Figure 5.1) may introduce errors to the PSDA results as the input motions are biased toward smaller intensity. This imbalance results in the discrepancy between PSDA and IDA methods observed in Figure 5.5b.

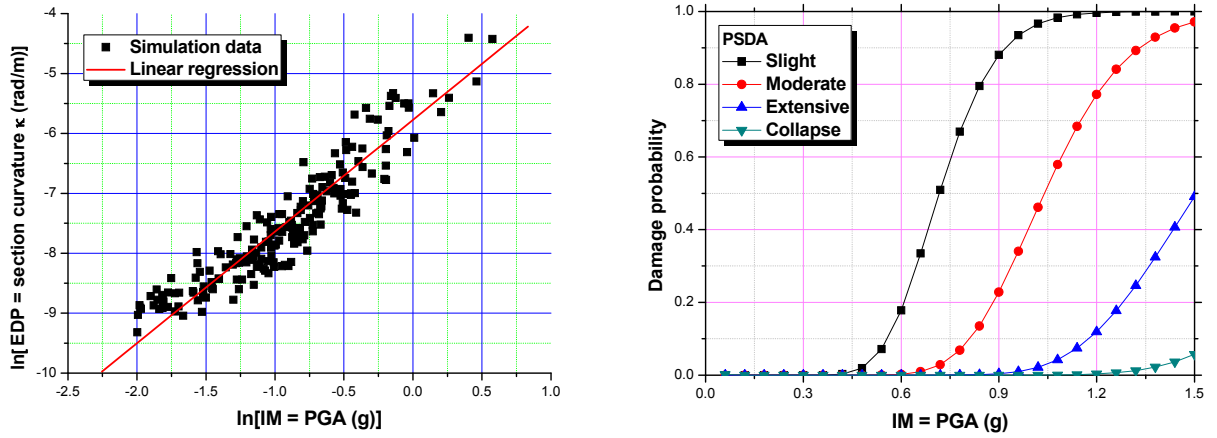

(a) Data points and bilinear regression

(b) Fragility curves

Figure 5.4 PSDA fragility analysis of Model E1.

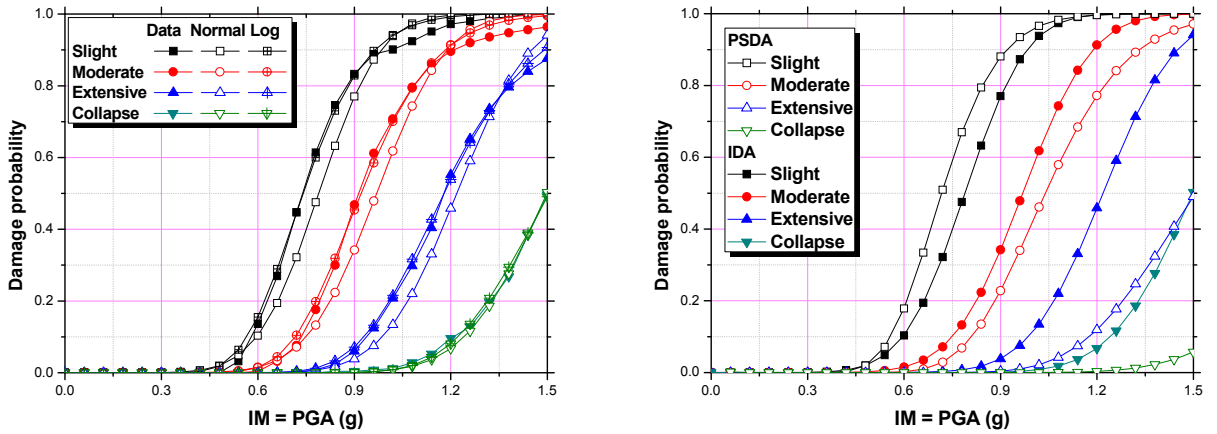

(a) IDA fragility curves and regression

(b) Comparison of PSDA and IDA

Figure 5.5 Fragility functions of Model E1 using PSDA and IDA methods.

5.4.2 Fragility Functions of Different Bridge Types

Taking into consideration the possible bias of PSDA, the following analyses utilize the IDA method to generate fragility curves for all six bridge models shown in Figure 5.2. Figure 5.6 compares the fragility curves of six different bridge models considered in this study for slight, moderate, extensive, and collapse damage states. The results show that models E2 and E3 perform the least favorably among the six bridge types. The more severe damage seen in models E2 and E3 is attributed to the seat-type connection at abutments, which leads to smaller dynamic loads carried at abutments, resulting in more loads being transferred to the columns. In contrast to the seat-type abutment, the isolation bearings at the pier top reduced the damage experienced by the columns, which is reflected by much lower fragility curves of models E4 and E5 than for models E2 and E3. The expansion joint of model E3 did not make much difference in terms of the bridge response compared to model E2. A similar trend is seen between models E4 and E5 for slight and moderate damage states. However, the expansion joint did make the isolated bridge more vulnerable to extensive and collapse damage, possibly attributable to the pounding between adjacent segments. Among all the models, model E1 performed the best for smaller earthquake intensities (i.e., PGA smaller than 0.7*g* for slight and moderate damage states and 1.0*g* for the extensive damage state), while model E6 performed the best for higher earthquake intensities for slight, moderate, and extensive damage states. The simply supported connection in model E6 reduced the seismic energy transferred from the deck to the column significantly, hence protecting the column from greater damage potential. The pin connection also limited extreme damage to the bearings and the span collapse under larger earthquakes. Both factors contributed to the superior performance of model E6 under larger earthquakes. At the collapse damage state, model E1 (a continuous bridge with integral abutments) is clearly the best structural type. Figure 5.6 shows that the structural characterizations of bridges play an important role in defining the damage potential of bridges under earthquake shaking.

5.5 COMPARISON OF FRAGILITY RESULTS FOR DYNAMIC SHAKING AND LATERIAL SPREADING

5.5.1 Simplified Procedure to Derive Fragility Functions for Lateral Spreading

Bridges can also experience liquefaction induced lateral spreading when subject to strong earthquakes. Embedded bridge components can attract large lateral loads from laterally spreading soil, particularly when a nonliquefied crust spreads laterally on top of underlying liquefied layers. The aforementioned six bridge models were then analyzed for lateral spreading cases, and fragility curves were derived to compare the similarities and differences between purely seismic dynamic shaking and lateral spreading. The equivalent static analysis procedure discussed in Chapter 2 was employed to simulate the bridge response under liquefaction-induced lateral spreading. In this procedure, free-field lateral spreading demands were imposed as displacements on the free ends of *p-y* springs attached to the bridge foundation, as shown in Figure 5.7. Inertia forces, which can occur simultaneously with lateral spreading forces, were imposed on the superstructure at connections with the piers and abutments, and also at the pile caps. The imposed inertia forces were consistent with the imposed free-field lateral spreading displacements based on the Newmark sliding block method (Brandenberg et al. 2007a). By analogy with the IDA method presented in the previous section, this analysis approach for lateral spreading is considered an "Incremental Static Analysis," since free-field ground displacements are incrementally increased while the bridge damage is monitored.

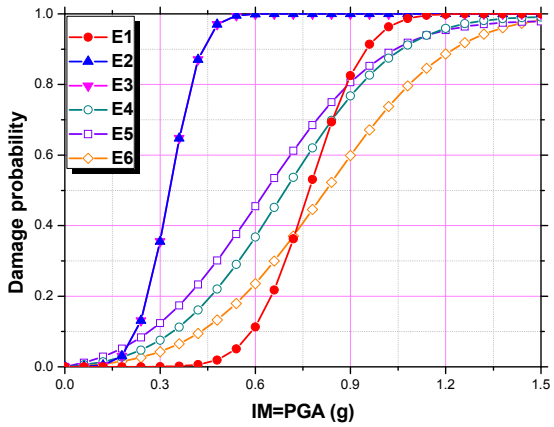

(a) Slight damage

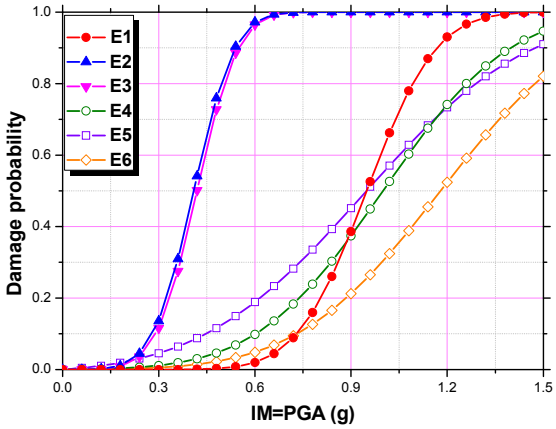

(b) Moderate damage

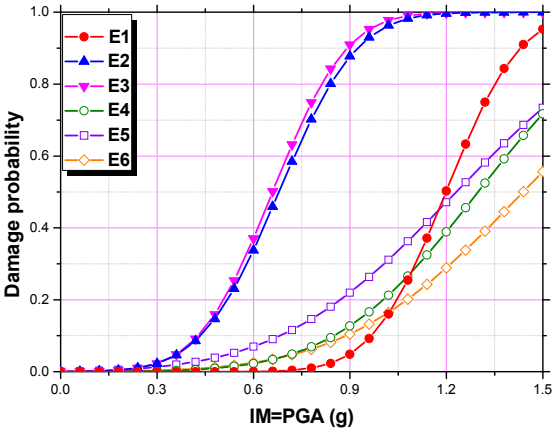

(c) Extensive damage

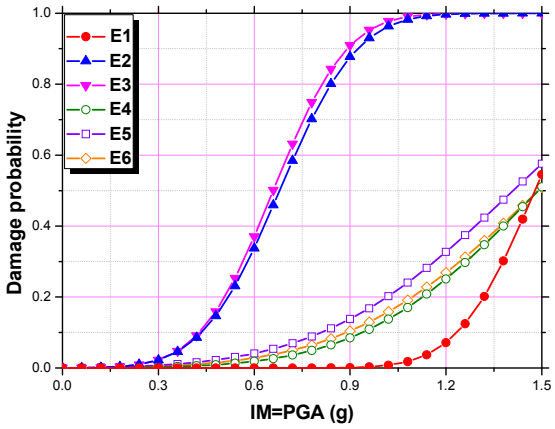

(d) Collapse damage

Figure 5.6 Fragility curves of six bridge models under seismic shaking.

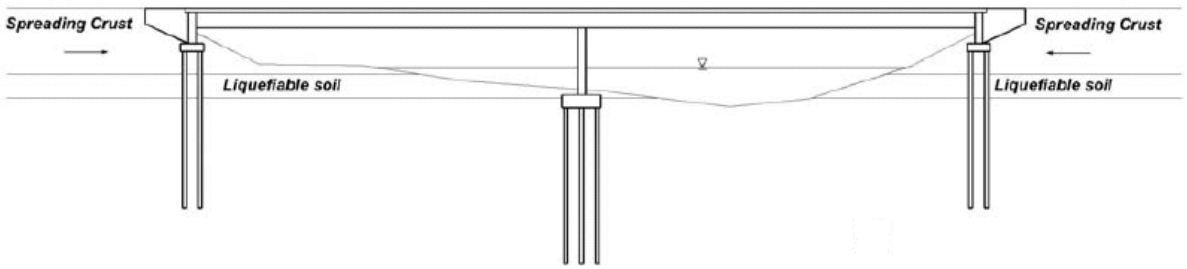

(a) Bridge under lateral spreading

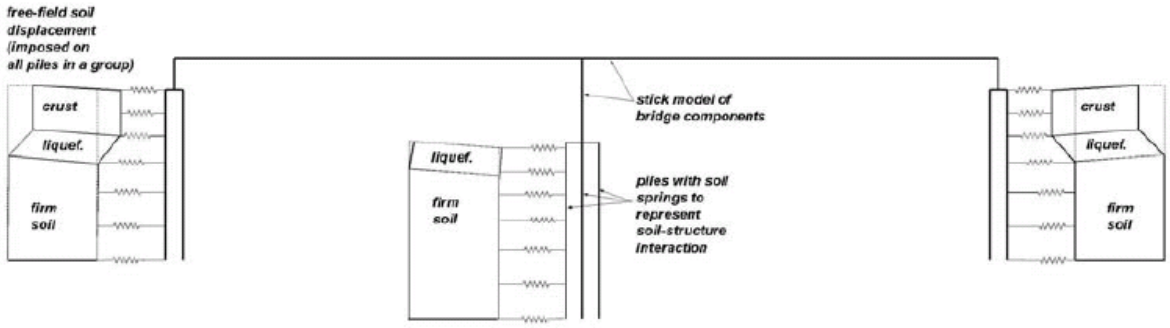

(b) Numerical modeling

Figure 5.7 Numerical modeling of lateral spreading to bridges.

Table 5.3 Probability properties of parameters of soil profile and foundation modeling.

Parameter		Median	Negative Variation	Positive Variation	Distribution
Crust Thickness	Embankment	6.0m	4.5m	7.5m	Normal
	In-situ Clay	3.0m	1.5m	4.5m	
Material Properties and Crust Strength[1]		φ'_{sand}=38º c'_{sand}=20.0kPa Su_{clay}=70.0kPa	Median Crust Strength×0.46	Median Crust Strength×2.17	Lognormal
$\Delta_{sand}/\Delta_{crust}$[2]		0.5	0.16	0.84	Uniform
Liquefied Sand m_p		0.050	0.025	0.075	Normal
y_{50} for p-y springs in crust	Embankment	y_{50}=0.20m	Median×0.5	Median×1.5	Normal
	In-situ clay	y_{50}=0.05m			
Axial Tip Capacity (Q_{tip})		1020.0kN per pile	Median×0.5	Median×1.5	Normal
Inertia Load[3]		a_{max}=0.4g	a_{max} =0.2g	a_{max} =0.6g	Normal
Liquefied sand thickness		2.0m	1.0m	4.0m	Lognormal

[1]Crust strength (P_{ult}) is computed by the procedure in Brandenberg et al. (2007a) and is assumed to be log-normally distributed.

[2]$\Delta_{sand}/\Delta_{crust}$ is the ratio between the displacement at the top of the loose sand to the displacement of the crust.

[3]Inertial load was increased linearly to reach a_{max} at 0.5m of ground displacement, after which it was kept constant.

The above six models were also evaluated for their performance under the liquefaction-induced lateral spreading; they are labeled as models P1 to P6 to distinguish the differences in foundation modeling from models E1 to E6. All superstructure properties of models P1 to P6 were the same as in models E1 to E6, respectively. However, the pile foundations were modeled by bilinear beam elements on a Winkler foundation with *p-y, t-z*, and *q-z* spring elements to simulate the soil lateral resistance, axial shaft friction, and pile tip end bearing resistance, respectively. The soil profile used in this study was representative of sites with a nonliquefiable clay crust over liquefiable loose sand over nonliquefied dense sand. Variations in the soil parameters were based on the USGS database of CPT soundings in the San Francisco Bay Area (USGS 2007). Figure 5.8 presents the sketch of a bridge founded on the soil profile. The layer properties and lateral spreading parameters are listed in Table 5.3 (as the median values). Soil properties were sampled from their respective distributions. From the information on soil profile, the properties of *p-y* elements were determined based on a nonliquefied soil profile and subsequently modified to account for the effects of liquefaction by (1) softening and weakening the *p-y* elements in the liquefied sand layer using a *p*-multiplier, and (2) softening (but not weakening) of the *p-y* elements in the nonliquefiable crust layer to account for the influence of the underlying liquefied sand using models derived by Brandenberg et al. (2007a). Softening of the *p-y* elements using this method indirectly accounts for the pinning effects of the bridge components on the spreading soils by coupling Newmark sliding block analyses with the load transfer behavior. Pinning effects are considered more rigorously in other studies (e.g., Martin et al. 2002; Boulanger et al. 2005).

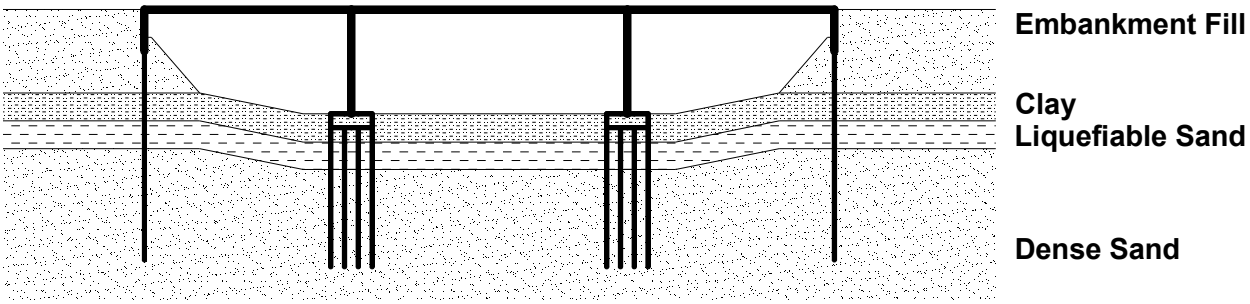

Figure 5.8 Sketch of simulation for bridge and soil profile with liquefiable sand layer.

Slightly different from the procedure and results presented in Chapters 3 and 4, the fragility analysis in this chapter was simplified; the structural properties for each bridge type were not varied with variability introduced by foundation and soil properties mainly. To simplify the fragility analysis, only two loading patterns were adopted. Figure 5.9 presents the deformed shape of bridge model P1 under two possible load cases for liquefaction-induced lateral spreading. The results were obtained by imposing the displacements on the free ends of the *p-y* elements to model lateral spreading demands. In load case I (Figure 5.9a), lateral spreading occurred in the left embankment and left pier foundation. Although the displacement load of lateral spreading was applied on the left side of the bridge, it is the right column that experienced larger deformation and, therefore, experienced more severe damage in this loading case. This is due to the left-to-right displacement of the entire bridge, which acted like a system to the imposed spreading demands. In load case II (Figure 5.9b), only the left pier foundation experienced lateral spreading displacement load. The analysis results show that the left column suffered the most damage, but the damage was much smaller than in load case I given the same displacement magnitude. Figure 5.9 shows that the location of lateral spreading demands directly affects the bridge response and damage levels. Furthermore, damage was not restricted to the components exposed to liquefaction and lateral spreading, as loads may shift to other components in competent soil. Accurately predicting the areal extent of liquefaction and the amount of ground displacement is often difficult, and imposing many different load combinations may be required to identify the most critical conditions for a particular bridge. The influence of various lateral spreading displacement combinations was partially addressed in deriving the fragility functions presented in Chapter 4 as the lateral spreading features were treated as randomly distributed.

5.5.2 Fragility Functions of Different Bridge Types under Liquefaction Induced Lateral Spreading

Corresponding to a static simulation procedure, First Order Second Moment (FOSM) and Monte Carlo methods were generally adopted to generate fragility functions. The FOSM method assumes that both the input properties and output responses follow either normal or log-normal distributions, and applies only first order terms in Taylor's expansion to estimate the mean and

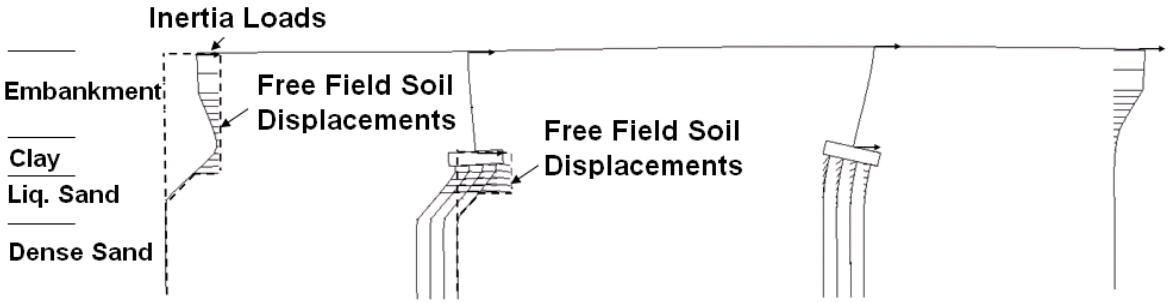

(a) Load case I: Lateral spreading at left abutment and pier

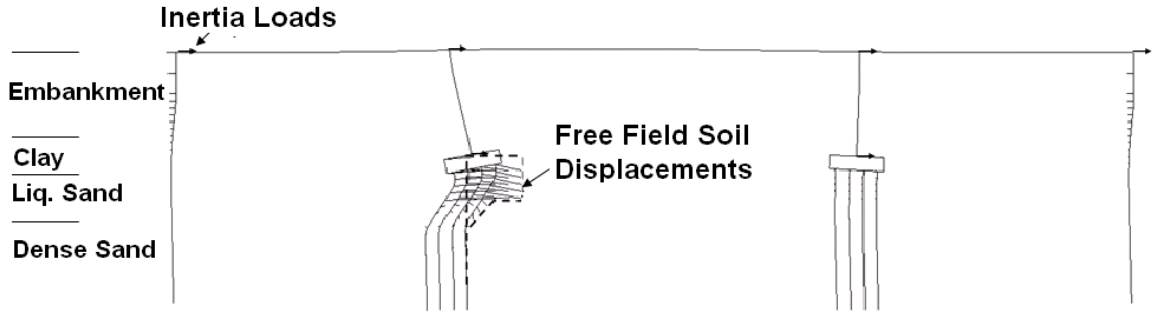

(b) Load case II: Lateral spreading at left pier

Figure 5.9 Bridge deformations under two lateral spreading load cases.

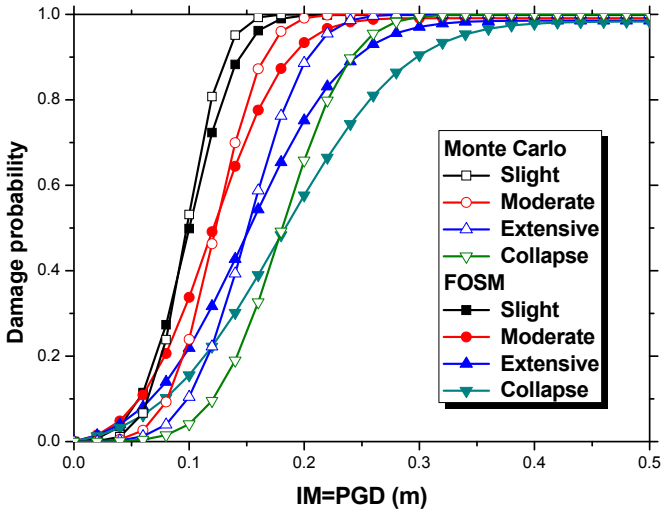

Figure 5.10 Fragility curves generated with Monte Carlo method and FOSM method.

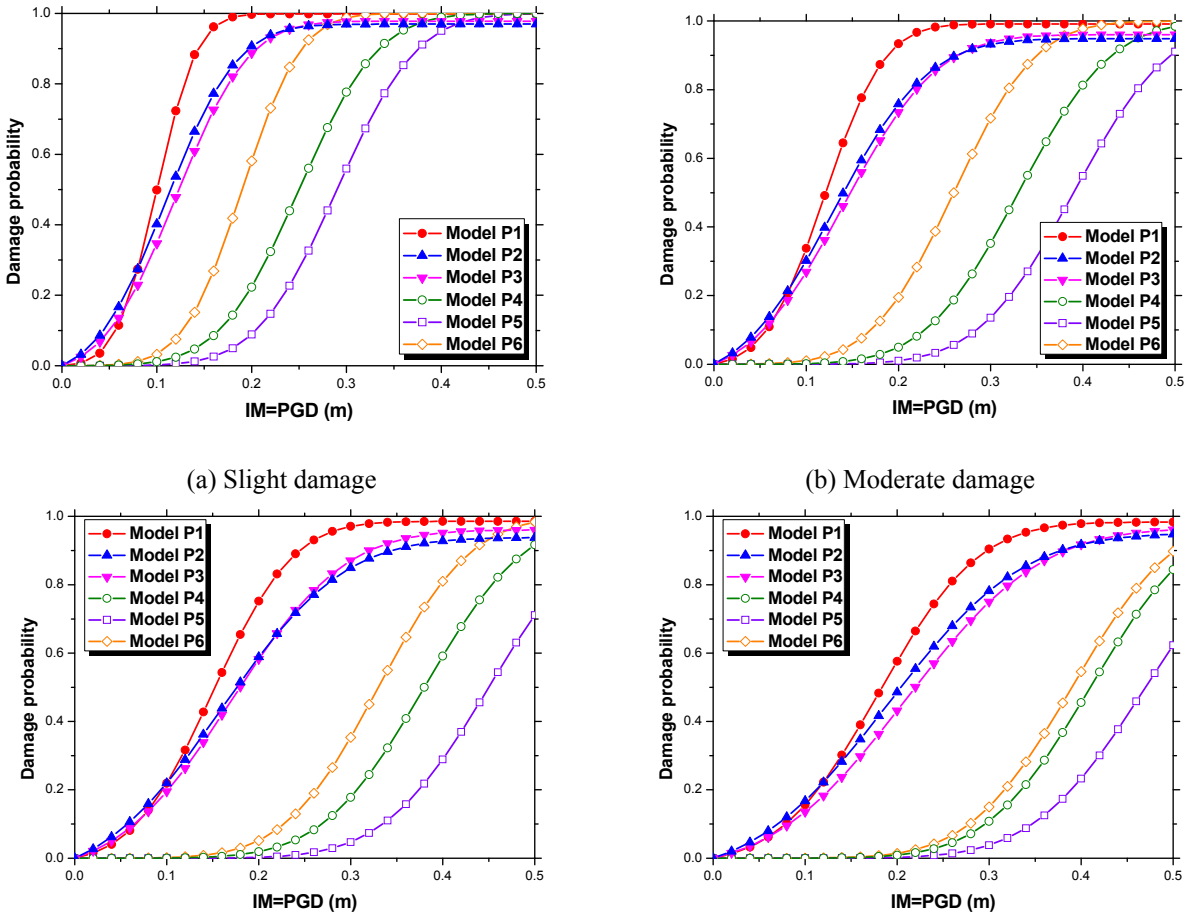

(a) Slight damage

(b) Moderate damage

(c) Extensive damage

(d) Collapse damage

Figure 5.11 Fragility curves of six bridge models under lateral spreading.

standard deviation of response if the mean and standard deviation of the input properties are known (Christian 2004), as shown below:

$$\mu_M = M\left(\mu_{x_1}, \mu_{x_2}, \cdots, \mu_{x_n}\right),\ \sigma_M = \sqrt{\sum_{i=1}^{n}\left(\frac{\partial M}{\partial x_i}\right)^2 \sigma_{x_i}^2} \tag{5.8}$$

The Monte Carlo method selects a large number of input combinations of stochastic variables from the predetermined distribution and uses these combinations to compute the distribution of the output response (Christian 2004). As shown in Table 5.3, eight separate probabilistic parameters were considered in this study. Figure 5.10 depicts the fragility curves derived with Monte Carlo and FOSM method for bridges under load case I, expressed as damage probability versus free-field lateral spreading displacement (PGD). The two methods produce

nearly identical median values, while the FOSM approach predicts larger variance. The following analyses adopt the FOSM method to save on computational effort.

The fragility curves of the six models were generated and compared in Figure 5.11. It is noted that the sequence of damage potential of the models under lateral spreading conditions is quite different compared to that under seismic shaking. Among the six models, model P1 performed the poorest and model P5 performs the best. Because the static load induced by lateral spreading at abutments and one pier was transferred to the other pier through the deck, the isolation bearings at both abutments and pier tops reduced the loads exerted on the columns, and, consequently, mitigated the damage to the pier. The seat-type abutments in models P2 and P3 resulted in a slightly smaller probability of damage compared to model P1. This observation is explained by the different loading mechanism due to lateral spreading.

For the loading case I considered, the displacement loads were applied at the ends of left abutment and the left pier foundation. The seat-type abutment limited the maximum load that was transferred from the abutment to the columns, resulting in a smaller probability of damage for the columns. The isolation bearing at the column top also limited the force being transferred to the columns, resulting in a smaller probability of damage, a conclusion similarly drawn for the seismic shaking. The expansion joint of model P3 did not make much difference in terms of the bridge response compared to model P2. However, the expansion joint in model P5 notably reduced the damage probability under lateral spreading when compared to model P4. Here, the expansion joint offered less constraint compared to the continuous deck, transferring only the contact forces once the gap closed. For a similar reason, the model P6 with simply supported connections incurred more damage into the column and the whole bridge compared to models P4 and P5. Similar to the analysis conducted of the models due to seismic shaking, the above fragility curves illustrate the effects of structural characterizations on the bridge response due to lateral spreading, although notably different from the cases under seismic shaking. One important difference to consider when comparing damage due to shaking with that from lateral spreading is that shaking loads are transient, whereas lateral spreading displacements are typically largest at the end of shaking with some locked-in residual value. Hence, gaps at abutments and expansion joints that close due to lateral spreading may remain closed following an earthquake.

Mean values of the fragility curves μ_{IM} represents the *IM* required to reach the specified damage state with 50% probability and, consequently, higher μ_{IM} , resulted in lower fragility

curves, i.e., better bridge performance. Hence, mean values of fragility functions μ_{IM} could possibly be a good indicator in evaluating the design effectiveness of different structural characterizations. Figure 5.12 compares the μ_{IM} values of reaching the slight, moderate, extensive, and collapse damage states for seismic shaking (Figure 5.12a), and lateral spreading (Figure 5.12b) loading conditions. The IM for the seismic shaking is the PGA of the input motion, while the IM for the lateral spreading situation is the free-field ground displacement. Clearly, the damage probabilities of different bridge models to seismic shaking and lateral spreading are quite different. In addition, the analyses in previous sections have demonstrated that structural characterizations may influence bridge response to seismic shaking and lateral spreading in different ways. Bridges with seat-type abutment (e.g., models E2~E3 and P2~P3) increased bridge damage under seismic shaking, but moderately protected bridges under lateral spreading conditions. Similar effects exist for expansion joints and simply supported connections. One striking structural property identified herein, is the effectiveness of pier isolation (e.g., models E4~E6 and P4~P6) in reducing the damages caused by both seismic shaking and lateral spreading. These conclusions could be very valuable for bridge engineers because a bridge designed and retrofitted to resist earthquake shaking only may not perform well under liquefaction-induced lateral spreading.

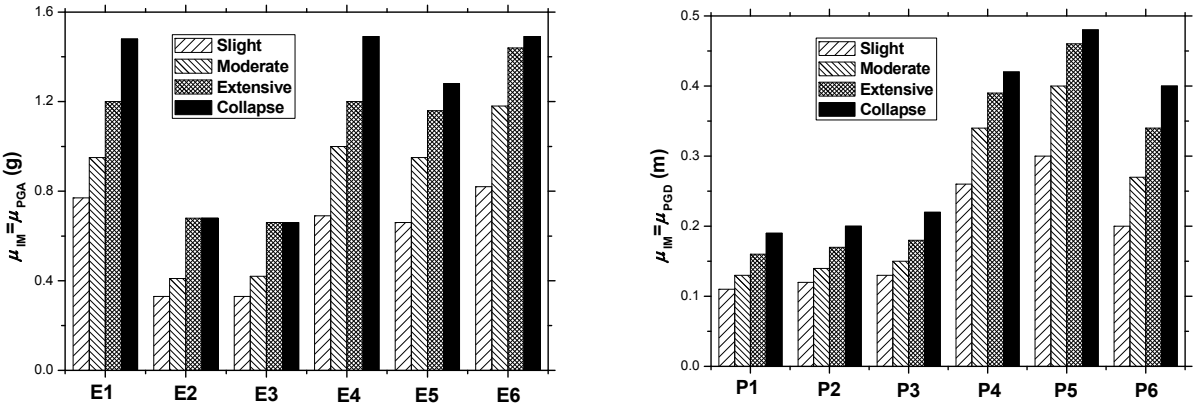

(a) Seismic shaking (b) Lateral spreading

Figure 5.12 Mean IM values for six bridge models to reach various damage states when subject to seismic shaking and lateral spreading.

5.6 SUMMARY

In this chapter, the fragility functions of six different classes of bridges were derived when subjected to both seismic shaking and liquefaction-induced lateral spreading. Two approaches were implemented, PSDA and IDA, to derive fragility curves under seismic shaking, while FOSM and Monte Carlo methods were adopted to generate fragility curves under lateral spreading situation. It was found that the fragility functions of bridges subjected to either ground shaking or lateral spreading showed significant correlation with structural characterizations. Under seismic shaking, isolation at the tops of the piers and at the abutments benefited the bridge's load-carrying capacity, but seat-type abutments made the columns more vulnerable. Furthermore, simply supported connections reduced the damage in columns, and expansion joints did not noticeably affect the bridge's seismic resistance. In contrast, under lateral spreading, isolation at both pier top and seat-type abutments protected columns from damage because a portion of the displacement demand imposed by the spreading soils was accommodated by the isolation components. Expansion joints slightly benefitted the bridge response as the gap closing absorbed part of the displacement demand imposed by lateral spreading. The simply supported connection, however, performed less favorably compared to a design using a continuous deck with isolation on pier tops. In summary, bridges have different resistant capacities to seismic shaking and liquefaction-induced lateral spreading, and the differences are explained with the different loading and load carrying mechanisms.

6 Conclusions and Future Work

6.1 RESEARCH FINDINGS AND CONCLUSIONS

The contents of this report constitute several important contributions to the analysis of bridges in liquefied and laterally spreading ground. First, the fragility functions provided in Chapter 4 are a significant improvement over previously-existing fragility functions for bridges in liquefied and laterally spreading ground. For example, the recommendations in HAZUS are known to be overly-conservative based on previous transportation network analysis simulations (e.g., Kiremidjian et al. 2006). This over-conservatism is largely because a systematic study to develop fragility functions for bridges in liquefied ground had simply not been conducted. The fragility functions presented in this report are significantly lower than the ones provided by HAZUS and in the opinion of the authors are much more reasonable.

Second, the global equivalent static analysis method described in Chapter 2 is a novel approach that adds significant value to the typical local analysis methods most commonly used to design foundations in liquefiable soils. The manner in which loads are transferred among components of the bridge through the superstructure has a significant effect on the boundary conditions imposed on the tops of the pier columns, which in turn affects the ability of the bridge to resist lateral spreading. Although local analysis methods will continue to be the most popular method for designing foundations in liquefied ground, guidance is provided on appropriate boundary conditions for the top of the pier column to envelope the range of responses observed in the global analyses.

Third, an example problem is provided showing in detail how the fragility functions can be incorporated into a PBEE framework to obtain mean annual rates of exceedance of various EDPs. The example began with a probabilistic seismic hazard analysis at a specific site, followed by a probabilistic liquefaction triggering evaluation, probabilistic lateral spreading ground surface displacement analysis, and finally integration with the fragility functions. This approach

shows tremendous promise as a more robust decision-making tool compared with prescriptive code-based approaches.

Fourth, a comparison between the fragility functions for a common set of bridges for ground shaking in the absence of liquefaction and for those subject to liquefaction and lateral spreading is provided. The fragility functions clearly show that different structural configurations result in different trends in the fragility functions. Therefore, both hazards should be considered when appropriate for retrofit decisions and design.

6.2 FUTURE WORK

A primary motivation for the work presented in this report was the influence of the overly-conservative fragility functions for bridges in liquefied ground on transportation network analyses. A natural progression of the work will be to implement these new fragility functions in the transportation network analyses to assess the reasonableness of the results compared with past earthquakes where liquefaction-induced damage has occurred. This type of analysis, beyond the scope of this report, will require coordination among various different research groups in the future.

The fragility functions quantify probability of exceeding EDPs conditioned on free-field lateral spreading ground displacement—which is itself a highly uncertain random variable—that is conditioned on ground motion and soil properties. Accuracy of a PBEE result is therefore dependent on accuracy of the free-field lateral spreading displacement estimates. Different methods for estimating lateral spreading deformations often produce results that differ by more than one order of magnitude, indicating that the methodologies have not fully matured into reasonable agreement. Significant future research will be required to (i) gather high-quality case history information for liquefaction-induced lateral spreads, and (ii) validate prediction methods with the case history data. Particular focus should be placed on conditions that render significantly different predictions using the various methodologies to help resolve errors.

The fragility functions were developed using static analysis methods. Work is currently ongoing to use dynamic inputs to the global bridge models to more realistically represent the effects of liquefaction and lateral spreading. These models are being used to validate the fragility functions developed with the static analysis procedures.

REFERENCES

Abdoun, T. et al. (2003). "Pile response to lateral spreads: Centrifuge modeling," *J. Geotech. Geoenviron. Engrg.,* ASCE*,* 129(10):869–878

American Petroleum Institute (1993). *Recommended Practice for Planning, Design, and Constructing Fixed Offshore Platforms*. API RP 2A - WSD, 20th ed., American Petroleum Institute.

Ashford, S. A., and K. M. Rollins (2002). "TILT: The Treasure Island Liquefaction Test: Final Report," *Rpt. SSRP-2001/17*, Dept. of Structural Engineering, University of California, San Diego, Calif.

Ashford, S. A., and T. Juirnarongrit (2006). "Push-over analyses of piles in laterally spreading soil," *Proceedings,* Seismic Performance and Simulation of Pile Foundations in Liquefied and Laterally Spreading Ground Conf.

Baker, J. W., and C. A. Cornell. (2006). "Vector-valued ground motion intensity measures for probabilistic seismic demand analysis," *PEER Report 2006/08*, Pacific Earthquake Engineering Research Center, University of California, Berkeley, Calif.

Basoz, N., and J. Mander (1999). *Enhancement of the Highway Transportation Module in HAZUS*, in *Report to National Institute of Building Sciences,* Washington, D.C.

Basöz, N. I., and A. S. Kiremidjian. (1998). "Evaluation of bridge damage data from the Loma Prieta and Northridge, California, Earthquakes," *MCEER Report 98/04*. Multidisciplinary Center for Earthquake Engineering Research, Buffalo, NY

Berrill, J. B et al. (2001). "Case study of lateral spreading forces on a piled foundation," *Geotechnique*, 51(6):501-517.

Boulanger, R. W., and I. M. Idriss (2006). "Liquefaction susceptibility criteria for silts and clays," *J. Geotech. Geoenviron. Engrg.,* ASCE, 132(11):1413-1426.

Boulanger, R. W. et al. (2003). "Pile foundations in liquefied and laterally spreading ground during earthquakes: centrifuge experiments and analyses," *Rpt. No. UCD/CGM-03/01*, University of California, Davis, Calif.

Boulanger, R. W. et al. (2004). "Nonlinear FEM analyses of soil-pile interaction in liquefying sand," *Proceedings*, Geotechnical Engineering for Transportation Projects, Geotechnical Special Publication No. 126, (M. K. Yegian and E. Kavazanjian, eds.), ASCE, pp. 470-478.

Boulanger, R. W. et al. (2007). "Seismic design of pile foundations for liquefaction effects," Earthquake Geotechnical Engineering, Fourth Intl. Conf. on Earthquake Geotechnical Engineering, Invited Lectures (K. D. Pitilakis, ed.), Springer, The Netherlands, pp. 277-302.

Boulanger, R. W., and K. Tokimatsu (2006). *Geotechnical Special Publication No. 145: Seismic Performance and Simulation of Pile Foundations in Liquefied and Laterally Spreading Ground*, ASCE Press, Reston, VA, 310 pgs.

Box, G. E. P., and M. E. Muller (1958). "A note on the generation of random normal deviates," *The Annals of Mathematical Statistics*, 29(2):610-611.

Brandenberg, S. J. et al. (2007a). "Liquefaction-induced softening of load transfer between pile groups and laterally spreading crusts," *J. Geotech. Geoenviro. Engrg.,* ASCE, 133(1):91-103.

Brandenberg, S. J. et al. (2007b). "Static pushover analyses of pile groups in liquefied and laterally spreading ground in centrifuge tests," *J. Geotech. Geoenviro. Engrg.,* ASCE, 133(9):1055-1066.

Brandenberg, S. J. et al. (2005). "Behavior of pile foundations in laterally spreading ground during centrifuge tests," *J. Geotech. Geoenviron. Engrg.*, ASCE, 131(11):1378-1391.

Brandenberg, S. J. (2005). "Behavior of pile foundations in liquefied and laterally spreading ground," Dept. of Civil Engineering, PhD Dissertation, University of California, Davis, Calif., 344 pgs.

Bray, J. D., and T. Travasarou (2007). "Simplified procedure for estimating earthquake-induced deviatoric slope displacements," *J. Geotech. Geoenviron. Engrg.*, ASCE, 133(4):381-392.

California Department of Transportation (2006). *Seismic Design Criteria*, Sacramento, Calif.

Caquot, A., and J. Kerisel (1948). "Tables for the calculation of passive pressure, active pressure, and bearing capacity of foundations," *Gautheir-Villars*, Paris.

Cetin, K. O. et al. (2004). "Standard penetration test-based probabilistic and deterministic assessment of seismic soil liquefaction potential," *J. Geotech. Geoenviron. Engrg.*, ASCE, 130(12):1314-1340.

Chen, W.-F., and L. Duan (2003). *Bridge Engineering: Seismic Design,* CRC Press, N.Y.

Christian, J. T. (2004). "Geotechnical engineering reliability: How well do we know what we are doing?" *J. Geotech. Geoenviron. Engrg.,* ASCE, 130(10):985-1003.

Choi, E., R. DesRoches, and B. Nielson (2004). "Seismic fragility of typical bridges in moderate seismic zones," *Engrg. Structures*, 26:187-199.

Dobry, R., V. Taboada, and L. Liu (1995). "Centrifuge modeling of liquefaction effects during earthquakes," *Proceedings,* 1st Intl. Conf. on Earthquake Geotechnical Engineering (K. Ishihara, ed.), Tokyo, Japan, 3:1291-1324.

Duncan, M. J., and R. L. Mokwa (2001). "Passive earth pressures: Theories and tests," *J. Geotech. Geoenviron. Engrg.,* ASCE, 127(3):248-257.

Elgamal, A. et al. (2008). "Three-dimensional seismic response of Humboldt Bay bridge-foundation-ground system," *J. Struct. Engrg.*, 134(7):1165-1176

Faris, A. T. (2004). "Probabilistic models for engineering assessment of liquefaction-induced lateral spreading displacements," Dept. of Civil Engineering., PhD dissertation, University of California, Berkeley, Calif.

Federal Emergency Management Agency (1999). "HAZUS, Earthquake Loss Estimation, Technical Manual," National Institute of Building Sciences, Washington D.C.

Federal Emergency Management Agency. (2007). *Multi-Hazard Loss Estimation Methodology, Earthquake Model*. HAZUS-MH MR3 Technical Manual. Washington, D.C.

Golesorkhi, R. (1989). "Factors influencing the computational determination of earthquake-induced shear stresses in sandy soils," Dept. of Civil Engineering, PhD dissertation, University of California, Berkeley, Calif.

Hamada, M. (1992). "Large ground deformations and their effects on lifelines: 1964 Niigata earthquake," *Case Studies of Liquefaction and Lifeline Performance during Past Earthquakes: Volume 1 Japanese Case Studies*, *Technical Report NCEER-92-0001*, State University of New York at Buffalo, 3:1-123.

Ishihara, K. (1985). "Stability of natural deposits durings earthquakes," *Proceedings,* Eleventh Intl. Conf. on Soil Mechanics and Foundation Engineering.

Kayen, R. et al. (2007). "Preliminary observations on the Niigata-Chuetsu Oki, Japan, earthquake of July 16, 2007," *EERI-GEER Web Report 2007–1 v.6,* August.

Karim, K. R. and F. Yamazaki (2001). "Effect of earthquake ground motions on fragility curves of highway bridge piers based on numerical simulation," *Earthq. Engrg. Struct. Dyn.,* 30:1839-1856.

Kashighandi, P. (2009). "Demand Fragility Surfaces for Bridges in Liquefied Laterally Spreading Ground," Dept. of Civil Engineering, University of California, Los Angeles, California.

Kiremidjian, A. et al. (2006). "Pacific Earthquake Engineering Research Center highway demonstration project," *Rpt. No. PEER 2006/*02, Pacific Earthquake Engineering Research Center, University of California, Berkeley, Calif.

Kumar, P. T. V., and D. K. Paul (2007). "Force-deformation behavior of isolation bearings," *J. Bridge Engrg.,* 12(4):527-529.

Knudsen, K. L. et al. (2009). "Development of a liquefaction hazard screening tool for Caltrans bridge sites," *Proceedings*, TCLEE 2009 Conference: 7th Intl. Conf. on Lifeline Earthquake Engineering. Oakland, Calif.

Kramer, S. L., and R. T. Mayfield (2007). "Return period of soil liquefaction," *J. Geotech. Geoenviron. Engrg.*, ASCE, 133(7):802-813.

Kramer, S. L., P. Arduino, and H. Shin (2008) "Using OpenSees for performance-based evaluation of bridges on liquefiable soils," *Rpt. No. PEER 2008/07*, Pacific Earthquake Engineering Research Center, University of California, Berkeley, Calif.

Lemnitzer, A. et al. (2009). "Lateral performance of full-scale bridge abutment wall with granular backfill," *J. Geotech. Geoenviron. Engrg.,* ASCE, 135(4):506-514.

LPILE Plus v5.0. A program for the analysis of piles and drilled shafts under lateral loads., Developed by ENSOFT, INC, *www.ensoftinc.com*.

Luco, N., and P. Bazzurro (2007). "Does amplitude scaling of ground motion records result in biased nonlinear structural drift response?" *Earthq. Engrg. Struct. Dyn.,* 36: 1813-1835.

Mackie, K. R., and B. Stojadinović (2003). "Seismic demands for performance-based design of bridges," *PEER Report No.2003/16*, Pacific Earthquake Engineering Research Center, University of California, Berkeley, Calif.

Mackie, K. R., and B. Stojadinović (2007). "Performance-based seismic bridge design for damage and loss limit states," *Earthq. Engrg. Struct. Dyn.,* 36(13):1953-1971.

Mackie, K. R., and B. Stojadinovic (2005). "Fragility basis for California highway overpass bridge seismic decision making," *PEER Report No. 2005/02*, Pacific Earthquake Engineering Research Center, University of California, Berkeley, Calif.

Malvick, E. J., B. L. Kutter, and R. W. Boulanger (2008). "Postshaking shear strain localization in a centrifuge model of a saturated sand slope," *J. Geotech. Geoenviron. Engrg.,* ASCE, 134(2):164-174.

Matlock, H. (1970). "Correlations of design of laterally loaded piles in soft clay." *Proceedings,* Offshore Technology Conference, Houston, TX, 1(1204):577-594.

Mazzoni, S., F. McKenna., M. H. Scott., G. L. Fenves et al. (2006). *OpenSees Command Language Manual.* University of California, Berkeley, Calif.

Mazindrani, Z. H., and M. H. Ganjali (1997). "Lateral earth pressure problem of cohesive backfill with inclined surface," *J. Geotech. Geoenviron. Engrg.,* ASCE, 123(2):110-112.

McKenna, F., M. H. Scott, and G. L. Fenves (2006). "Open system for earthquake engineering simulation user command-language manual," Pacific Earthquake Engineering Research Center, University of California, Berkeley, Calif., 465 pgs.

Mokwa, R. L., and J. M. Duncan (2001). "Experimental evaluation of lateral-load resistance of pile caps," *J. Geotech. Geoenviron. Engrg.,* ASCE, 127(2):185-192.

Mononobe, N. and H. Matsuo (1929). "On the determination of earth pressures during earthquakes," *Proceedings,* World Engineering Congress, 9 pgs.

Newmark, N. M. (1965). "Effects of earthquakes on dams and embankments," *Geotechnique*, London, 15(2), 139–160.

Nielson, B. G., and R. DesRoches (2007). "Seismic fragility methodology for highway bridges using a component level approach," *Earthq. Engrg. Struct. Dyn.,* 36:823-839.

Okabe, S. (1926). "General theory of earth pressures," *J. Japan Society of Civil Engineering*, 12(1).

Olson, S. M. and T. D. Stark (2002). "Liquefied strength ratio from liquefaction case histories," *Canadian Geotechnical Journal*, 39:629-647.

Ovesen, N. K. (1964). "Anchor slabs, calculation methods and model tests," *Bull. No. 16*, The Danish Geotechnical Institute, Copenhagen.

Padgett, J. E., B. G. Nielson, and R. DesRoches (2008). "Selection of optimal intensity measures in probabilistic seismic demand models of highway bridge portfolios," *Earthq. Engrg. Struct. Dyn.,* 37(5):711-725.

Paik, K. H., and R. Salgado (2003). "Estimation of active earth pressure against rigid retaining walls considering arching effects," *Géotechnique*, 53(7):643-653.

Porter, K., R. Kennedy, and R. Bachman (2007). "Creating fragility functions for performance-based earthquake engineering," *Earthq. Spectra*, 23(2):471-489.

Priestley, M. J. N., F. Seible, and G. M. Calvi (1996). *Seismic Design and Retrofit of Bridges*, John Wiley & Sons, N.Y.

Rollins, K. M., and A. Sparks (2002). "Lateral resistance of full-scale pile cap with gravel backfill," *J. Geotech. Geoenviron. Eng.,* ASCE, 128(9):711-723.

Rollins, K. M. et al. (2005). "Lateral resistance of a full-scale pile group in liquefied sand," *J. Geotech. Geoenviron. Engrg.,* ASCE, 131(1):115-125.

Romstad, K. et al. (1995). "Experimental measurements of bridge abutment behavior," *Rpt. No. UCD-STR-95-1*, Structural Engineering Group, University of California, Davis, Calif.

Shin, H. et al. (2008). "Seismic response of a typical highway bridge in liquefiable soil," *Proceedings, Geotechnical Earthq. Engineering and Soil Dynamics IV Conf.*, Sacramento, California, CD Rom.

Slide v 5.0 A program for slope stability analysis, Developed by Rocscience. www.rocscience.com.

Spencer, E. (1967). A method of analysis of the stability of embankments assuming parallel inter-slice forces, *Geotechnique*, 17(1), 11-26.

Terzaghi, K. (1936). "A fundamental fallacy in earth pressure computations," *J. of the Boston Society of Civil Engineers.* April.

Tokimatsu, K., Suzuki, H., and Suzuki, Y. (2001). "Back-calculated *p-y* relation of liquefied soils from large shaking table tests," *Fourth Intl. Conf. on Recent Advances in Geotechnical Earthq. Engineering and Soil Dynamics*, (S. Prakash, ed.), University of Missouri–Rolla, Paper 6.24.

Transportation Research Board (2002). "Comprehensive specification for the seismic design of bridges," *National Cooperative Highway Research Program Report 472*, National Research Council, 47 pp.

United States Geological Survey (USGS). (2007). *CPT data Alameda County Online database*. http://earthquakeusgsgov/regional/nca/cpt/data/?map=alameda.

Wilson, J. C. (2003). Repair of new long-span bridges damaged by the 1995 Kobe earthquake," *J. Performance of Constructed Facilities*, 17(4):196-205.

Wilson, D. W., R. W. Boulanger, and B. L. Kutter (1998). "Signal processing for and analyses of dynamic soil-pile-interaction experiments," *Proceedings*, Centrifuge 98, Kimura (Kusakabe and Takemura, eds.), Balkema, Rotterdam, 1:135-140.

Wilson, D. W., R. W. Boulanger, and B. L. Kutter (2000). "Seismic lateral resistance of liquefying sand," *J. Geotech. Geoenviron. Engrg.,* ASCE, 126(10):898-906.

Xtract, v.3.0.7. A program for the analysis of structural cross sections. TRC/Imbsen Software Systems. www.imbsen.com.

Yasuda, S., and J. B. Berrill (2000). "Observations of the earthquake response of foundations in soil profiles containing saturated sands," *Proceedings,* GeoEng 2000 Conf., Melbourne, Australia.

Zhang, J., and Y. Huo (2009). "Evaluating effectiveness and optimum design of isolation devices for highway bridges using fragility function method," *Engrg. Structures*, 31(8):1648-1660.

Zhang, J., Y. Huo, S.J. Brandenberg, P. Kashighandi (2008). "Effects of structural characterizations on fragility functions of bridges subjected to seismic shaking and lateral spreading," *Earthquake Engineering and Engineering Vibration,* 7(4):369-382.

Zhang. J., and N. Makris (2002a). "Kinematic response functions and dynamic stiffnesses of bridge embankments," *Earthq. Engrg. Struct. Dyn.,* 31:1933-1966.

Zhang. J., and N. Makris (2002b). "Seismic response analysis of highway overcrossings including soil-structure interaction," *Earthq. Engrg. Struct. Dyn.,* 31:1967-1991.

Zhang, Y. et al. (2008). "Two-dimensional nonlinear earthquake response analysis of a bridge-foundation-ground system," *Earthq. Spectra*, 24(2):343-386

Zhu, D., and Q. Qian (2000). "Determination of passive earth pressure coefficients by the method of triangular slices," *Can. Geotech. J.*, 37(2):485-491.

PEER REPORTS

PEER reports are available individually or by yearly subscription. PEER reports can be ordered at http://peer.berkeley.edu/publications/peer_reports.html or by contacting the Pacific Earthquake Engineering Research Center, 325 Davis Hall mail code 1792, Berkeley, CA 94720. Tel.: (510) 642-3437; Fax: (510) 665-1655; Email: peer_editor@berkeley.edu

PEER 2011/01 *Demand Fragility Surfaces for Bridges in Liquefied and Laterally Spreading Ground.* Scott J. Brandenberg, Jian Zhang, Pirooz Kashighandi, Yili Huo, and Minxing Zhao. March 2011.

PEER 2010/05 *Guidelines for Performance-Based Seismic Design of Tall Buildings.* Developed by the Tall Buildings Initiative. November 2010.

PEER 2010/04 *Application Guide for the Design of Flexible and Rigid Bus Connections between Substation Equipment Subjected to Earthquakes.* Jean-Bernard Dastous and Armen Der Kiureghian. September 2010.

PEER 2010/03 *Shear Wave Velocity as a Statistical Function of Standard Penetration Test Resistance and Vertical Effective Stress at Caltrans Bridge Sites.* Scott J. Brandenberg, Naresh Bellana, and Thomas Shantz. June 2010.

PEER 2010/02 *Stochastic Modeling and Simulation of Ground Motions for Performance-Based Earthquake Engineering.* Sanaz Rezaeian and Armen Der Kiureghian. June 2010.

PEER 2010/01 *Structural Response and Cost Characterization of Bridge Construction Using Seismic Performance Enhancement Strategies.* Ady Aviram, Božidar Stojadinović, Gustavo J. Parra-Montesinos, and Kevin R. Mackie. March 2010.

PEER 2009/03 *The Integration of Experimental and Simulation Data in the Study of Reinforced Concrete Bridge Systems Including Soil-Foundation-Structure Interaction.* Matthew Dryden and Gregory L. Fenves. November 2009.

PEER 2009/02 *Improving Earthquake Mitigation through Innovations and Applications in Seismic Science, Engineering, Communication, and Response. Proceedings of a U.S.-Iran Seismic Workshop.* October 2009.

PEER 2009/01 *Evaluation of Ground Motion Selection and Modification Methods: Predicting Median Interstory Drift Response of Buildings.* Curt B. Haselton, Ed. June 2009.

PEER 2008/10 *Technical Manual for Strata.* Albert R. Kottke and Ellen M. Rathje. February 2009.

PEER 2008/09 *NGA Model for Average Horizontal Component of Peak Ground Motion and Response Spectra.* Brian S.-J. Chiou and Robert R. Youngs. November 2008.

PEER 2008/08 *Toward Earthquake-Resistant Design of Concentrically Braced Steel Structures.* Patxi Uriz and Stephen A. Mahin. November 2008.

PEER 2008/07 *Using OpenSees for Performance-Based Evaluation of Bridges on Liquefiable Soils.* Stephen L. Kramer, Pedro Arduino, and HyungSuk Shin. November 2008.

PEER 2008/06 *Shaking Table Tests and Numerical Investigation of Self-Centering Reinforced Concrete Bridge Columns.* Hyung IL Jeong, Junichi Sakai, and Stephen A. Mahin. September 2008.

PEER 2008/05 *Performance-Based Earthquake Engineering Design Evaluation Procedure for Bridge Foundations Undergoing Liquefaction-Induced Lateral Ground Displacement.* Christian A. Ledezma and Jonathan D. Bray. August 2008.

PEER 2008/04 *Benchmarking of Nonlinear Geotechnical Ground Response Analysis Procedures.* Jonathan P. Stewart, Annie On-Lei Kwok, Yousseff M. A. Hashash, Neven Matasovic, Robert Pyke, Zhiliang Wang, and Zhaohui Yang. August 2008.

PEER 2008/03 *Guidelines for Nonlinear Analysis of Bridge Structures in California.* Ady Aviram, Kevin R. Mackie, and Božidar Stojadinović. August 2008.

PEER 2008/02 *Treatment of Uncertainties in Seismic-Risk Analysis of Transportation Systems.* Evangelos Stergiou and Anne S. Kiremidjian. July 2008.

PEER 2008/01 *Seismic Performance Objectives for Tall Buildings.* William T. Holmes, Charles Kircher, William Petak, and Nabih Youssef. August 2008.

PEER 2007/12 *An Assessment to Benchmark the Seismic Performance of a Code-Conforming Reinforced Concrete Moment-Frame Building.* Curt Haselton, Christine A. Goulet, Judith Mitrani-Reiser, James L. Beck, Gregory G. Deierlein, Keith A. Porter, Jonathan P. Stewart, and Ertugrul Taciroglu. August 2008.

PEER 2007/11 *Bar Buckling in Reinforced Concrete Bridge Columns.* Wayne A. Brown, Dawn E. Lehman, and John F. Stanton. February 2008.

PEER 2007/10 *Computational Modeling of Progressive Collapse in Reinforced Concrete Frame Structures.* Mohamed M. Talaat and Khalid M. Mosalam. May 2008.

PEER 2007/09 *Integrated Probabilistic Performance-Based Evaluation of Benchmark Reinforced Concrete Bridges.* Kevin R. Mackie, John-Michael Wong, and Božidar Stojadinović. January 2008.

PEER 2007/08 *Assessing Seismic Collapse Safety of Modern Reinforced Concrete Moment-Frame Buildings.* Curt B. Haselton and Gregory G. Deierlein. February 2008.

PEER 2007/07 *Performance Modeling Strategies for Modern Reinforced Concrete Bridge Columns.* Michael P. Berry and Marc O. Eberhard. April 2008.

PEER 2007/06 *Development of Improved Procedures for Seismic Design of Buried and Partially Buried Structures.* Linda Al Atik and Nicholas Sitar. June 2007.

PEER 2007/05 *Uncertainty and Correlation in Seismic Risk Assessment of Transportation Systems.* Renee G. Lee and Anne S. Kiremidjian. July 2007.

PEER 2007/04 *Numerical Models for Analysis and Performance-Based Design of Shallow Foundations Subjected to Seismic Loading.* Sivapalan Gajan, Tara C. Hutchinson, Bruce L. Kutter, Prishati Raychowdhury, José A. Ugalde, and Jonathan P. Stewart. May 2008.

PEER 2007/03 *Beam-Column Element Model Calibrated for Predicting Flexural Response Leading to Global Collapse of RC Frame Buildings.* Curt B. Haselton, Abbie B. Liel, Sarah Taylor Lange, and Gregory G. Deierlein. May 2008.

PEER 2007/02 *Campbell-Bozorgnia NGA Ground Motion Relations for the Geometric Mean Horizontal Component of Peak and Spectral Ground Motion Parameters.* Kenneth W. Campbell and Yousef Bozorgnia. May 2007.

PEER 2007/01 *Boore-Atkinson NGA Ground Motion Relations for the Geometric Mean Horizontal Component of Peak and Spectral Ground Motion Parameters.* David M. Boore and Gail M. Atkinson. May. May 2007.

PEER 2006/12 *Societal Implications of Performance-Based Earthquake Engineering.* Peter J. May. May 2007.

PEER 2006/11 *Probabilistic Seismic Demand Analysis Using Advanced Ground Motion Intensity Measures, Attenuation Relationships, and Near-Fault Effects.* Polsak Tothong and C. Allin Cornell. March 2007.

PEER 2006/10 *Application of the PEER PBEE Methodology to the I-880 Viaduct.* Sashi Kunnath. February 2007.

PEER 2006/09 *Quantifying Economic Losses from Travel Forgone Following a Large Metropolitan Earthquake.* James Moore, Sungbin Cho, Yue Yue Fan, and Stuart Werner. November 2006.

PEER 2006/08 *Vector-Valued Ground Motion Intensity Measures for Probabilistic Seismic Demand Analysis.* Jack W. Baker and C. Allin Cornell. October 2006.

PEER 2006/07 *Analytical Modeling of Reinforced Concrete Walls for Predicting Flexural and Coupled–Shear-Flexural Responses.* Kutay Orakcal, Leonardo M. Massone, and John W. Wallace. October 2006.

PEER 2006/06 *Nonlinear Analysis of a Soil-Drilled Pier System under Static and Dynamic Axial Loading.* Gang Wang and Nicholas Sitar. November 2006.

PEER 2006/05 *Advanced Seismic Assessment Guidelines.* Paolo Bazzurro, C. Allin Cornell, Charles Menun, Maziar Motahari, and Nicolas Luco. September 2006.

PEER 2006/04 *Probabilistic Seismic Evaluation of Reinforced Concrete Structural Components and Systems.* Tae Hyung Lee and Khalid M. Mosalam. August 2006.

PEER 2006/03 *Performance of Lifelines Subjected to Lateral Spreading.* Scott A. Ashford and Teerawut Juirnarongrit. July 2006.

PEER 2006/02 *Pacific Earthquake Engineering Research Center Highway Demonstration Project.* Anne Kiremidjian, James Moore, Yue Yue Fan, Nesrin Basoz, Ozgur Yazali, and Meredith Williams. April 2006.

PEER 2006/01 *Bracing Berkeley. A Guide to Seismic Safety on the UC Berkeley Campus.* Mary C. Comerio, Stephen Tobriner, and Ariane Fehrenkamp. January 2006.

PEER 2005/16 *Seismic Response and Reliability of Electrical Substation Equipment and Systems.* Junho Song, Armen Der Kiureghian, and Jerome L. Sackman. April 2006.

PEER 2005/15 *CPT-Based Probabilistic Assessment of Seismic Soil Liquefaction Initiation.* R. E. S. Moss, R. B. Seed, R. E. Kayen, J. P. Stewart, and A. Der Kiureghian. April 2006.

PEER 2005/14 *Workshop on Modeling of Nonlinear Cyclic Load-Deformation Behavior of Shallow Foundations.* Bruce L. Kutter, Geoffrey Martin, Tara Hutchinson, Chad Harden, Sivapalan Gajan, and Justin Phalen. March 2006.

PEER 2005/13 *Stochastic Characterization and Decision Bases under Time-Dependent Aftershock Risk in Performance-Based Earthquake Engineering.* Gee Liek Yeo and C. Allin Cornell. July 2005.

PEER 2005/12 *PEER Testbed Study on a Laboratory Building: Exercising Seismic Performance Assessment.* Mary C. Comerio, editor. November 2005.

PEER 2005/11 *Van Nuys Hotel Building Testbed Report: Exercising Seismic Performance Assessment.* Helmut Krawinkler, editor. October 2005.

PEER 2005/10 *First NEES/E-Defense Workshop on Collapse Simulation of Reinforced Concrete Building Structures.* September 2005.

PEER 2005/09 *Test Applications of Advanced Seismic Assessment Guidelines.* Joe Maffei, Karl Telleen, Danya Mohr, William Holmes, and Yuki Nakayama. August 2006.

PEER 2005/08 *Damage Accumulation in Lightly Confined Reinforced Concrete Bridge Columns.* R. Tyler Ranf, Jared M. Nelson, Zach Price, Marc O. Eberhard, and John F. Stanton. April 2006.

PEER 2005/07 *Experimental and Analytical Studies on the Seismic Response of Freestanding and Anchored Laboratory Equipment.* Dimitrios Konstantinidis and Nicos Makris. January 2005.

PEER 2005/06 *Global Collapse of Frame Structures under Seismic Excitations*. Luis F. Ibarra and Helmut Krawinkler. September 2005.

PEER 2005//05 *Performance Characterization of Bench- and Shelf-Mounted Equipment.* Samit Ray Chaudhuri and Tara C. Hutchinson. May 2006.

PEER 2005/04 *Numerical Modeling of the Nonlinear Cyclic Response of Shallow Foundations.* Chad Harden, Tara Hutchinson, Geoffrey R. Martin, and Bruce L. Kutter. August 2005.

PEER 2005/03 *A Taxonomy of Building Components for Performance-Based Earthquake Engineering.* Keith A. Porter. September 2005.

PEER 2005/02 *Fragility Basis for California Highway Overpass Bridge Seismic Decision Making*. Kevin R. Mackie and Božidar Stojadinović. June 2005.

PEER 2005/01 *Empirical Characterization of Site Conditions on Strong Ground Motion.* Jonathan P. Stewart, Yoojoong Choi, and Robert W. Graves. June 2005.

PEER 2004/09 *Electrical Substation Equipment Interaction: Experimental Rigid Conductor Studies.* Christopher Stearns and André Filiatrault. February 2005.

PEER 2004/08 *Seismic Qualification and Fragility Testing of Line Break 550-kV Disconnect Switches.* Shakhzod M. Takhirov, Gregory L. Fenves, and Eric Fujisaki. January 2005.

PEER 2004/07 *Ground Motions for Earthquake Simulator Qualification of Electrical Substation Equipment.* Shakhzod M. Takhirov, Gregory L. Fenves, Eric Fujisaki, and Don Clyde. January 2005.

PEER 2004/06 *Performance-Based Regulation and Regulatory Regimes.* Peter J. May and Chris Koski. September 2004.

PEER 2004/05 *Performance-Based Seismic Design Concepts and Implementation: Proceedings of an International Workshop.* Peter Fajfar and Helmut Krawinkler, editors. September 2004.

PEER 2004/04 *Seismic Performance of an Instrumented Tilt-up Wall Building.* James C. Anderson and Vitelmo V. Bertero. July 2004.

PEER 2004/03 *Evaluation and Application of Concrete Tilt-up Assessment Methodologies.* Timothy Graf and James O. Malley. October 2004.

PEER 2004/02 *Analytical Investigations of New Methods for Reducing Residual Displacements of Reinforced Concrete Bridge Columns.* Junichi Sakai and Stephen A. Mahin. August 2004.

PEER 2004/01 *Seismic Performance of Masonry Buildings and Design Implications.* Kerri Anne Taeko Tokoro, James C. Anderson, and Vitelmo V. Bertero. February 2004.

PEER 2003/18 *Performance Models for Flexural Damage in Reinforced Concrete Columns.* Michael Berry and Marc Eberhard. August 2003.

PEER 2003/17 *Predicting Earthquake Damage in Older Reinforced Concrete Beam-Column Joints.* Catherine Pagni and Laura Lowes. October 2004.

PEER 2003/16 *Seismic Demands for Performance-Based Design of Bridges.* Kevin Mackie and Božidar Stojadinović. August 2003.

PEER 2003/15 *Seismic Demands for Nondeteriorating Frame Structures and Their Dependence on Ground Motions.* Ricardo Antonio Medina and Helmut Krawinkler. May 2004.

PEER 2003/14 *Finite Element Reliability and Sensitivity Methods for Performance-Based Earthquake Engineering.* Terje Haukaas and Armen Der Kiureghian. April 2004.

PEER 2003/13 *Effects of Connection Hysteretic Degradation on the Seismic Behavior of Steel Moment-Resisting Frames.* Janise E. Rodgers and Stephen A. Mahin. March 2004.

PEER 2003/12 *Implementation Manual for the Seismic Protection of Laboratory Contents: Format and Case Studies.* William T. Holmes and Mary C. Comerio. October 2003.

PEER 2003/11 *Fifth U.S.-Japan Workshop on Performance-Based Earthquake Engineering Methodology for Reinforced Concrete Building Structures.* February 2004.

PEER 2003/10 *A Beam-Column Joint Model for Simulating the Earthquake Response of Reinforced Concrete Frames.* Laura N. Lowes, Nilanjan Mitra, and Arash Altoontash. February 2004.

PEER 2003/09 *Sequencing Repairs after an Earthquake: An Economic Approach.* Marco Casari and Simon J. Wilkie. April 2004.

PEER 2003/08 *A Technical Framework for Probability-Based Demand and Capacity Factor Design (DCFD) Seismic Formats*. Fatemeh Jalayer and C. Allin Cornell. November 2003.

PEER 2003/07 *Uncertainty Specification and Propagation for Loss Estimation Using FOSM Methods.* Jack W. Baker and C. Allin Cornell. September 2003.

PEER 2003/06 *Performance of Circular Reinforced Concrete Bridge Columns under Bidirectional Earthquake Loading*. Mahmoud M. Hachem, Stephen A. Mahin, and Jack P. Moehle. February 2003.

PEER 2003/05 *Response Assessment for Building-Specific Loss Estimation.* Eduardo Miranda and Shahram Taghavi. September 2003.

PEER 2003/04 *Experimental Assessment of Columns with Short Lap Splices Subjected to Cyclic Loads*. Murat Melek, John W. Wallace, and Joel Conte. April 2003.

PEER 2003/03 *Probabilistic Response Assessment for Building-Specific Loss Estimation.* Eduardo Miranda and Hesameddin Aslani. September 2003.

PEER 2003/02 *Software Framework for Collaborative Development of Nonlinear Dynamic Analysis Program.* Jun Peng and Kincho H. Law. September 2003.

PEER 2003/01 *Shake Table Tests and Analytical Studies on the Gravity Load Collapse of Reinforced Concrete Frames*. Kenneth John Elwood and Jack P. Moehle. November 2003.

PEER 2002/24 *Performance of Beam to Column Bridge Joints Subjected to a Large Velocity Pulse.* Natalie Gibson, André Filiatrault, and Scott A. Ashford. April 2002.

PEER 2002/23 *Effects of Large Velocity Pulses on Reinforced Concrete Bridge Columns.* Greg L. Orozco and Scott A. Ashford. April 2002.

PEER 2002/22 *Characterization of Large Velocity Pulses for Laboratory Testing.* Kenneth E. Cox and Scott A. Ashford. April 2002.

PEER 2002/21 *Fourth U.S.-Japan Workshop on Performance-Based Earthquake Engineering Methodology for Reinforced Concrete Building Structures*. December 2002.

PEER 2002/20 *Barriers to Adoption and Implementation of PBEE Innovations.* Peter J. May. August 2002.

PEER 2002/19 *Economic-Engineered Integrated Models for Earthquakes: Socioeconomic Impacts.* Peter Gordon, James E. Moore II, and Harry W. Richardson. July 2002.

PEER 2002/18 *Assessment of Reinforced Concrete Building Exterior Joints with Substandard Details.* Chris P. Pantelides, Jon Hansen, Justin Nadauld, and Lawrence D. Reaveley. May 2002.

PEER 2002/17 *Structural Characterization and Seismic Response Analysis of a Highway Overcrossing Equipped with Elastomeric Bearings and Fluid Dampers: A Case Study.* Nicos Makris and Jian Zhang. November 2002.

PEER 2002/16 *Estimation of Uncertainty in Geotechnical Properties for Performance-Based Earthquake Engineering.* Allen L. Jones, Steven L. Kramer, and Pedro Arduino. December 2002.

PEER 2002/15 *Seismic Behavior of Bridge Columns Subjected to Various Loading Patterns.* Asadollah Esmaeily-Gh. and Yan Xiao. December 2002.

PEER 2002/14 *Inelastic Seismic Response of Extended Pile Shaft Supported Bridge Structures.* T.C. Hutchinson, R.W. Boulanger, Y.H. Chai, and I.M. Idriss. December 2002.

PEER 2002/13 *Probabilistic Models and Fragility Estimates for Bridge Components and Systems.* Paolo Gardoni, Armen Der Kiureghian, and Khalid M. Mosalam. June 2002.

PEER 2002/12 *Effects of Fault Dip and Slip Rake on Near-Source Ground Motions: Why Chi-Chi Was a Relatively Mild M7.6 Earthquake.* Brad T. Aagaard, John F. Hall, and Thomas H. Heaton. December 2002.

PEER 2002/11 *Analytical and Experimental Study of Fiber-Reinforced Strip Isolators*. James M. Kelly and Shakhzod M. Takhirov. September 2002.

PEER 2002/10 *Centrifuge Modeling of Settlement and Lateral Spreading with Comparisons to Numerical Analyses***.** Sivapalan Gajan and Bruce L. Kutter. January 2003.

PEER 2002/09 *Documentation and Analysis of Field Case Histories of Seismic Compression during the 1994 Northridge, California, Earthquake.* Jonathan P. Stewart, Patrick M. Smith, Daniel H. Whang, and Jonathan D. Bray. October 2002.

PEER 2002/08 *Component Testing, Stability Analysis and Characterization of Buckling-Restrained Unbonded Braces™.* Cameron Black, Nicos Makris, and Ian Aiken. September 2002.

PEER 2002/07 *Seismic Performance of Pile-Wharf Connections.* Charles W. Roeder, Robert Graff, Jennifer Soderstrom, and Jun Han Yoo. December 2001.

PEER 2002/06 *The Use of Benefit-Cost Analysis for Evaluation of Performance-Based Earthquake Engineering Decisions*. Richard O. Zerbe and Anthony Falit-Baiamonte. September 2001.

PEER 2002/05 *Guidelines, Specifications, and Seismic Performance Characterization of Nonstructural Building Components and Equipment*. André Filiatrault, Constantin Christopoulos, and Christopher Stearns. September 2001.

PEER 2002/04 *Consortium of Organizations for Strong-Motion Observation Systems and the Pacific Earthquake Engineering Research Center Lifelines Program: Invited Workshop on Archiving and Web Dissemination of Geotechnical Data, 4–5 October 2001*. September 2002.

PEER 2002/03 *Investigation of Sensitivity of Building Loss Estimates to Major Uncertain Variables for the Van Nuys Testbed.* Keith A. Porter, James L. Beck, and Rustem V. Shaikhutdinov. August 2002.

PEER 2002/02 *The Third U.S.-Japan Workshop on Performance-Based Earthquake Engineering Methodology for Reinforced Concrete Building Structures*. July 2002.

PEER 2002/01 *Nonstructural Loss Estimation: The UC Berkeley Case Study.* Mary C. Comerio and John C. Stallmeyer. December 2001.

PEER 2001/16 *Statistics of SDF-System Estimate of Roof Displacement for Pushover Analysis of Buildings.* Anil K. Chopra, Rakesh K. Goel, and Chatpan Chintanapakdee. December 2001.

PEER 2001/15 *Damage to Bridges during the 2001 Nisqually Earthquake.* R. Tyler Ranf, Marc O. Eberhard, and Michael P. Berry. November 2001.

PEER 2001/14 *Rocking Response of Equipment Anchored to a Base Foundation.* Nicos Makris and Cameron J. Black. September 2001.

PEER 2001/13 *Modeling Soil Liquefaction Hazards for Performance-Based Earthquake Engineering.* Steven L. Kramer and Ahmed-W. Elgamal. February 2001.

PEER 2001/12 *Development of Geotechnical Capabilities in OpenSees.* Boris Jeremić. September 2001.

PEER 2001/11 *Analytical and Experimental Study of Fiber-Reinforced Elastomeric Isolators*. James M. Kelly and Shakhzod M. Takhirov. September 2001.

PEER 2001/10 *Amplification Factors for Spectral Acceleration in Active Regions.* Jonathan P. Stewart, Andrew H. Liu, Yoojoong Choi, and Mehmet B. Baturay. December 2001.

PEER 2001/09 *Ground Motion Evaluation Procedures for Performance-Based Design.* Jonathan P. Stewart, Shyh-Jeng Chiou, Jonathan D. Bray, Robert W. Graves, Paul G. Somerville, and Norman A. Abrahamson. September 2001.

PEER 2001/08 *Experimental and Computational Evaluation of Reinforced Concrete Bridge Beam-Column Connections for Seismic Performance*. Clay J. Naito, Jack P. Moehle, and Khalid M. Mosalam. November 2001.

PEER 2001/07 *The Rocking Spectrum and the Shortcomings of Design Guidelines.* Nicos Makris and Dimitrios Konstantinidis. August 2001.

PEER 2001/06 *Development of an Electrical Substation Equipment Performance Database for Evaluation of Equipment Fragilities*. Thalia Agnanos. April 1999.

PEER 2001/05 *Stiffness Analysis of Fiber-Reinforced Elastomeric Isolators.* Hsiang-Chuan Tsai and James M. Kelly. May 2001.

PEER 2001/04 *Organizational and Societal Considerations for Performance-Based Earthquake Engineering.* Peter J. May. April 2001.

PEER 2001/03 *A Modal Pushover Analysis Procedure to Estimate Seismic Demands for Buildings: Theory and Preliminary Evaluation.* Anil K. Chopra and Rakesh K. Goel. January 2001.

PEER 2001/02 *Seismic Response Analysis of Highway Overcrossings Including Soil-Structure Interaction.* Jian Zhang and Nicos Makris. March 2001.

PEER 2001/01 *Experimental Study of Large Seismic Steel Beam-to-Column Connections.* Egor P. Popov and Shakhzod M. Takhirov. November 2000.

PEER 2000/10 *The Second U.S.-Japan Workshop on Performance-Based Earthquake Engineering Methodology for Reinforced Concrete Building Structures.* March 2000.

PEER 2000/09 *Structural Engineering Reconnaissance of the August 17, 1999 Earthquake: Kocaeli (Izmit), Turkey.* Halil Sezen, Kenneth J. Elwood, Andrew S. Whittaker, Khalid Mosalam, John J. Wallace, and John F. Stanton. December 2000.

PEER 2000/08 *Behavior of Reinforced Concrete Bridge Columns Having Varying Aspect Ratios and Varying Lengths of Confinement.* Anthony J. Calderone, Dawn E. Lehman, and Jack P. Moehle. January 2001.

PEER 2000/07 *Cover-Plate and Flange-Plate Reinforced Steel Moment-Resisting Connections.* Taejin Kim, Andrew S. Whittaker, Amir S. Gilani, Vitelmo V. Bertero, and Shakhzod M. Takhirov. September 2000.

PEER 2000/06 *Seismic Evaluation and Analysis of 230-kV Disconnect Switches.* Amir S. J. Gilani, Andrew S. Whittaker, Gregory L. Fenves, Chun-Hao Chen, Henry Ho, and Eric Fujisaki. July 2000.

PEER 2000/05 *Performance-Based Evaluation of Exterior Reinforced Concrete Building Joints for Seismic Excitation.* Chandra Clyde, Chris P. Pantelides, and Lawrence D. Reaveley. July 2000.

PEER 2000/04 *An Evaluation of Seismic Energy Demand: An Attenuation Approach.* Chung-Che Chou and Chia-Ming Uang. July 1999.

PEER 2000/03 *Framing Earthquake Retrofitting Decisions: The Case of Hillside Homes in Los Angeles.* Detlof von Winterfeldt, Nels Roselund, and Alicia Kitsuse. March 2000.

PEER 2000/02 *U.S.-Japan Workshop on the Effects of Near-Field Earthquake Shaking.* Andrew Whittaker, ed. July 2000.

PEER 2000/01 *Further Studies on Seismic Interaction in Interconnected Electrical Substation Equipment.* Armen Der Kiureghian, Kee-Jeung Hong, and Jerome L. Sackman. November 1999.

PEER 1999/14 *Seismic Evaluation and Retrofit of 230-kV Porcelain Transformer Bushings.* Amir S. Gilani, Andrew S. Whittaker, Gregory L. Fenves, and Eric Fujisaki. December 1999.

PEER 1999/13 *Building Vulnerability Studies: Modeling and Evaluation of Tilt-up and Steel Reinforced Concrete Buildings.* John W. Wallace, Jonathan P. Stewart, and Andrew S. Whittaker, editors. December 1999.

PEER 1999/12 *Rehabilitation of Nonductile RC Frame Building Using Encasement Plates and Energy-Dissipating Devices.* Mehrdad Sasani, Vitelmo V. Bertero, James C. Anderson. December 1999.

PEER 1999/11 *Performance Evaluation Database for Concrete Bridge Components and Systems under Simulated Seismic Loads.* Yael D. Hose and Frieder Seible. November 1999.

PEER 1999/10 *U.S.-Japan Workshop on Performance-Based Earthquake Engineering Methodology for Reinforced Concrete Building Structures.* December 1999.

PEER 1999/09 *Performance Improvement of Long Period Building Structures Subjected to Severe Pulse-Type Ground Motions.* James C. Anderson, Vitelmo V. Bertero, and Raul Bertero. October 1999.

PEER 1999/08 *Envelopes for Seismic Response Vectors.* Charles Menun and Armen Der Kiureghian. July 1999.

PEER 1999/07 *Documentation of Strengths and Weaknesses of Current Computer Analysis Methods for Seismic Performance of Reinforced Concrete Members.* William F. Cofer. November 1999.

PEER 1999/06 *Rocking Response and Overturning of Anchored Equipment under Seismic Excitations.* Nicos Makris and Jian Zhang. November 1999.

PEER 1999/05 *Seismic Evaluation of 550 kV Porcelain Transformer Bushings.* Amir S. Gilani, Andrew S. Whittaker, Gregory L. Fenves, and Eric Fujisaki. October 1999.

PEER 1999/04 *Adoption and Enforcement of Earthquake Risk-Reduction Measures.* Peter J. May, Raymond J. Burby, T. Jens Feeley, and Robert Wood.

PEER 1999/03 *Task 3 Characterization of Site Response General Site Categories.* Adrian Rodriguez-Marek, Jonathan D. Bray, and Norman Abrahamson. February 1999.

PEER 1999/02 *Capacity-Demand-Diagram Methods for Estimating Seismic Deformation of Inelastic Structures: SDF Systems.* Anil K. Chopra and Rakesh Goel. April 1999.

PEER 1999/01 *Interaction in Interconnected Electrical Substation Equipment Subjected to Earthquake Ground Motions.* Armen Der Kiureghian, Jerome L. Sackman, and Kee-Jeung Hong. February 1999.

PEER 1998/08 *Behavior and Failure Analysis of a Multiple-Frame Highway Bridge in the 1994 Northridge Earthquake.* Gregory L. Fenves and Michael Ellery. December 1998.

PEER 1998/07 *Empirical Evaluation of Inertial Soil-Structure Interaction Effects.* Jonathan P. Stewart, Raymond B. Seed, and Gregory L. Fenves. November 1998.

PEER 1998/06 *Effect of Damping Mechanisms on the Response of Seismic Isolated Structures.* Nicos Makris and Shih-Po Chang. November 1998.

PEER 1998/05 *Rocking Response and Overturning of Equipment under Horizontal Pulse-Type Motions.* Nicos Makris and Yiannis Roussos. October 1998.

PEER 1998/04 *Pacific Earthquake Engineering Research Invitational Workshop Proceedings, May 14–15, 1998: Defining the Links between Planning, Policy Analysis, Economics and Earthquake Engineering.* Mary Comerio and Peter Gordon. September 1998.

PEER 1998/03 *Repair/Upgrade Procedures for Welded Beam to Column Connections.* James C. Anderson and Xiaojing Duan. May 1998.

PEER 1998/02 *Seismic Evaluation of 196 kV Porcelain Transformer Bushings.* Amir S. Gilani, Juan W. Chavez, Gregory L. Fenves, and Andrew S. Whittaker. May 1998.

PEER 1998/01 *Seismic Performance of Well-Confined Concrete Bridge Columns.* Dawn E. Lehman and Jack P. Moehle. December 2000.

ONLINE REPORTS

The following PEER reports are available by Internet only at http://peer.berkeley.edu/publications/peer_reports.html

PEER 2011/101 *Report of the Eighth Planning Meeting of NEES/E-Defense Collaborative Research on Earthquake Engineering.* Convened by the Hyogo Earthquake Engineering Research Center (NIED), NEES Consortium, Inc. February 2011.

PEER 2010/111 *Modeling and Acceptance Criteria for Seismic Design and Analysis of Tall Buildings.* Task 7 Report for the Tall Buildings Initiative - Published jointly by the Applied Technology Council. October 2010.

PEER 2010/110 *Seismic Performance Assessment and Probabilistic Repair Cost Analysis of Precast Concrete Cladding Systems for Multistory Buildlings.* Jeffrey P. Hunt and Božidar Stojadinovic. November 2010.

PEER 2010/109 *Report of the Seventh Joint Planning Meeting of NEES/E-Defense Collaboration on Earthquake Engineering. Held at the E-Defense, Miki, and Shin-Kobe, Japan, September 18–19, 2009.* August 2010.

PEER 2010/108 *Probabilistic Tsunami Hazard in California.* Hong Kie Thio, Paul Somerville, and Jascha Polet, preparers. October 2010.

PEER 2010/107 *Performance and Reliability of Exposed Column Base Plate Connections for Steel Moment-Resisting Frames.* Ady Aviram, Božidar Stojadinovic, and Armen Der Kiureghian. August 2010.

PEER 2010/106 *Verification of Probabilistic Seismic Hazard Analysis Computer Programs.* Patricia Thomas, Ivan Wong, and Norman Abrahamson. May 2010.

PEER 2010/105 *Structural Engineering Reconnaissance of the April 6, 2009, Abruzzo, Italy, Earthquake, and Lessons Learned.* M. Selim Günay and Khalid M. Mosalam. April 2010.

PEER 2010/104 *Simulating the Inelastic Seismic Behavior of Steel Braced Frames, Including the Effects of Low-Cycle Fatigue.* Yuli Huang and Stephen A. Mahin. April 2010.

PEER 2010/103 *Post-Earthquake Traffic Capacity of Modern Bridges in California.* Vesna Terzic and Božidar Stojadinović. March 2010.

PEER 2010/102 *Analysis of Cumulative Absolute Velocity (CAV) and JMA Instrumental Seismic Intensity (I_{JMA}) Using the PEER–NGA Strong Motion Database.* Kenneth W. Campbell and Yousef Bozorgnia. February 2010.

PEER 2010/101 *Rocking Response of Bridges on Shallow Foundations.* Jose A. Ugalde, Bruce L. Kutter, Boris Jeremic

PEER 2009/109 *Simulation and Performance-Based Earthquake Engineering Assessment of Self-Centering Post-Tensioned Concrete Bridge Systems.* Won K. Lee and Sarah L. Billington. December 2009.

PEER 2009/108 *PEER Lifelines Geotechnical Virtual Data Center.* J. Carl Stepp, Daniel J. Ponti, Loren L. Turner, Jennifer N. Swift, Sean Devlin, Yang Zhu, Jean Benoit, and John Bobbitt. September 2009.

PEER 2009/107 *Experimental and Computational Evaluation of Current and Innovative In-Span Hinge Details in Reinforced Concrete Box-Girder Bridges: Part 2: Post-Test Analysis and Design Recommendations.* Matias A. Hube and Khalid M. Mosalam. December 2009.

PEER 2009/106 *Shear Strength Models of Exterior Beam-Column Joints without Transverse Reinforcement.* Sangjoon Park and Khalid M. Mosalam. November 2009.

PEER 2009/105 *Reduced Uncertainty of Ground Motion Prediction Equations through Bayesian Variance Analysis.* Robb Eric S. Moss. November 2009.

PEER 2009/104 *Advanced Implementation of Hybrid Simulation.* Andreas H. Schellenberg, Stephen A. Mahin, Gregory L. Fenves. November 2009.

PEER 2009/103 *Performance Evaluation of Innovative Steel Braced Frames.* T. Y. Yang, Jack P. Moehle, and Božidar Stojadinovic. August 2009.

PEER 2009/102 *Reinvestigation of Liquefaction and Nonliquefaction Case Histories from the 1976 Tangshan Earthquake.* Robb Eric Moss, Robert E. Kayen, Liyuan Tong, Songyu Liu, Guojun Cai, and Jiaer Wu. August 2009.

PEER 2009/101 *Report of the First Joint Planning Meeting for the Second Phase of NEES/E-Defense Collaborative Research on Earthquake Engineering.* Stephen A. Mahin et al. July 2009.

PEER 2008/104 *Experimental and Analytical Study of the Seismic Performance of Retaining Structures.* Linda Al Atik and Nicholas Sitar. January 2009.

PEER 2008/103 *Experimental and Computational Evaluation of Current and Innovative In-Span Hinge Details in Reinforced Concrete Box-Girder Bridges. Part 1: Experimental Findings and Pre-Test Analysis.* Matias A. Hube and Khalid M. Mosalam. January 2009.

PEER 2008/102 *Modeling of Unreinforced Masonry Infill Walls Considering In-Plane and Out-of-Plane Interaction.* Stephen Kadysiewski and Khalid M. Mosalam. January 2009.

PEER 2008/101 *Seismic Performance Objectives for Tall Buildings.* William T. Holmes, Charles Kircher, William Petak, and Nabih Youssef. August 2008.

PEER 2007/101 *Generalized Hybrid Simulation Framework for Structural Systems Subjected to Seismic Loading.* Tarek Elkhoraibi and Khalid M. Mosalam. July 2007.

PEER 2007/100 *Seismic Evaluation of Reinforced Concrete Buildings Including Effects of Masonry Infill Walls.* Alidad Hashemi and Khalid M. Mosalam. July 2007.

The Pacific Earthquake Engineering Research Center (PEER) is a multi-institutional research and education center with headquarters at the University of California, Berkeley. Investigators from over 20 universities, several consulting companies, and researchers at various state and federal government agencies contribute to research programs focused on performance-based earthquake engineering.

These research programs aim to identify and reduce the risks from major earthquakes to life safety and to the economy by including research in a wide variety of disciplines including structural and geotechnical engineering, geology/seismology, lifelines, transportation, architecture, economics, risk management, and public policy.

PEER is supported by federal, state, local, and regional agencies, together with industry partners.

PEER reports can be ordered at http://peer.berkeley.edu/publications/peer_reports.html or by contacting

Pacific Earthquake Engineering Research Center
University of California, Berkeley
325 Davis Hall, mail code 1792
Berkeley, CA 94720-1792
Tel: 510-642-3437
Fax: 510-642-1655
Email: peer_editor@berkeley.edu

ISSN 1547-0587X